

DISS. ETH NO. 21073

StarlETH & Co. – Design and Control of Legged Robots with Compliant Actuation

A dissertation submitted to

ETH ZURICH

for the degree of

Doctor of Sciences

presented by

Marco Hutter

Master of Science in Mechanical Engineering
ETH Zurich, Switzerland

Born August 10th, 1985
Citizen of Oberriet-Kriessern SG, Switzerland

accepted on the recommendation of

Prof. Roland Siegwart, ETH Zurich
Prof. Oussama Khatib, Stanford University
Prof. Rolf Pfeifer, University of Zurich
Prof. Jonas Buchli, ETH Zurich

2013

Acknowledgments

First of all, I would like to thank my supervisor and mentor, Roland Siegwart for giving me the opportunity to do a PhD at the Autonomous Systems Lab (ASL). It was a terrific time with amazing people not only as researchers but also as friends. I want to thank Oussama Khatib for giving me the unique opportunity to spend time at the Artificial Intelligence Lab in Stanford. I got to know a new research area that fundamentally directed me into the right channels. I'm also proud and grateful that Rolf Pfeifer (University of Zurich), a leading expert in this field, agreed to join my committee. A big thanks goes also to Jonas Buchli for many fruitful discussions (at interesting locations and situations) and for establishing valuable collaborations with the robotics groups at USC and IIT.

In terms of funding, the research for this dissertation was supported by the Swiss National Science Foundation (SNF) through the National Centre of Competence in Research Robotics and through project 200021_119965/1, as well as through the Hans-Eggenberger-Foundation that paid for a big part of the hardware development.

This work would not have been possible without the contributions and support of countless people. These are, first and foremost, the other and former members of our group, Mark H. Höpfinger, Christian Gehring, Michael Blösch, David Remy, and very recently Péter Fankhauser, who I wish to thank for the intensive collaboration and all the fun that we had over the past years at the KKZ. They are great colleagues and I'm looking forward to continue working with them! I further thank Hannes Sommer for his help with some mathematical proofs. A special thanks goes also to the collaborators during my time in Stanford Samir Menon, Rolo Philippsen, and Luis Sentis for interesting discussions about whole-body control as well as to Claudio Semini, legged robots chief engineer at the time at IIT, for helpful exchange of design ideas.

During my time at ETH I also had the chance to collaborate with a large number of undergraduate and graduate students who helped trying out new

ideas. For their trust in choosing me as their supervisor and their contributions I would particularly like to thank Sebastian Altwegg, Soumaya Amri, Michael Blösch, Markus Brändle, Péter Fankhauser, Christian Gehring, Stefan Haag, Claude Hostenstein, Jemin Hwangbo, Andreas Ioannides, Lea Koch, Martin Latta, Andreas Lauber, Alex Liniger, Fabio Löhr, Thomas Mantel, Marco Morales, Dominik Näf, Philip Omlin, Astrid Schlestein, Remo Ughini, Thomas Wartmann, and all the members of the focus teams Pegasus and ARAC.

For their help in building prototypes and the exceptional quality of their work, I would like to thank Thomas Baumgartner, Stefan Bertschi, Markus Bühler, Dario Fenner, and Martin Latta. Without the support of these people, none of our hardware developments would have been possible, and we would never have reached the level of quality at which we are now. A special thanks goes also to Mischa Kolbe for making an awesome microlecture movie about our research. Similarly, I want to thank the administrative staff of the ASL, Cornelia Della Casa, Margot Fox, Eve Lassere, but foremost Luciana Borsatti, for making our life easier.

And finally, I am deeply grateful to my family, Tanja, Jimmy and all the (non-research) friends for all the support they gave me to reach this point.

Zurich, March 2013

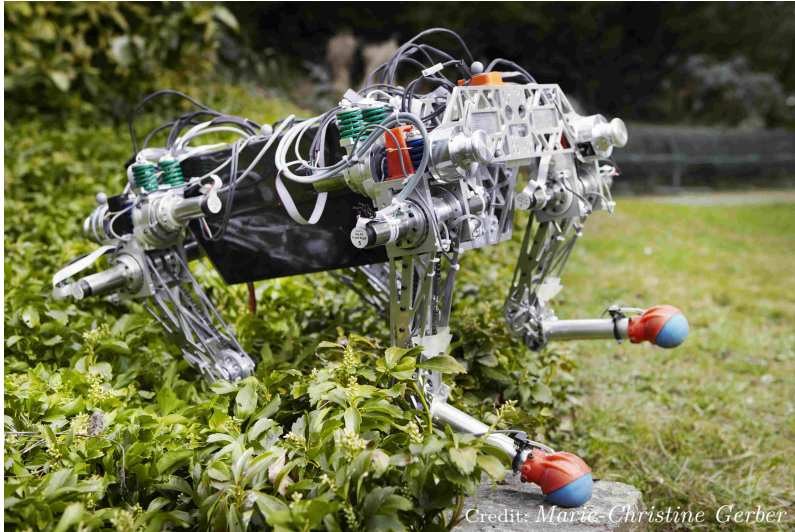
Abstract

The present dissertation addresses the design and control of a quadrupedal robot that achieves locomotion skills ranging from static walking to dynamic running. By combining novel techniques in the field of *system design*, *actuation*, and *control*, this work is a step towards closing the gap between legged robotic devices and their natural counterparts.

Inspired by nature, where elastic elements in muscles and tendons largely contribute to the impressive locomotion capabilities, the quadruped robot StarLETH is built mechanically compliant. In each of the twelve joints, serial springs provide the necessary robustness to perform dynamic maneuvers. They improve energetic efficiency by intermittently storing energy, and they enable precise torque control for elaborate interaction with the environment. We specifically engineer the mechanical properties of the actuators to support the natural dynamics of running gaits and provide low-level control techniques to precisely regulate the joint torque and position.

The performance of the applied design, actuation, and low-level control approach is evaluated in planar single leg hopping experiments. To this end, the motion is generated and stabilized by emulating bio-inspired locomotion templates. Thereby, the leg can passively recover as much as 64% of the energy, while the peak power and speed at the joint are more than four times higher than at the corresponding motor. These findings are highly consistent with different biomechanical studies and the underlying control principles can be directly extended to multi-legged systems.

Legged systems continuously interact with their surroundings through multiple permanently changing contact points in order to keep balance or propel themselves forward. Dealing with the corresponding high-dimensional, nonlinear, non-smooth and underactuated system dynamics represents a very challenging control problem. In this context, we present a hierarchical task-space inverse dynamics framework that is based on projected, support consistent equations of motion. Using prioritized least square optimization, the complex behavior of a robotic system evolves through simultaneous execu-



tion of different motion tasks such as ensuring stability, moving a foot point, or keeping certain posture while optimally distributing the joint torques or contact forces.

The proposed method is evaluated in a series of experiments on the developed quadrupedal robot StarETH. Static locomotion is optimized with respect to energetic efficiency or robustness against slippage while handling position and torque saturation limitations. Even on rough terrain, the robot can robustly walk by exploiting internal force directions. It can smoothly change its contact situation by interpolating between subsequent stance configurations. Building on similar principles as for single legged hopping, the quadruped is able to perform dynamic trotting gaits even under substantial external disturbances such as an unanticipated change in ground elevation or a kick on the main body. The experimental section is concluded with energetic measurements during long term trotting and followed by a discussion and comparison with the biological counterparts.

Keywords: Quadruped Robot, High Compliant Series Elastic Actuation, Hierarchical Operational Space Control, Inverse Dynamics, Dynamic Locomotion

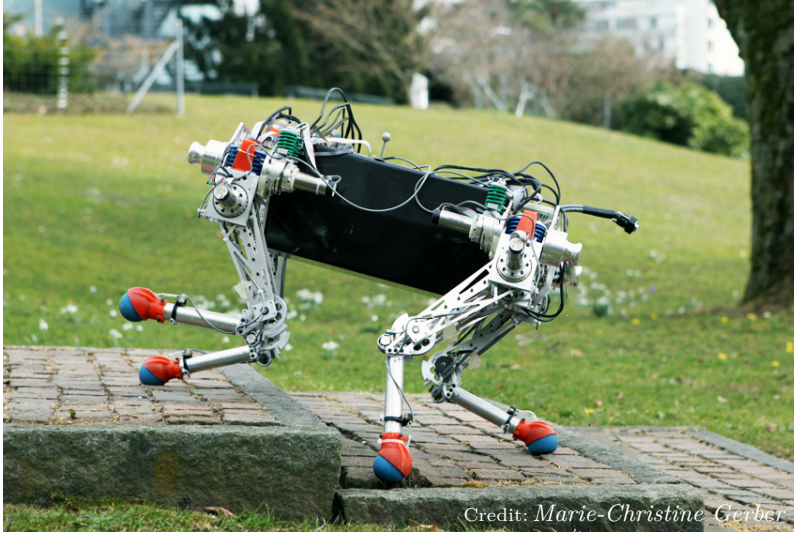
Kurzfassung

Die vorliegende Arbeit beschäftigt sich mit der Konstruktion und Regelung eines vierbeinigen Roboters, welcher sich sowohl langsam und statisch in unwegsamem Gelände fortbewegen kann, gleichermassen aber auch fähig ist, dynamisch zu rennen. Durch Einsatz modernster Methoden aus den Bereichen Systemdesign, Antriebs- und Regelungstechnik ist es gelungen, die Laufrobotik einen Schritt näher an die Biologie zu bringen.

Bei der Konzipierung unseres Roboterhundes Star*LETH* liessen wir uns von der Natur inspirieren. Anstelle von Muskeln und Sehnen, welche durch ihre Federwirkungen erheblich zu einer schnellen und energieeffizienten Fortbewegung beitragen, ist Star*LETH* mit Federn in Serie zu den Gelenksmotoren ausgestattet. Dies stellt die nötige Robustheit für dynamische Manöver sicher, erhöht die Energieeffizienz beim Rennen durch zwischenzeitliche Energiespeicherung und ermöglicht eine sehr fortschrittliche Interaktion mit der Umgebung dank präziser Kraftregelung. Die mechanischen Eigenschaften dieser Federn sind so optimiert, dass sie die natürliche Systemdynamik von dynamischen Gangarten maximal unterstützen.

Die Leistungsfähigkeit des mechanischen Designs, der Serie-elastischen Aktuatoren, sowie der Regelstrukturen wurde zuerst in Experimenten mit einem einzelnen Bein evaluiert. Durch Nachbilden einer stark vereinfachten Dynamik des menschlichen Rennens konnten planare Hüpfbewegungen generiert und stabilisiert werden. Dank der Federn wird 64% der Energie passiv rückgewonnen und gleichzeitig werden Spitzengeschwindigkeiten und -leistungen am Gelenk mehr als vervierfacht. Die Resultate zeigen erstaunliche Ähnlichkeiten zu verschiedenen biomechanischen Studien und können direkt auf mehrbeinige Systeme übertragen werden.

Laufroboter interagieren an ständig wechselnden Kontaktpunkten mit der Umgebung um sich fortzubewegen und zu stabilisieren. Für die Regelung dieser hochdimensionalen, nicht-linearen, nicht-glatten und unteraktuierten Systemdynamik haben wir eine Methode entwickelt, welche auf einer Invertierung der Kontakt-konsistenten Systemdynamik basiert. Dazu werden



die verschiedenen Aufgaben wie Balance halten, einen Fusspunkt verschieben, eine gewisse Haltung einnehmen oder auch Kontaktkräfte und Motormomente optimal verteilen als Fehlerquadratminimierungen ausgedrückt und mit unterschiedlichen Prioritäten behandelt.

Diese Regelstruktur wurde folglich in einer Vielzahl von Experimenten mit StarLETH getestet. So kann zum Beispiel eine Gangart auf Motoreffizienz oder Sicherheit gegen Rutschen der Fusspunkte optimiert werden. Gleichzeitig garantiert unser Algorithmus, dass Drehmoment- und Winkel-limitierungen eingehalten werden. Durch das Aufbringen von internen Kontaktkräften ist der Roboter sogar fähig, sich während statischem Gehen auf unebenem Gelände festzuhalten und mittels Interpolation eine kontinuierliche Kraft- und Drehmomentverteilung trotz ständig wechselnden Kontaktpunkten zu erreichen. StarLETH beherrscht nicht nur statische Gangarten, sondern kann auch schnell und dynamisch trotten, selbst unter Einfluss von erheblichen Störungen wie Erhebungen im Boden oder externen Stößen. Der experimentelle Teil wird abgerundet mit Energiemessungen beim Trotten über eine längere Distanz. Schlussendlich werden alle Resultate in der Diskussion nochmals aufgegriffen und mit biomechanischen Studien verglichen.

Stichworte: vierbeiniger Roboter, Serie-elastische Aktuatoren, hierarchische Regelung, inverse Dynamik, dynamisches Laufen

List of Symbols

System modeling

n_q	number of generalized coordinates
n_b	number of un-actuated base coordinates
n_r	number of actuated joint coordinates
n_s	number of active contacts
n_u	number of <i>truly-underactuated</i> coordinates
n_c	number of <i>overconstrained</i> directions
n_m	number of minimal coordinates
\mathbf{q}	generalized coordinates
\mathbf{q}_b	generalized base coordinates
\mathbf{q}_r	generalized joint coordinates
τ	actuator torque
\mathbf{S}	actuated joint selection matrix
\mathbf{M}	mass matrix
\mathbf{h}	sum of Coriolis, centrifugal and gravitational forces
\mathbf{J}	Jacobian
\mathbf{J}_R	rotational Jacobian
\mathbf{F}_s	contact force vector
\mathcal{F}_s	contact impulse vector
\mathbf{r}	position vector
\mathbf{p}	impulse vector
\mathbf{L}	angular momentum
Ω_i	angular velocity of body i
δ	variational delta
\mathbf{N}_s	support null-space projector
$\mathcal{N}()$	null-space operator
\mathbf{P}	generalized projector on constraint consistent manifold
τ_0	null-space torque
ξ	minimal coordinates

Least square problem

\mathbf{A}	task matrix
\mathbf{N}	null space projector matrix
\mathbf{b}	task vector
\mathbf{x}	optimization variable
\mathbf{W}	cost weighting matrix
n_T	number of (linear) tasks

SLIP template

k_σ	SLIP stiffness
α_σ	SLIP angle of attack
l_σ	SLIP leg length during flight
m_σ	SLIP lumped point mass parameter

System parameters

k_{HAA}	joint stiffness in HAA, HFE, KFE, AFE
l_i	length of segment i
s_i	distance joint to COG of segment i
θ, Θ	inertia value and tensor of body i w.r.t. COG_i
m_i	mass of segment i
φ_j	joint angle
φ_{gb}	gearbox angle
φ_m	motor angle
δ_s	spring deflection
k_{SEA}, d_{SEA}	stiffness and damping of the series elasticity
τ_j	spring resp. joint torque
$\hat{\delta}$	spring deflection amplitude
\bar{x}_p	spring pre-compression
E_{kin}	kinetic energy
m_F	mass of the spring in the shank
r_P	knee pulley radius
h_{HC}	height hip center
r_F	relative foot position
κ_a	motor torque constant
κ_i	speed constant
L_a	motor inductance
R	motor resistance
U_a	motor voltage
I_m	motor current

θ_m	motor and gearbox inertia
γ_{gb}	gearbox transmission ratio
η_{gb}	gearbox efficiency
I_0	no load current
n_0	no load speed
k_p^{cur}, k_i^{cur}	proportional, integral gain current loop
k_p^{vel}, k_i^{vel}	proportional, integral gain velocity loop
$k_p^\tau, k_i^\tau, k_d^\tau$	proportional, integral and derivative gain torque loop
$k_1^\varphi, k_2^\varphi, k_3^\varphi$	LQR gains for joint position control

Control

L	open loop transfer function
T	complementary sensitivity (closed loop transfer function)
S	sensitivity
C	controller transfer function
P	plant transfer function
Z	impedance
K	dynamic stiffness

Subscripts and superscripts

B, b	base
H	hip
S	shank
T	thigh
HC	hip center
*	periodic solutions
-, +	value prior/after to an event
m	motor
j	joint
gb	gearbox
s	support
p_i	arbitrary point
v	virtual
g	gravitational
N	relative normal direction

Acronyms

AFE	ankle flexion/extension
ASL	Autonomous Systems Laboratory
BVP	boundary value problem
BW	bandwidth
CAD	computer aided design
CAN	controller area network
COG	center of gravity
COP	center of pressure
COT	cost of transport
DARPA	Defense Advanced Research Projects Agency
DOF	degrees of freedom
EOM	equations of motion
ETH	Eidgenössische Technische Hochschule
GIE	generalized inertia ellipsoid
GRF	ground reaction force
HAA	hip abduction/adduction
HD	harmonic drive
HFE	hip flexion/extension
IMU	inertial measurement unit
KFE	knee flexion/extension

LCP	linear complementary problem
LF	left-front
LH	left-hind
LIP	linear inverted pendulum
LiPo	Lithium polymer battery
LQR	linear quadratic regulator
MBS	multi-body system
NCCR	National Centre of Competence in Research
OSC	operational space control
PDW	passive dynamic walking/walker
PDR	passive dynamic running/runner
PI²	policy improvement with path integrals
QP	quadratic program
RF	right-front
RH	right-hind
ROS	robot operating system
SDA	series damping actuator
SEA	series elastic actuator
SL	simulation laboratory
SLIP	spring loaded inverted pendulum
SLIPic	spring loaded inverted pendulum with impact compensation
SNF	Swiss National Science Foundation
Star¹ETH	springy tetrapod with articulated robotic legs
SVD	singular value decomposition
TF	transfer function
VMC	virtual model control

Contents

1	Introduction	1
1.1	Motivation and Objectives	2
1.2	State of the Art in Legged Robotics	5
1.2.1	Design and Actuation Principles	5
1.2.2	Control	9
1.3	Approach and Contribution	12
1.4	Thesis Outline	14
2	System Modeling	15
2.1	Floating Base Multi-Body Dynamics	16
2.2	Contact Models	17
2.2.1	Soft Contact	17
2.2.2	Hard Contact	18
2.3	Constraint Consistent Dynamics	19
2.3.1	Constraint Projector	19
2.3.2	Minimal Coordinates	21
2.4	Contact Switches and Impact Collisions	22
2.4.1	Impulse Transfer	23
2.4.2	Energy Loss	23
2.5	Analytical Representation	24
2.6	Summary	25
3	System Design	27
3.1	Star <i>LETH</i> - a Compliant Quadruped Robot	28
3.1.1	Why Quadrupeds?	28
3.1.2	Dimension and Structure	29
3.1.3	Main Body Design	30
3.1.4	Leg Configuration	30
3.2	Single Leg Design	32

3.2.1	Mechanical Structure	32
3.2.2	Modular Foot Design	33
3.3	Actuator Design	36
3.3.1	Possible Arrangements	37
3.3.2	Hardware Realization	38
3.4	Electronics	40
3.5	Software	41
3.5.1	Analytical Kinematics and Dynamics	42
3.5.2	State Estimation	42
3.6	Summary	42
4	Low-Level SEA Control	43
4.1	Control Structure	44
4.1.1	Motor as a Torque Source	44
4.1.2	Motor as a Position Source	45
4.1.3	Implementation	45
4.2	Joint Torque Control	47
4.2.1	PI Feedback Control	48
4.2.2	Velocity Feedforward Compensation	49
4.2.3	Stability and Passivity	50
4.3	Joint Position Control	51
4.3.1	Disturbance Modeling	52
4.3.2	LQR Control	52
4.4	Hardware Optimization	54
4.4.1	Exploiting Internal Collisions	54
4.4.2	Combined SEA and SDA Setup	56
4.4.3	Comparison	57
4.5	Summary	58
5	Model-Based Locomotion Control	59
5.1	Generalized Virtual Model Control	60
5.2	Inverse Dynamics of Floating Base Systems	61
5.3	Hierarchical Least Square Optimization	64
5.3.1	Iterative Null-Space Projection	64
5.3.2	Sequence of Constrained Optimization	66
5.3.3	Inequality Constraints	66
5.4	Sequential Hierarchical OSC	67
5.4.1	Motion Optimization	67
5.4.2	Force/Torque Optimization	68
5.4.3	Relation to Other Work	68
5.4.4	Advantages and Drawbacks	69

5.5	Combined Hierarchical OSC	70
5.5.1	Relation to Other Work	71
5.5.2	Advantages and Drawbacks	71
5.6	Hybrid OSC	72
5.6.1	Problem Description	72
5.6.2	Disturbance Compensation Task	73
5.7	Summary	74
6	Motion Generation	75
6.1	SLIP Template	76
6.1.1	Self-Stability and Dead-Beat Control	77
6.1.2	Template of an Articulated Leg	80
6.2	Dynamic Gaits	82
6.2.1	Single Leg Locomotion	83
6.2.2	Quadrupedal Locomotion	83
6.3	Static Gaits	85
6.4	Summary	86
7	Single Leg Experiments	87
7.1	Experimental Setup	88
7.2	Single Leg Running Control	89
7.2.1	Virtual Model Control	89
7.2.2	Task-Space Inverse Dynamics	90
7.2.3	Optimization and Learning	91
7.3	Locomotion with Point Foot	93
7.3.1	Controllability	93
7.3.2	Efficiency	94
7.3.3	Mechanical Limitations	95
7.4	Locomotion with Foot Element	97
7.4.1	Ankle Joint Stiffness and Control Optimization	97
7.4.2	Experimental Validation	99
7.5	Summary	100
8	Quadruped Experiments	101
8.1	Experimental Setup	102
8.2	Performance Evaluation	103
8.2.1	Payload	103
8.2.2	Robustness	104
8.3	Static Gaits	106
8.3.1	Actuator Efficiency Optimization	107
8.3.2	Contact Force Optimization	108

8.3.3	Joint Torque Limitation	108
8.3.4	Joint Position Limitation	109
8.3.5	Terrain Dependent Optimization	112
8.3.6	Smooth Contact Force Distribution	114
8.3.7	Hybrid OSC	115
8.4	Dynamic Gaits	116
8.4.1	Running and Walking Trot	118
8.4.2	Contact Force and Joint Torque Optimization	119
8.4.3	Stability and Robustness	120
8.4.4	Energy Consumption	120
8.5	Summary	122
9	Discussion and Conclusion	123
9.1	Discussion of Contributions	123
9.1.1	Compliant Design	123
9.1.2	SEA Control	124
9.1.3	Model-Based Locomotion Control	125
9.2	Comparison to Biology	125
9.3	Future Work	127
A	Appendix	129
A.1	Global Optimality for a Hierarchical Least Square Optimization	130
A.2	Block Matrix Pseudo-Inversion	133
A.3	Kinetic Energy Loss	135
A.4	Null-Space Calculation using SVD	136
A.5	Relation to Prioritized OSC	137
A.6	Hybrid OSC – Simplification for End-Effector Control	139
A.6.1	Preamble and Notation	139
A.6.2	Generic Hybrid OSC	139
A.6.3	End-Effector Simplification	140
A.7	Spring Characteristics	142
A.8	Internal Collision in Unidirectional Spring	143
A.8.1	Impulsive Change in Speed	143
A.8.2	Reduction in Oscillation Amplitude	144
A.8.3	Reduction in Oscillation Period	145
A.9	Choice of Task-Space Control Gains	146
	Bibliography	147
	Curriculum Vitae	167
	List of Publications	168

List of Tables

3.1	Specifications of Starl <i>ETH</i>	30
8.1	Static walking experiments with different optimization objectives	107
8.2	Motion task priorities for dynamic locomotion with Starl <i>ETH</i> .	116

List of Figures

1.1	Traditional quadrupedal robots with electric actuation	2
1.2	Legged robots exploiting passive dynamics	3
1.3	Hydraulic quadrupedal robots of Boston Dynamics and IIT .	5
1.4	Electrically actuated quadrupeds with compliant elements . .	7
1.5	Application of SEAs in torque controlled robots and prostheses	8
1.6	Thesis contribution	13
2.1	Kinematic representation of a floating base system	16
3.1	Star <i>LETH</i> : a compliant quadruped for dynamic locomotion. .	27
3.2	Kinematic structure and dimensions of Star <i>LETH</i>	29
3.3	Different leg configurations of Star <i>LETH</i>	31
3.4	System description of a planar leg version	33
3.5	Compliant ball foot with contact sensor	34
3.6	Lightweight foot with passive compliant ankle joint	35
3.7	Possible SEA arrangements	37
3.8	CAD visualization of HAA, HFE, and KFE actuators	39
3.9	Electronics and real-time simulation and control environment	40
4.1	High and low output mass model	44
4.2	Cascaded SEA control structure	46
4.3	SEA feedback torque control performance	48
4.4	SEA feedforward compensator for improved impedance	49
4.5	Stability and passivity of torque control	51
4.6	LQR joint position control for active damping	52
4.7	SEA position control performance	53
4.8	Internal collisions in a uni-directionally loaded spring	54
4.9	Phase shortening and higher damping	55
4.10	Combined SEA-SDA arrangement	56
4.11	Experiments with the combined SEA-SDA actuator	57

5.1	Truly-underactuated and over-constrained support configuration	63
5.2	Global optimality in convex and non-convex problems	67
5.3	Typical signal flow for position tracking in an OSC framework	72
6.1	SLIP running on uneven ground	77
6.2	Fixed point stability of controlled and uncontrolled running .	79
6.3	Stability analysis of SLIP with impact compensation	81
6.4	Acceleration control by foot-placement	82
6.5	Foot positioning in dynamic gaits	84
6.6	Foothold and COG trajectory generation in static gaits . . .	85
7.1	Planar single leg test bench setup	88
7.2	2D single leg running experiment	93
7.3	Hopping experiments to study energetic efficiency	94
7.4	Impact analysis of planar hopping	96
7.5	Numerical optimization of the ankle stiffness and actuator input	98
7.6	Hopping experiments with a passive ankle joint	99
8.1	Experimental setting for Star <i>LETH</i>	103
8.2	Payload evaluation in standup experiment	104
8.3	Robustness evaluation in a drop experiment	105
8.4	Joint torque distribution w/ and w/o torque limitation	109
8.5	Motion disturbance due to torque limitation	110
8.6	Compensation for joint angle limitation	111
8.7	Static walking experiment on a half-cylinder	113
8.8	Contact force interpolation	114
8.9	Swing leg compensation in hybrid OSC	115
8.10	Picture series of a trotting gait	117
8.11	Experimental data of a walking and running trot	118
8.12	Force and torque distribution in a trotting gait	119
8.13	External disturbance while trotting	121
9.1	Muscle contraction and power in steady state running	126
A.1	Identified spring characteristics of HFE and KFE	142
A.2	Illustration of phase shortening	145

Chapter 1

Introduction

Research in legged robotics has always fascinated mankind with the idea to build systems that are not tied to streets or artificial environments but that can operate virtually anywhere. 45 years after the first autonomous walking robot (Frank, 1968; McGhee, 1967, Figure 1.1(a)), this field currently faces a large push from an increasing demand for robotic solutions that step out of a factory building and support us in our daily life. Boosted by technological advances, but also called for by recent environmental disasters (e.g. Fukushima 2011), different large-scale projects (e.g. DARPA’s Robotics Challenge) are starting to support the existing research community towards closing the performance gap between robots and their biological counterparts. From a research point of view, we can identify four important properties that need to be commonly improved with novel legged robots: *versatility*, *speed*, *efficiency*, and *robustness*. These systems should offer different modes of locomotion spanning the range from running to climbing. They should be able to robustly interact with the environment and to cope with significant uncertainties or disturbances, while at the same time using only small amount of energy to quickly propel them forward.

Animals and humans unite these coarse specifications in perfection. We can move in rough and highly unstructured terrain, can easily climb over obstacles the size of our leg length, or move along steep slopes by carefully selecting footholds and precisely moving our limbs to keep balance at all times. On less demanding surfaces, however, we switch to periodic gaits (such as walking or running) which are largely driven by the natural dynamics of our mechanical structure (Cavagna et al., 1977; Dickinson et al., 2000) and are hence fast and energetically efficient. Unifying all this in a single robotic device poses fundamental challenges to *system design*, *actuation*, and *control*.

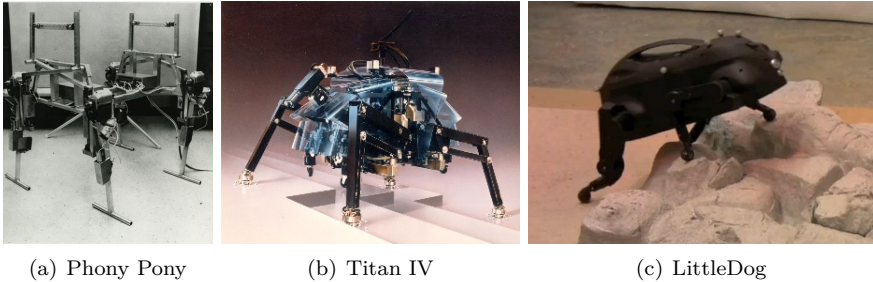


Figure 1.1: Traditional quadrupedal robots such as Phony Pony (Frank, 1968), the Titan series (Hodoshima et al., 2004), or Little Dog (Murphy et al., 2010) are built with a stiff drive train making them unsuited for dynamic maneuvers.

1.1 Motivation and Objectives

Over the past decades, the robotics community was able to successfully reduce the performance gap between robots and nature in terms of *versatility* by building on their strong background in industrial robotic arms. The resulting humanoids (e.g. Honda’s ASIMO (Sakagami et al., 2002), Toyota’s humanoid (Tajima et al., 2009), the HRP series (Hirukawa et al., 2005)) or quadrupedal machines (e.g. TITAN series (Hodoshima et al., 2004, Figure 1.1(b)), LittleDog (Murphy et al., 2010, Figure 1.1(c)), ALoF (Remy et al., 2011a)) are built mechanically rigid and are driven by stiff actuators with large gearbox transmissions and high-gain controllers. The rigid structure cancels out any undesired dynamic effect (i.e. passive oscillations) and allows precisely following preplanned kinematic joint trajectories. To extend the field of application beyond a deterministic environment with perfect motion planning and execution, these robotic devices are more and more equipped with extensive (and expensive) force/torque sensor technologies and corresponding control capabilities. This paradigm shift from position to force/torque control opens new capabilities to interact with other robots or with its surrounding (Ott et al., 2006). While enabling a large variety of motion skills, the “stiff” robot concept has a substantial drawback that is reflected in terms of robustness and efficiency. The lack of robustness becomes particularly apparent in highly dynamic maneuvers. Peak loads occurring at the intermittent ground contacts harm the gearboxes and force/torque sensors since the system is unable to passively adapt to this interaction to prevent damage to themselves or their surroundings. Joints and links are neither backdrivable nor decoupled and

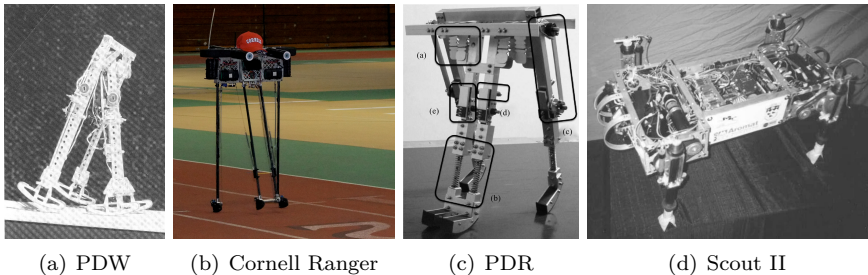


Figure 1.2: Passive dynamics was extensively studied in so called passive dynamic walkers (McGeer, 1990a) and the same principles were adopted by the Cornell Ranger setting the world record in efficient long distance walking (Bhounsule et al., 2012). The integration of springs enables passive running (Owaki et al., 2011) and opens large possibilities to achieve efficient and fast dynamic locomotion with quadrupeds (e.g. Scout II developed by Battaglia, 1999)

hence the entire inertia of the rigidly connected system is seen at the end-effector. This can be a safety problem both for the robot and its environment. Low energetic efficiency results from the fact that “stiff” actuation principles allow in practice only for a unidirectional energy conversion. There are no means for intermittent energy storage or recuperation and the entire power required at the joints has to be actively delivered by the drive train. As a result, locomotion can be compared to stop-and-go traffic in the city. Moreover, the high peak power to accelerate requires powerful and large actuators which makes the system unnecessarily big and heavy.

In contrast thereto, the high energetic *efficiency* and locomotion *speed* found in nature can be attributed to a large extent to the exploitation of passive pendulum- and spring dynamics (Alexander, 2003; Geyer et al., 2006; Kuo, 2001). The pendulum motion passively supports the swing leg phase while walking such that nearly no torque at the hip joint is required to move the leg forward. This principle was adapted in so called passive dynamic walkers (PDW) introduced by McGeer (1990a,b, Figure 1.2(a)) and was lately extensively exploited when the Cornell Ranger was setting the world record in long distance walking with a low cost of transport (Bhounsule et al., 2012, Figure 1.2(b)). Passive spring dynamics on the other hand evolve due to compliant elements in muscles and tendons that allow for mechanical storage of potential energy after landing and to release it again before lift-off (Alexander, 1990; Cavagna et al., 1964). As outlined by Alexander (2002), the exploitation of these elastic properties has a beneficial impact in three

ways. First, intermittent energy storage allows reducing the metabolic cost of locomotion. Second, as the tendons can recoil elastically much faster than muscles can shorten, animals can jump further due to an increased peak power. Third, tendon elasticity affects the control of muscles, enhancing force control at the expense of position control. These biomechanical findings initiated a fundamental shift in the development of robotic systems for dynamic maneuvers away from the classical paradigm “the stiffer, the better”. Along the lines of Raibert’s seminal work on hopping robots based on pneumatic pistons (Raibert, 1986), these principles were adopted by the community to develop robotic legs that use mechanical springs not only to protect the system from landing impact but also to enable dynamic gaits by means of temporary energy storage. As an augmentation of PDWs, implementing mechanical springs can even enable passive dynamic running (PDR) (Owaki et al., 2011, Figure 1.2(c)) or support efficient and fast locomotion of legged machines (e.g. Battaglia, 1999, Figure 1.2(d)). Unfortunately, compliant robots that exploit natural dynamics are inherently hard to control and are thus gravely limited with respect to their application, respectively *versatility*.

So far, the presented systems and solution share one substantial drawback: They either solve the *versatility* OR the *efficiency* problem, but to the best of our knowledge, legged robotic devices that unite both properties are still not available. One of the main reasons is that combining these fields requires joint effort from a design and control engineering point of view. This strongly motivated us to address these topics by a hand-in-hand development of legged systems, actuation principles, and control structures. Our goal is to provide the research community with an inherently compliant and fully torque controllable legged system. To this end, we developed the quadrupedal platform Star $LETH$ (Springy Tetrapod with Articulated Robotic Legs). The four-legged setup enables a large diversity in gaits or modes of locomotion that ranges from static walking with at least three simultaneous contact points to highly dynamic running gaits with a full flight phase. We jointly developed the mechanics and control principles of compliant and very robust series elastic actuators that allow for precise joint torque and position control as well as for energy storage and hence exploitation of the system’s natural dynamics. Such engineering advances open wide opportunities for us roboticists to develop and study various novel control concepts and to bring them from simulations into hardware applications. It further fosters the understanding of locomotion principles found in nature and represents a small step towards closing the existing gap between legged robots and the natural counterparts.

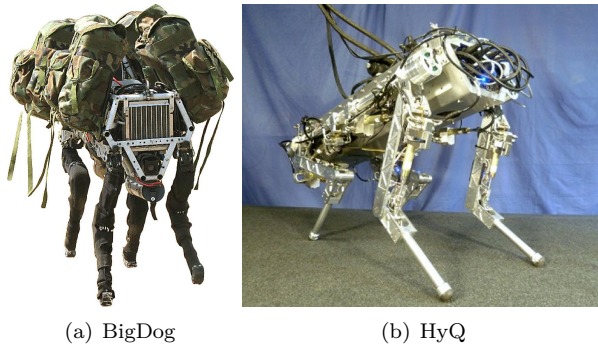


Figure 1.3: BigDog (Raibert et al., 2008) and HyQ (Semini et al., 2011) are large-scale hydraulically actuated quadrupedal robots. Hydraulic actuation is known to be robust and powerful but energetically highly inefficient.

1.2 State of the Art in Legged Robotics

This section gives an overview on relevant research about *design*, *actuation*, and *control* of legged and in particular quadrupedal robotic systems with the focus on recent achievements and research results that have an impact on our approach. Readers that are interested in a historical review of legged robotics are referred to (Gonzales de Santos et al., 2006; Raibert, 1986; Song and Waldron, 1988). A very complete overview on different actuation principles and their application in legged systems can be found in (Semini, 2010).

1.2.1 Design and Actuation Principles

The design of legged robots with respect to size and research focus is tightly coupled with the applied actuation principle.

Hydraulic Systems

Advanced development related to legged robotics is nowadays inevitably linked to recent achievements of Boston Dynamics (2012). Highly elaborated quadrupedal robots like BigDog (Buehler et al., 2005; Raibert et al., 2008, Figure 1.3(a)) or more recently LS3 have not only benchmarked this area but got also large public attention not least due to their large-scale military application. Unfortunately, there is nearly no information about their

systems accessible for the research community. Very promising research results with a comparable platform in terms of weight, size, and actuation principle are published along the development of HyQ (Semini et al., 2011, Figure 1.3(b)). All these devices are driven by impact-robust hydraulic actuators that have the highest power to weight ratio among standard actuation principles (Hollerbach et al., 1991). While these heavy, huge and bulky systems clearly set the state of the art in terms of *versatility* and *speed*, they are rather difficult to handle and require substantial installations. Furthermore, hydraulic systems are known as highly inefficient from an energetic point of view. To illustrate this with numbers, we know from Semini (2010) that the leakage flow in every valve of HyQ and BigDog is about 0.35 l/min . At an operating pressure of about 200 bar, this amounts to an energy loss in BigDog (16 valves) of about $16 \cdot 0.35 \text{ l/min} \cdot 200 \text{ bars} \approx 2 \text{ kW}$ without doing anything. Other estimations based on experimental data available for BigDog resulted in a dimensionless cost of transport (COT) (Kuo, 2007) in the order of 15 (Ruina and Cortell, 2011) which is substantially higher than some electrically driven robots or values found in animals (Kuo, 2007).

A further drawback of hydraulic actuation illustrated by Zinn et al. (2004), is its high output stiffness characteristics. The virtually infinite impedance generates high impact loads during collisions. Hence, these actuators have very poor inherent safety characteristics. The integration of torque sensing and control capability can reduce this only to certain extent. It allows for zero low-frequency impedance which ensures an excellent force control characteristics, but, above the control bandwidth, joint torque control is ineffective at reducing the end-effector impedance. Hence, large impact collisions in dynamic maneuvers can harm the environment or the system itself.

Compliant Systems

A particularly promising approach to overcome the drawbacks of stiff systems and to develop inherently safe, robust, and energetic efficient robots is the use of mechanical springs. The working principle is very similar to the muscular-tendon system that we find in the natural counterparts (Alexander, 1990). The elastic elements decouple the actuator from the link or the end-effector which provides low output impedance across the frequency spectrum and hence ensures perfect impact resistance (Zinn et al., 2004). It mitigates the limitations of high impedance actuators and allows for direct usage of widely available and largely scalable electric motors in combination with gearboxes. Thereby, systems become very user friendly, clean, and can be operated in labor environment. The springs further allow temporarily storing kinetic energy and thus preserving it throughout the gait cycle. Thereby, they can,

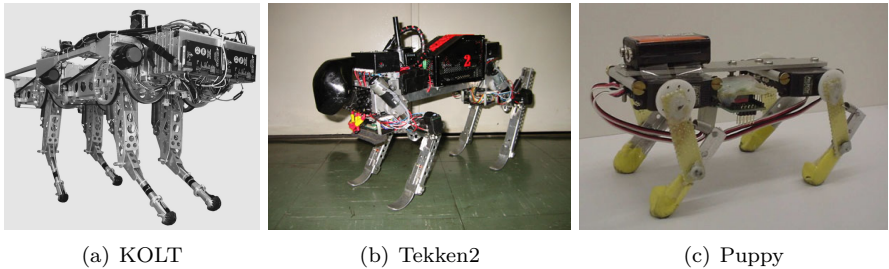


Figure 1.4: Electrically actuated quadrupedal robots of various size like Stanford KOLT (Nichol et al., 2004), Tekken 2 (Kimura et al., 2007), or Puppy (Iida et al., 2005) use compliant elements to support dynamic gaits.

in a purely passive way, largely contribute to the natural system dynamics and thus improve locomotion efficiency and enable running at high speeds.

Initiated by Raibert’s seminal research on hopping robots with pneumatic pistons (Raibert et al., 1986; Raibert, 1986; Raibert et al., 1983), researchers employed mechanical compliance in various configurations to enable dynamic gaits. Depending on the particular design, springs are integrated directly in prismatic legs (Ahmadi and Buehler, 2006; Gregorio et al., 1994, 1997; Taghird, 1993) or in the knee and ankle joints of articulated designs (Berkemeier and Desai, 1996; Curran and Orin, 2008; De Man et al., 1998a,b; Grimes and Hurst, 2012; Hurst, 2008; Hyon and Mita, 2002; Nichol and Waldron, 2002; Palmer et al., 2003). In all these robots, motion emerges to a large extent passively from the mechanical dynamics and the actuators are merely used to shape the motion and to compensate for friction and impact losses. Similar approaches were also used to develop quadrupedal robots of very different scale such as the KOLT (Nichol et al., 2004, Figure 1.4(a)), Scout series (Poulakakis et al., 2005, Figure 1.2(d)), Tekken series (Kimura et al., 2007, Figure 1.4(b)), or Puppy series (Iida et al., 2005, Figure 1.4(c)). Like the single legs, these more complex systems use the springs not only to absorb impact shocks at landing but also to enable dynamic gaits by means of temporary energy storage.

In fact, not only legged robots profit from compliant mechanisms, but also humans. To support fast and efficient running of handicapped athletes, prosthetic devices, such as Oscar Pistorius’ artificial carbon-fiber limbs (Camporesi, 2008), are built to act as springs in the lower extremities (Weyand and Bundle, 2010). This replaces the most important functionality of the ankle joint during running namely efficiently storing and releasing energy.

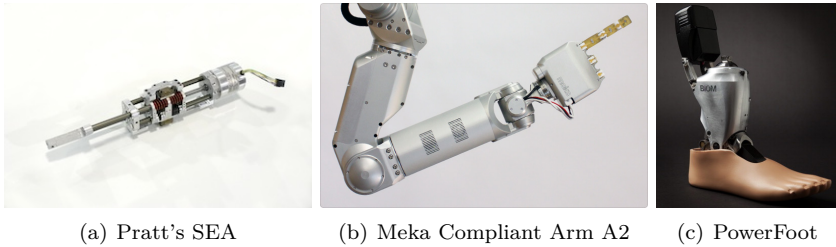


Figure 1.5: Using the principles of Pratt’s first torque controllable SEAs (a), different robotic arms and hands (b) were developed for research purpose. SEAs are also applied in active prostheses like the PowerFoot BiOM (c).

Series Elastic Actuation

Compliant elements are not only used to enable and support dynamic locomotion. Based on work done by Pratt and Williamson (1995, Figure 1.5(a)), people started to use so called series elastic actuators (SEA) for precise and low impedance force control (Pratt et al., 2002). To this end, spring deflection is measured using position encoders and actively controlled to adjust the desired torque output. The advantages of impact robustness and force/torque controllability motivated different groups to apply these ideas in robotic devices. A large research branch evolved in the field of grasping and manipulation where SEAs are used in dexterous robotic hands or arms like for example the ones developed by Meka Robotics (2011, Figure 1.5(b)). In the same line, research groups also built legged systems or humanoid platforms like HUME (Slovich et al., 2012), BIOBIPED (Radkhah et al., 2011), COMAN (Moro et al., 2011; Tzagarakis and Li, 2011) or M2V2 (Pratt and Krupp, 2008) to name a few. A large spectrum of applications can also be found in the field of rehabilitation robotics as assistive devices (Pratt et al., 2004b), therapeutic support (Vallery et al., 2008) or artificial limbs. Worldwide, research labs and companies are developing powered prostheses which restore ankle (Au and Herr, 2008; SpringActive, 2013; Versluys et al., 2009) or even knee motion (Pfeifer et al., 2012). The first of these devices that reached the clinical market (PowerFoot BiOM, iWalk, Cambridge, MA; Figure 1.5(c)) uses a series elastic actuator to provide powered push-up (Au et al., 2007). These robotic legs can help disabled people to normalize their walking gaits (Herr and Grabowski, 2012).

Despite the advantages that make SEAs perfectly suited to interact with humans or the environment, the intrinsic compliance is a drawback for the

control performance. Due to the mechanical low-pass filtering, the closed loop control bandwidth significantly drops in comparison to rigidly actuated devices and requires to carefully design the overall system, actuator, and control strategy.

1.2.2 Control

The progress in hardware, sensor, and actuator development of the last years is making torque controllable robots widely available for a broad range of research projects. Such systems can softly interact with their environment and are hence ideally suited for legged locomotion, manipulation, or human-machine interaction. This fundamental change away from *stiff, position* controlled devices as employed in traditional industrial robot arms towards *compliant, torque* controlled robots opens wide opportunities to bring novel and very sophisticated control concepts from simulations into real world applications. Instead of slow, static walking based on kinematic motion planning and execution (Gonzales de Santos et al., 2006), these new principles allow for agile, highly dynamic, and versatile maneuvers (e.g. Coros et al., 2011). Torque controllability enables adapting the motion and behavior of the robot to external influences, but also to distribute the joint torques and contact forces in a clever way to improve robustness while walking.

Controlling a legged robot can be classified into three layers that are *motion generation*, *motion control*, and *actuator control*. Motion generation deals with general concepts to create the behavior of the system, often without any knowledge of the final realization. Motion control transfers the desired behavior into high-level actuator commands such as joint torque or position demand signals. Actuator control finally regulates each joint independently. This strongly depends on the actuator type and is often tightly coupled with the mechanical implementation.

Motion Generation

Different research directions have been extensively engaged with the first part. For example, the field of animation has been working for a long time towards creating natural looking motion with gradually increasing physics based approaches. Some of these methods demonstrated astonishing locomotion skills for quadrupedal systems (e.g. Coros et al., 2011). Other groups are developing very powerful techniques that allow to numerically optimize even for highly difficult maneuvers (Schultz and Mombaur, 2010). Moreover, continuously increasing computational power allows to exploit optimization techniques or in particular model predictive strategies in real-time control of

reasonably complex devices (Tassa et al., 2012). Other approaches which are inspired by nature and in particular neurophysiology and biomechanics, use Dynamic Movement Primitives (Schaal, 2003) or simplified templates (Full and Koditschek, 1999) to generate the motion for robots of very different morphology. Planning, optimization, and learning methods are of course not limited to the internal robot state but can in fact be expanded to traverse very challenging terrain that requires careful foothold selection. In the DARPA learning locomotion challenge, different groups pushed the state of the art in this area (e.g. Kalakrishnan et al., 2010; Kolter et al., 2011; Neuhaus et al., 2011; Zucker et al., 2011).

Motion Control

The probably best established method to stabilize a desired motion of torque controllable legged systems is so called *virtual model control* introduced by Pratt et al. (1997). Virtual forces acting on a body are distributed to the different contact points and subsequently mapped to the individual joint torques. This controller has successfully proven its applicability for various robots not at last due to its simplicity. Control gains for the virtual elements can be adjusted in an intuitive way and the computational effort to generate the joint torques reduces to a matrix multiplication with Jacobians that are accurately available. Virtual model control is a static method that takes only kinematic system properties into account.

In most cases, the control engineer has additionally access to descriptions of the system dynamics which allows designing much more elaborated control concepts. A particularly interesting and widely used approach is *inverse dynamics*. Given a desired motion, the multi-body system dynamics of the robot is inverted to generate required joint torques. While this works straight forward for fix-base manipulators, it is only recently applied to floating base systems such as legged robots, i.e. to systems that are not rigidly attached to the environment and that are hence underactuated. To this end, the system dynamics are first projected onto a support consistent manifold using methods such as the dynamically consistent support null-space (Sentis, 2007), linear projection (Aghili, 2005), orthogonal projection (Mistry et al., 2010), or others. Subsequently, this reduced dimensional description is inverted.

To control the behavior of complex systems with a large number of degrees of freedom in an intuitive way, it is preferable to describe the desired dynamics only at particularly interesting points instead for the complete system. To give some examples, this can be controlling the center of gravity to ensure stability, performing stepping or grasping tasks with hands or feet, keeping a certain optimal posture, or applying a desired contact force. This is

called task or operational space control (OSC), which is used synonymously in this work. Using different control gains and priorities, it can be ensured that important or high precision tasks are accurately executed while other less important tasks are only fulfilled as well as possible without impairing the ones with higher priority. Such a differentiation is not a purely robotic construct: Various behavioral and neuro-scientific studies (e.g. Saltzman and Kelso, 1987; Schaal and Schweighofer, 2005; Scholz and Schoner, 1999) have indicated that humans show a very similar task decomposition with high-gain control for example in reaching task with the hand, and compliant null-space posture control.

Such prioritized control formulations were first proposed by Hanafusa et al. (1981) and Nakamura et al. (1987) in the context of inverse kinematics control and were later picked up by Siciliano and Slotine (1991). Along the lines of the seminal work on OSC by Khatib (1987), his group extended these ideas to floating base systems. They set up a software framework to solve inverse task-space dynamics with various priorities for both motion as well as force/torque tasks which guarantees that a task never impairs a higher prioritized task (e.g. Sentis, 2010). Philippsen et al. (2011) recently released this powerful software package for the public.

Actuator Control

The final realization of a desired behavior on a robotic platform requires high-performance actuator control. This topic is very hardware specific and strongly coupled with the mechanical design and its integration in the overall system. The main difficulty thereby is the continuously changing model at the actuator output while the robot interacts with the environment at different locations. As documented in the seminal papers by Colgate and Hogan (1989); Hogan (1988), this requires that the joint actuator is *stable* and *passive*.

There are two different approaches in terms of SEA control structure. The first documented controller by Pratt and Williamson (1995) regulates the motor force as a function of the desired output torque using a PID structure with feedforward acceleration compensation. To ensure passivity, the integrator has to be augmented with a roll-off (Williamson, 1995) which leads to an undesired steady state error. One of the major disadvantages when controlling the motor force is gearbox friction, stiction, or backlash that is nearly impossible to model and hence hard to compensate. This can be improved by using disturbance observers (Kong et al., 2009, 2012) and by augmenting it with model-based strategies by (Paine and Sentis, 2012). As a different way to overcome these deficiencies, Pratt et al. (2004a) later suggested to close

the motor velocity loop and hence to locally regulate the undesired gearbox dynamics. Similar encoder based principles were also applied by Wyeth (2006) and by Vallery et al. (2007) who addressed the issues of stability and passivity in very detail.

1.3 Approach and Contribution

The vision at the beginning of this project was to develop and control a quadrupedal robot that combines *versatility*, *speed*, *efficiency*, and *robustness*. This electrically driven dog should be able to perform different gaits from static walking to dynamic running. Such an engineering project requires research in three areas, namely **system**, **actuator**, and **control** development (Figure 1.6). In our eyes, it is crucial to tackle these topics not independently but to consider them as tightly connected and foster progress at the intersection areas.

To realize the four coarse specifications, we attempt to unify existing solutions based on compliant actuation in one single device. This ranges from one ending of the spectrum, where mainly bio-inspired researchers are using elastic elements to enhance the natural dynamics of the system, to the other ending, where springs are solely applied in a closed loop setup as robust force or torque sensor for control. To combine these advantages we developed highly compliant series elastic actuators that protect the gearbox, can intermittently store energy, and enable precise, low-impedance torque control. Thereby, control is not exclusively considered as a software problem. The actuator properties are specifically designed for the final quadrupedal system with a combination of springs and dampers to improve controllability while optimizing the efficiency of energy storage.

The developed actuators were first tested on a single planar leg to validate their performance and applicability. Various experiments showed good torque and position control performance in comparison to state of the art solutions. Inspired by templates which describe the biomechanical locomotion principles with astonishing accuracy, we use a generalized version of virtual model control (Pratt et al., 1997) to emulate different spring-damper behaviors during ground contact interaction. Combining this with angle of attack control similar to (Raibert, 1986), the single leg can robustly and quickly locomote between different target points. We experimentally demonstrated high energetic efficiency by exploiting the natural dynamics introduced by the elastic elements. Thereby more than 60% of the mechanical work is passively stored in the spring after landing and released before lift-off. In the same experiment the peak power and speed at the joint are more than four times

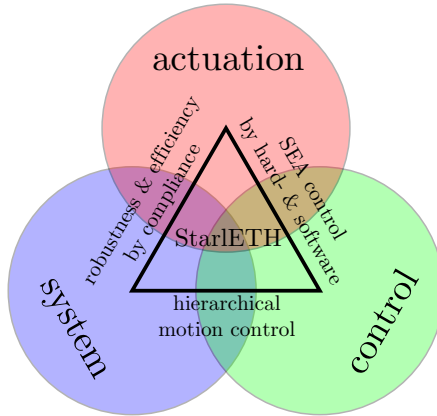


Figure 1.6: The presented work is contributing to three core pillars: *system design*, *actuation*, and *control*.

higher than at the corresponding motor. These results confirm that highly compliant SEAs are a very valuable actuation approach for legged systems.

Based on these findings, we created *StarETH*, a fully actuated (12 DOF) four-legged robot that resembles the dimensions and weight properties of a medium-sized dog. To control such complex machines under continuously changing ground support, we elaborated a task-space inverse dynamics control framework based on hierarchical least square optimization. This combines advantages from prioritized task decompositions (e.g. Sentis and Khatib, 2005) with kinematic projections for inverse dynamics (e.g. Mistry et al., 2010). It allows generating nearly arbitrary behaviors by simultaneously executing a set of motion tasks while optimizing the ground contact forces or joint torques. We put a strong focus on demonstrating the applicability of each and every presented concept in real hardware experiments using *StarETH*. This ranges from pure performance evaluation of robustness and payload capabilities, over static walking on different ground, to dynamic running under significant external disturbances. To the best of our knowledge, this is the first experimental demonstration of hierarchical task-space inverse dynamics control on a fully torque controlled legged platform without (low-gain) joint position stabilization. The results highlight the value and applicability of the proposed **system**, **actuator**, and **control** package and is considered as a significant step towards fulfilling our mission statement of developing and controlling a quadrupedal robot that unifies *versatility*, *speed*, *efficiency*, and *robustness*.

1.4 Thesis Outline

This introduction is followed in Chapter 2 by a description of modeling tools for floating base multi-body systems. We present methods to deal with the contact constraints as well as with impact collisions which results in a constraint consistent description of the system dynamics. We further elaborate the theoretical background to generate an analytical representation of the system dynamics as required for controller design.

One of the major contributions attributes to the development of the quadrupedal robot *StarLETH* as summarized in Chapter 3. The description is tiered into quadruped, single leg, and series elastic actuator design. We discuss different design guidelines and choices that led to the actual robotic prototype. We further outline the electronics and software environment, a combined C/C++ realtime simulation and control tool that allows efficient controller testing and validation in computer based simulations and real hardware experiments.

In Chapter 4 we discuss how to control highly compliant SEAs in a way that allows exploiting the beneficial properties introduced by the mechanical elasticity but preserves high torque and position control performance. To this end we do not consider control as pure software problem but strongly improve controllability by a sophisticated hardware design. To balance the robot, we use task-space inverse dynamics described in Chapter 5. Using a hierarchical least-square optimization, different motion and force/torque tasks are handled simultaneously with different priorities. We outline and compare a sequential and a combined method as well as a hybrid setup that combines fast low-level joint position control with inverse dynamics. In Chapter 6 we describe different locomotion templates that help understanding the mechanical principles behind walking and running in nature, and which are used for motion generation of single-legged hopping and quadrupedal running gaits.

Starting with the archetype of dynamic locomotion, namely single-legged running (Chapter 7), we present a series of experimental results. This test bench validation highlights some of the beneficial properties of the applied system, actuation, and control principles with respect to robustness, controllability, and especially efficiency. Combining the individual building blocks, we finally successfully perform a variety of walking and running experiments with *StarLETH* (Chapter 8).

A large part of the research progress within this thesis is hard to capture in numbers, formulas, or figures. As an illustration of the findings we made a movie collection of most experiments which is accessible at:

<http://leggedrobotics.ethz.ch/phdthesis-mahutter>

Chapter 2

System Modeling

Legged robots belong to the class of floating base or free-floating systems, i.e. to systems that are not rigidly connected to their environment like a robotic arm, but can move anywhere in space using the ground as support. They have an unactuated base and interact with the environment through multiple and continuously changing contact points to stand still or propel them forward.

This chapter provides the theoretical background to model the kinematics and dynamics of floating base multi-body systems (MBS). Using the concept of generalized coordinates, we outline how to handle the ground contact constraints and the resulting reaction forces. Based on that, constraint consistent equations of motion (EOM) are introduced and different projectors for the underlying mapping are summarized. We further show how to handle instantaneous changes in the contact situation that are accompanied by collisions with impulsive forces and an associated energy loss. The presented methods are required for theoretical investigations in the hardware design process, to create model-based control strategies, and to validate the proposed solutions in simulations as accurately as possible. We additionally provide the theoretical background for a software tool to analytically derive the EOM based on projected Newton-Euler equations.

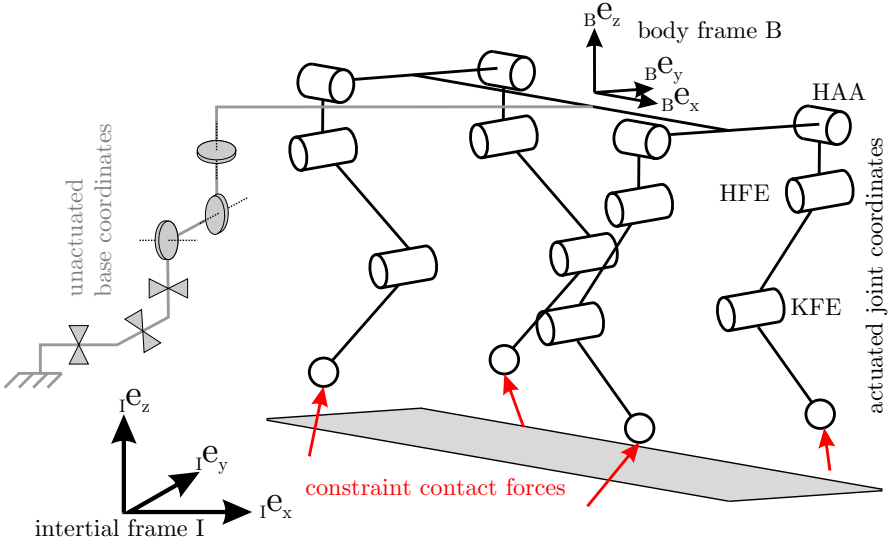


Figure 2.1: The kinematic structure of a floating base system is described by actuated joint coordinates \mathbf{q}_r and unactuated base coordinates \mathbf{q}_b . The contact forces \mathbf{F}_s occur due to the contact constraints.

2.1 Floating Base Multi-Body Dynamics

To represent the motion of floating base systems, we use the concept of *generalized coordinates*. To this end, system kinematics and dynamics are described as a function of the n_q -dimensional vector

$$\mathbf{q} = \begin{pmatrix} \mathbf{q}_b \\ \mathbf{q}_r \end{pmatrix}, \quad (2.1)$$

which is composed of the n_b -dimensional vector \mathbf{q}_b describing the unactuated floating base coordinates and the $n_r = n_q - n_b$ dimensional actuated joint coordinates \mathbf{q}_r . As depicted in Figure 2.1, one of the robot's links is dedicated as the base with the body fixed frame B which can be arbitrarily displaced with respect to the inertial frame I . The position ($\in \mathbb{R}^3$) and orientation ($\in SO(3)$) of this link in space are measured with respect to the inertial frame I using the unactuated floating base coordinates \mathbf{q}_b . For simplicity, we keep the formalism in this report on Euler respectively Tait-Bryan angles ($n_b = 6$, $\mathbf{q}_b = (x, y, z, \alpha, \beta, \gamma)^T$). If necessary, this is transformed to quaternions and vice versa without explicit mention.

All kinematic properties such as position vectors $\mathbf{r}(\mathbf{q})$ or Jacobians $\mathbf{J}(\mathbf{q}) = \frac{\partial \mathbf{r}(\mathbf{q})}{\partial \mathbf{q}}$ as well as the system dynamics are expressed as a function of generalized coordinates \mathbf{q} . Correspondingly, the EOM are written as

$$\mathbf{M}\ddot{\mathbf{q}} + \mathbf{h} + \mathbf{J}_s^T \mathbf{F}_s = \mathbf{S}^T \boldsymbol{\tau}, \quad (2.2)$$

with the mass matrix $\mathbf{M}(\mathbf{q})$, the force vector $\mathbf{h}(\mathbf{q}, \dot{\mathbf{q}})$ as the sum of Coriolis, centrifugal and gravitational forces, and the actuator torque $\boldsymbol{\tau}$. The selection matrix $\mathbf{S} = [\mathbf{0}_{n_r \times n_b} \quad \mathbf{I}_{n_r}]$ separates the n_r actuated joint coordinates $\mathbf{q}_r = \mathbf{S}\mathbf{q}$ from the unactuated floating base coordinates \mathbf{q}_b .

The reaction forces at the contact points $\mathbf{F}_s \in \mathbb{R}^{3n_s \times 1}$ are mapped into the generalized coordinate space using the $3n_s \times n_q$ dimensional support Jacobian $\mathbf{J}_s = \frac{\partial \mathbf{r}_s}{\partial \mathbf{q}}$ that is given by a partial derivation of the contact point vector $\mathbf{r}_s \in \mathbb{R}^{3n_s \times 1}$ after \mathbf{q} . Vectors \mathbf{r}_s and \mathbf{F}_s represent stacked vectors of the position $\mathbf{r}_{s_i} \in \mathbb{R}^{3 \times 1}$ respectively force $\mathbf{F}_{s_i} \in \mathbb{R}^{3 \times 1}$ at the n_s active contact points. The definition of *active* contact in this context is that the corresponding contact is closed, i.e. the relative normal (N) distance between the contact point and the environment is and remains closed ($r_{s_i}^N = \dot{r}_{s_i}^N = \ddot{r}_{s_i}^N = 0$) with a pressure force exerted between them ($F_{s_i}^N \geq 0$). This formulation is independent of the choice of contact model and is valid if the robot stands still or slides in (local) tangential direction along a surface. In contrast thereto, the calculation of the corresponding forces \mathbf{F}_s strongly depends on the actual contact model.

2.2 Contact Models

In general, two different approaches of *soft* and *hard* models can be distinguished for contact analysis and handling. This is well summarized by Gilardi and Sharf (2002).

2.2.1 Soft Contact

The *soft contact* approach, also known as continuous model, explicitly accounts for the deformation of the bodies during contact. The definition of an active contact is slightly different in this context as the model requires certain penetration $r_{s_i}^N \leq 0$ and not necessarily zero velocity. The contact force is expressed as an explicit function of the local indentation respectively its rate and can be seen as a relatively stiff spring-damper model at the point of contact

$$\mathbf{F}_{s_i} = f(\mathbf{r}_{s_i}, \dot{\mathbf{r}}_{s_i}, \mathbf{r}_{s_i}^0), \quad (2.3)$$

with $\mathbf{r}_{s_i}^0$ being the contact point when the bodies first touched. This approach provides an intuitive description of the real behavior of the system, in particular, when including contact friction. More importantly, it is naturally suitable for contact modeling and complex contact scenarios involving multiple contacts and bodies. Due to its simplicity, most simulation engines including the one used by us (Schaal, 2009) are based on soft contacts. However, in most applications and in particular when interested in fast simulation of the MBS behavior, the contact parameters such as stiffness and damping are tuned as numerical parameters in a trade-off between accuracy and stiffness of the differential equations. The actual values are often not related to a physical contact model at all.

2.2.2 Hard Contact

In contrast thereto, the *hard contact* approach assumes that the interaction between the objects occurs in short time and that the configuration of impacting bodies does not change significantly. The contact forces between bodies are not a function of force elements but result from algebraic constraints that prohibit mutual penetration. For all closed contacts ($r_{s_i}^N = \dot{r}_{s_i}^N = 0$) it must hold that either the acceleration in normal contact direction or the force is positive but never both. These unilateral constraints can be described with linear complementary problems (LCP):

$$\ddot{r}_{s_i}^N \geq 0, \quad F_{s_i}^N \geq 0, \quad \ddot{r}_{s_i}^N F_{s_i}^N = 0. \quad (2.4)$$

Special treatment of the tangential directions additionally allows to integrate stiction ($F_{s_i}^T < \mu F_{s_i}^N$) and friction ($F_{s_i}^T = \mu F_{s_i}^N$) effects into this formalism. As a result, it is possible to formulate the system dynamics including all possible constraints and transitions at once. The interested reader is referred to (Glocker, 1995; Pfeiffer and Glocker, 1996) for a very detailed and precise discussion.

When focusing on control instead of simulation, the contact situation and complementary condition is in most cases a priori known from sensor information. As a further simplification, contact slippage is often neglected such that the contact constraint reduces to

$$\dot{\mathbf{r}}_s = \mathbf{J}_s \dot{\mathbf{q}} = \mathbf{0}, \quad (2.5)$$

$$\ddot{\mathbf{r}}_s = \mathbf{J}_s \ddot{\mathbf{q}} + \dot{\mathbf{J}}_s \dot{\mathbf{q}} = \mathbf{0}. \quad (2.6)$$

Combining the contact constraint for generalized accelerations (2.6) with the system dynamics (2.2) yields a closed form solution for the contact forces:

$$\mathbf{F}_s = (\mathbf{J}_s \mathbf{M}^{-1} \mathbf{J}_s^T)^{-1} (\mathbf{J}_s \mathbf{M}^{-1} (\mathbf{S}^T \boldsymbol{\tau} - \mathbf{h}) + \dot{\mathbf{J}}_s \dot{\mathbf{q}}). \quad (2.7)$$

This is of great benefit as it gives direct access to estimated contact forces solely based on the description of the MBS dynamics and without any further contact force sensor information.

2.3 Constraint Consistent Dynamics

Following the well-established nomenclature and formalism introduced by Khatib (1987) and extended by Sentis (2007) for floating base systems, we can define the *dynamically consistent support null-space matrix* as

$$\mathbf{N}_s = \mathbf{I} - \mathbf{M}^{-1} \mathbf{J}_s^T (\mathbf{J}_s \mathbf{M}^{-1} \mathbf{J}_s^T)^{-1} \mathbf{J}_s. \quad (2.8)$$

\mathbf{N}_s defines a generalized space of motion with no acceleration or force coupling effects on the supporting links. Additional properties of this projector can be looked up in (Sentis, 2007). Substituting the solution for the contact force (2.7) into the EOM (2.2) results in

$$\mathbf{M}\ddot{\mathbf{q}} + \mathbf{N}_s^T \mathbf{h} + \mathbf{J}_s^T (\mathbf{J}_s \mathbf{M}^{-1} \mathbf{J}_s^T)^{-1} \dot{\mathbf{J}}_s \dot{\mathbf{q}} = \mathbf{N}_s^T \mathbf{S}^T \boldsymbol{\tau}. \quad (2.9)$$

By further including the support constraint (2.6) which implies $\dot{\mathbf{J}}_s \dot{\mathbf{q}} = -\mathbf{J}_s \ddot{\mathbf{q}}$, the *constraint consistent equations of motion* can be compactly formulated as

$$\mathbf{N}_s^T (\mathbf{M}\ddot{\mathbf{q}} + \mathbf{h}) = \mathbf{N}_s^T \mathbf{S}^T \boldsymbol{\tau}. \quad (2.10)$$

As described by Righetti et al. (2011a), the *dynamically consistent support null-space matrix* \mathbf{N}_s belongs to a large class of projectors that can be understood as linear operators \mathbf{P} that map the system dynamics onto the constraint consistent manifold such that the EOM are independent of the contact forces

$$\mathbf{P} (\mathbf{M}\ddot{\mathbf{q}} + \mathbf{h}) = \mathbf{P} \mathbf{S}^T \boldsymbol{\tau}. \quad (2.11)$$

The sufficient requirement on the operator \mathbf{P} is

$$\mathbf{P} \mathbf{J}_s^T = \mathbf{0} \quad \forall \dot{\mathbf{q}}. \quad (2.12)$$

2.3.1 Constraint Projector

The choice of the constraint manifold projector \mathbf{P} is not unique. Instead, there exist different methods that can be reduced to this general formulation by appropriately choosing the projection matrix.

Dynamically Consistent Support Null-Space

Direct substitution of the contact constraints as done in (2.10) is equivalent to choosing

$$\mathbf{P}_{N_s} = \mathbf{N}_s^T. \quad (2.13)$$

Operational Space Control

OSC was introduced by Khatib (1987) and later augmented to floating base systems by Sentis (2007). As outlined in Appendix A.5, this control method can be expressed in the general form by

$$\mathbf{P}_{OSC} = \mathbf{S}\mathbf{N}_s\mathbf{M}^{-1}. \quad (2.14)$$

QR Decomposition

Mistry et al. (2010) introduced another well-established projector that is based on a QR decomposition of $\mathbf{J}_s^T = \mathbf{Q}[\mathbf{R}^T \ \mathbf{0}]^T$ with the orthogonal matrix $\mathbf{Q}^T = \mathbf{Q}^{-1}$ and the upper right triangular matrix \mathbf{R} . This method has the advantage that it is a purely kinematic construct and does not contain any inverted mass matrix (cf. \mathbf{P}_{N_s} , \mathbf{P}_{OSC}). By splitting $\mathbf{Q} = [\mathbf{Q}_c \ \mathbf{Q}_u]$ into constrained and unconstrained components, the manifold projector is written as

$$\mathbf{P}_{QR} = \mathbf{Q}_u^T. \quad (2.15)$$

The QR decomposition gives additionally direct access to the contact force

$$\mathbf{F}_s = \mathbf{R}^{-1}\mathbf{Q}_c^T (\mathbf{S}^T \boldsymbol{\tau} - \mathbf{M}\ddot{\mathbf{q}} + \mathbf{h}). \quad (2.16)$$

Kinematic Null-Space

A very simple approach is to use the pseudo-inverse \mathbf{J}_s^{T+} of the transposed support Jacobian \mathbf{J}_s^T and to define

$$\mathbf{P}_{J_s} = \mathbf{I} - \mathbf{J}_s^T \mathbf{J}_s^{T+}. \quad (2.17)$$

The proof of $\mathbf{P}_{J_s} \mathbf{J}_s^T = \mathbf{0}$ follows directly from the Moore-Penrose pseudo inverse property $\mathbf{J}_s^T \mathbf{J}_s^{T+} \mathbf{J}_s^T = \mathbf{J}_s^T$. This method is again only a function of kinematic system properties and was applied e.g. by Aghili (2004).

SVD Null-Space

Similar to the previous method, it is also possible to use the SVD null-space calculation

$$\mathbf{P}_{svd} = \mathcal{N}(\mathbf{J}_s^T) \quad (2.18)$$

defined by a singular value decomposition (SVD) as outlined in Appendix A.4. The orthogonality of the projector matrix can be beneficial for later optimization methods.

Comparison and Selection of Projector Matrix

While the choice of \mathbf{P} is often not relevant from a theoretical point of view or for ideal simulations, it can still influence the implementation in real hardware experiments. As we will discuss a bit more in detail in Chapter 5, methods that are purely based on kinematic properties can be beneficial as they are less prone for numerical or modeling errors. The control methods we develop in this work are independent of the projector. Since most of the related research results that have been published with supporting experiments are based on the QR approach, we use $\mathbf{P} = \mathbf{P}_{QR} = \mathbf{Q}_u^T$ in the experiments to be comparable.

2.3.2 Minimal Coordinates

A widely used concept for support consistent descriptions is minimal coordinates. While such a representation will not be used in the context of this thesis, it nicely illustrates the working principle of support consistent projections. A floating base robot in contact with the environment implies that the n_q generalized coordinates cannot be arbitrarily chosen but have to be consistent with the support constraint, i.e. $\mathbf{q} = \mathbf{q}_{\text{consistent}}$ (2.6). In fact, the system has only $n_m = n_q - \text{rank}(\mathbf{J}_s)$ degrees of freedom and its dynamics can hence be fully described using n_m **minimal** coordinates

$$\boldsymbol{\xi} = \boldsymbol{\xi}(\mathbf{q}), \quad \mathbf{Q}_\xi := \frac{\partial \mathbf{q}}{\partial \boldsymbol{\xi}}. \quad (2.19)$$

To study the relation between generalized and minimal coordinates, we consider virtual displacements indicated by δ . It holds that arbitrary virtual displacements in minimal coordinates $\delta \boldsymbol{\xi}$ produce only virtual displacements in generalized coordinates that are consistent with the support constraints

$$\delta \mathbf{q}_{\text{consistent}} = \frac{\partial \mathbf{q}}{\partial \boldsymbol{\xi}} \delta \boldsymbol{\xi} = \mathbf{Q}_\xi \delta \boldsymbol{\xi}. \quad (2.20)$$

Consistent in this context means that virtual displacements are not allowed to produce a displacement at the contact point:

$$\delta \mathbf{r}_{s,\text{consistent}} = \frac{\partial \mathbf{r}_s}{\partial \mathbf{q}} \delta \mathbf{q}_{\text{consistent}} = \mathbf{J}_s \mathbf{Q}_\xi \delta \xi = \mathbf{0} \quad \forall \xi, \quad (2.21)$$

$$\Rightarrow \mathbf{J}_s \mathbf{Q}_\xi = \mathbf{0}. \quad (2.22)$$

Comparing (2.22) with (2.12), we realize that \mathbf{Q}_ξ can again be seen as a projector matrix $\mathbf{P} = \mathbf{Q}_\xi^T$. Since we consider the contact constraint as an ideal constraint, it has to hold that a support consistent virtual displacement does not produce any virtual work (*principle of virtual work*):

$$\delta \mathbf{q}_{\text{consistent}}^T (\mathbf{M}\ddot{\mathbf{q}} + \mathbf{h} + \mathbf{J}_s^T \mathbf{F}_s - \mathbf{S}^T \boldsymbol{\tau}) = 0 \quad \forall \delta \mathbf{q}_{\text{consistent}}, \quad (2.23)$$

$$\delta \xi^T \mathbf{Q}_\xi^T (\mathbf{M}\ddot{\mathbf{q}} + \mathbf{h} + \mathbf{J}_s^T \mathbf{F}_s - \mathbf{S}^T \boldsymbol{\tau}) = 0 \quad \forall \delta \xi. \quad (2.24)$$

Using (2.22) and substituting $\ddot{\mathbf{q}} = \mathbf{Q}_\xi \ddot{\xi} + \dot{\mathbf{Q}}_\xi \dot{\xi}$, the EOM can be written as a function of minimal coordinates as

$$\mathbf{Q}_\xi^T \mathbf{M} \mathbf{Q}_\xi \ddot{\xi} + \mathbf{Q}_\xi^T (\mathbf{h} + \mathbf{M} \dot{\mathbf{Q}}_\xi \dot{\xi}) = \mathbf{Q}_\xi^T \mathbf{S}^T \boldsymbol{\tau}. \quad (2.25)$$

The change from generalized coordinates \mathbf{q} to minimal coordinates ξ allows analyzing the dynamics of a floating base system without considering additional constraints. However, the choice of mechanically meaningful minimal coordinates that would allow for a useful interpretation is only possible in simple cases. Additionally, like the projections introduced before, the concept of minimal coordinates suffers from the discontinuity when the contact situation changes, which enforces to switch the coordinate set.

2.4 Contact Switches and Impact Collisions

A hard contact model requires subdividing the analysis of the system dynamics into two intervals, before and after a change in the contact situation respectively an impact. The impact itself is a complex physical phenomenon which occurs when two or more bodies collide with each other. The characteristic of an impact is a very short duration with high peak forces that results in a rapid dissipation of energy and large accelerations. To model the process of energy transfer and dissipation, various coefficients are employed, such as the coefficient of restitution and the impulse ratio. Idealizing the process, respectively considering the impact as an infinitesimally short process requires to include instantaneous changes in velocities if bodies are making contact.

2.4.1 Impulse Transfer

To resolve the contact impulse, we use the integrated EOM over a single point in time $\{t_0\}$

$$\int_{\{t_0\}} (\mathbf{M}\ddot{\mathbf{q}} + \mathbf{h} + \mathbf{J}_s^T \mathbf{F}_s - \mathbf{S}^T \boldsymbol{\tau}) dt = \mathbf{M}(\dot{\mathbf{q}}^+ - \dot{\mathbf{q}}^-) + \mathbf{J}_s^T \mathcal{F}_s = \mathbf{0}, \quad (2.26)$$

with the impulsive force \mathcal{F}_s and the pre- respectively post-impact generalized velocities $\dot{\mathbf{q}}^-$ and $\dot{\mathbf{q}}^+$. Assuming a perfect inelastic collision with a Newtonian collision law (Glocker, 2001), all contact points that are considered part of the collision instantaneously come to rest ($\dot{\mathbf{r}}_s^+ = \mathbf{J}_s \dot{\mathbf{q}}^+ = \mathbf{0}$). Combining this post-impact constraint with the integrated EOM (2.26), we can solve for the impulsive force as

$$\mathcal{F}_s = (\mathbf{J}_s \mathbf{M}^{-1} \mathbf{J}_s^T)^{-1} \mathbf{J}_s \dot{\mathbf{q}}^- = \boldsymbol{\Lambda}_s \dot{\mathbf{r}}_s^-. \quad (2.27)$$

Analyzing this formalism a bit more in detail by considering the basic mechanics that defines *impulse = mass · speed*, we identify the inertia that is seen at the support point as the so called *end-effector inertia*

$$\boldsymbol{\Lambda}_s = (\mathbf{J}_s \mathbf{M}^{-1} \mathbf{J}_s^T)^{-1}. \quad (2.28)$$

Substituting (2.27) into (2.26) yields the instantaneous change in generalized velocities

$$\Delta \dot{\mathbf{q}} = \dot{\mathbf{q}}^+ - \dot{\mathbf{q}}^- = -\mathbf{M}^{-1} \mathbf{J}_s^T (\mathbf{J}_s \mathbf{M}^{-1} \mathbf{J}_s^T)^{-1} \mathbf{J}_s \dot{\mathbf{q}}^-. \quad (2.29)$$

Using again the nomenclature introduced previously for the dynamically consistent support null-space projector \mathbf{N}_s , the post-impact generalized velocities are determined by

$$\dot{\mathbf{q}}^+ = \left(\mathbf{I} - \mathbf{M}^{-1} \mathbf{J}_s^T (\mathbf{J}_s \mathbf{M}^{-1} \mathbf{J}_s^T)^{-1} \mathbf{J}_s \right) \dot{\mathbf{q}}^- = \mathbf{N}_s \dot{\mathbf{q}}^-. \quad (2.30)$$

The result that is obtained by satisfying the post impact contact constraint is intuitively clear. Using the support null-space projector \mathbf{N}_s , the pre-impact velocity $\dot{\mathbf{q}}^-$ is projected onto the support consistent manifold.

2.4.2 Energy Loss

The instantaneous change in the contact situation is always associated with a kinetic energetic loss. This can be quantified in generalized coordinates

or as a function of the end-effector inertia and the change in velocity at the support point by

$$E_{loss} = \Delta E_{kin} = -\frac{1}{2} \Delta \dot{\mathbf{q}}^T \mathbf{M} \Delta \dot{\mathbf{q}} \quad (2.31)$$

$$= -\frac{1}{2} \Delta \dot{\mathbf{r}}_s^T \boldsymbol{\Lambda}_s \Delta \dot{\mathbf{r}}_s = -\frac{1}{2} \dot{\mathbf{r}}_s^{-T} \boldsymbol{\Lambda}_s \dot{\mathbf{r}}_s. \quad (2.32)$$

Since only part of the derivation was given by Schmiechler and Waldron (2000), the entire proof for (2.31) and (2.32) is compactly outlined in appendix A.3.

2.5 Analytical Representation

We use projected Newton-Euler equations to analytically derive the EOM. This method can be understood as projection of the conservation of impulse \mathbf{p} and angular momentum \mathbf{L} onto generalized coordinates

$$\sum \mathbf{J}_{COG_i}^T \dot{\mathbf{p}}_i + \mathbf{J}_{R_i}^T \dot{\mathbf{L}}_{COG_i} - \mathbf{J}_{COG_i}^T \mathbf{F}_{g_i} - \mathbf{J}_{s_i}^T (-\mathbf{F}_{s_i}) - \mathbf{J}_{R_i}^T \boldsymbol{\tau}_i = \mathbf{0}, \quad (2.33)$$

with the impulse $\mathbf{p}_i(\mathbf{q}) = m_i \dot{\mathbf{r}}_{COG_i}$, the angular momentum $\mathbf{L}_{COG_i} = \boldsymbol{\theta}_i \boldsymbol{\Omega}_i$, gravitational forces \mathbf{F}_{g_i} , support forces \mathbf{F}_{s_i} , and external torques $\boldsymbol{\tau}_i$ evaluated for all links i . The change of impulse and angular momentum is

$$\dot{\mathbf{p}}_i = m_i \ddot{\mathbf{r}}_{COG_i}, \quad (2.34)$$

$$\dot{\mathbf{L}}_{COG_i} = \boldsymbol{\theta}_i \dot{\boldsymbol{\Omega}}_i + \boldsymbol{\Omega}_i \times \boldsymbol{\theta}_i \boldsymbol{\Omega}_i, \quad (2.35)$$

whereby $\boldsymbol{\Omega}_i \in \mathbb{R}^{3 \times 1}$ and $\boldsymbol{\theta}_i \in \mathbb{R}^{3 \times 3}$ are the angular velocity and inertia w.r.t. the COG of link i , respectively. Using the kinematic relations

$$\ddot{\mathbf{r}}_{COG_i} = \mathbf{J}_{COG_i} \ddot{\mathbf{q}} + \dot{\mathbf{J}}_{COG_i} \dot{\mathbf{q}}, \quad (2.36)$$

$$\boldsymbol{\Omega}_i = \mathbf{J}_{R_i} \dot{\mathbf{q}}, \quad (2.37)$$

$$\dot{\boldsymbol{\Omega}}_i = \mathbf{J}_{R_i} \ddot{\mathbf{q}} + \dot{\mathbf{J}}_{R_i} \dot{\mathbf{q}}, \quad (2.38)$$

as a function of the translational Jacobians $\mathbf{J}_{COG_i} = \frac{\partial \mathbf{r}_{COG_i}}{\partial \mathbf{q}}$ and the rotational Jacobian $\mathbf{J}_{R_i} = \frac{\partial \boldsymbol{\Omega}_i}{\partial \mathbf{q}}$, the elements of the EOM (2.2) are:

$$\mathbf{M} = \sum \mathbf{J}_{COG_i}^T m_i \mathbf{J}_{COG_i} + \mathbf{J}_{R_i}^T \boldsymbol{\theta}_i \mathbf{J}_{R_i}, \quad (2.39)$$

$$\mathbf{h} = \sum \mathbf{J}_{COG_i}^T m_i \dot{\mathbf{J}}_{COG_i} \dot{\mathbf{q}} + \mathbf{J}_{R_i}^T (\boldsymbol{\theta}_i \dot{\mathbf{J}}_{R_i} \dot{\mathbf{q}} + \boldsymbol{\Omega}_i \times \boldsymbol{\theta}_i \boldsymbol{\Omega}_i) - \mathbf{J}_{COG_i}^T \mathbf{F}_{g_i} \quad (2.40)$$

$$\mathbf{J}_s^T \mathbf{F}_s = \sum \mathbf{J}_{s_i}^T \mathbf{F}_{s_i}, \quad (2.41)$$

$$\mathbf{S}^T \boldsymbol{\tau} = \sum \mathbf{J}_{R_i}^T \boldsymbol{\tau}_i. \quad (2.42)$$

2.6 Summary

The kinematics and dynamics of legged systems are described by a floating base representation and generalized coordinates. We apply a hard contact model such that the contact forces origin from algebraic constraints. Using a generic class of support null-space projectors, the EOM can be stated on a constraint consistent manifold. This reduced dimensional description is independent of contact forces and particularly useful for model-based control design. The application of a hard contact model further entails that a switch in the contact situation needs to be analyzed by the impulse dynamics. It is associated with an instantaneous change in velocity and an energy loss. This chapter finally provided the theoretical background to generate an analytical description of the MBS which is later used in our control framework.

Chapter 3

System Design

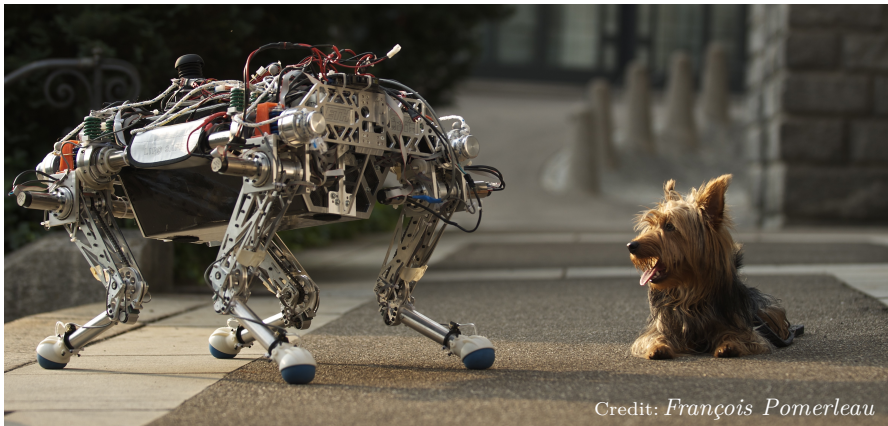


Figure 3.1: StarlETH is a compliant quadrupedal robot for dynamic locomotion. Design guidelines for legged systems that are specifically built for dynamic maneuvers can be directly adopted from their counterparts in nature. For example, to reduce the leg inertia, segments should be built as lightweight as possible and heavy components, such as actuators, should be placed close to the main body. This allows for faster swing leg motion and additionally decreases the impact energy losses at touchdown. Elastic elements should decouple actuators and joints in order to make the system inherently robust against landing collisions, to allow passive adaptation, and to enable temporary storage of energy (Alexander, 1990). To maximize mobility, one should aim for a large range of motion in all joints and thus tightly integrate all mechanical and electrical components.

In this chapter we show how these coarse design guidelines have been realized in the quadrupedal robot Starl*ETH* (Figure 3.1). We outline the mechanical properties of the complete system and its four legs that can be operated individually. The legs can be equipped with two different types of feet elements to robustly and energetically efficiently interact with the environment, namely a soft rubber ball with contact sensors based on air pressure measurement, and a passive ankle joint with springs imitating the function of the Achilles tendon. The main focus is put on compliant joint actuation as we consider this as the key element when combining *versatility*, *speed*, *efficiency*, and *robustness* in one single robotic device. We discuss and compare different SEA arrangements and present the final hardware realization. To make the entire robot lightweight and powerful, it is essential to jointly design and tightly integrate the system mechanics and actuation. The chapter is completed by a description of the electronic setup and the centralized software environment for simulation and control.

3.1 Starl*ETH*— a Compliant Quadruped Robot

Starl*ETH* (Springy Tetrapod with Articulated Robotic Legs) is a quadruped robot that features four identical, completely symmetric articulated legs connected to a rigid main body. With a body length of about 0.5 m, segment lengths of 0.2 m, and a total weight of 23 kg, this robot has roughly the overall dimension of a medium-sized dog (Figure 3.2). A summary of the mass properties and joint actuation specifications is given in Table 3.1.

3.1.1 Why Quadrupeds?

The decision for a quadrupedal design is mainly motivated by the fact that we seek for a legged platform that can perform a large variety of gaits from dynamic running on flat ground to statically stable climbing over challenging terrain. Four is the minimal number of legs that is needed to statically locomote with point feet. In contrast thereto, a bipedal robot would require actuated feet elements which drastically increase the mechanical complexity, the mass of the end-effectors, and hence the impact losses at landing as well as the actuator effort for swing leg motion. A further advantage of the multi-contact situation is the large footprint which enables different load distributions to optimize actuator efficiency, contact stability, or even to perform sophisticated climbing maneuvers by clinging to the ground. With all these advantages, it is not a coincidence that nature has designed the most advanced (large-scale) animals with four legs.

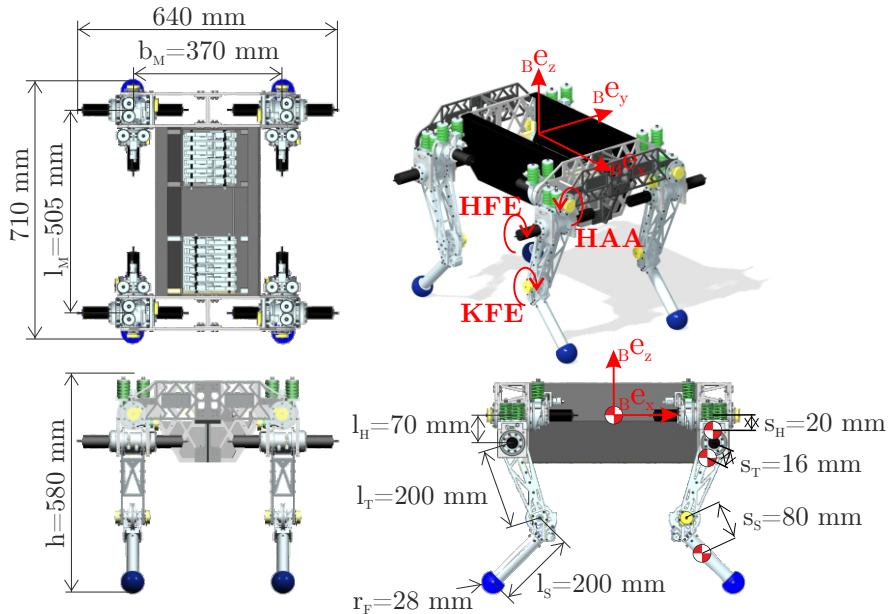


Figure 3.2: StarLETH has four symmetric legs each with three actuators arranged similar to mammals with successive HAA, HFE, and KFE. The dimensions and weight resemble a medium-sized dog.

3.1.2 Dimension and Structure

The choice of the size and dimensions of StarLETH is driven by different elements. An important requirement is that the robot can be safely operated by a single person without large test bench installations. At the same time, the machine has to be large and powerful enough to carry sophisticated sensor equipment and onboard power. These contradictory goals in combination with the available motor and electronic components impose tight size and weight restrictions.

StarLETH is built to perform dynamic running (e.g. Gehring et al., 2013; Hutter et al., 2013a,b) as well as static walking in challenging terrain (e.g. Hoepflinger et al., 2010c; Hutter et al., 2012b). This variety in gaits requires to make a compromise in body width b_M between supporting static stability with a large foot print and facilitating dynamic locomotion by a narrow leg arrangement.

A large point for discussion in the research community is the structural

Table 3.1: Specifications of Star*ETH* in addition to Figure 3.2.

total mass	23	kg	max./min. $\varphi_{j,HAA}$	-45/45	$^{\circ}$
- m_M (body)	13	kg	max./min. $\varphi_{j,HFE}$	-80/80	$^{\circ}$
- m_H (hip)	0.6	kg	max./min. $\varphi_{j,KFE}$	-175/60	$^{\circ}$
- m_T (thigh)	1.56	kg	max. joint torque	30	Nm
- m_S (shank)	0.32	kg	max. joint speed	600	$^{\circ}/s$
payload	25	kg			

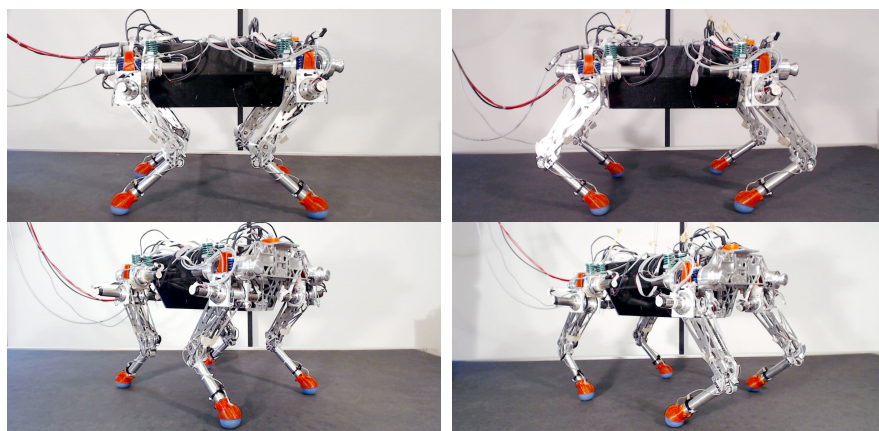
design. On one side, the system should be naturally compliant to ensure safe interaction with the environment. On the other side, a precise and fully actuated kinematic structure is preferable to control the robot. To satisfy both requirements, we build the individual links as rigid as possible and integrate well known and specifically tuned compliances in the torque controllable joints.

3.1.3 Main Body Design

The main body is manufactured as a monocoque based on a carbon-fiber sandwich structure with aluminum front- and back connectors. This stiff structure guarantees minimal (unobservable) body deflections with a total weight of less than 2kg. It contains well protected and cooled by active air circulation all electronic parts such as motor controllers and sensor boards. At the same time, the aluminum construction satisfies the tolerances to attach the hip abduction drive units.

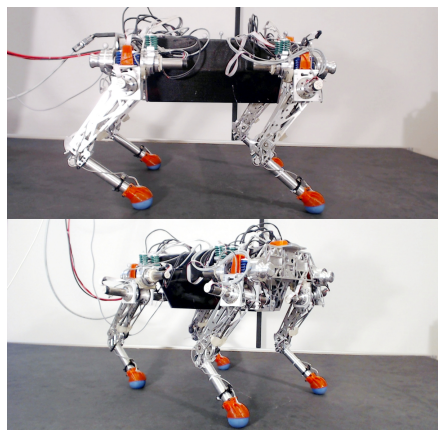
3.1.4 Leg Configuration

A critical element to enable a variety of gaits on different types of terrain is joint mobility respectively ground clearance. It is hence preferable to apply articulated legs in contrast to a prismatic design that is mostly used for pure dynamic gaits (e.g. Poulakakis et al., 2005; Raibert, 1986). The resulting kinematic structure of Star*ETH* (see Figures 2.1 and 3.2) consists of 12 actuated rotational degrees of freedom. The joints are arranged similar to mammals with successive hip abduction/adduction (HAA), hip flexion/extension (HFE), and knee flexion/extension (KFE). All legs and segments are built in a completely symmetric way with modular plug-interfaces at the hip as well as at the knee joint. This makes manufacturing cheaper and allows to quickly (<5 min) exchange the shank and thigh modules as required to replace certain parts during maintenance or to change the leg configuration. Although there exist different theoretical and simulation studies indicating that the



(a) X-configuration

(b) O-configuration



(c) M-configuration

(d) XO-configuration

Figure 3.3: Due to a fully symmetric design of all links and a modular interface in the knee and hip joint, the configuration of the legs can be arbitrarily changed within short time.

most common *X-configuration* is best suited for quadruped robots (for a detailed discussion see (Semini, 2010, chap. 3.2.4)), there is no clear evidence on this. To our best knowledge, experimental studies with a sophisticated platform are still missing. Figure 3.3 depicts some possible leg configurations we can implement on StarlETH, whereby exactly the same parts are used in any of them: the default *X-configuration* (Figure 3.3(a)), the *O-configuration* (Figure 3.3(b)), the mammalian *M-configuration* (Figure 3.3(c)), and the unusual *XO-configuration* (Figure 3.3(d)). While a detailed differentiation is beyond the scope of this thesis, a set of dynamic trotting experiments was successfully conducted for prove of concept (see video link in Section 1.4). As all our controllers are fully model-based, all experiments are conducted with the same control parameters but different default postures.

3.2 Single Leg Design

The single leg as depicted in Figure 3.4(a) was designed as a planar version (HFE and KFE) for test bench evaluation (Chapter 7) and augmented with the hip abduction actuator for the final integration in StarlETH.

3.2.1 Mechanical Structure

In the development of the mechanical structure, we put emphasis on keeping the inertia of the moving segments minimal. This was achieved through a dense integration and a lightweight construction using high-tensile aluminum. All actuators are concentrated at the main body, driving the individual joints by chain and cable pulley transmissions (Figure 3.4(b)). A single, weight optimized drive unit containing harmonic drive gearboxes and two brushless motors for HFE and KFE serves itself as the hip joint axis. StarlETH features a high power to weight ratio as each leg, detached from the main body and including all three actuator units, weights roughly 3.3 kg. This results in an average actuator weight of about 1.1 kg, which is comparable with high-performance stand-alone SEA solutions using equivalent motors (see e.g. Paine and Sentis, 2012). The compact design with the chain and cable pulley transmissions further results in a joint mobility which is significantly higher than what can be achieved with a design based on linear actuators (see e.g. Semini et al., 2011). The leg can be completely extended and retracted ($\varphi_{j,KFE} \in [-175^\circ, +60^\circ]$) while the hip joint can undergo a swing angle of $\varphi_{j,HFE} \in [-80^\circ, +80^\circ]$. The abduction angle range of $\varphi_{j,HAA} \in [-45^\circ, +45^\circ]$ is only limited due to cabling. This mobility is crucial when it comes to specialized maneuvers like standing up, walking in rough terrain, or climbing

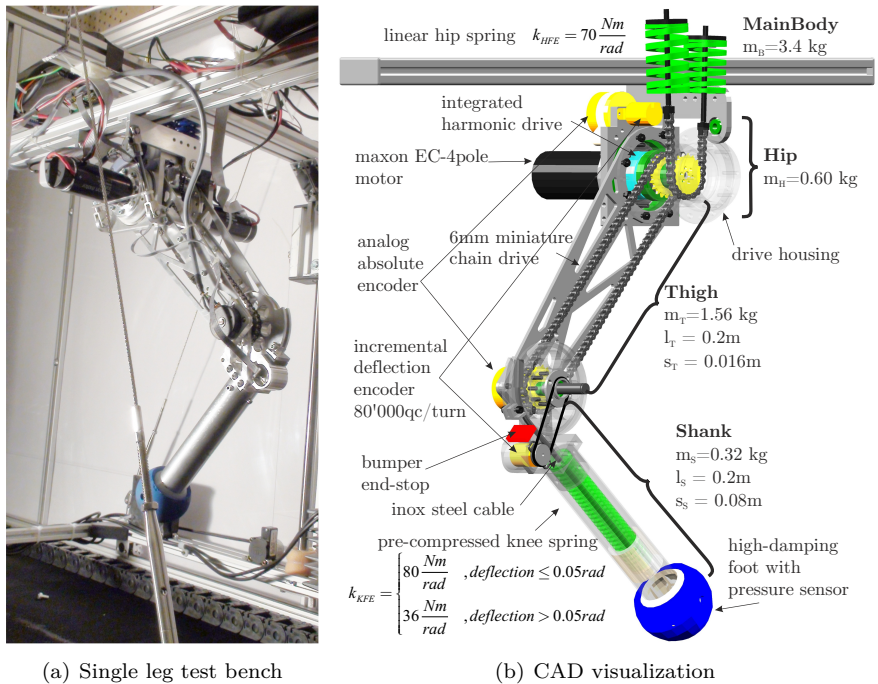


Figure 3.4: System description of a planar version of the single including a visualization of the SEA principle for HFE and KFE.

obstacles. For safety reasons, the drive transmission respectively the chain is dimensioned as the weakest part with a breaking point that is slightly below the gearbox specifications. This ensures fast and cheap maintenance in case of mechanical failure when the system is involuntarily overloaded.

3.2.2 Modular Foot Design

The leg can be equipped with a tactile ball foot or with a passive compliant ankle joint. The latter solution is beneficial from an energetic point of view but is only used for planar running experiments due to its passivity and directionality.

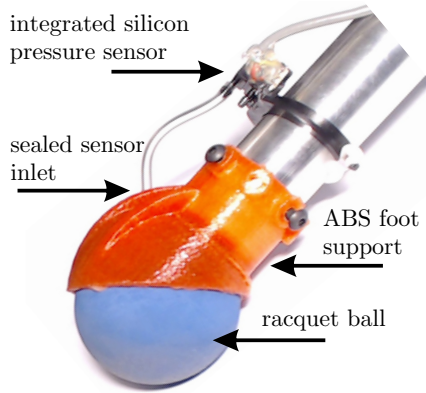


Figure 3.5: The compliant, lightweight, and highly damped rubber feet are equipped with a *Freescale Semiconductor MPXV5004* pressure sensor that provides sensitive and reliable information about the absolute contact force.

Compliant Ball Foot

To detect ground contact, a differential pressure sensor (*Freescale Semiconductor MPXV5004*) is incorporated with a sealed, air-filled racquet ball and used as soft and tactile foot element (Figure 3.5). Thereby, tiny pressure changes in the ball are registered and used to reliably determine the current contact situation. This sensor measures only an amplitude value for the overall contact force. In return, the lightweight design (total foot weight is about 70 g) is perfectly robust against impulsive forces and additionally provides useful compliance and damping at the point of contact.

Compliant Ankle Joint

To optimize energetic efficiency of legged locomotion, it is crucial to keep damping small, to ensure large energy storage capabilities, and to minimize impact losses. In particular the latter energy drain is often disregarded but can be substantial for an articulated, 2-segmented leg, as the impulses are propagated through the structure and instantaneously lower the main body speed after landing. A comparison of different robotic legs with known mass and geometric parameters (Stanford KOLT (Nichol, 2005; Nichol and Waldron, 2002; Nichol et al., 2004), OLIE (De Man et al., 1998a,b), the leg designed by Curran and Orin (2008); Knox and Schmiedeler (2007) and two legs developed at our lab by Hutter et al. (2013c)) shows an energy loss of

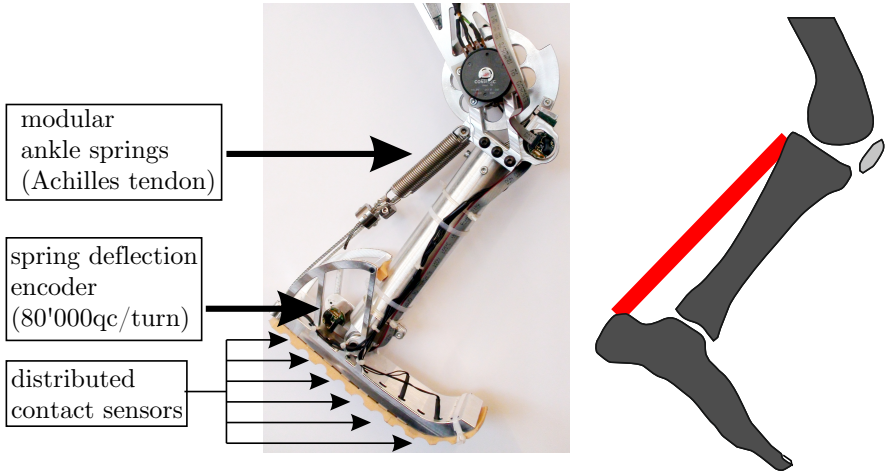


Figure 3.6: A robotic foot with a compliant ankle joint is used to increase running efficiency. Inspired by a human leg, springs emulate the behavior of the Achilles tendon and Soleus muscle while an orthopedic foot sole ensures a soft impact. Distributed contact switches and a spring deflection encoder provide information about the contact situation and ankle joint torque.

$12\% \pm 4\%$ when evaluating (2.32) at a reasonable inner knee elongation angle of about 120° ¹. Due to the kinematic coupling, this drastically increases the more the knee joint is extended. An experimental confirmation is given in Section 7.3.3. As the impact energy loss is proportional to the mass of the most distal segment (compare with (2.32)), efficiency can be increased by integrating an additional lightweight foot segment. To this end, we manufactured a structurally optimized foot (Figure 3.6) as a single high-tensile aluminum part that has a total weight of only 125 g. It includes a high resolution joint encoder ($80'000 \text{ qc/rev}$), 10 digital distributed ground contact switches, and an orthopedic foot sole. Inspired by biology, the foot is equipped with modular springs emulating the behavior of the Achilles tendon and Soleus muscle to intermittently store energy during contact phase. In the depicted setup, the two exchangeable ankle springs (56 g) produce a rotational stiffness of $k_{AFE} = 10 \text{ Nm/rad}$.

¹ 180° would be completely stretched

3.3 Actuator Design

The goals of *versatility* and *efficiency* seem to be contradictory when it comes to actuation and control (Kuo, 2007). To make systems *versatile*, it is desirable to have actuators with high-performance torque and position tracking capabilities. This seeks for stiff actuators with high bandwidth and high feedback gains that can nearly arbitrarily shape the motion of the system. To make them energetically *efficient* on the other hand, it is preferable to let the passive system dynamics perform most of the locomotion and only shape and maintain it. This can be only achieved by compliant actuation.

A particularly interesting approach that tries to combine these two contradictory requirements is series elastic actuation (SEA). Unlike rigid actuators, SEAs employ an elastic element in series with the mechanical energy source. This gives them several beneficial properties such as force controllability with low mechanical impedance, robustness to impact loads, increased power and velocity output, and the capability of mechanical energy storage. At a first glance, all these properties seem to perfectly fit the requirements of legged robotic systems.

Following the first documented design rules for such actuators provided by Robinson et al. (1999), the designer is suggested to select the compliance element as a function of the desired control bandwidth. There are different groups that provide such SEA solutions both as linear (e.g. Paine and Sentis, 2012; Pratt et al., 2002) and rotary setups (e.g. Donald and Li, 2012; Kong et al., 2012; Sensinger and Weir, 2005; Tsagarakis et al., 2009). A characterization and comparison of these solutions among each other mostly reduces to comparing control bandwidth and power(-density). To perform well in this competition, the series compliance inevitably needs to be chosen stiff or even highly damped (Hurst and Rizzi, 2004) as it acts like a mechanical 2nd order low pass filter.

The analysis of the actuation principles for locomotion as they are employed by nature slightly changes these design objectives. Humans and animals have a rather low control bandwidth in their actuators for disturbance rejection (depending on study somewhere in the range of 4 – 8 Hz (e.g. Fitzpatrick et al., 1992)), still they are able to perform highly complicated and versatile tasks. Moreover, different biomechanical studies showed clear evidence that the muscular tendon system acts to a large extent as a mechanical spring to store and return elastic energy (Cavagna et al., 1964, 1977). It was found that the long and compliant Achilles tendon is an impressive example: In a hopping kangaroo or a running human, the Achilles tendon alone conserves as much as 35% of the mechanical energy required for a stride

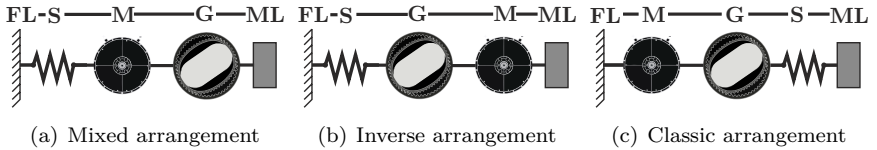


Figure 3.7: For HAA (a), HFE (b), and KFE (c) we employ different SEA arrangements of the motor (M), gearbox (G), and spring (S) between the fixed link (FL) and moving link (ML).

(Alexander, 1988; Farley et al., 1993). Ker et al. (1987) found that more than 50% of the total energy turnover in human running during one stance phase (100 J) is mechanically stored with about 35 J as strain energy in the Achilles tendon and about 17 J in compliant elements in the foot.

Transferring this knowledge from biomechanics into robotics implies that we need to consider SEA design as an “embodied” approach (Pfeifer and Scheier, 2001), or in other words, the compliant actuator has to be engineered hand-in-hand with the entire robot and its application. To this end, we adapt the design guidelines defined by Robinson et al. (1999). Starting with (i) a concept of the leg respectively quadruped robot as well as desired locomotion speed and stride frequency, we can extrapolate (ii) the desired joint stiffness to support the motion passively as well as the motor specifications in terms of speed and torque requirements. This is an iterative process and can only be conducted to a small extent without actually building the device. As a simplification, we designed all our actuators based on a set of springs with equal dimensions but different stiffness. This allows for fine-tuning the passive system dynamics without remanufacturing any component.

3.3.1 Possible Arrangements

The classical SEA arrangement as it was designed and patented by Pratt and Williamson (1995, 1997) has the gearbox output shaft connected through a spring with the successive link. This is schematically depicted in a rotary setup in Figure 3.7(c) and we will refer to this as the *classic* arrangement with the individual components *motor* (M), *gearbox* (G), and *spring* (S) between the *fixed link* (FL) and *moving link* (ML). Talking about *fixed link* in this context refers always to the predecessor link while the moving link is the successor link (e.g. FL = thigh, ML = shank).

In addition to this classic configuration, there are different other possibilities to arrange these components. The main reason for changing the order

of energy source M and G and the spring S as in Figures 3.7(a) and 3.7(b) is to be able to remotely locate the springs anywhere on the fixed link. This makes it often possible to achieve a more compact design or even to reduce the weight. In return, and this is a clear drawback, the mechanical decoupling element is not located between the gearbox output and the moving link. Hence, in an impact at landing, the output mass and also the rigidly connected gearbox and motor mass encounter an instantaneous change in velocity. Given an impulsive force \mathcal{F}_i acting on link i in actuator direction, the load that may harm the gearbox amounts to $\mathcal{F}_{gb,i} = \frac{m_M+m_G}{m_M+m_G+m_{ML}} \mathcal{F}_i^1$ in the *mixed* setup (Figure 3.7(a)) and to $\mathcal{F}_{gb,i} = \frac{m_G}{m_M+m_G+m_{ML}} \mathcal{F}_i^1$ in *inverse* setup (Figure 3.7(b)). Correspondingly, these designs are less tolerant to impacts as the standard SEA arrangement. Furthermore, the rigid connection to the output requires to assign the motor inertia to the moving link. This increases the overall mass of the moved segment and hence lowers the acceleration during flight phase.

3.3.2 Hardware Realization

Most existing SEAs are based on the combination of an electric motor and a gearbox which delivers high power at a moderate speed. In our robot, we decided to use *Maxon EC-4pole brushless 200 W* motors in combination with *Harmonic Drive CSG-14 Units* with a 1:100 reduction. The choice for a rotary setup is motivated by the fact that it allows for high joint mobility and hence supports the versatility aspect of the whole design. Using *Harmonic Drive Units* further keeps the weight extremely low, the design compact, and prevents any backlash in the system. All actuators are designed to deliver 30 Nm torque with a maximal turning speed of more than 600 °/s. Joint angles and spring deflections (*AVAGO AEDA3300* 80'000 °c/rev), as well as the motor angles (*AVAGO HEDL 2000* °c/rev) are precisely measured by incremental quadrature encoders. The joint springs can freely move such that frictional effects are immaterial and the identified spring characteristic shows a negligible hysteresis (Appendix A.7).

The hip actuators HAA and HFE are built as the *mixed* (Figure 3.7(a)) and *inverse* (Figure 3.7(b)) arrangement, respectively. This has the advantage that springs can be “remotely” stored on the main body or the hip module to make the design very compact. We implement the rotary compliance by two antagonistically precompressed springs ($k_{HAA} = 100 \text{ Nm/rad}$, $k_{HFE} = 70 \text{ Nm/rad}$) in combination with a cable pulley (HAA, 3 mm inox

¹These formulations result from an impact analysis of three rigidly connected masses which all encounter the same velocity change.

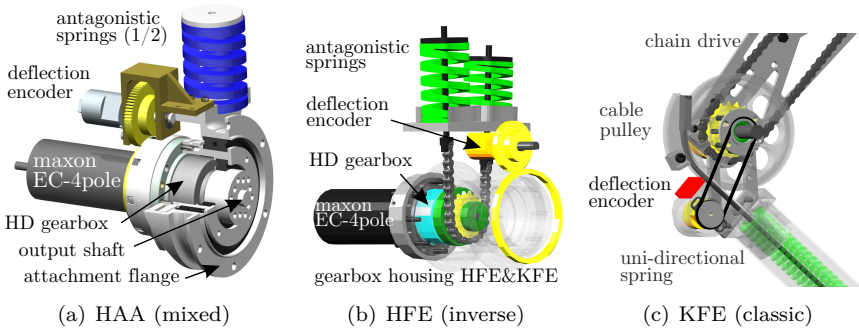


Figure 3.8: Three SEAs for StarLETH: HAA is rigidly attached to the main body (a). The KFE motor (not depicted) is integrated in the mirrored drive unit of HFE (b) with the chain drive connecting to the knee joint (c).

steel) or chain drive (HFE, 6 mm pitch). To minimize the drawback of the additional mass that is rigidly connected to the moving link, both motors are placed directly on or, in case of HFE, in the rotation axis. Thereby, their contribution to the segment inertia remains minimal. Since the main oscillatory motion during stance phase of running is generated by the knee joint, the compliances of HAA and HFE have a rather low contribution to the useful passive dynamics and are hence mainly selected to achieve good torque and joint position control performance. This requires a careful selection of the spring stiffness: Springs that are too stiff let the unloaded leg oscillate at frequencies that are impossible to control with the limited bandwidth of the actuators, while springs that are too compliant require large travel distances in the actuators to produce a desired force during stance phase. This would decrease the force control bandwidth and drastically reduce the overall performance.

The knee actuation concept was implemented as the *classic* arrangement (Figure 3.7(c)). This setup was chosen as the inertia of the most distal link has the largest influence on impact losses and the swing leg performance. To further reduce the overall leg inertia, the KFE motor and gearbox are located in the hip axis and connected through a miniature chain drive to the knee joint. The spring of KFE is the main contributor in passively storing and releasing energy and it is hence mainly defined by the desired system dynamics.

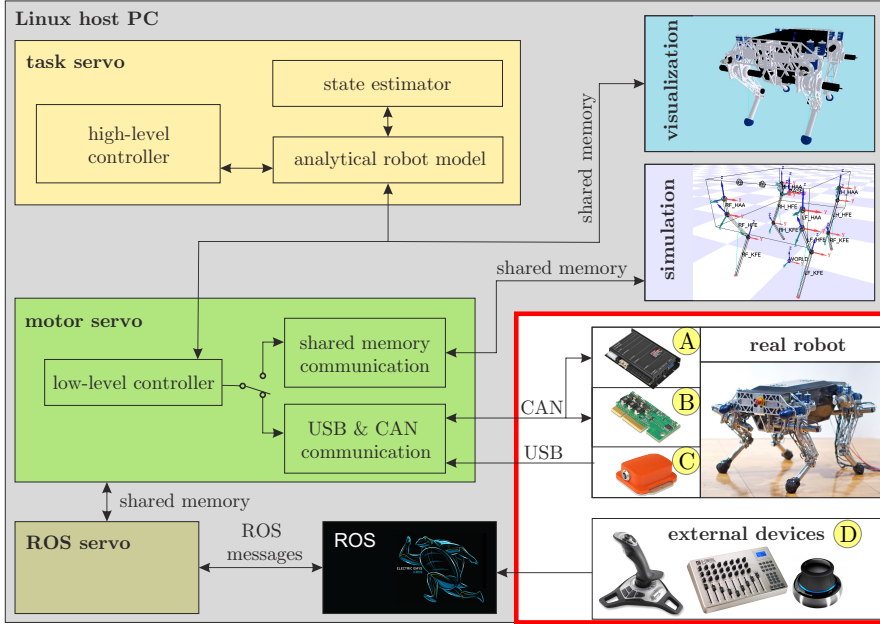


Figure 3.9: The real-time simulation and control environment is based on SL (Schaal, 2009). The framework allows an immediate switch between simulation and actual robot by changing the communication interface.

3.4 Electronics

The electronics setup of Star $LETH$ is summarized in Figure 3.9. The joint motors are regulated by 12 *Maxon EPOS2 70/10* control modules (A) that are connected through 4 parallel operating CAN buses with the host PC. Using the same communication interface, custom-made sensor boards based on *Maxon EPOS2 36/2* modules (B) provide the sensor signals of the additional joint encoders and foot contact sensors. These components are located well protected within the main body of Star $LETH$. A *X-sense MTi* inertial measurement unit (IMU) (C) is attached to the main body to measure body acceleration and rotation rates as required for state estimation. Different input devices are used by the operator to steer the robot and to give high-level commands (D). Star $LETH$ can be externally powered or autonomously operated with an onboard PC and standard LiPo batteries (≈ 1.7 kg additional weight).

3.5 Software

Safe debugging and testing of complex and computationally intensive control strategies requires a powerful and reliable software setup. After several iterations through different configurations, we realized a framework as depicted in Figure 3.9. It is based on a single centralized host PC that conducts the entire high-level control part. The software contains the real-time simulation and control environment SL (Schaal, 2009), which is used as a MBS engine, for visualization of the robot and its environment, as well as for handling the internal messaging between the different servos through shared memory. It additionally provides tools for data logging and post-processing.

As a core element, the *motor servo* is responsible for timing and coordination of the individual modules. It contains all low-level regulators (position, velocity, torque) and signal filters. Using either shared memory to access the simulation, or a CAN gateway to communicate with the actual robot (red box), there is the possibility to run simulations and experiments (even in parallel) with exactly the same controller implementation. This is advantageous for development, since it avoids code reimplementations, simplifies debugging and testing, and ensures certain safety if the controllers show good robustness in the simulation.

The *ROS servo* provides an interface to the *robotic operating system* that cannot meet the hard real-time constraints of SL itself. This connection opens the door to a huge set of existing sensor drivers and software packages. In our current setup, it is mainly used for external devices such as a 3D joystick, gamepad, or MIDI controller to steer the robot.

Finally, the *task servo* includes all high-level control, state-estimation, and motion planning tools. To decouple it completely from the MBS simulation, global kinematics and dynamics are implemented analytically (Section 3.5.1). In addition to speed, the clear separation between the model used in the controller and the simulation ensures that only actual sensor signals coming from the robot or the simulation are passed from the motor servo to the task servo, which makes the simulation as realistic as possible. Sensor noise, imperfect state estimation, or (intentionally) introduced model errors allow to examine the robustness of the controller and hence to limit the problematic of unstable plant inversion before testing it on the hardware.

This software environment is operated at 400 Hz for hardware experiments. However, the rate-limiting factor is the data connection of the CAN bus system between the host PC and the motor controllers. Although we managed to parallelize 4 channels (1 per leg), the bit rate of 1 MBits/s confines the overall loop cycle time.

3.5.1 Analytical Kinematics and Dynamics

To generate an analytical model of the MBS dynamics, we developed the open-source software package *proNEu* (Hutter et al., 2011a) based on the MATLAB Symbolic Math Toolbox (The MathWorks, 2013). It requires as input a relative kinematic tree of the MBS as a function of arbitrarily defined generalized coordinates. This includes a description of the rotation and translation of the COG of each link with respect to its predecessor. Based on this input, global kinematics are generated by Euler rotations and finally, all dynamic properties are calculated using the projected Newton-Euler equations outlined in Section 2.5.

3.5.2 State Estimation

To assess the base location and orientation with respect to the inertial frame, we developed in (Bloesch et al., 2012a) a state estimator framework based on an extended Kalman filter. This combines accelerometer and gyroscope measurements for state prediction with the kinematic information from the precise joint sensors in the update step. In contrast to most available solutions, this framework does not make any assumption about the environment but considers the contact points as augmented states of the system. It hence allows not only for precise estimation of the floating base position and orientation but additionally provides a sparse elevation map of the temporary contact points.

3.6 Summary

Star*LETH* is a dog-sized, fully actuated quadrupedal robot. It is built to perform different gaits from static walking in rough terrain to dynamic trotting. In the design process we put emphasis on a lightweight and highly integrated construction with all actuators concentrated at the main body. The leg segments are completely symmetric with modular interfaces in all joints which allow to quickly change the robot configuration. The legs can be equipped with two complementary feet such as a compliant ball foot and a passive ankle joint to increase the energetic efficiency. To actuate Star*LETH*, we developed highly compliant SEAs of different mechanical structure to protect the gearbox from landing impact, to enable precise torque control, and to intermittently store substantial amount of energy during stance phase. To simplify controller testing and implementation, the software setup was based on a centralized host PC with a real-time control and simulation environment.

Chapter 4

Low-Level SEA Control

Legged systems are facing two fundamentally different periods in locomotion that are defined as *stance* and *swing* phase. This separation is not only reflected in a very different plant model that each joint actuator experiences at its output, but also in two different control objectives.

During *stance phase* on one side, the system has a high output mass since the main body is comparably heavy and the ground does not move at all (Figure 4.1(a)). In this phase, the joint actuators should enable compliant interaction with the environment and adapt to ground elevation. They must regulate the body attitude even under substantial external disturbances by producing appropriate support forces at the contact points. Additionally, to make locomotion energetically efficient, the mechanical properties of the actuators should be designed to efficiently store energy in the passive elements after touchdown and to release it again before lift-off. In other words, the series elasticity must have *minimal damping* to maximally support the vertical mass-spring oscillation that characterizes most running gaits. This requirement is in line with the properties of tendons of humans and animals, that are, in fact, excellent biological springs with nearly no hysteresis and an efficiency of about 95% (Alexander, 2002; Novacheck, 1998). Building SEAs with low natural damping further simplifies precise torque control, as the output torque is only related to position deflections and not largely influenced by velocity dependent friction that is often hard to measure or model.

During *swing phase* on the other side, the leg is freely moving in air, which corresponds to a model of low output mass (Figure 4.1(b)). In this contact-free situation, the joint actuator should quickly *control the position* of the foot point to maintain and balance a locomotion gait. Thereby, the series elasticity in the joint is undesired as it creates deflections and oscillations that hamper

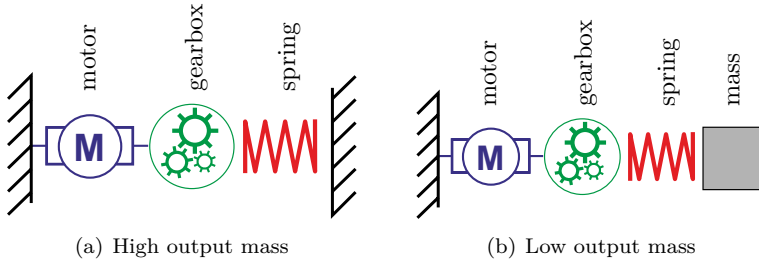


Figure 4.1: The joint actuators of legged systems are facing a high output mass during stance phase and a low output mass during swing phase.

fast and precise foot positioning. This causes a “damping dilemma” as the joint should have low damping during stance phase and high damping during swing phase. A proper controller design can compensate to some extent for these adverse effects by actively damping the joint motion. However, as the motor has bandwidth and saturation limitations, regulation by software is often insufficient and hence needs to be achieved by additional means. To solve the “damping dilemma” without increasing actuator complexity, we propose two hardware design concepts based on internal collisions in a setup with a unidirectional compression spring and nonlinear damping in a combined series spring-damper arrangement.

4.1 Control Structure

This section first introduces and compares the two commonly used control structures for SEAs based on direct motor current and cascaded motor velocity control. Considering the advantages for our implementation, the outer joint torque and position control loops are subsequently designed based on the latter setup.

4.1.1 Motor as a Torque Source

An electric motor is in literature generally known as torque source (Isermann, 2005). On the lowest control level, the electric circuit (A) is regulated using a current controller (B) to achieve a desired motor torque $\tau_m = \kappa_a I_m$ that accelerates the rotor and gearbox respectively. This inner feedback loop of the motor electronics is typically very fast ($\text{BW} \geq 1 \text{ kHz}$) and hence we can assume $I_m = I_{m,\text{des}}$ for further control design.

The first class of SEA control designs makes use of this linear relation between motor current and torque, and commands the setting value $I_{m,\text{des}}$ as a function of the desired and actual joint torque τ_j at the series elasticity:

$$I_{m,\text{des}} = C_{\tau \rightarrow I}^{FB} (\tau_{j,\text{des}} - \tau_j) + C_{\tau \rightarrow I}^{FF}. \quad (4.1)$$

This uses a feedback controller $C_{\tau \rightarrow I}^{FB}$ to minimize the error of the command signal and a feedforward compensator $C_{\tau \rightarrow I}^{FF}$. In the early work of Pratt and Williamson (1995), $C_{\tau \rightarrow I}^{FB}$ is designed as PID control with roll-off and the feedforward compensation $C_{\tau \rightarrow I}^{FF}$ is used to counteract the external load and to accelerate the motor respectively. More elaborated approaches use model-based techniques and disturbance observers (e.g. Kong et al., 2009; Paine and Sentis, 2012). A major difficulty and disadvantage with this direct method is to establish accurate models to properly compensate for the (nonlinear) gearbox friction, stiction, or backlash.

4.1.2 Motor as a Position Source

To overcome these deficiencies, Pratt et al. (2004a) later suggested to consider the combination of motor and gearbox as a position controlled device. To this end, an additional cascading feedback loop (C) can be used for regulating the motor speed (D). This is described in a generic formulation as

$$I_{m,\text{des}} = C_{\dot{\varphi}_m \rightarrow I}^{FB} (\dot{\varphi}_{m,\text{des}} - \dot{\varphi}_m) + C_{\dot{\varphi}_m \rightarrow I}^{FF}. \quad (4.2)$$

The feedback part $C_{\dot{\varphi}_m \rightarrow I}^{FB} = k_p^{vel} + \frac{k_i^{vel}}{s}$ is mostly implemented as a PI-controller. Additional feedforward compensation $C_{\dot{\varphi}_m \rightarrow I}^{FF}$ further improves the reference tracking behavior. In contrast to the previous method, this cascaded motor velocity loop compensates for undesired gearbox friction effects, typically with a bandwidth in the order of 100 Hz.

Convinced by these benefits, different groups (e.g. Pratt et al., 2004a; Vallery et al., 2007; Wyeth, 2006) realized such a cascaded structure and designed the outer spring torque control loop as

$$\dot{\varphi}_{m,\text{des}} = C_{\tau \rightarrow \dot{\varphi}_m}^{FB} (\tau_{j,\text{des}} - \tau_j) + C_{\tau \rightarrow \dot{\varphi}_m}^{FF}. \quad (4.3)$$

The feedback compensator $C_{\tau \rightarrow \dot{\varphi}_m}^{FB} = k_p^\tau + \frac{k_i^\tau}{s} + k_d^\tau s$ is mostly realized as a PID controller while the FF part is used to compensate for the joint motion.

4.1.3 Implementation

The choice for the right control structure is greatly influenced by the mechanical properties of the actuator and plant but also the available control

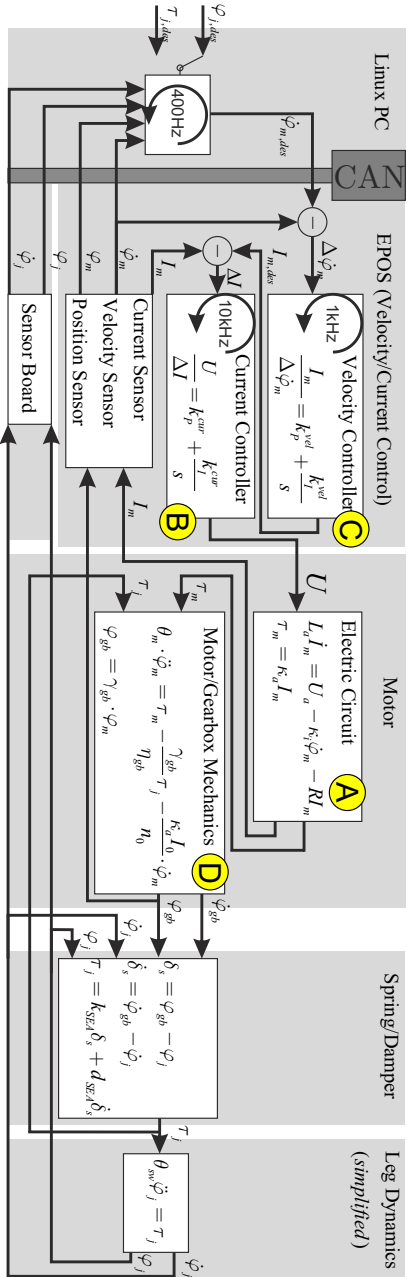


Figure 4.2: Our SEA controllers are built in a cascaded structure with joint position and torque control implemented on a Linux host PC that is connected over CAN to EPOS2 motor velocity controllers.

Parameters					
I_m	motor current	L_a	motor inductance	R	motor resistance
U_a	motor voltage	k_a	torque constant	k_i	speed constant
θ_m	motor and gearbox inertia	γ_{gb}	gearbox transmission ratio	η_{gb}	gearbox efficiency
I_0	no load current	n_0	no load speed	δ_s	spring deflection
φ_m	motor angle	φ_{gb}	gearbox angle	φ_j	joint angle
τ_j	spring resp. joint torque	θ_{sw}	lumped swing leg inertia		

electronics. We decided to use a cascaded, motor velocity based structure due to the following reasons:

Mechanic Properties: The actuator consists of a harmonic drive gearbox, which is generally known as rather hard to model especially for frequently alternating load direction. Additionally, the spring in series is highly compliant in comparison to other SEAs and hence needs large travel distances to actually build up a desired spring force.

Control Electronics: The final control electronics need to be integrated onboard with tight weight and size restrictions. Hence, we cannot rely on large-scale equipment as often used in a test bench setup, but have to utilize existing, high-performance motor controllers in combination with small-scale sensor boards. Such a setup entails longer communication paths, delays, less deterministic and synchronized timing, and finally a lower loop cycle time. In our implementation, the spring torque control loop runs at 400 Hz limited by the communication bit rate of the underlying CAN bus. The low-level velocity and current PID+FF control loops are operating at 1 kHz and 10 kHz respectively – perfectly timed and highly optimized. It is hence advantageous, to have the undesired motor and gearbox dynamics locally controlled.

For the subsequent simulation results, the entire structure as depicted in Figure 4.2 was rebuilt in MATLAB/Simulink including saturation, sampling, discretization, and filtering effects. To simplify the notation, gearbox transmission is omitted in the following formulations ($\varphi_{gb} = \varphi_m$).

4.2 Joint Torque Control

In Star ETH , the identified spring characteristics in all three joints (HAA, HFE, and KFE) show nearly perfect linearity with minimal hysteresis effects (see also illustration in Figures A.1(a) and A.1(b)). A linear, least square model fit results in a regression coefficient of $R = 0.999$ and a mean absolute error smaller than $\overline{|e|} = 0.08$ Nm for all joints. Hence, the springs are well suited as precise torque sensors by measuring the deflection

$$\delta_s = \varphi_m - \varphi_j, \quad (4.4)$$

$$\tau_j = k_{SEA} \delta_s, \quad (4.5)$$

and an integration of additional load cells that are expensive and might break under peak load can be avoided.

For designing the joint torque controller, different aspects need to be considered. In terms of performance, the closed loop system has to achieve

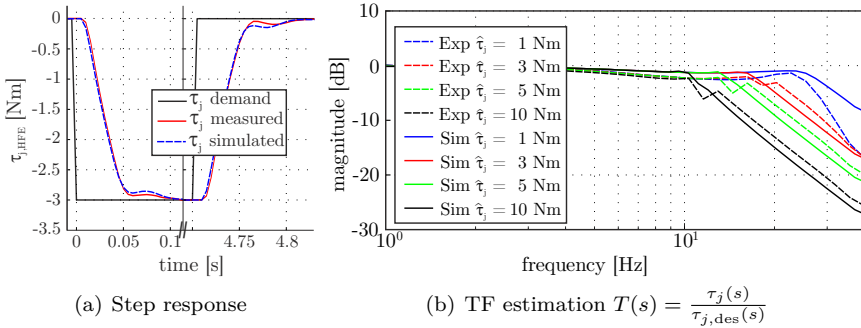


Figure 4.3: Experimental and simulated results of the SEA torque controller with a blocked output shaft show a fast step answer (a) with no overshoot and small delay due to the communication and control loop cycle time. The transfer function (TF) estimation of $T(s) = \frac{\tau_j(s)}{\tau_{j,des}(s)}$ (b) indicates a bandwidth of up to 28 Hz for small amplitudes; about 11 Hz remain when saturation effects occur.

good tracking and good disturbances rejection. To ensure stability also in case of interaction with different types of environment, it further must be stable as well as passive (Colgate, 1988).

4.2.1 PI Feedback Control

Good tracking performance is usually characterized by a high closed loop control bandwidth and low maximal gain amplification. Given the rather uncomplicated linear plant dynamics $P = \frac{\tau_j}{\dot{\varphi}_{m,des}} = \frac{k_{SEA}\varphi_m}{\dot{\varphi}_{m,des}}$ of the simplified high output mass model of the velocity controlled motor and spring with blocked output shaft $\varphi_j = \dot{\varphi}_j = 0$, we implement as feedback regulator a PI controller

$$C_{\tau \rightarrow \dot{\varphi}_m}^{FB} = k_p^\tau + \frac{k_i^\tau}{s} \quad (4.6)$$

with a slow integrator. Thereby, k_p^τ and k_i^τ represent the proportional and integral gain, respectively. Figure 4.3(a) shows the response to a desired step input of 3 Nm in simulation and experiment. The system can follow the reference signal in about 30 ms. A transfer estimation of $T(s) = \frac{\tau_j(s)}{\tau_{j,des}(s)}$ based on a logarithmic chirp for the demand joint torque is depicted in Figure 4.3(b). The bandwidth varies between 28 Hz for 1 Nm (blue), 20 Hz for 3 Nm (red), 15 Hz for 5 Nm (green), and 11 Hz for 10 Nm (black). These results emphasize the drawback of high compliance: with increasing amplitudes, the

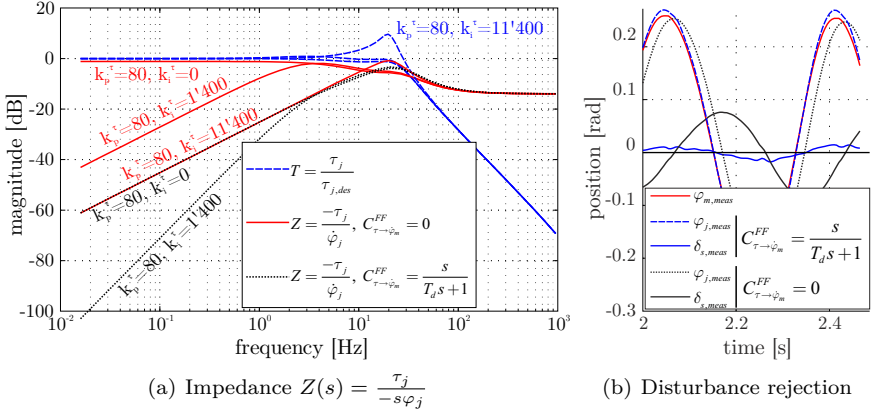


Figure 4.4: Using an additional disturbance compensator $C_{\tau \rightarrow \dot{\varphi}_m}^{FF}$ significantly lowers the impedance $Z(s)$ without changing the reference tracking behavior $T(s)$ (black dotted). In contrast, increased integrator gains lower the impedance (red solid) but increase the overshoot (blue dashed) (a). In a zero torque experiment ($k_i^\tau = 0$) with external disturbance, the measured error signal can be lowered to a large extent by the disturbance compensator (b).

bandwidth substantially drops due to saturation effects. However, the performance of our actuators is well-comparable with some of the best values found in literature for electrical SEAs by Pratt and Williamson (1995)(5-25 Hz), Vallery et al. (2007)(16 Hz), Kong et al. (2009)(10 Hz), or Sensinger and Weir (2005)(19 Hz).

4.2.2 Velocity Feedforward Compensation

In addition to a fast reference signal response, good disturbance rejection is crucial. This is particularly important in the field of haptics or human assistive devices and is mostly characterized by the output impedance¹

$$Z(s) = \frac{\tau_j(s)}{-\dot{\varphi}_j(s)}. \quad (4.7)$$

¹There is some confusion in literature about impedance. In the different work of Hogan and Colgate, impedance $Z(s)$ is defined as *the dynamic relationship between velocity input and force output at some physical location*. Other researchers in particular when working with SEAs, use the relation between position input and force output as impedance. In this thesis we follow the definition of Hogan and Colgate and call the latter one dynamic stiffness $K(s) = \frac{\tau_j(s)}{-\varphi_j(s)}$.

Good disturbance rejection means that the impedance needs to be as low as possible over the entire frequency spectrum. For high frequent disturbances, above the control bandwidth, the impedance and dynamic stiffness correspond to the mechanical spring properties ($Z(j\omega)|_{\omega \rightarrow \infty} = d_{SEA}$, $K(j\omega)|_{\omega \rightarrow \infty} = k_{SEA}$). This emphasizes the benefit of compliant systems with low natural damping and stiffness in comparison to mechanically stiff devices, as the former reject high frequent disturbances much better as they occur, e.g. in an impact. To improve disturbance rejection for low frequencies with pure feedback control, the integrator gains must be increased ($C_{\tau \rightarrow \dot{\varphi}_m}^{FF} = 0$, Figure 4.4(a), red solid). While lowering the impedance for low frequencies, increased integrator gains degrade the reference tracking behavior (blue dashed), can lead to a loss of stability and passivity (Vallery et al., 2007), and require for additional damping. To overcome this trade-off between good impedance and good reference tracking behavior, we include a simple disturbance compensator for the measured joint velocity $\dot{\varphi}_j$

$$C_{\tau \rightarrow \dot{\varphi}_m}^{FF} = \frac{\dot{\varphi}_j(s)}{T_d s + 1}, \quad (4.8)$$

with the time constant T_d . As depicted in Figure 4.4(a) (black dotted), this reduces the impedance at low frequencies without influencing the reference tracking behavior. The performance was validated in an experiment with the spring torque controlled to zero. As illustrated in a zero-torque experiment, applying the feedforward compensator significantly decreases the occurring deflections (Figure 4.4(b), blue solid) in comparison to pure feedback control (Figure 4.4(b), black solid).

4.2.3 Stability and Passivity

The proposed torque control structure needs to fulfill stability and passivity. The former criterion is evaluated by the poles of the closed loop system $T(s) = \frac{\tau_j(s)}{\tau_{j,des}(s)}$. As depicted in Figure 4.5(a), increasing the integrator too much will destabilize the system. Passivity on the other hand is required to guarantee stability when interacting with any other passive system. In our case this is a combination between all other joint actuators and links of the robot as well as the environment. It is evaluated by considering the impedance or admittance of the system. As outlined in (Colgate, 1988), the following conditions have to hold:

- $Z(s)$ is asymptotically stable
- $Re(Z(j\omega)) \geq 0$

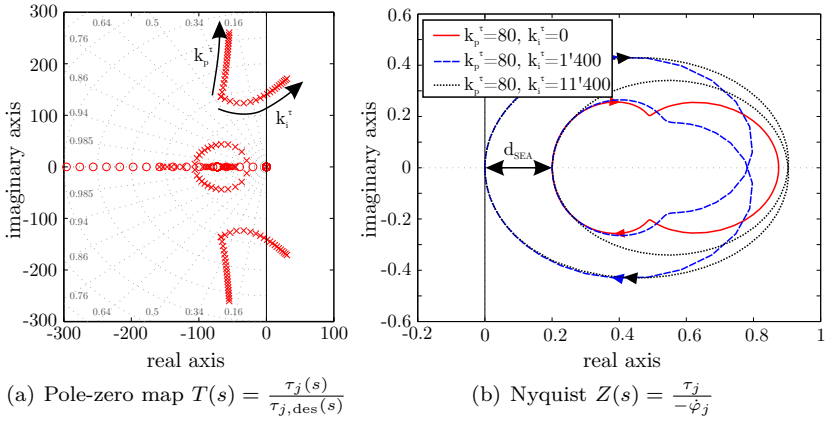


Figure 4.5: Increasing the integrator gains can destabilize the system as poles become positive (a). Passivity of system is guaranteed ($Re(Z(j\omega)) \geq 0$) since the mechanical damping d_{SEA} pushes the high frequencies to the right half plane (b).

Vallery et al. (2007) give some theoretical boundaries for the choice of control gains that guarantee passivity. However, as their study does not include mechanical damping in the motor dynamics as well as in the series elasticity, these boundaries are very conservative. Mechanical damping d_{SEA} pushes the Nyquist plot (Figure 4.5(b)) into the right half plane for high frequencies such that no passivity problems occur even for very high integrator gains that would lead to an unacceptable large overshoot (see T_{\max} in Figure 4.4(a)).

4.3 Joint Position Control

The standard approach to regulate the joint position φ_j by a SEA is to build upon the torque regulator introduced beforehand. Thereby, the desired actuator torque $\tau_{j,\text{des}}$ is commanded as a function of the measured (φ_j) and desired ($\varphi_{j,\text{des}}$) joint position, again mostly with a PID controller whereby the P-gain and D-gain represent the virtual joint stiffness and damping, respectively. Since the dynamics of this additional outer cascading structure needs typically to be significantly slower than the inner loop, this works only well for low-gain joint position control. Such approach is not sufficient when it comes to fast and precise swing leg positioning, as the motor should be able to actively damp out the natural mass-spring oscillations that occur due to the system compliance.

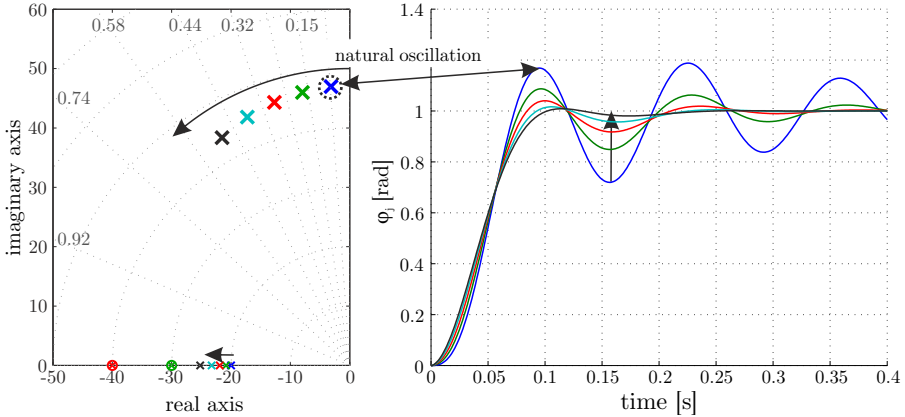


Figure 4.6: A LQR joint position controller allows increasing damping without sacrificing speed: the oscillating poles of $T(s) = \frac{\varphi_j(s)}{\varphi_{j,\text{des}}(s)}$ are shifted to higher damped regions which largely improves the step response.

4.3.1 Disturbance Modeling

To model the disturbances occurring in a swing leg, the inertia of all moved segments is lumped in a single parameter θ_{sw} . For example, to control HFE, θ_{sw} contains the inertia of the thigh and shank around the HFE axis. The dynamic behavior of this inertia can be expressed as a function of the motor angle φ_m , joint angle φ_j , stiffness k_{SEA} and damping d_{SEA} :

$$\theta_{sw}\ddot{\varphi}_j = k_{SEA}(\varphi_m - \varphi_j) + d_{SEA}(\dot{\varphi}_m - \dot{\varphi}_j). \quad (4.9)$$

This simplified swing leg dynamics induces typically poles of the entire system in the order of 10 Hz. In comparison thereto, the motor velocity control loop is much faster and achieves a bandwidth in the order of 100 Hz (Hutter et al., 2011c). Therefore, the spring-mass dynamics dominates the closed loop behavior and the internal motor dynamics (Figure 4.2 (A)-(D)) can be neglected for further position control design ($\dot{\varphi}_m = \dot{\varphi}_{m,\text{des}}$).

4.3.2 LQR Control

For fast and highly damped joint position control we implement an LQR (linear quadratic regulator) control structure based on joint and motor encoder measurements:

$$\dot{\varphi}_m = k_1^\varphi(\varphi_{m,\text{des}} - \varphi_m) - k_2^\varphi(\varphi_{j,\text{des}} - \varphi_j) + k_3^\varphi(\dot{\varphi}_{j,\text{des}} - \dot{\varphi}_j). \quad (4.10)$$

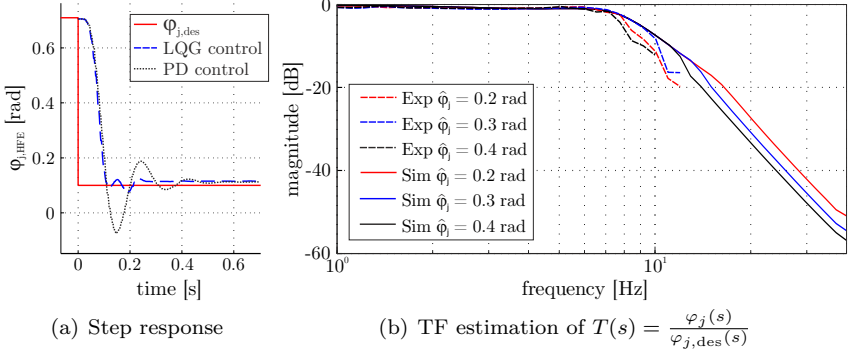


Figure 4.7: The proposed LQR joint position controller (blue dashed) performs significantly better than the initial cascaded PD setup (black dotted)(a). A bandwidth of about 9 Hz in combination with high damping ($T_{max} < 1dB$) was achieved in simulations and experiments (b).

As we have accurate position and speed measurements of the joint and motor, there is direct access to the full state of the simplified plant and hence no need for an observer. Combining (4.9) and (4.10), whereby $\varphi_{m,des} = \varphi_{j,des} + \text{const}$ and $\dot{\varphi}_{j,des} = 0$, the closed loop joint position transfer function is given by:

$$\frac{\varphi_j(s)}{\varphi_{j,des}(s)} = \frac{(k_1^\varphi - k_2^\varphi + k_3^\varphi s)(k_{SEA} + sd_{SEA})}{\theta_{sw}s^2(s + k_1^\varphi) + (s + k_1^\varphi - k_2^\varphi + k_3^\varphi s)(k_{SEA} + sd_{SEA})}. \quad (4.11)$$

To determine for example the control gains for HFE², we choose the state weighting matrix $Q_{LQR} = \tilde{C}^T \tilde{C}$ with $\tilde{C} = \text{diag}([1, 10, 0.1])$ and the control effort weighting parameter $r_{LQR} = 0.1$. In fact, proper adjustment of the control gains $k_1^\varphi > k_2^\varphi > 0$ and $k_3^\varphi > 0$ shifts the poles of (4.11) from the natural spring-mass oscillations (circle in the pole-zero map of Figure 4.6) to higher damped regions while keeping the response time of the system constant. This helps fine-tuning the control gains in hardware experiments.

The proposed control strategy was tested in simulation and hardware experiments and a significant improvement in comparison to a standard cascaded PD setup is achieved (Figure 4.7(a)). The closed loop transfer function was estimated with a logarithmic chirp (Figure 4.7(b)) applied in hardware experiments (dashed) and the detailed simulation (solid). The LQR controller achieves a bandwidth of about 9 Hz while ensuring high damping respectively almost no oscillations ($T_{max} < 1dB$).

² $\theta_{sw} = 0.03 \text{ kg/m}^2$, $k_{SEA} = k_{HFE} = 70 \text{ Nm/rad}$, and $d_{SEA} = d_{HFE} = 0.2 \text{ Nms/rad}$

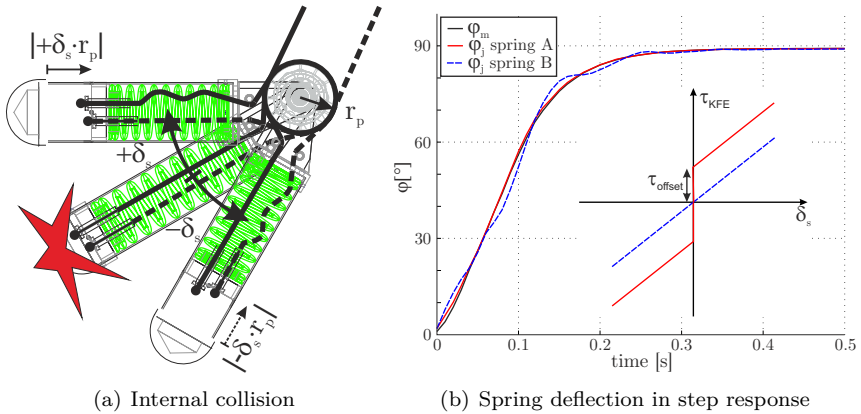


Figure 4.8: Internal collisions occur due to the uni-directional cable pulley setup in a bi-directional knee joint since the velocity has to be inverted when crossing the neutral position (a). The more the spring is pre-compressed (red solid), the smaller the undesired deflections during swing leg motion (b).

4.4 Hardware Optimization

Analyzing and evaluating the simplified swing leg model (4.9) for the knee results in a high eigenfrequency as a result of the low shank inertia. Hence, active damping of the knee oscillations during flight phase is barely achievable by motor control alone, in particular since the shank has substantial kinetic energy at the point of lift-off. Consequently, other means for damping during flight phase need to be employed. To keep the design lightweight, no additional couplings, brakes, or other adjustable dampers (Boyle et al., 2000) can be used. Instead, we take advantage of the fact that the knee is always loaded in the same direction during stance phase and crossings of the neutral position ($\tau_{KFE} = 0$) occur only during swing phase.

4.4.1 Exploiting Internal Collisions

In a first concept (Figure 4.8(a)), we use a single compression spring placed within the shank. The lower ending of the spring is tied to two cables (solid and dashed) which are connected to the knee motor placed at the hip joint. This setup provides additional damping of the unloaded leg by exploiting the *pre-loaded spring characteristic* and *internal dynamic effects* of the uni-directionally loaded spring.

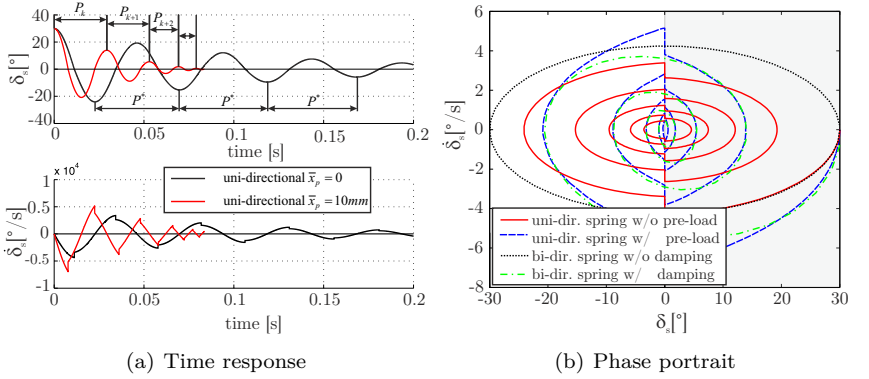


Figure 4.9: Spring pre-compression and internal collisions when crossing the neutral position cause phase shortening (a) and higher damping (b).

Pre-loaded Spring Characteristic

Pre-compressing the uni-directional spring by a distance \bar{x}_p leads to a non-linear characteristic with an offset at the neutral position of $\tau_{\text{offset}} = k_{SEA} \frac{\bar{x}_p}{r_p}$ (Figure 4.8(b), spring characteristic), such that external loads smaller than τ_{offset} do not lead to a spring deflection. Hence, the disturbance due to shank acceleration during swing phase motion implies only negligible oscillations as shown in the experimental step response in Figure 4.8(b). The nonlinear offset further increases the local stiffness for small deflections and hence additionally shortens the oscillation period P as illustrated in Figure 4.9(a) and discussed in detail in Appendix A.8.3.

Impact Speed Loss

Whenever the knee is crossing the neutral position (Figure 4.8(a)), the direction of motion of the spring must change. This instantaneous speed reversion has to result from a mechanical collision within the spring. Thereby, energy is lost and the deflection speed $\dot{\delta}_s$ ($-$ = before collision, $+$ = after collision) is slowed down (Figure 4.9(b)). By applying impulse equations along the spring and in rotational direction (eq. (A.50)), the relative change in velocity can be expressed as a function of the shank inertia around the knee joint $\theta_{S,KFE} = \theta_S + m_S s_S^2$, the spring mass m_F , and the pulley radius r_P :

$$\frac{\dot{\delta}_s^+}{\dot{\delta}_s^-} = \frac{\theta_{S,KFE} - m_F r_P^2}{\theta_{S,KFE} + m_F r_P^2} = \epsilon < 1. \quad (4.12)$$

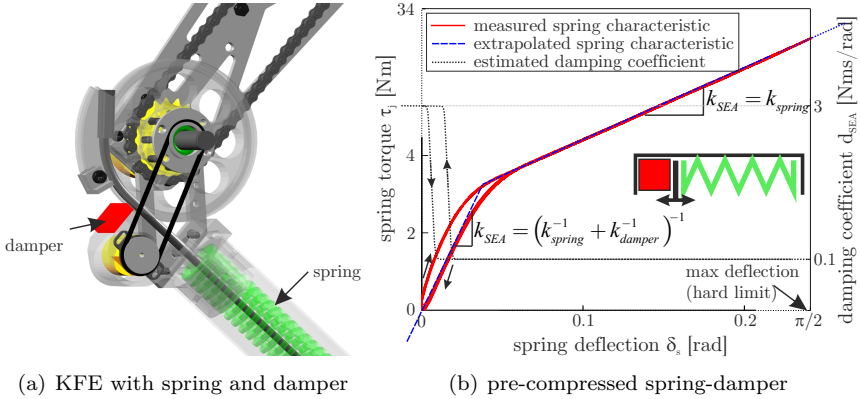


Figure 4.10: The combination of a series elasticity and a damper (a) results in a non-linear spring-damper characteristic (b). This shows minimal damping and a linear, hysteresis-free torque-deflection ratio during stance (high deflection region) and high damping with hysteresis during flight phase (low deflection region).

These impulsive energy losses at zero crossings reduce the oscillation amplitude $\hat{\delta}_k$. As outlined in eq. (A.55), the equivalent damping ratio $\frac{\hat{\delta}_{k+1}}{\hat{\delta}_k}$ can be expressed as a function of the spring pre-compression \bar{x}_p and pulley radius by:

$$\frac{\frac{1}{2}r_p\hat{\delta}_{k+1}^2 + \bar{x}_p\hat{\delta}_{k+1}}{\frac{1}{2}r_p\hat{\delta}_k^2 + \bar{x}_p\hat{\delta}_k} = \epsilon^4. \quad (4.13)$$

By varying \bar{x}_p , the damping ratio $\frac{\hat{\delta}_{k+1}}{\hat{\delta}_k}$ can be increased from ϵ^2 for $\bar{x}_p = 0$ to ϵ^4 for $\bar{x}_p \gg \frac{1}{2}r_p\hat{\delta}_k$.

4.4.2 Combined SEA and SDA Setup

The second concept to prevent oscillations during flight while keeping damping low during stance is based on a combination of series elastic (SEA) with series damping actuation (SDA) (Figure 4.10(a)). In this design, a steel spring is pre-compressed against a damper unit, which creates an overall nonlinear spring-damping characteristic as depicted in Figure 4.10(b). If the leg is in ground contact, the actuator is operating in the linear, low damped region of the spring (SEA), allowing for efficient energy storage and precise torque control based on deflection measurement. During flight phase, the knee crosses

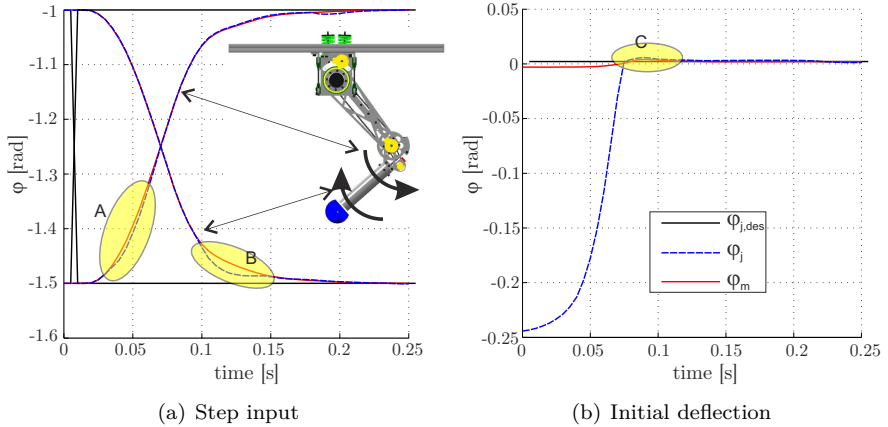


Figure 4.11: High damping in the unloaded knee joint (swing phase) enables precise position control with minimal deflection for demand step inputs (a) and nearly no overshoot for initial joint deflections (b).

the neutral position $\tau_{KFE} = 0$ and hence experiences high-damping and high stiffness (SDA). Similar to the previous method, the high stiffness/high damping range can be scaled by changing the amount of pre-compression. Disturbances smaller than the pre-compression create practically no deflection. For motor position step inputs in both directions, there occur only minimal tracking errors in the region of maximal positive acceleration (Figure 4.11(a),(A,B)). Furthermore, initial joint deflections (Figure 4.11(b)) are immediately damped out with no overshoot (C).

4.4.3 Comparison

Both solutions ensure a highly improved damping behavior for the swing phase without impairing torque controllability and energy storage during stance phase. As a common drawback, the non-linearity or hysteresis effects around the neutral position degrade the torque controllability in the non-contact phase. This is not an issue so far as the swing leg requires anyway position control. The benefit of the spring-damper solution is the immediate overcritical damping when the joint crosses the neutral position and the low mechanical complexity for the cabling. Correspondingly, this method was finally realized in Star $LETH$.

4.5 Summary

The applied control structure for the highly compliant SEAs is cascaded with an inner motor current and velocity control loop. To regulate the joint torque, we integrate a PI feedback loop and feedforward disturbance compensator. This allows to simultaneously achieve good closed loop performance (28 Hz small amplitude BW) and low impedance. The controller is designed to ensure coupled stability with any type of environment as the system is stable and passive. For fast and precise swing leg joint position control, we propose a LQR control structure that can actively damp undesired joint oscillations. In the knee joint, we additionally improve position controllability by mechanical means. To this end, two approaches based on internal collisions and a combined SEA/SDA joint are compared from a theoretical aspect and in hardware experiments with a single leg setup.

Chapter 5

Model-Based Locomotion Control

Legged locomotion is a challenging control problem as it involves balancing an underactuated robot with many degrees of freedom in continuously alternating contact situation with the environment. To tackle this problem we use model-based control strategies based on kinematic and dynamic information that generate the desired actuator torque commands.

A widely used concept to shape the behavior of legged systems is virtual model control introduced by Pratt et al. (2001). In this static method, the joint torques are adjusted to create the same reaction as if external forces would be applied. Following basic mechanical principles, this control method can be generalized such that the robot can emulate the effect of an arbitrary set of virtual forces and moments.

In most cases, there exists not only a kinematic description of the robot but a model of the MBS dynamics such that it is theoretically possible to impose a largely arbitrary behavior using the concept of floating base inverse dynamics. In most applications, the desired behavior evolves by simultaneously executing a set of motion tasks of different priority such as shifting the COG, moving a foot point, or keeping certain posture. At the same time, the robot should optimally distribute the contact forces, e.g. to guarantee safety against slippage or to minimize the actuator effort. To realize this, we have developed a control framework based on least square optimization for *hierarchical task-space inverse dynamics control* which ensures that critical tasks are fulfilled by all means while less important ones are only fulfilled as good as possible. We present two compulsory methods: The outlined *sequential* approach controls motion and force/torque tasks with different priorities

purely based on inversion of kinematic system properties. It represents a missing cornerstone linking kinematic projections (e.g. Mistry et al., 2010) with a hierarchical task description (e.g. Sentis and Khatib, 2005) for floating base systems. To additionally handle *truly-underactuated* systems where some degrees remain uncontrollable, this method is further extended to a *combined* formulation that enforces consistency with the EOM. A theoretical analysis indicates that a lot of existing solutions are in fact only a special case of the presented approach.

To achieve good control performance with naturally compliant legged systems, it is often insufficient to consider the robot as a perfectly torque controllable device. This is particularly true for fast and precise maneuvers where the elasticity in the joints substantially influences the control characteristics. In this context, we propose to apply a hybrid setup whereby part of the robot remains locally position controlled to improve performance, while at the same time, the remainder of the robot compensates for coupling effects in an inverse dynamics framework. This is a final module on the way to transfer the presented inverse dynamics methods from idealized simulations to real hardware experiments.

5.1 Generalized Virtual Model Control

Virtual model control (VMC) as introduced by Pratt et al. (2001) is a static method which generates desired joint torques to produce the same effect on the system as if there were external (virtual) forces \mathbf{F}_{v_i} acting at specified locations \mathbf{r}_{v_i} . To derive a generalized form of VMC for floating base systems, we apply the *principle of virtual work* which states that variations in work must cancel for all virtual displacements of the MBS. A virtual displacement at an arbitrary point p_i can be written as

$$\delta \mathbf{r}_{p_i} = \delta \mathbf{r}_b + \delta \boldsymbol{\varphi}_b \times \mathbf{r}_{bp_i} + \delta \mathbf{r}_{bp_i} = [\mathbf{I} \quad -\tilde{\mathbf{r}}_{bp_i} \quad \mathbf{J}_{bp_i}] \begin{pmatrix} \delta \mathbf{r}_b \\ \delta \boldsymbol{\varphi}_b \\ \delta \mathbf{q}_r \end{pmatrix}, \quad (5.1)$$

with $\delta \mathbf{r}_b$ and $\delta \boldsymbol{\varphi}_b$ being the variation in position and rotation of the base node b with respect to an inertial frame. The skew-symmetric matrix $\tilde{\mathbf{r}}_{bp_i} = -\tilde{\mathbf{r}}_{bp_i}^T$ corresponds to the cross-multiplication matrix $\tilde{\mathbf{r}}_{bp_i} \boldsymbol{\varphi}_b = \mathbf{r}_{bp_i} \times \boldsymbol{\varphi}_b$ of the relative position vector \mathbf{r}_{bp_i} from base b to point p_i . The relative position variation $\delta \mathbf{r}_{bp_i} = \mathbf{J}_{bp_i} \delta \mathbf{q}_r$ is expressed by a variation in generalized joint coordinates $\delta \mathbf{q}_r$ projected by the relative Jacobian $\mathbf{J}_{bp_i} = \frac{\partial \mathbf{r}_{bp_i}}{\partial \mathbf{q}_r}$. With this parametrization of an arbitrary field of variations the virtual work generated

by external and internal forces results in

$$\begin{aligned} \delta W &= \delta \mathbf{q}_r^T \boldsymbol{\tau} + \sum_i \delta \mathbf{r}_{p_i}^T \mathbf{F}_{p_i} \\ &= [\delta \mathbf{r}_b^T \quad \delta \varphi_b^T \quad \delta \mathbf{q}_r^T] \left(\begin{pmatrix} 0 \\ 0 \\ \boldsymbol{\tau} \end{pmatrix} + \sum_i \begin{bmatrix} \mathbf{I} \\ \tilde{\mathbf{r}}_{bp_i} \\ \mathbf{J}_{bp_i}^T \end{bmatrix} \mathbf{F}_{p_i} \right) = \mathbf{0} \quad \forall \begin{pmatrix} \delta \mathbf{r}_b \\ \delta \varphi_b \\ \delta \mathbf{q}_r \end{pmatrix}, \\ \rightarrow 0 &= \sum_i \mathbf{F}_{p_i}, \end{aligned} \quad (5.2)$$

$$\rightarrow 0 = \sum_i \mathbf{r}_{bp_i} \times \mathbf{F}_{p_i}, \quad (5.3)$$

$$\rightarrow 0 = \boldsymbol{\tau} + \sum_i \mathbf{J}_{bp_i}^T \mathbf{F}_{p_i}, \quad (5.4)$$

with $\sum_i \mathbf{F}_{p_i} = \sum_i \mathbf{F}_{g_i} - \sum_i \mathbf{F}_{v_i} - \sum_i \mathbf{F}_{s_i}$ representing all external forces such as the gravitational forces (\mathbf{F}_{g_i}), virtual control forces ($-\mathbf{F}_{v_i}$), and the contact forces ($-\mathbf{F}_{s_i}$). Equations (5.2) and (5.3) correspond to the force respectively torque equilibrium of all external loads and are used to determine the unknown ground contact forces \mathbf{F}_{s_i} . In most cases, this is done by a pseudo-inversion according to

$$\begin{pmatrix} \mathbf{F}_{s_1} \\ \vdots \\ \mathbf{F}_{s_{n_s}} \end{pmatrix} = \begin{bmatrix} \mathbf{I} & \dots & \mathbf{I} \\ \tilde{\mathbf{r}}_{s_1} & \dots & \tilde{\mathbf{r}}_{s_{n_s}} \end{bmatrix}^+ \begin{bmatrix} \sum \mathbf{F}_{g_i} - \sum \mathbf{F}_{v_i} \\ \sum \mathbf{r}_{g_i} \times \mathbf{F}_{g_i} - \sum \mathbf{r}_{v_i} \times \mathbf{F}_{v_i} \end{bmatrix}. \quad (5.5)$$

However, in a contact situation with more independent contact forces than equilibrium constraints, additional conditions can be defined (Pratt, 1995) or numerical optimization routines can be executed (e.g. to minimize slippage, Bloesch et al., 2011). Given all external forces, the desired joint torques are extracted from (5.4):

$$\boldsymbol{\tau} = - \sum_i \mathbf{J}_{bg_i}^T \mathbf{F}_{g_i} + \sum_i \mathbf{J}_{bv_i}^T \mathbf{F}_{v_i} + \sum_i \mathbf{J}_{bs_i}^T \mathbf{F}_{s_i}. \quad (5.6)$$

For simplicity of notation, we avoided the inclusion of external moments $\boldsymbol{\tau}_i^a$. They can be simply added in the formalism with the corresponding rotational Jacobian as $\sum_i \mathbf{J}_{R_i}^T \boldsymbol{\tau}_i^a$.

5.2 Inverse Dynamics of Floating Base Systems

The goal of the inverse dynamics method is to compute the necessary joint torques $\boldsymbol{\tau}$ that will realize a desired motion respectively acceleration $\ddot{\mathbf{q}} =$

$\ddot{\mathbf{q}}_{\text{des}}$ as a function of the current state $(\mathbf{q}, \dot{\mathbf{q}})$ of the robot. The problem can be solved straight forward for fixed-base manipulators as $\boldsymbol{\tau} = \mathbf{M}\ddot{\mathbf{q}} + \mathbf{h}$. However, the problem becomes ill posed at first glance for floating base systems due to the contact forces which are a direct function of the applied joint torque ($\mathbf{M}\ddot{\mathbf{q}} + \mathbf{h} + \mathbf{J}_s^T \mathbf{F}_s = \mathbf{S}^T \boldsymbol{\tau}$, (2.2)). An obvious solution is to consider them as measurable external forces as done e.g. in (Nakanishi et al., 2007). The same authors later write that this approach is undesirable since force sensors must exist at all contact points, and are typically noisy and delayed if filtered (Mistry, 2009). These deficiencies can be overcome by working with the constrained dynamics ($\mathbf{P}(\mathbf{M}\ddot{\mathbf{q}} + \mathbf{h}) = \mathbf{P}\mathbf{S}^T \boldsymbol{\tau}$, (2.11)) in a reduced dimensional space. Given desired generalized accelerations $\ddot{\mathbf{q}}$, the joint torque can be calculated through pseudo-inversion

$$\boldsymbol{\tau} = (\mathbf{P}\mathbf{S}^T)^+ \mathbf{P}(\mathbf{M}\ddot{\mathbf{q}} + \mathbf{h}) + \mathbf{N}_{PS}\boldsymbol{\tau}_0, \quad (5.7)$$

with the pseudo-inverse $(\mathbf{P}\mathbf{S}^T)^+$, the null-space projector $\mathbf{N}_{PS} = \mathcal{N}(\mathbf{P}\mathbf{S}^T)$, and the null-space torque $\boldsymbol{\tau}_0$. As it was proven by Righetti et al. (2011a), the joint torque $\boldsymbol{\tau}$ calculated by inverse dynamics (5.7) is independent of the choice of \mathbf{P} , i.e. all projectors presented in Section 2.3.1 result in the same controller. The choice of \mathbf{P} remains only important from a computational point of view. Righetti et al. (2011a) concludes that this constitutes a strong argument for the use of the simplest projection possible that uses only kinematic parameters to compute the control output.

Depending on the properties of $\mathbf{P}\mathbf{S}^T \in \mathbb{R}^{n_m \times n_r}$ respectively the support Jacobian $\mathbf{J}_s = [\mathbf{J}_{s_b} \quad \mathbf{J}_{s_r}] = \begin{bmatrix} \frac{\partial \mathbf{r}_s}{\partial \mathbf{q}_b} & \frac{\partial \mathbf{r}_s}{\partial \mathbf{q}_r} \end{bmatrix}$, we have to make two important differentiations:

Definition 1 (truly-underactuated). *A system is called truly-underactuated if there are not enough ground contact constraints to independently control the n_b unactuated base coordinates \mathbf{q}_b . $n_u = n_m - \text{rank}(\mathbf{P}\mathbf{S}^T) = n_b - \text{rank}(\mathbf{J}_{s_b})$ coordinates remain uncontrollable.*

This entails that the pseudo inversion may not fulfill the desired dynamics but only minimizes $\|\mathbf{P}(\mathbf{M}\ddot{\mathbf{q}} + \mathbf{h}) - \mathbf{P}\mathbf{S}^T \boldsymbol{\tau}\|_2$. In this case, special attention has to be paid when choosing the desired accelerations $\ddot{\mathbf{q}}$ such that they are achievable.

Definition 2 (overconstrained). *A system is called overconstrained if there exist $n_c = n_r - \text{rank}(\mathbf{P}\mathbf{S}^T) = \text{rank}(\mathbf{J}_s) - \text{rank}(\mathbf{J}_{s_b})$ internal force directions respectively a null-space matrix $\mathbf{N}_{PS} = \mathcal{N}(\mathbf{P}\mathbf{S}^T) \in \mathbb{R}^{n_r \times n_c}$.*

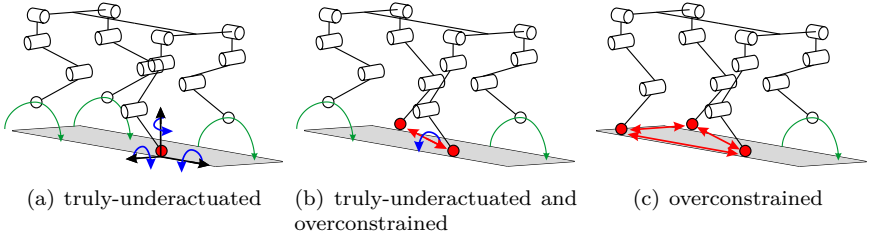


Figure 5.1: A quadruped robot with point feet is *truly-underactuated* ((a); $n_c = 0$, $n_u = 3$) in single leg support, *truly-underactuated* and *overconstrained* ((b); $n_c = 1$, $n_u = 1$) in double support, and *overconstrained* ((c); $n_c = 3$, $n_u = 0$) during static walking with three simultaneous points of contact.

This means that the torque vector $\boldsymbol{\tau}$ can be changed by an arbitrary internal torque vector $\boldsymbol{\tau}_0$ without impairing the desired motion $\dot{\mathbf{q}}$. Instead, these internal torques $\boldsymbol{\tau}_0$ can be used to optimize the load distribution.

A quadrupedal robot is the ideal platform to highlight these different contact properties. In contrast to most bipedal systems that have extended foot elements which constrain position and orientation of the foot segment, we employ on StarLETH only point feet. Each contact point implies three independent contact constraints that allow controlling some of the six unactuated base coordinates.

The most simple case with a single leg in contact that constrains only three degrees of freedom corresponds to a *truly-underactuated* system with $n_u = 3$ uncontrollable directions (Figure 5.1(a)). As the robot cannot apply torque around the point contact, the three blue rotational directions remain uncontrolled.

An *overconstrained* situation can be realized with three (or more) contact points that are not aligned in a singular configuration (e.g. on a single line). As depicted in Figure 5.1(c), the $n_c = 3$ internal directions result from 9 independent contact constraints with only 6 unactuated base coordinates. Thereby, the robot can produce internal forces between the contact points (red arrows) without changing the actual motion.

A quadrupedal robot can also be *truly-underactuated* and *overconstrained* at the same time (Figure 5.1(b)): Two simultaneous contact points allow to generate a single internal force between them (red arrow). At the same time, the system is not able to apply a momentum around the line of support (blue arrow).

5.3 Hierarchical Least Square Optimization

To prepare for prioritized task-space inverse dynamics, we introduce in this section the concept of hierarchical least square optimization of a set of n_T linear equations

$$\mathbf{A}_i \mathbf{x} = \mathbf{b}_i, \quad (5.8)$$

with the optimization variable \mathbf{x} . Problems of the same priority $i \geq 1$, with $i = 1$ being the highest priority, are stacked in matrix \mathbf{A}_i and vector \mathbf{b}_i . As it will be shown later, motion tasks as well as joint torque and contact force tasks can be brought into this linear form whereby the optimization variable is the joint acceleration and joint torque, respectively. In the proposed hierarchical framework, the goal is to solve each task as good as possible in a least square sense

$$\min_{\mathbf{x}} \|\mathbf{A}_i \mathbf{x} - \mathbf{b}_i\|_2, \quad (5.9)$$

without influencing task of higher priority. There exist different methods to solve this problem such as e.g. iterative null-space projection (Section 5.3.1) or as a sequence of constrained quadratic programs (QP) (Section 5.3.2).

5.3.1 Iterative Null-Space Projection

The requirement that a task is not allowed to influence any task with higher priority can be formulated by defining \mathbf{x} as a sum of task specific \mathbf{x}_i pre-multiplied with the null-space projection matrix \mathbf{N}_i of higher prioritized tasks:

$$\mathbf{x} = \sum_{k=1}^{n_T} \mathbf{N}_k \mathbf{x}_k. \quad (5.10)$$

The null-space projector \mathbf{N}_i is defined as $\mathbf{N}_i = \mathcal{N} \left([\mathbf{A}_1^T \quad \dots \quad \mathbf{A}_{i-1}^T]^T \right)$ with $\mathbf{N}_1 = \mathbf{I}$ and the sufficient property

$$\mathbf{A}_i \mathbf{N}_j = \mathbf{0} \quad \forall i < j. \quad (5.11)$$

There exist different methods for null-space projector calculation. In this thesis, we use the singular value decomposition (SVD) outlined in Appendix A.4. Using property (5.11), the prioritized minimization problem (5.9) can be

solved for each task individually by inserting (5.10) and solving for \mathbf{x}_i :

$$\mathbf{A}_i \mathbf{x} - \mathbf{b}_i = \mathbf{A}_i \sum_{k=1}^{n_T} \mathbf{N}_k \mathbf{x}_k - \mathbf{b}_i \quad (5.12)$$

$$\mathbf{x}_i = (\mathbf{A}_i \mathbf{N}_i)^+ \left(\mathbf{b}_i - \mathbf{A}_i \sum_{k=1}^{i-1} \mathbf{N}_k \mathbf{x}_k \right). \quad (5.13)$$

The calculation sequence of the optimization procedure is implemented as:

Algorithm 1 Hierarchical Least Square Optimization

```

 $n_T$  = Number of Tasks
 $\mathbf{x} = \mathbf{0}$  % initial optimal solution
 $\mathbf{N}_1 = \mathbf{I}$  % initial null-space projector
for  $i = 1 \rightarrow n_T$  do
   $\mathbf{x}_i = (\mathbf{A}_i \mathbf{N}_i)^+ (\mathbf{b}_i - \mathbf{A}_i \mathbf{x})$ 
   $\mathbf{x} = \mathbf{x} + \mathbf{N}_i \mathbf{x}_i$ 
   $\mathbf{N}_{i+1} = \mathcal{N} \left( [\mathbf{A}_1^T \ \dots \ \mathbf{A}_i^T]^T \right)$ 
end for

```

Lemma 1 (Task invariance). *Using formulation (5.10) ensures due to property (5.11) that tasks with higher priority are not influenced by tasks with lower priority, respectively that $\mathbf{x}_{j>i}$ has no influence on task i .*

Proof.

$$\mathbf{A}_i \mathbf{x} - \mathbf{b}_i \stackrel{(5.10)}{=} \mathbf{A}_i \sum_{k=1}^{n_T} \mathbf{N}_k \mathbf{x}_k - \mathbf{b}_i \stackrel{(5.11)}{=} \mathbf{A}_i \sum_{k=1}^i \mathbf{N}_k \mathbf{x}_k - \mathbf{b}_i \quad (5.14)$$

□

Lemma 2 (Global optimality). *Formulation (5.13) is globally optimal in the sense that there exists no other solution \mathbf{x} that fulfills a task i better in the least square sense, while all higher priority tasks $j < i$ are equally good satisfied.*

Proof. See Appendix A.1. □

Lemma 3 (Exact task). *Task i is exactly fulfilled in a least square sense ($\mathbf{A}_i \mathbf{x} - \mathbf{b}_i = \mathbf{0}$) if the rows of $\mathbf{A}_i \mathbf{N}_i$ are linearly independent.*

Proof. This follows through inserting (5.13) into (5.14) and using the Moore-Penrose pseudo inverse $\mathbf{A}_i \mathbf{N}_i (\mathbf{A}_i \mathbf{N}_i)^+ = \mathbf{I}$ for row independent matrices. □

Due to its simplicity, the experiments in Chapter 8 are all based on an implementation of this method.

5.3.2 Sequence of Constrained Optimization

Every single step of the hierarchical least square optimization corresponds to a quadratic optimization with the linear constraint that tasks of higher priority are not allowed to change:

$$\begin{aligned} \min_{\mathbf{x}} \quad & \|\mathbf{A}_i \mathbf{x} - \mathbf{b}_i\|_2 \\ \text{s.t.} \quad & \underbrace{\begin{bmatrix} \mathbf{A}_1 \\ \vdots \\ \mathbf{A}_{i-1} \end{bmatrix}}_{\hat{\mathbf{A}}_{i-1}} \mathbf{x} - \underbrace{\begin{pmatrix} \mathbf{b}_1 \\ \vdots \\ \mathbf{b}_{i-1} \end{pmatrix}}_{\hat{\mathbf{b}}_{i-1}} = \mathbf{c}. \end{aligned} \quad (5.15)$$

Note: As long as $\hat{\mathbf{A}}_{i-1}$ has full column rank, the cost \mathbf{c} is $\mathbf{0}$.

This sequence of constrained quadratic optimization can be solved using a standard QP solver (Björck, 1996).

5.3.3 Inequality Constraints

To describe the behavior of complex legged robots, it is often required to integrate inequality constraints

$$\mathbf{A}_i \mathbf{x} \leq \mathbf{b}_i, \quad (5.16)$$

in the proposed control framework, e.g. to handle joint angle limitation or motor torque saturation on task-space level. One possibility is to activate the corresponding inequality task as equality tasks (with high priority) as soon as the inequality constraint is violated and to shift all remaining tasks to lower priorities. This corresponds to constraining the optimization problem (see Section 5.3.2). Given the convex structure of the least square formulation as depicted in Figure 5.2(a), global optimality of the solution is still guaranteed. This would not be possible for a non-convex problem (Figure 5.2(b)). However, to handle multiple independent inequality tasks, it is required to iterate through all possible combinations of active and inactive constraints, which can become computationally intensive. While this approach works well for our applications, the interested reader is referred to (Kanoun et al., 2011) for a more elaborated method based on a sequence of QPs (Section 5.3.2) using slack variables.

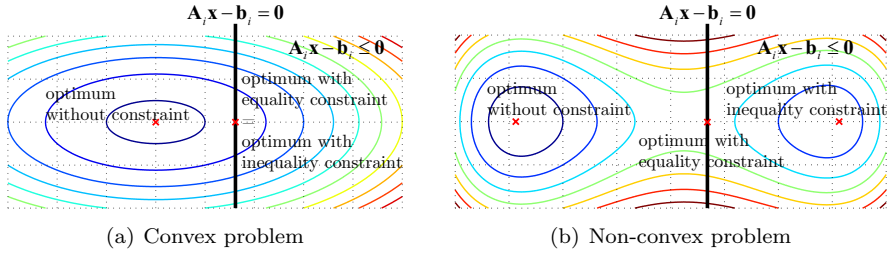


Figure 5.2: Global optimality of the solution under inequality constraints is only guaranteed if the problem is convex as in our formulation.

5.4 Sequential Hierarchical OSC

In this section, we describe an approach that allows sequentially optimizing a set of motion and force/torque tasks with different priorities. First, desired task-space dynamics of various points are combined in a hierarchical way to generate support consistent generalized accelerations. Second, contact force and joint torques are optimized using the same tool.

This two-step algorithm benefits from a very simple formulation and implementation. It is computationally fast and numerically robust since it requires only inversion of (well-conditioned) kinematic system properties that are generally accurately available and which can be analytically stated before runtime.

5.4.1 Motion Optimization

The motion of a complex robotic system evolves through a combination of individual motion tasks of different priorities ($\mathbf{A}_i^q, \mathbf{b}_i^q, \mathbf{x} = \dot{\mathbf{q}}$), each of them describing the dynamics of a particularly interesting point in task-space. The generalized accelerations $\ddot{\mathbf{q}}$ are optimized such that the motion for every task point $\ddot{\mathbf{r}}_i = \mathbf{J}_i \ddot{\mathbf{q}} + \dot{\mathbf{J}}_i \dot{\mathbf{q}}$ matches a desired task acceleration $\ddot{\mathbf{r}}_{i,\text{des}}$ as well as possible in a least square sense

$$\min_{\ddot{\mathbf{q}}} \|\ddot{\mathbf{r}}_i - \ddot{\mathbf{r}}_{i,\text{des}}\|_2, \quad (5.17)$$

$$\mathbf{A}_i^q = \mathbf{J}_i, \quad \mathbf{b}_i^q = \ddot{\mathbf{r}}_{i,\text{des}} - \dot{\mathbf{J}}_i \dot{\mathbf{q}}. \quad (5.18)$$

In most cases, $\ddot{\mathbf{r}}_{i,\text{des}} = \ddot{\mathbf{r}}_i^{FF} + \mathbf{k}_p(\mathbf{r}_{i,\text{des}} - \mathbf{r}_i) + \mathbf{k}_d(\dot{\mathbf{r}}_{i,\text{des}} - \dot{\mathbf{r}}_i)$ is described as an impedance control problem including a position \mathbf{k}_p and velocity \mathbf{k}_d

feedback gain. To account for the support constraint (2.6), it is necessary to choose the constraint satisfaction as the task with the highest priority P_1^q by defining $\mathbf{A}_1^q = \mathbf{J}_s$ and $\mathbf{b}_1^q = -\mathbf{J}_s \dot{\mathbf{q}}$. Thereby, \mathbf{J}_s represents the stacked Jacobian of all active contact points.

5.4.2 Force/Torque Optimization

Applying inverse dynamics for an *overconstrained* robot does not yield a unique solution but has an associated null-space that allows to change the load or torque distribution without influencing the resulting motion. To exploit this, we formulate a set of force/torque tasks $(\mathbf{A}_i^\tau, \mathbf{b}_i^\tau, \mathbf{x} = \boldsymbol{\tau})$ for hierarchical least square optimization. Fulfilling the system dynamics (2.11) as well as possible is formulated as

$$\min_{\boldsymbol{\tau}} \quad \left\| \mathbf{Q}_u^T \mathbf{S}^T \boldsymbol{\tau} - \mathbf{Q}_u^T (\mathbf{M}\ddot{\mathbf{q}} + \mathbf{h}) \right\|_2, \quad (5.19)$$

$$\mathbf{A}_i^\tau = \mathbf{Q}_u^T \mathbf{S}^T, \quad \mathbf{b}_i^\tau = \mathbf{Q}_u^T (\mathbf{M}\ddot{\mathbf{q}} + \mathbf{h}). \quad (5.20)$$

Note: any other projector can be used here (Section 2.3.1).

Quadratic optimization problems in joint torques, e.g. to optimize for energy efficiency, can be written as

$$\min_{\boldsymbol{\tau}} \quad \left\| \mathbf{W}_\tau \boldsymbol{\tau} - \mathbf{b}_\tau \right\|_2, \quad (5.21)$$

$$\mathbf{A}_i^\tau = \mathbf{W}_\tau, \quad \mathbf{b}_i^\tau = \mathbf{b}_\tau, \quad (5.22)$$

and finally contact force optimization objectives can be transformed using (2.16) into a least square problem that is linear in joint torques $\boldsymbol{\tau}$:

$$\min_{\boldsymbol{\tau}} \quad \left\| \mathbf{W}_F \mathbf{F}_s - \mathbf{b}_F \right\|_2, \quad (5.23)$$

$$\mathbf{A}_i^\tau = \mathbf{W}_F \mathbf{R}^{-1} \mathbf{Q}_c^T \mathbf{S}^T, \quad \mathbf{b}_i^\tau = \mathbf{b}_F + \mathbf{W}_F \mathbf{R}^{-1} \mathbf{Q}_c^T (\mathbf{M}\ddot{\mathbf{q}} + \mathbf{h}). \quad (5.24)$$

The matrices \mathbf{W}_τ and \mathbf{W}_F correspond to weighted selection matrices. This approach produces solutions that are consistent with the EOM as long as Lemma 3 is fulfilled for (5.20). By taking (5.20) with highest priority $(\mathbf{A}_1^\tau, \mathbf{b}_1^\tau)$, consistency is guaranteed if the system is not *truly-underactuated*.

5.4.3 Relation to Other Work

A recent study by Righetti et al. (2013), which is a summary of several previous work by the same group (Righetti et al., 2010, 2011b), investigates inverse dynamics based on QR decomposition in combination with contact

force as well as joint torque optimization. They propose a generalized inversion method

$$\boldsymbol{\tau} = \overline{\mathbf{Q}_u^T \mathbf{S}^T} \mathbf{Q}_u^T (\mathbf{M}\ddot{\mathbf{q}} + \mathbf{h}) + \left(\mathbf{I} - \overline{\mathbf{Q}_u^T \mathbf{S}^T} \mathbf{Q}_u^T \mathbf{S}^T \right) \mathbf{W}^{-1} \boldsymbol{\tau}_0, \quad (5.25)$$

with the weighted pseudo-inverse $\overline{\mathbf{Q}_u^T \mathbf{S}^T} = \mathbf{W}^{-1} \mathbf{S} \mathbf{Q}_u (\mathbf{Q}_u^T \mathbf{S}^T \mathbf{W}^{-1} \mathbf{S} \mathbf{Q}_u)^{-1}$, and showed that this special inversion minimizes the quadratic cost function

$$\begin{aligned} \min_{\boldsymbol{\tau}} \quad & \frac{1}{2} \boldsymbol{\tau}^T \mathbf{W} \boldsymbol{\tau} - \boldsymbol{\tau}_0^T \boldsymbol{\tau} \\ \text{s.t.} \quad & \mathbf{Q}_u^T (\mathbf{M}\ddot{\mathbf{q}} + \mathbf{h}) = \mathbf{Q}_u^T \mathbf{S}^T \boldsymbol{\tau} \end{aligned} \quad (5.26)$$

as a function of a positive-definite weighting matrix \mathbf{W} and null-space torques $\boldsymbol{\tau}_0$. Proper choice of \mathbf{W} and $\boldsymbol{\tau}_0$ allows to additionally include optimization of contact forces.

The weighted pseudo-inverse method turns out to be a special case of the hierarchical optimization presented in this thesis with the support consistent dynamics (5.20) fulfilled with highest priority and a single optimization task (\mathbf{A}_2^τ , \mathbf{b}_2^τ). As there are only two priorities, it can be written as a constrained optimization (5.15):

$$\begin{aligned} \min_{\mathbf{x}} \quad & \|\mathbf{A}_2^\tau \mathbf{x} - \mathbf{b}_2^\tau\|_2 \\ = \min_{\mathbf{x}} \quad & \mathbf{x}^T \mathbf{A}_2^{\tau T} \mathbf{A}_2^\tau \mathbf{x} - 2\mathbf{b}_2^{\tau T} \mathbf{A}_2^\tau \mathbf{x} \\ \text{s.t.} \quad & \mathbf{Q}_u^T (\mathbf{M}\ddot{\mathbf{q}} + \mathbf{h}) = \mathbf{Q}_u^T \mathbf{S}^T \boldsymbol{\tau} \end{aligned} \quad (5.27)$$

Comparing (5.27) with (5.26) yields $\mathbf{W} = \mathbf{A}_2^{\tau T} \mathbf{A}_2^\tau$ and $\boldsymbol{\tau}_0 = \mathbf{b}_2^{\tau T} \mathbf{A}_2^\tau$. In fact, the potential of the hierarchical method goes beyond the weighted pseudo-inverse without increasing computational complexity. First, there is no need for \mathbf{A}_2^τ to be positive definite and an arbitrary combination of joint torque and contact force tasks can be handled. Second, the optimization task can be further subdivided into different priorities.

5.4.4 Advantages and Drawbacks

The presented method establishes a link between existing work on hierarchical task-space control (e.g. Sentis and Khatib, 2005) and inverse dynamic methods based on kinematic projections (e.g. Mistry et al., 2010). The formulation of a set of motion (\mathbf{A}_i^q , \mathbf{b}_i^q , $\mathbf{x} = \ddot{\mathbf{q}}$) and force/torque (\mathbf{A}_i^τ , \mathbf{b}_i^τ , $\mathbf{x} = \boldsymbol{\tau}$) objectives is very simple and intuitive, and the hierarchical least square problem can be solved efficiently. Since it requires only inverting kinematic system properties that are mostly accurately available and well-conditioned, the method is computationally robust.

However, as this method does not enforce consistency with the EOM when generating the desired motion $\ddot{\mathbf{q}}$, this approach is not well suited for *truly-underactuated* systems. Lemma 3 is not fulfilled for the inverse dynamics task (5.20) and hence the optimized joint torques $\boldsymbol{\tau}$ satisfy the system dynamics not exactly but only as good as possible in the least square sense. This can be an issue if the desired motion is not well chosen. To blindly apply the proposed methodology for *truly-underactuated* systems, we extend our framework to a *combined* approach (Section 5.5) that enforces consistency with the system dynamics. This comes along with the inevitable drawback that it is not anymore purely based on kinematic properties.

5.5 Combined Hierarchical OSC

For the *combined* optimization we formulate the two steps of motion ($\mathbf{A}_i^q, \mathbf{b}_i^q, \mathbf{x} = \ddot{\mathbf{q}}$) and force/torque ($\mathbf{A}_i^r, \mathbf{b}_i^r, \mathbf{x} = \boldsymbol{\tau}$) generation defined for the *sequential* approach as one single hierarchical least square optimization problem ($\mathbf{A}_i^c, \mathbf{b}_i^c, \mathbf{x} = \boldsymbol{\nu}$) by extending the optimization variable to

$$\boldsymbol{\nu} = \begin{pmatrix} \ddot{\mathbf{q}} \\ \boldsymbol{\tau} \end{pmatrix}. \quad (5.28)$$

By this combination we can ensure consistency of the solution with the EOM and hence apply the method blindly for any type of systems. It further offers the possibility to freely mix motion with force/torque tasks in a hierarchical way.

Using the combined optimization vector, the dynamics of floating base systems (2.11) are written as a least square problem:

$$\mathbf{Q}_u^T (\mathbf{M}\ddot{\mathbf{q}} + \mathbf{h}) = \mathbf{Q}_u^T \mathbf{S}^T \boldsymbol{\tau}, \quad (5.29)$$

$$\mathbf{A}_i^c = \mathbf{Q}_u^T \begin{bmatrix} -\mathbf{M} & \mathbf{S}^T \end{bmatrix}, \quad \mathbf{b}_i^c = \mathbf{Q}_u^T \mathbf{h}. \quad (5.30)$$

Taking (5.30) at highest priority, dynamic consistency is ensured because Lemma 3 holds for $\mathbf{A}_1^c \mathbf{N}_1^c = \mathbf{Q}_u^T \begin{bmatrix} -\mathbf{M} & \mathbf{S}^T \end{bmatrix}$.

Proof. \mathbf{Q} is orthogonal and hence $\mathbf{Q}_u^T \in \mathbb{R}^{n_m \times n_q}$ has rank n_m . Given that the mass matrix \mathbf{M} is invertible, the matrix $\begin{bmatrix} -\mathbf{M} & \mathbf{S}^T \end{bmatrix} \in \mathbb{R}^{n_q \times (n_q + n_r)}$ has rank n_q . Using *Sylvester's rank inequality* it follows directly that \mathbf{A}_1^c has full rank ($\text{rank}(\mathbf{A}_1^c) = n_m$). \square

In the combined method, motion tasks (5.18) are stated as

$$\min_{\boldsymbol{\nu}} \|\ddot{\mathbf{r}}_i - \ddot{\mathbf{r}}_{i,\text{des}}\|_2, \quad (5.31)$$

$$\mathbf{A}_i^c = \begin{bmatrix} \mathbf{J}_i & \mathbf{0} \end{bmatrix}, \quad \mathbf{b}_i^c = \ddot{\mathbf{r}}_{i,\text{des}} - \dot{\mathbf{J}}_i \dot{\mathbf{q}}. \quad (5.32)$$

Similar thereto, joint torque optimization objectives can be written as

$$\min_{\boldsymbol{\nu}} \quad \|\mathbf{W}_\tau \boldsymbol{\tau} - \mathbf{b}_\tau\|_2, \quad (5.33)$$

$$\mathbf{A}_i^c = [\mathbf{0} \quad \mathbf{W}_\tau], \quad \mathbf{b}_i^c = \mathbf{b}_\tau, \quad (5.34)$$

while contact force objectives (5.24) are transformed to

$$\min_{\boldsymbol{\nu}} \quad \|\mathbf{W}_F \mathbf{F}_s - \mathbf{b}_F\|_2 \quad (5.35)$$

$$\mathbf{A}_i^c = \mathbf{W}_F \mathbf{R}^{-1} \mathbf{Q}_c^T [-\mathbf{M} \quad \mathbf{S}], \quad \mathbf{b}_i^c = \mathbf{W}_F \mathbf{R}^{-1} \mathbf{Q}_c^T (\mathbf{b} + \mathbf{g}) + \mathbf{b}_F. \quad (5.36)$$

5.5.1 Relation to Other Work

This framework is a general and compact formulation of (Sentis, 2007) and similar to work presented by de Lasa and Hertzmann (2009). As an advantage over the latter method, the use of constrained dynamics as done here allows to reduce the dimensionality of the problem without loss of generality. This is possible since contact forces, joint torques, and accelerations are rigidly coupled through the support constraint.

5.5.2 Advantages and Drawbacks

Augmenting the optimization variable to simultaneously contain joint accelerations $\ddot{\mathbf{q}}$ and joint torques $\boldsymbol{\tau}$ ensures consistency with the EOM also for *truly-underactuated* systems. It further opens the possibility of arbitrarily mixing motion tasks with force/joint torque optimization objectives.

As a drawback, stacking the optimization variable is inevitably accompanied by the inclusion of the mass matrix in the optimization matrix \mathbf{A}_i^c . The mass matrix is often prone to modeling errors and badly conditioned, e.g. because of heavy base and light-weight end-effectors (see also Featherstone, 2004). While this is not an issue for ideal simulations, it can largely dominate in hardware experiments as documented by Nakanishi et al. (2008) and lead to numerical problems or a loss of controller robustness. Additionally, stacking the optimization variables increases the dimensionality and hence requires computationally more effort than solving both problems sequentially.

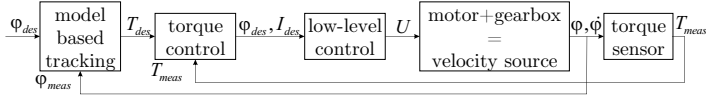


Figure 5.3: A position tracking task in an inverse dynamics framework requires joint torque controllability. This leads to a cascaded structure and can reduce the performance of fast position tracking tasks.

5.6 Hybrid OSC

This section describes a hybrid control setup to combine fast swing leg position control with the inverse dynamics framework presented beforehand.

5.6.1 Problem Description

Inverse dynamics controllers make the assumption of a perfect torque controllable robot. This is by definition true when working in a simulation environment, but does not hold for real robots. Common electrical actuators in particular require high gearbox reductions and are consequently not backdrivable. For practical purposes, they must be considered as a velocity rather than a torque source, and joint torque controllability can only be retrieved by including additional torque sensors. In Figure 5.3, we illustrate the typical signal flow when performing a simple joint position control task using an inverse dynamics framework. First, a task-space tracking controller generates desired accelerations as a function of the reference error like $\ddot{\varphi}_j = k_p(\varphi_{j,des} - \varphi_j) + k_d(\dot{\varphi}_{j,des} - \dot{\varphi}_j)$ and, using inverse dynamics, establishes desired joint torques. The subsequent torque controller translates demanded joint torque signals into motor commands such as motor current or velocity. On the lowest level finally, the motor is regulated. Since the achievable controller fidelity (in terms of bandwidth and feedback gains) is lowered within every additional loop of the cascaded structure, inverse dynamics based position regulation can greatly limit performance in practice. This is not an issue for “soft” tasks as required for interacting with the environment, but is disadvantageous when it comes to fast and precise position control as for example during swing leg motion. In such situation, the local performance can be significantly improved by applying a position controller on joint level which directly sets the desired motor commands (cf. LQR structure for SEAs presented in Section 4.3).

We accordingly propose a *hybrid control* setup: Parts of the robot that are conducting high-performance tracking tasks (in particular swing leg control)

are locally position controlled, while the remainder of the robot compliantly interacts with the environment in an inverse dynamics framework.

5.6.2 Disturbance Compensation Task

To capture the influence of the motion of the position controlled joints on the remainder of the system, it is necessary to include a task in the inverse dynamics framework which models their behavior as accurately as possible.

Acceleration Measurement

The obvious way for describing the disturbance is to measure the acceleration at the position controlled joints $\ddot{\mathbf{q}}_p$ and to include a task in the sequential or the combined approach such as

$$\begin{aligned} \mathbf{A}_i^q &= \mathbf{S}_p, & \mathbf{b}_i^q &= \ddot{\mathbf{q}}_p \\ \mathbf{A}_i^c &= [\mathbf{S}_p \quad \mathbf{0}], & \mathbf{b}_i^c &= \ddot{\mathbf{q}}_p, \end{aligned} \quad (5.37)$$

with \mathbf{S}_p being the selection matrix of the position controlled joints ($\mathbf{q}_p = \mathbf{S}_p \mathbf{q}$). Unfortunately, measuring the joint acceleration $\ddot{\mathbf{q}}_p$ by double differentiation of the joint encoder signal is inapplicable in practice due to sensor noise. However, as a valid simplification for slow maneuvers it is possible to expect the motion to be non-accelerated and hence to set $\ddot{\mathbf{q}}_p \approx \mathbf{0}$.

Torque Measurement

When it comes to highly dynamic maneuvers, disturbances due to acceleration effects become significant and a non-accelerated motion assumption is improper. Instead, we can make use of accurately available joint torque measurements at the position controlled joints $\tilde{\boldsymbol{\tau}}_p$ and include a task which keeps the torque constant for the next control step:

$$\mathbf{A}_i^c = [\mathbf{0} \quad \mathbf{S}_p \mathbf{S}^T], \quad \mathbf{b}_i^c = \tilde{\boldsymbol{\tau}}_p. \quad (5.38)$$

This method is especially valid for a compliant system with low bandwidth torque actuators. In fact, as outlined in Appendix A.6, it can be shown that including this torque task corresponds to estimating the acceleration at the position controlled joints as a function of the measured torque and desired motion of the inverse dynamics framework.

5.7 Summary

This chapter introduced two control concepts used for legged robotic systems, namely virtual model control and inverse dynamics. The former one, a static method, allows emulating virtual forces acting on the system, while the latter one can superimpose nearly arbitrary dynamics. We have combined inverse dynamics based on kinematic projections with a hierarchical task decomposition using least square optimization. This results in a very compact, simple to implement, and numerically robust framework to control complex robotic devices by describing the desired task-space dynamics at multiple locations and with different priorities. This includes for example the COG motion, end-effector positioning, whole body postures, but also contact force and joint torque optimization. The framework is finally augmented to a hybrid controller which allows locally regulating part of the robot by high-performance position controllers while the remainder of the robot is controlled by inverse dynamics. All proposed methods are applied in different hardware experiments in Chapters 7 and 8.

Chapter 6

Motion Generation

The highest level in control of legged systems is dedicated to motion generation. Gait patterns and precise foothold locations need to be chosen to propel the robot forward, to react against external disturbances, and to cope with challenging terrain. Humans and animals can do this in perfection. They can climb in very difficult environment by carefully selecting the footholds, and likewise walk or run nearly effortlessly on less challenging ground while maintaining balance even in case of large external disturbances.

Biomechanists have been focusing for a long time on understanding the underlying principles that enable this incredible locomotion performance. To this end, they try to condense the complex whole-body dynamics into simplified templates that describe the most important features of walking or running. For example, linear inverted pendulums (LIP) are used to explain human balancing or walking (e.g. Winter, 1995). A second, widely accepted template in the biomechanics and robotics community is the spring loaded inverted pendulum (SLIP) (Alexander, 1990; Blickhan, 1989), in which the rigid leg of the LIP is replaced by a massless spring that better represents the physical properties of elastic muscles and tendons. Different experiments have shown that the SLIP model describes the COG motion and ground reaction forces (GRF) of human and animal gaits with astonishing accuracy (Blickhan and Full, 1993; Full and Koditschek, 1999; Geyer et al., 2006). Despite its simplicity, it further allows explaining some self-stabilizing effects of locomotion found in nature. As our robotic leg is mechanically very similar to the SLIP model, we analyze and extend it to investigate the locomotion properties of our device.

Understanding the basic locomotion principles through these templates also significantly contributes to the mechanical design of robotic systems

and to the development of control algorithms for balancing *dynamic gaits*. For example, the LIP dynamics is widely used in bipedal walking with humanoids (Kajita et al., 2001) and to determine capture points (Pratt et al., 2006) to quantify stability properties. The SLIP template on the other side has already served as a qualitative model for the groundbreaking robots at the MIT Leg Lab in the 1980's and a lot of other systems that were built for highly dynamic locomotion. In most of these robots, be it single-legged hopping (Raibert et al., 1984) or quadrupedal trotting (Raibert et al., 1983), dynamic balancing and adjusting forward or sideward speed is solely achieved by regulating the ground contact points based on template predictions. Using similar foot placement concepts, Coros et al. (2011) recently published impressive locomotion skills with a simulated dog. Convinced by the results, we adopted the framework to Star $LETH$ to generate the motion for different types of dynamic gaits (Gehring et al., 2013).

The application of dynamic gaits works only well on level ground. As soon as it comes to conquer challenging terrain with sparsely available footholds, the robot has to switch to *static gaits*. The feet are moved one after the other in a predefined order such that the quadruped robot has at least three legs in simultaneous contact. At the same time, the main body is shifted between the successive support polygons to ensure maximum static stability in any situation. Major progress in this field was achieved within the DARPA learning locomotion challenge, where different groups (e.g. Kalakrishnan et al., 2010; Kolter et al., 2011; Neuhaus et al., 2011; Zucker et al., 2011) developed optimization and learning strategies to traverse substantial obstacles of different shape. While a full knowledge transfer is beyond the scope of this thesis, we adopt some of the underlying methods to our quadrupedal device.

6.1 SLIP Template

Biomechanical studies suggest that the dynamics of the COG in running gaits (which include bounding, trotting, or galloping), in walking gaits, and in particular in single-legged hopping can be described by the model of a spring loaded inverted pendulum (SLIP) (Alexander, 1990; Blickhan, 1989; Geyer et al., 2006). The SLIP template as depicted in Figure 6.1 is described by a point mass m_σ attached to a massless prismatic spring with resting length $l_{\sigma,0}$ and leg stiffness k_σ . During flight phase, the model is only subject to the law of gravitation and follows a parabolic trajectory. The leg length and angle of attack are brought to the desired landing configuration $l_{\sigma,0}$ and $\alpha_{\sigma,0}$ respectively. When the leg strikes the ground, the motion of the COG is redirected by the exerted spring force in the leg $F_\sigma = k_\sigma (l_{\sigma,0} - l_\sigma)$ that

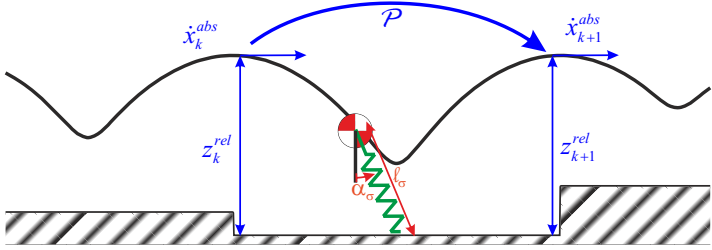


Figure 6.1: SLIP running is analyzed on a step-to-step basis between successive apex¹ transits by a Poincaré map \mathcal{P} .

acts between a fixed ground contact point and the COG:

$$m_\sigma \ddot{\mathbf{r}}_\sigma = \mathbf{F}_\sigma + m_\sigma \mathbf{g}, \quad (6.1)$$

where $\mathbf{r}_\sigma = (x, z)^T$ is the position of the point-mass and $\mathbf{g} = (0, -g)^T$ is the gravitational acceleration vector. Unfortunately, there exist no analytical solution for this differential equation but only approximations (Geyer et al., 2005; Schwind and Koditschek, 2000).

6.1.1 Self-Stability and Dead-Beat Control

There is evidence that dynamic locomotion found in humans and animals is profiting from passive stabilization effects such that external disturbances can be compensated without large feedback control effort. Different studies have shown that these self-stability properties can be reproduced with the SLIP template (Geyer et al., 2002, 2006; Ghigliazza et al., 2005; Schmitt and Holmes, 2000; Seipel and Holmes, 2005; Seyfarth et al., 2001, 2002). To this end, the SLIP dynamics are analyzed on a step-to-step basis, where one step is defined as the period between two successive apex¹ transits. The mapping of the state variables $\mathbf{x}_k = (z, \dot{x})_k^T$ at apex over one full period (Figure 6.1) can be described in a Poincaré map as

$$\mathbf{x}_{k+1} = \mathcal{P}(\mathbf{x}_k, \alpha_{\sigma,0}, l_{\sigma,0}, k_\sigma, m_\sigma). \quad (6.2)$$

A motion is called periodically stable, if it is periodic $\mathbf{x}_k = \mathbf{x}_{k+1} = \mathbf{x}^*$ and if deviations from this periodic solution decrease from one step to the next. Stability is assessed via linearization of the Poincaré map \mathcal{P} as state errors

¹apex = highest point in flight curve with $\dot{z} = 0$

propagate in one step over the monodromy matrix $\mathbf{M}_{\mathcal{P}}$:

$$\Delta \mathbf{x}_{k+1} = \left. \frac{\partial \mathcal{P}}{\partial \mathbf{x}} \right|_{\mathbf{x}^*} \Delta \mathbf{x}_k + \mathcal{O}(\Delta \mathbf{x}_k^2) = \mathbf{M}_{\mathcal{P}} \mathbf{x}_k + \mathcal{O}(\Delta \mathbf{x}_k^2). \quad (6.3)$$

The eigenvalues of $\mathbf{M}_{\mathcal{P}}$ determine the stability: As the SLIP model is energetically conservative, the first eigenvalue λ_1 is equal to one since apex height z_k and forward speed \dot{x}_k are coupled by the given energy level. If the second eigenvalue $|\lambda_2| < 1$, an (energy conserving) error will vanish, and the periodic solution is called asymptotically stable. Figure 6.2(a) depicts the surface of passively stable fixed points as a function of the parameters stiffness k_σ , angle of attack α_σ , and apex height z_k . If a system is operated at one of these fixed points, disturbances, e.g. variations in ground elevation are passively rejected (Figure 6.2(b)).

Instead of relying purely on passive stability, the ground elevation disturbance rejection can be maximized by including a dead beat controller that ensures apex height conservation ($z_k = z_{k+1}$) in every single stride. Since the system is energy conservative, this automatically implies that the locomotion speed remains constant ($\dot{x}_k = \dot{x}_{k+1}$) as well. A dead beat controller searches for fixed points on the surface depicted in Figure 6.2(a) as a function the measured relative apex height z_k and spring stiffness k_σ . As there is no closed form solution for the SLIP dynamics, they are generated by forward simulation. Unfortunately, working with relative apex height on a step-to-step basis (e.g. Ernst et al., 2009) comes along with a loss of fixed point stability (Figure 6.2(c)) and already numerical errors will lead to a drift away from the nominal fixed point in long term simulations. In case of an imperfect model in the deadbeat controller, this method completely fails.

To overcome this deficiency, we present in (Hutter et al., 2010a) an extended method that is robust against numerical errors, imperfect sensor signals, and modeling errors. To this end, the relative height $z_k = \frac{1}{2}g \cdot t_{\text{fall}}^2$ is measured by the time of flight t_{fall} after apex and augmented with a boundary value problem (BVP) for the stance phase. Given the additional knowledge about the impact angle, lift-off angle, and downward velocity $\dot{z}_{TD} = -g \cdot t_{\text{fall}}$ we solve a stance phase BVP using a standard single shooting method. This allows to estimate in real time the absolute velocity \dot{x}_k and the model parameter $\frac{k_\sigma}{m_\sigma}$. As a result, drift problems are fully avoided and modeling errors can be robustly handled.

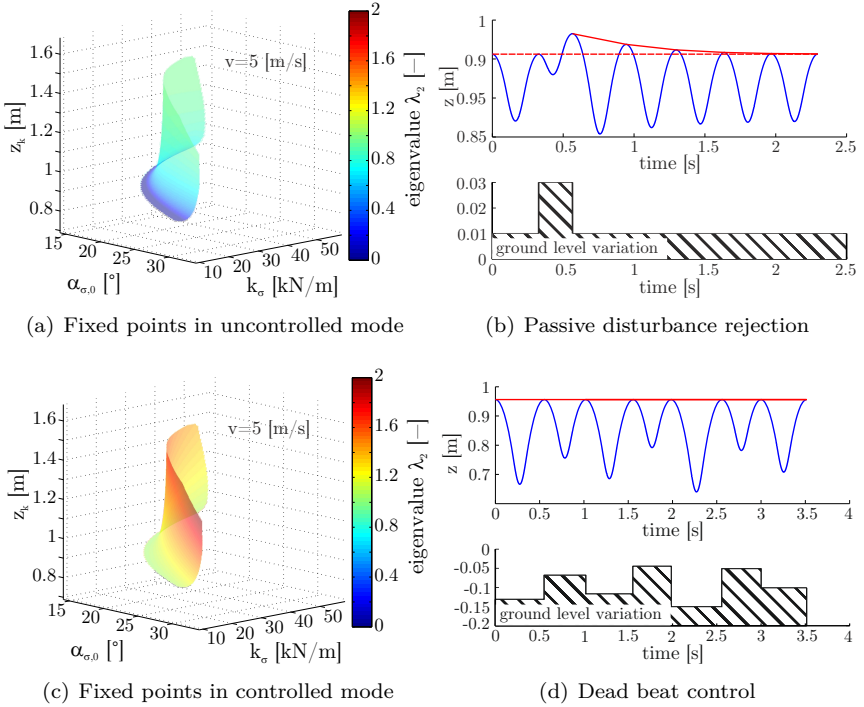


Figure 6.2: The fixed point stability analysis of uncontrolled (a) and controlled (c) running shows different eigenvalues. If the angle of attack is kept constant (b), disturbances are passively rejected. By integrating a deadbeat controller based on relative height measurements, large disturbances are rejected (d) but self-stability is lost.

6.1.2 Template of an Articulated Leg

The fundamental difference between the SLIP template and a real robotic device is the massless leg assumption. Since the main body is never completely decoupled from the foot point, impulses are transferred and lead to an instantaneous change in the COG velocity and in a drop of kinetic energy even in case of an extremely lightweight construction. This raises the research question, how it effects the passive stability and hence disturbance rejection properties during locomotion. For investigation, we propose a SLIP model with impact compensation (SLIPic). At the point of landing, the pre-impact COG velocity $\dot{\mathbf{r}}_{COG}^- = \mathbf{J}_{COG} \dot{\mathbf{q}}^-$ is instantaneously changed to $\dot{\mathbf{r}}_{COG}^+ = \mathbf{J}_{COG} \dot{\mathbf{q}}^+$ using the impact equation (2.30). To keep the template dynamics energy conservative, the associated energy loss ΔE_{kin} is compensated by a virtual spring elongation to $l_{\sigma,0}^+ = l_{\sigma,0}^- + \Delta l_{\sigma}$:

$$\begin{aligned} E_{spring} &= \Delta E_{kin} \\ \frac{1}{2} k_{\sigma} \Delta l_{\sigma}^2 &= \frac{1}{2} m_{\sigma} \left(\dot{\mathbf{r}}_{COG}^-{}^2 - \dot{\mathbf{r}}_{COG}^+{}^2 \right) \\ \rightarrow \Delta l_{\sigma} &= \sqrt{\frac{m_{\sigma}}{k_{\sigma}} \left(\dot{\mathbf{r}}_{COG}^-{}^2 - \dot{\mathbf{r}}_{COG}^+{}^2 \right)} \end{aligned} \quad (6.4)$$

In other words, instead of tracking the dynamics of a single SLIP model, we first track the dynamics of a model with leg length $l_{\sigma,0}^-$ (which defines the kinematic positions at touchdown) and then switch to a model with leg length $l_{\sigma,0}^- + \Delta l_{\sigma}$ (which defines the ground contact forces during stance and the leg length at lift-off).

Improved Self-Stability

Using the model parameters of our real robotic leg (Section 3.2), we can perform the same stability analysis of single-legged locomotion. As depicted in Figure 6.3(a), the inclusion of impact at landing substantially increases the basin of attraction respectively the range of parameters that yields stable fixed points. These results are similar to those documented by Rummel and Seyfarth (2008), but must have a different origin. In their work they base the analysis on massless segments, which limits the explanation to the non-linear relation between the force acting on the point mass and the torque in the knee. For our study we have a SLIP equal stance phase with a linear spring. The stabilization effects must hence originate entirely from the collision. A somehow intuitive explanation is that an increase in forward velocity automatically results in a higher impact and consequently in larger COG

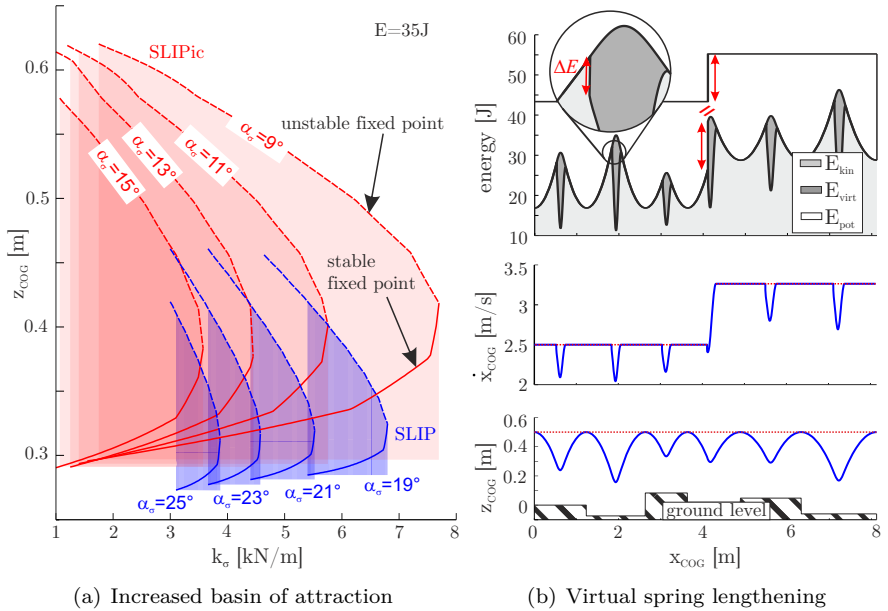


Figure 6.3: The stability of the SLIP template is increased when including the impact occurring in an articulated robotic leg (a). Virtual spring lengthening can be used to compensate for the impact losses and to change energy level (b).

speed loss in the opposite direction. This holds equivalently for the normal direction.

Augmented Dead-Beat Control

Virtual spring elongation is so far only used to compensate for impact energy loss. By considering Δl_σ as an additional control parameter, we have, in contrast to the energy conservative SLIP model, means of changing the energy level and hence to independently modulate forward speed or hopping height while keeping the continuous dynamics of the SLIP model. As an example (Figure 6.3(b)), this can be used to change the forward velocity while keeping the height constant over rough terrain. Such virtual leg lengthening is later used for single leg hopping experiments (Section 7.2).

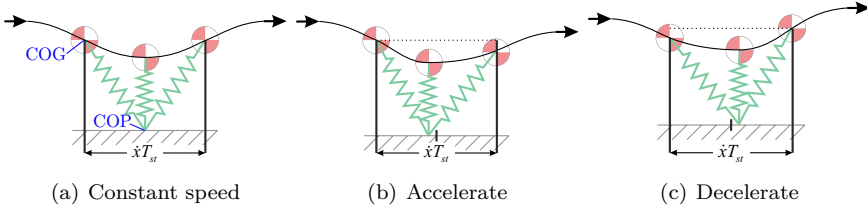


Figure 6.4: This picture illustrates a running motion from left to right with landing, maximal compression, and lift-off configuration. A symmetrical motion with zero net acceleration is achieved if the foot is placed in the middle of the COG-print (a). Shifting the foot position to the back accelerates the system (b) while shifting it to the front decelerates it (c).

6.2 Dynamic Gaits

Templates cannot only be used to deepen the understanding of locomotion principles but help additionally to design control strategies to stabilize and maintain *dynamic locomotion gaits*. Such gaits are characterized by inherent instability as the robot automatically falls if the legs are not appropriately positioned. For illustration, we consider a SLIP model which represents the leg of a monopod runner or the virtual leg of a biped or quadruped robot. In the first phase before maximal compression, the center of pressure (COP) is in front of the COG and decelerates the motion. In the second phase after maximal compression, the COP is behind the COG and hence accelerates it. To maintain a constant forward velocity we need to ensure that the nominal foot position will generate zero net acceleration on the main body (Figure 6.4(a)). Following the notation of Raibert (1986), zero net acceleration of the symmetric SLIP template is achieved if the contact point is placed in the middle of the COG-print, i.e., in the middle of the projected travel distance of the COG during stance phase. Despite the fluctuation in speed during stance phase, the length of the COG-print can be estimated to $\dot{x}T_{st}$ as a function of the average locomotion speed \dot{x} and the stance duration T_{st} .

To change forward velocity or to react upon errors, the foot location is offset from the nominal center of the COG-print. Placing the contact location behind the center of the COG-print shortens the deceleration phase and thus leads to a net acceleration of the system (Figure 6.4(b)). If the contact point is in front of the center of the COG-print, the acceleration phase gets shorter and the system is slowed down (Figure 6.4(c)). Combining this with the nominal foothold location in a controller yields the desired contact position

in forward direction as

$$x_F = \frac{1}{2}\dot{x}T_{st} + k_R^{FB}(\dot{x}_{\text{des}} - \dot{x}), \quad (6.5)$$

where $k_R^{FB} < 0$ corresponds to the feedback gain and \dot{x}_{des} to the desired forward speed.

6.2.1 Single Leg Locomotion

To transfer this controller to single-legged hopping with the articulated leg, we slightly reformulate it. First, knowing that the angle of attack α is rather small for the achieved forward locomotion speed \dot{x} , we linearize $\sin\left(\frac{x_F}{l_\sigma}\right) \approx \frac{x_F}{l_\sigma}$. Second, as the stance time is only minimally changing as a function of the speed, we keep it constant and replace it by a feedforward gain k_R^{FF} . Third, as we are operating in a planar test bench with limited horizontal travel distance, the controller is augmented with a saturating proportional controller k_R^{pos} for the desired travel position. Finally, due to the articulated design, the system encounters a horizontal impulse at landing which leads to an instantaneous change in forward velocity \dot{x} . To compensate for this asymmetry beforehand, we introduce an experimentally tuned offset angle α_0 such that the system performs a vertical jump at the nominal state ($x = 0, \dot{x} = 0$). This yields an augmented angle of attack controller as

$$\alpha(x, \dot{x}) = k_p^{FF}\dot{x} + k_R^{FB}(k_R^{pos} \text{sat}(x_{\text{des}} - x) - \dot{x}) + \alpha_0. \quad (6.6)$$

6.2.2 Quadrupedal Locomotion

As it was demonstrated by Raibert et al. (1986), the control principles for single-legged running can be directly transferred to multi-legged systems by including “virtual” reference frames and contact points as indicated in Figure 6.5(b). Our implementation is based on the work of Coros et al. (2011) and was adapted to our needs by Gehring et al. (2013). In this thesis, only the most important points are outlined for the sake of completeness. The additional element in quadrupedal locomotion is interleg coordination respectively the timing of the footfall pattern which is decoded in a so called *gait graph*. In Figure 6.5(a) this is depicted for a walking trot whereby the black bars indicate that the corresponding legs are in ground contact. The current position (green bar) of this symmetric gait is close to the middle of the swing phase of the left-front and right-hind leg pair (compare with Figure 6.5(b)).

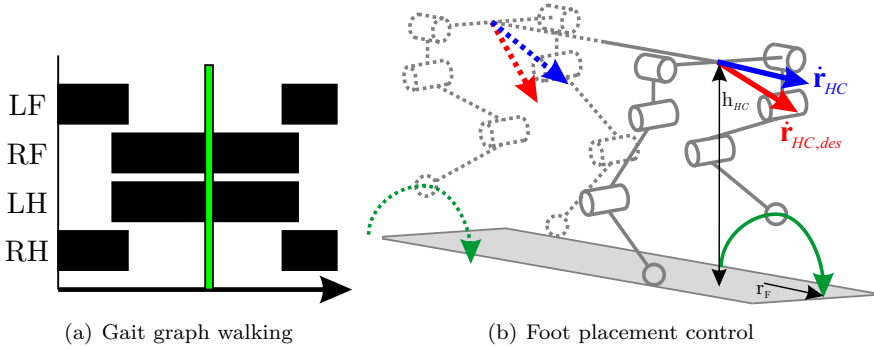


Figure 6.5: Timing of the contact points for every gait is defined by a gait graph (a) and the swing foot is positioned as a function of the speed at the corresponding hip reference frame (b) to maintain balance.

Similar to the single leg situation, the desired foothold locations are determined to maintain forward motion and to recover balance when the robot is pushed or when it encounters unanticipated variations in the terrain. Our framework considers every leg independently. To this end, we define two reference frames located in the middle of the front and back leg pair respectively. The swing leg offset relative to the nominal standing position is determined by

$$\mathbf{r}_F = \frac{1}{2}\dot{\mathbf{r}}_{HC,des}T_{st} + k_R^{FB}(\dot{\mathbf{r}}_{HC,des} - \dot{\mathbf{r}}_{HC})\sqrt{h_{HC}}. \quad (6.7)$$

The feedforward contribution remains equal to the previous formulation (6.5) with $\dot{\mathbf{r}}_{HC,des} \in \mathbb{R}^{2 \times 1}$ being the desired velocity in the horizontal plane at the corresponding hip reference frame and the stance duration time T_{st} which is defined by the gait pattern beforehand. The feedback term depends on the actual velocity $\dot{\mathbf{r}}_{HC}$ at the respective reference frame. To make the control gain independent of the hip height h_{HC} above ground, it is scaled with $\sqrt{h_{HC}}$. This scaling factor originates from the Froude number (Vaughan and O'Malley, 2005) that is largely accepted by biomechanics to be a fundamental criterion for dynamic similarities indicating that speed \dot{x} is proportional to the square root of a characteristic length such as the hip height $\sqrt{h_{HC}}$. For the implementation, the feedback gain is always chosen to be $k_p^{FB} = -0.4$. Given the initial foot location as well as the subsequent stepping location \mathbf{r}_F , we define a spline parameterization of the swing leg trajectory that guarantees sufficient ground clearance. For all dynamic gaits applied in this work, the main body orientation is kept constant and the base position is moved

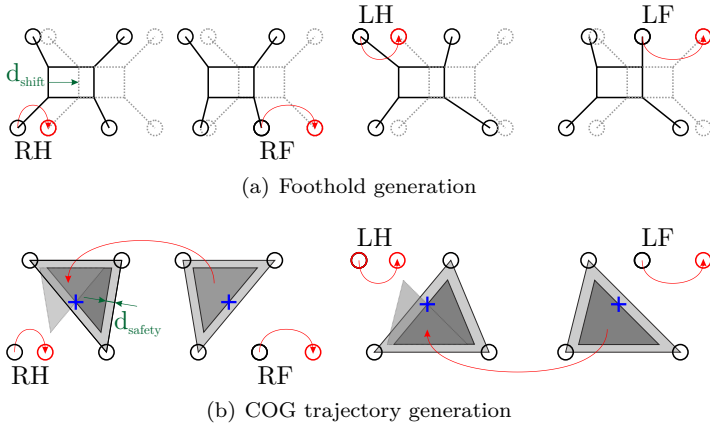


Figure 6.6: During static walking, the footholds are preplanned by shifting a default configuration d_{shift} ahead (a). Subsequently, the COG trajectory is generated by minimizing the body motion while guaranteeing a safety margin d_{safety} (b).

forward in the body fixed frame (${}_B\dot{x}_b = v_{\text{des}}$, ${}_B\dot{y}_b = 0$) with a superimposed vertical oscillation (${}_I z_b(t)$) to change the appearance.

So far, *motion generation* respectively foothold selection is solely a function of internal states of the robot to maintain and stabilize a dynamic gait. This works well on comparably level ground whereby changes in ground elevation are considered as disturbances and compensated by reactive stepping. When it comes to traverse challenging terrains however, the robot has to switch to a static gait and plan the sparsely available foothold locations as a function of the terrain

6.3 Static Gaits

Static gaits are characterized to be stable at any point of time and hence preferred when it comes to slow walking or challenging terrain. Following the early work by McGhee et al. (1968) we employ a static quadrupedal crawl gait that is favored by most animals for low speed locomotion and which represents the optimal gait to maximize static stability¹. Thereby, the robot continuously executes a stereotypic footfall pattern right-hind (RH), right-front (RF), left-hind (LH), left-front (LF). The proposed locomotion

¹static stability defines that the projected COG lies within the support polygon

algorithm starts from an initial stance configuration that defines the default foothold locations with respect to the body. In every step, the default configuration is shifted about some fixed distance d_{shift} ahead to determine the subsequent swing leg position (Figure 6.6(a)). Given the timing and location sequence for the footholds, the main body motion trajectory is generated. To this end, a constant safety margin d_{safety} is defined as the minimal distance between the base location and the corresponding support polygon projected onto a horizontal plane. With this boundary condition, the way points of the base location are determined for two successive steps ahead by searching for intersecting areas of the safe support triangles (Figure 6.6(b)) and hence minimizing the main body motion. The actual target position is then determined by interpolation as a function of the gait phase.

6.4 Summary

Legged locomotion is a complex interaction between a large number of links and actuators. However, the most important features can be described with astonishing accuracy by very simple motion templates such as SLIP. This helps not only to understand the biomechanical principles of walking and running but provides means for controlling the robotic counterparts. In this chapter, we studied stability and control properties of this template and augmented it with collision compensation for a more accurate description of an articulated robotic leg. We further used the template to determine desired foothold locations as a function of the forward speed to maintain and stabilize single-legged hopping and quadrupedal running gaits. In addition to that, we outlined motion generation for static gaits with three legs in ground contact. As this gait ensures continuous stability, it finds application in low speed walking or when it comes to crossing challenging terrain.

Chapter 7

Single Leg Experiments

Single-legged hopping is the archetype of all running gaits. Already the seminal work by Raibert in the 1980's on balancing legged systems first investigated a planar monopod before extending the findings nearly one to one to 3D hopping and later to multi-legged systems. Experimenting with single legs is used to validate the performance of hardware and control while keeping the complexity minimal and avoiding interleg coordination.

To evaluate our system, we created a single leg test bench (Figure 7.1) composed of a planar leg version that incorporates two actuators for flexion/extension at the hip and knee joint. By building on the previously outlined principles, the single leg can robustly locomote between different target points. During flight phase, the impact angle is adjusted to keep balance and to accelerate the system forward accordingly. During stance, the torque controlled SEAs shape the motion to virtually behave like a SLIP template. To this end, we use the concepts of virtual model control and task-space inverse dynamics to emulate a the spring force or COG dynamics respectively. Thereby, the benefit of highly compliant SEAs for improving energetic efficiency becomes apparent as the mechanical elasticity is compressed to temporarily store energy and to release it again before lift-off. Similar to the role of muscles and tendons in humans or animals, this passively supports the vertical oscillation and significantly reduces the amount of energy the motors need to introduce. As further advantages, peak power and maximal speed requirements of the electric motor can be lowered by factors.

The principles of exploiting passive dynamics can be maximized by using optimization methods in simulation or by applying learning techniques on the hardware. However, the limitations are defined to a large extent by the system mechanics and actuation. Some of them can be overcome by

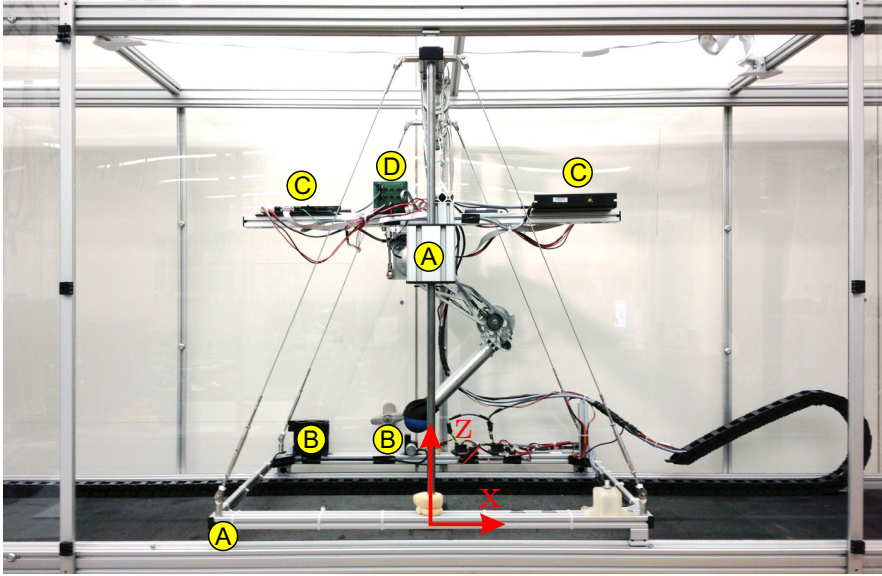


Figure 7.1: The proposed actuation and control methods were thoroughly tested with this planar single leg test bench that can freely move in horizontal (x) and vertical (z) direction but has a blocked main body pitch angle.

augmenting the leg with an additional lightweight foot element. This reduces impact losses and additionally supports the motion by springs that represent the functionality of an Achilles tendon.

7.1 Experimental Setup

The planar leg depicted in Figure 7.1 has two actuated degrees of freedom for hip and knee flexion/extension. Supported by low-friction guiding units (A) it can freely move in horizontal (x) and vertical (z) direction while all other degrees of freedom are blocked. To get ground truth data, the base position in both directions is precisely measured using incremental wire sensors (B). The single leg carries the motor controllers (C) and sensor boards (D) attached to the main body such that the total weight including the vertical guiding unit represent about a quarter of StarLETH. The control setup is identical to the description in Section 3.5 with a host PC connecting through CAN bus to the motor controllers and sensor boards.

7.2 Single Leg Running Control

An intuitive control approach for single-legged running emerges directly from observation of running gaits of humans or animals that can be accurately described by the SLIP template (Section 6.1). During flight phase, the leg follows a ballistic curve and the foot needs to be appropriately positioned to keep balance and to adjust the locomotion speed. The underlying angle of attack control is explained in detail in Section 6.2.1. During stance phase, the leg undergoes a spring like compression after landing and expands again before lift-off to redirect the body motion. Although the mechanical properties of the leg are built to support this oscillation passively, energy has to be introduced to compensate for damping and impact losses and to balance and maintain periodic hopping. This section summarizes how such a stance behavior is achieved by the feedback methods *virtual model* and *inverse dynamics control*, and how it can be pushed to the limits using *optimization and learning techniques*.

7.2.1 Virtual Model Control

Single-legged hopping can be controlled by applying a virtual force \mathbf{F}_v at the main body. For achieving a SLIP-like oscillation, a spring-damper force element is emulated in vertical direction by

$$F_v^z = k_\sigma (l_0 - (z_b - z_s)) + d_\sigma (-\dot{z}_b), \quad (7.1)$$

with the desired spring stiffness k_σ and damping coefficient d_σ , as well as the base and foot height z_b and z_s respectively. According to the virtual leg lengthening (6.4), the parameter l_0 represents the unloaded spring length which is larger than the impact leg length and hence used to (virtually) compensate for energy losses. For periodic hopping, the damping parameter d_σ is kept zero. However, when it comes to special maneuvers, damping can be activated, e.g. to immediately stop while running. Due to bandwidth limitation of the actuator, the virtual stiffness is bounded by $\max(k_\sigma) \approx \omega_{BW}^2 m_\sigma$, with ω_{BW} being the actuator bandwidth and m_σ the total leg mass. To stabilize forward running motion and to improve agility, the virtual force in horizontal direction is modulated based on a simple proportional position controller

$$F_v^x = \text{sat}(k_x (x_{b,\text{des}} - x_b)) \in [-F_{\max}^x, F_{\max}^x]. \quad (7.2)$$

To avoid slipping or tipping over, the horizontal force is limited by a saturation function $\text{sat}(\cdot)$. As the segments are lightweight in comparison to the base, we additionally compensate for the heavy base mass by a force at the

main body $\mathbf{F}_g = [0, -m_\sigma g]^T$. Using the force equilibrium (5.2), the contact force yields $\mathbf{F}_s = \mathbf{F}_v - \mathbf{F}_g$. As the virtual force \mathbf{F}_v as well as the gravitational force \mathbf{F}_g directly act on the main body ($\mathbf{r}_{bv} = \mathbf{r}_{bg} = \mathbf{0}$, $\mathbf{J}_{bv} = \mathbf{J}_{bg} = \mathbf{0}$), the desired joint torques can be calculated according to (5.6) by

$$\boldsymbol{\tau} = \mathbf{J}_{bs}^T \mathbf{F}_s = \mathbf{J}_{bs}^T (\mathbf{F}_v - \mathbf{F}_g), \quad (7.3)$$

with the relative support point Jacobian $\mathbf{J}_{bs} = \frac{\partial \mathbf{r}_b - \partial \mathbf{r}_s}{\partial \mathbf{q}_j}$.

To ensure efficient excitation, we additionally constrain the knee joint motion such that the motor always introduces energy into the system ($P_{m,KFE} > 0$). As the knee is only loaded in positive direction ($\tau_{KFE} > 0$), this constraint can be expressed in terms of motor velocity by $\dot{\varphi}_m > 0$. The application of virtual model control to emulate the SLIP-like force between the contact point and the COG is very robust and intuitive. The few parameters for the virtual force element can be theoretically predicted and hand-tuned in hardware experiments with low effort. However, the method has limitations as it does not account for dynamic effects.

7.2.2 Task-Space Inverse Dynamics

Task-space inverse dynamics techniques as described in Sections 5.2 to 5.5 cannot only emulate a SLIP-like force acting on the system, but moreover shape the entire dynamics to behave exactly like the template. Instead of high-gain position tracking of a predefined stance phase trajectory, we directly use the locomotion template as the desired task-space dynamics. Single-legged hopping in stance phase is not *truly-underactuated* and hence the sequential method is perfectly suited. To generate the desired accelerations $\ddot{\mathbf{q}}$, the contact constraint has to be ensured with highest priority

$$\mathbf{A}_1 = \mathbf{J}_s, \quad (7.4)$$

$$\mathbf{b}_1 = -\dot{\mathbf{J}}_s \dot{\mathbf{q}}. \quad (7.5)$$

With second priority, the COG or base¹ dynamics of the prototype has to match the motion template. This is defined by reformulating the EOM of the SLIP model (6.1) such that

$$\mathbf{A}_2 = \mathbf{J}_b, \quad (7.6)$$

$$\mathbf{b}_2 = \ddot{\mathbf{r}}_b - \dot{\mathbf{J}}_b \dot{\mathbf{q}} = \frac{1}{m_\sigma} \mathbf{F}_\sigma + \mathbf{g} - \dot{\mathbf{J}}_b \dot{\mathbf{q}}, \quad (7.7)$$

¹In our mechanical design with the lightweight segments, base and COG nearly coincide. Hence, the base is taken as reference position.

with \mathbf{F}_σ being a function of the deflection of the emulated spring between base and contact point. Using Algorithm 1 (page 65), this hierarchical problem is solved for the desired generalized accelerations. In this simple case with two contact constraints and two COG task-space accelerations that are all linearly independent, the solution can be directly calculated by an inversion of a single stacked Jacobian:

$$\ddot{\mathbf{q}} = \begin{bmatrix} \mathbf{J}_s \\ \mathbf{J}_b \end{bmatrix}^{-1} \begin{pmatrix} -\dot{\mathbf{J}}_s \dot{\mathbf{q}} \\ \frac{1}{m_\sigma} \mathbf{F}_\sigma + \mathbf{g} - \dot{\mathbf{J}}_b \dot{\mathbf{q}} \end{pmatrix}. \quad (7.8)$$

The support consistent generalized accelerations are subsequently utilized to solve for the joint torque. The constraint actuator selection matrix \mathbf{PS}^T has full rank and can be inverted such that the joint torque calculates to

$$\boldsymbol{\tau} = (\mathbf{PS}^T)^{-1} \mathbf{P} (\mathbf{M}\ddot{\mathbf{q}} + \mathbf{h}). \quad (7.9)$$

In contrast to virtual model control, this template-based inverse dynamics control does not only superimpose a corresponding force but shapes the entire dynamics of the articulated robotic leg to the template. By using the previously described SLIPic dynamics that accounts also for energy losses and speed changes due to the impact at landing, we can theoretically and in idealized simulations achieve a perfect template matching (Hutter et al., 2010b). However, due to modeling errors and actuator limitations, the output motion of the real robotic device will always differ from the underlying template. The interested reader can consult a detailed study by Gehring et al. (2011) about the implementation of this method on the single leg test bench.

7.2.3 Optimization and Learning

With the previously discussed feedback control methods, motion generation is restricted to spring-mass templates. Due to the simplicity and robustness, these models have been successfully used in applications with legged robotic devices. However, they describe the entire system only to certain extent and cannot be used to push the performance to its limits. Instead, it is necessary to apply numerical *optimization* and *learning* techniques to generate the stance phase motion.

Optimization in Simulation

For a simultaneous optimization of the actuator input $\mathbf{u}(t)$ and part of the system parameters \mathbf{p} (e.g. joint stiffness), we use the framework presented

by Remy (2011). This tool minimizes the mechanical actuator work $P_{mech} = \boldsymbol{\tau}^T \dot{\mathbf{u}}$ as a function of \mathbf{u} and \mathbf{p} while guaranteeing that the solution is periodic ($\mathbf{x}^{k+1} = \mathcal{P}(\mathbf{x}^k, \mathbf{p}, \mathbf{u}) = \mathbf{x}^*$) with a fixed hopping height h and hopping period T_{hop} :

$$\begin{aligned} \min_{\mathbf{p}, \mathbf{u}(t)} \quad & f(\mathbf{x}^*, \mathbf{p}, \mathbf{u}(t)) = \int_0^{T_{hop}} \max(0, \boldsymbol{\tau}^T \dot{\mathbf{u}}) dt \\ \text{s.t.} \quad & \mathcal{P}(\mathbf{x}^*, \mathbf{p}, \mathbf{u}(t)) - \mathbf{x}^* = 0 \\ & \max(z(t)) - h = 0. \end{aligned} \quad (7.10)$$

In our implementation, the motor actuation $\mathbf{u}(t)$ is described as a time-based Fourier series with 3 coefficients:

$$\mathbf{u}(t) = \sum_{i=0}^3 a_i \sin\left(i \frac{2\pi}{T} t\right) + b_i \cos\left(i \frac{2\pi}{T} t\right). \quad (7.11)$$

This has the benefit that continuity in the motor command can be guaranteed and that it can be accounted for the motor bandwidth limitation by keeping the number of Fourier coefficients small. We extensively applied this method in the work of Latta et al. (2010) to generate feedforward motor commands for an optimal exploitation of the natural dynamics of the system. Although large effort was put into model identification, modeling errors forced us to superimpose feedback controllers. This has the same effect as when using the motion templates: The controller enforces a desired behavior and thereby limits the system performance.

Adaptive Control and Learning

An attempt to overcome this deficiency of artificial (or simulative) motion generation is to apply online optimization techniques. In an earlier work (Hutter et al., 2009c), we used adaptive control to shape the motion trajectories to improve robustness against slippage. A step that goes far beyond this is reinforcement learning or in particular the PI^2 algorithm (Theodorou et al., 2010) that was successfully applied to the single leg (Fankhauser et al., 2013). A detailed report on the results of optimizing precise long jumps, maximal high jumps, and periodic hopping can be found in (Fankhauser et al., 2012). In a two-step approach, control policies are first optimized in simulation and afterwards refined in real hardware experiments. However, the achieved energetic running efficiency is barely better than the template-based motion generation approach.

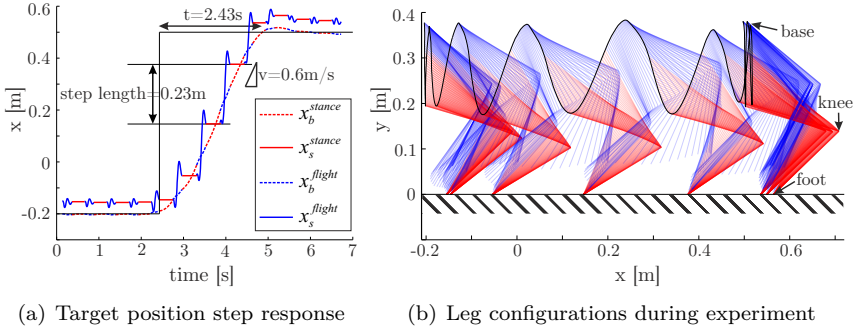


Figure 7.2: The proposed control structure allows to quickly and precisely locomote to a target location (a). Thereby, the leg undergoes substantial vertical oscillations (b).

7.3 Locomotion with Point Foot

To assess the performance of the mechanical structure and control algorithms in terms of *controllability* and *efficiency*, we conducted various experiments with the single leg test bench.

7.3.1 Controllability

Controllability and robustness of our robot is qualitatively evaluated in planar running experiments. To this end, hopping height is modified by changing the length l_0 of the virtual spring element (7.1). Gait transitions from rest to hopping are initiated by a short vertical force offset. To bring the robot to an immediate stop, virtual damping d_σ is increased to an overcritical value. Changing the vertical stiffness k_σ adjusts the hopping frequency. The virtual forces in horizontal direction (7.2) in combination with the angle of attack control (6.6) allow to balance the robot under external disturbances and to reach arbitrary goal positions without any overshoot. Thereby, step lengths of about 0.25 m and a top speed of about 0.6 m/s is achieved (Figure 7.2(a)). Although the body mass experiences huge vertical oscillations (Figure 7.2(b)), the mechanical cost of transport in this experiment with energy expenditure taken as the integral of positive mechanical motor power is about $COT = 0.9$. This efficiency can be attributed to a large extent to the passive compliance in the knee joint which undergoes substantial displacement during the stance phase.

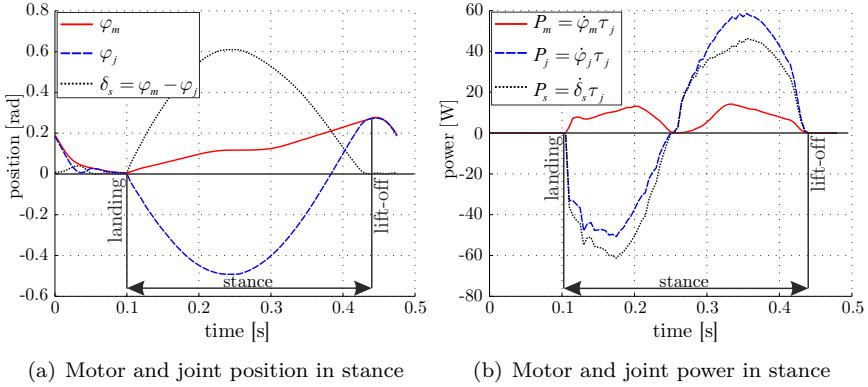


Figure 7.3: The experimental results of stationary hopping indicate the benefit of the large compliance in the knee joint. The motor travel distance (and its speed) is only a fractional part of the joint motion (a). The motor introduces energy during the entire stance phase with small peak power and zero negative work (b).

7.3.2 Efficiency

Efficiency is evaluated in stationary hopping experiments ($x_{\text{des}} = \dot{x}_{\text{des}} = 0$). Figure 7.3(a) depicts the knee joint and motor position during a single stance phase. As expected, the spring compliance ensures that the travel distance of the motor (red solid) is much smaller than the actual joint motion (blue dashed). Furthermore, the motor is always delivering positive power (Figure 7.3(b), red solid). The spring passively stores energy (integral area of the black dotted) after impact and returns it before lift-off. Already after landing while the main body still performs a downward motion and the leg is effectively decelerated, the motor is introducing energy. This is in strong contrast to a stiff actuation approach in which breaking and accelerating needs to be actively done by the motor.

To quantify the mechanical efficiency of energy storage in single-legged hopping, we define the hopping efficiency as

$$\eta = 1 - \frac{\int_T \max(P_m, 0) dt}{\int_T \max(P_j, 0) dt}. \quad (7.12)$$

Since electric energy recuperation is generally not possible for a setup with a highly non-backdrivable gearbox, we use the notation $\max(P, 0)$. This formulation indicates how much of the positive mechanical work ($P_j = \dot{\varphi}_j \tau_j$)

needed by the joint to perform a hopping cycle can be provided passively and how much the motor needs to contribute ($P_m = \dot{\varphi}_m \tau_j$). The closer η is to 1, the lower fraction of energy is coming from the motor. Negative numbers of η mean that the motor has to provide more positive work than it is needed at the joint. This case can occur with SEAs if the joint compliance is not well aligned with the natural system dynamics or if large control action is required.

The experiments showed an efficiency coefficient $\eta = 0.64$, that means about 64% of the positive work required for hopping is passively stored and released while about 36% needs to be provided by the actuator to compensate for damping or impact losses. Although a direct comparison of these values to nature needs to be critically examined, studies with humans (e.g. Ker et al., 1987; Lichtwark and Wilson, 2005) or animals (e.g. Alexander, 1988; Farley et al., 1993) showed that nature recovers substantial fraction of the hopping energy purely mechanically. They provide numbers in the order of 35% for mechanical energy storage in the Achilles tendon and 50% or more for the total energy recuperation.

Additionally to the energetic efficiency, we are interested in speed and power amplifications that can be achieved with a highly compliant SEA. Values for the maximal joint speed in relation to the maximal motor speed ($\omega_{rel} = \frac{\dot{\varphi}_{j,\max}}{\dot{\varphi}_{m,\max}} = 4.7$), as well as the maximal joint power in relation to the maximal motor power ($P_{rel} = \frac{P_{j,\max}}{P_{m,\max}} = 4.1$) clearly support the expectations as both are largely amplified by the spring.

7.3.3 Mechanical Limitations

The performance limitations in terms of hopping efficiency are defined by the mechanical design of the hardware device respectively by the damping and friction effects, as well as by the impact losses at landing. Damping and friction is dominated by the quality of the springs and bearings. Collision losses on the other hand are defined by the leg kinematics and mass distribution of the entire design. In Section 2.4.2 we showed that the energy loss in a plastic impact collision can be written as

$$E_{loss} = E_{kin}^+ - E_{kin}^- = -\frac{1}{2} \dot{\mathbf{r}}_s^{-T} \mathbf{\Lambda}_s \dot{\mathbf{r}}_s^- . \quad (7.13)$$

The highest energy loss occurs if the pre-impact speed $\dot{\mathbf{r}}_s^-$ is aligned with the eigenvector \mathbf{e}_1 which corresponds to the greatest eigenvalue λ_1 of the foot point inertia $\mathbf{\Lambda}_s$. Asada (1983) and Schmiedeler and Waldron (2000) propose a visual interpretation by plotting the generalized inertia ellipsoid (GIE) with the perpendicular axis $1/\sqrt{\lambda_{1,2}} \mathbf{e}_{1,2}$. Investigation of different

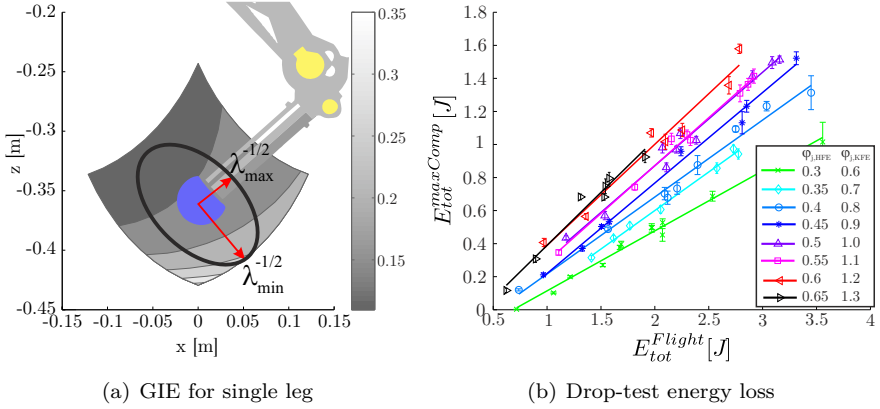


Figure 7.4: A GIE analysis (a) indicates that the pre-impact velocity should be perpendicular to the shank in order to minimize the impact losses. Measurements of the energy loss in drop-down experiments (b) with nearly no compliance at the contact point confirm the theory that energy losses are gradually increasing for smaller knee bending angles.

landing configurations for the single leg based on the GIE (Figure 7.4(a)) indicates that impact energy losses are minimal if the pre-impact velocity $\dot{\mathbf{r}}_s^-$ is nearly perpendicular to the inertia main axis of the segment that is colliding with the ground. For stationary hopping with a 2-segmented leg, this requires a crouched position with a large knee bending angle. Ideally the shank segment is close to horizontal (dark area, energy loss < 15%). On the other hand, more outreached leg configurations (bright area, energy loss > 25%) have a higher end-effector inertia in vertical direction and hence significantly more energy drain with the same vertical pre-impact speed.

To confirm this theoretical prediction, we conducted a set of impact experiments. In reality, a contact collision is not an instantaneous process but it induces extremely high accelerations at the different segments over a short period of time. The related energy loss is very difficult to capture in measurements as we would need accurate velocity information shortly before and after impact. To get around this, we propose to measure how much of the COG energy during flight phase

$$E_{tot}^{Flight} = mg(z_{COG} - z_0) + \frac{1}{2}m\dot{\mathbf{r}}_{COG}^2, \quad (7.14)$$

can be preserved until the mid-stance point. At that point, the velocity of

all segments is zero and the knee spring is maximally compressed

$$E_{tot}^{maxComp} = mg(z_{COG} - z_0) + \int_0^{\delta_{s,max}} \tau_{KFE}(\delta_s) d\delta_s. \quad (7.15)$$

The height energy is always expressed w.r.t. the body height at landing z_0 and the energy in the spring is given by the integral over the spring torque $\tau_{KFE}(\delta_s)$. Since energy is constant during flight phase, all available measurements between apex (highest point in flight curve) and touchdown are used to estimate the pre-impact energy (7.14). The energy at maximal compression can be determined with high precision as we do not have to account for kinetic energy which is prone to sensor noise. The total energy loss is composed of impact losses as well as the damping losses in the series elasticity and the joint.

The results of multiple dropping tests are depicted in Figure 7.4(b). Taking the height relative to the leg length at impact ensures that only the actual jumping height contributes to the potential energy. For a constant landing configuration the dependency between the energy level (7.14) and the energy loss (2.32) is linear, with an increasing slope for less crouched configurations. This is in agreement with the theory: Since a different starting height changes only the norm of $\dot{\mathbf{r}}_s^- = \dot{\mathbf{r}}_{COG}^- = (0, \dot{z}^-)^T$ but not its direction, (2.32) reduces to $\Delta E_{kin} = -\frac{1}{2} \dot{\mathbf{r}}_s^{-T} \mathbf{\Lambda}_s \dot{\mathbf{r}}_s^- = -\frac{1}{2} \lambda_{22} \dot{z}^{-2}$ with the geometric scalar λ_{22} , and the relation $\frac{\Delta E_{kin}}{E_{tot}^-} = \frac{-1/2 \lambda_{22} \dot{z}^{-2}}{1/2 m \dot{z}^{-2}} = -\frac{\lambda_{22}}{m}$ becomes constant. In conclusion, to keep λ_{22} small, it is indispensable to minimize the contact segment mass and to align the inertia main axis perpendicular to the impact direction – requirements that seek for an additional foot element.

7.4 Locomotion with Foot Element

To overcome the mechanical limitations of a 2-segmented leg in terms of impact losses and energy storage capabilities, we designed and built a passive, lightweight foot segment with springs at the ankle joint that imitate the Achilles tendon principle (Figure 3.6). We applied numerical optimization techniques to tune the ankle joint stiffness and validated the augmented leg in stationary hopping experiments.

7.4.1 Ankle Joint Stiffness and Control Optimization

To find the optimal ankle joint stiffness with respect to energetic hopping efficiency, we used the numerical optimization strategy outlined in Section 7.2.3

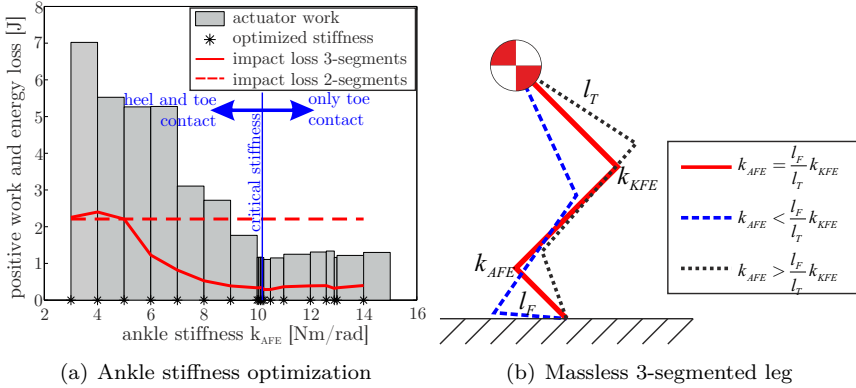


Figure 7.5: The positive actuator work minimization (7.10) shows minimal energy consumption for a stiffness around the critical stiffness (a). This value is close to the theoretical optimum of the ankle stiffness of a massless 3-segmented leg (b)(Seyfarth et al., 2001).

and simultaneously searched for the actuator input $\mathbf{u} = \varphi_m(t)$ as well as the ankle joint stiffness $\mathbf{p} = k_{AFE}$. The solution of the optimization problem is depicted in Figure 7.5(a): The bars indicate the value of the cost function (positive actuator work), the red solid line the impact loss of the 3-segmented leg in comparison to the 2-segmented leg (red dashed line). The actuator work as well as the total impact loss is reduced by increasing the stiffness. Up to the critical stiffness (about 10 Nm/rad) the ankle spring is compliant enough to allow for a double contact phase (heel makes contact), above that, only the toe touches ground. The obtained results are close to the theoretical predictions by Seyfarth et al. (2001) for a massless leg which showed that $k_{AFE} = \frac{l_F}{l_T} k_{KFE}$ is required for a symmetric bending (Figure 7.5(b)). Our optimized results indicate that, in terms of energetic efficiency, making the ankle springs stiffer is beneficial. In the time between toe and heel contact, a considerable amount of energy is stored and the vertical heel speed is reduced such that the second impact at the heel is comparably small. Going beyond the critical stiffness where the leg experiences only toe contact does not improve efficiency anymore. However, considering controllability of the system, double contact is advantageous: since the ankle is not actuated, the system in point contact is *truly-underactuated* and full controllability is only regained in the double support phase. In summary, we propose to choose the stiffness just below the critical stiffness.

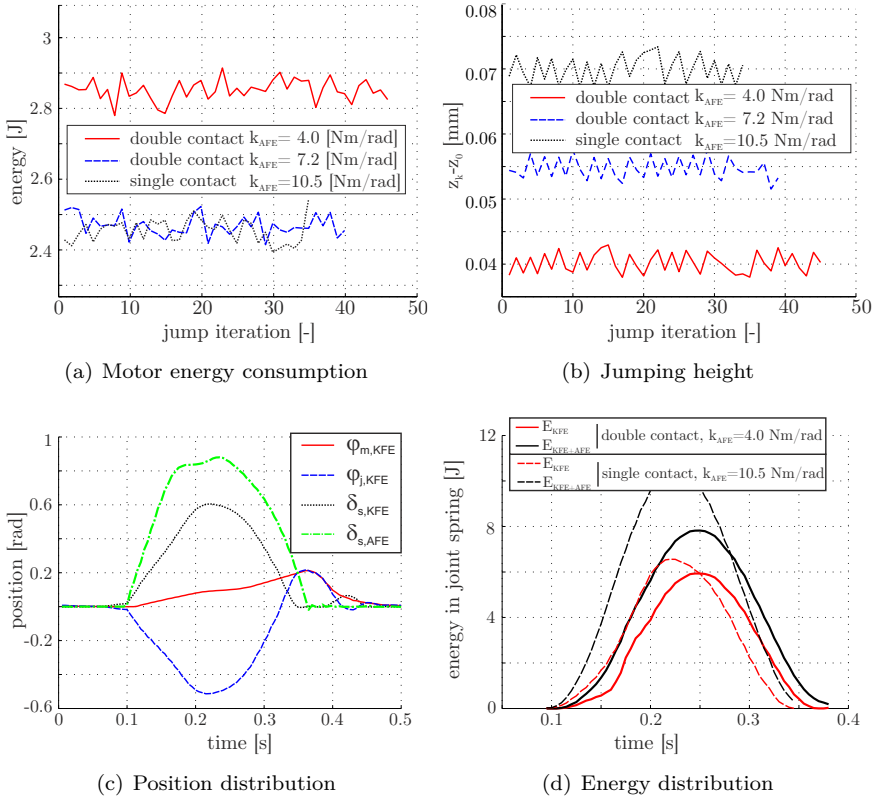


Figure 7.6: The passive foot segment was tested in single-legged running experiments using a varying ankle joint stiffness. Increasing the stiffness is beneficial up to the critical stiffness (a,b). The ankle compliance additionally improves the hopping efficiency by storing energy (c,d).

7.4.2 Experimental Validation

To be directly comparable with the results collected with the ball foot, we implement the same virtual model controller (Section 7.2.1) in the 3-segmented leg for single-legged running with different ankle joint stiffness k_{AFE} . The application of a foot segment shows a reduction of motor energy consumption (Figure 7.6(a)): a compliant ankle spring (4.0 Nm/rad (red solid), 2.85 J) requires more energy compared to the stiffer springs (7.2 Nm/rad (blue dashed), 10.5 Nm/rad (black dotted), both 2.45 J). Evaluating the hopping height (Figure 7.6(b)) shows the same tendency. Hence, the optimization results could

be approved: as long as the heel still touches the ground, increasing the stiffness results in a remarkable improvement. As soon as the critical stiffness (only toe touches the ground) is reached, making the ankle stiffer does not improve the overall performance. The hopping experiment with an ankle stiffness of 10 Nm/rad (Figure 7.6(c)) further highlights that the proposed control strategy provides only positive actuator power ($\dot{\varphi}_j > 0$ during the entire stance phase). The power and velocity amplifications remain at the same level as with the 2-segmented design (Section 7.3.2) while the hopping efficiency (7.12) can be increased up to 70%. This energetic improvement can be entirely assigned to the ankle. Comparing the stiffest and the most compliant ankle joint shows that the energy stored in the knee remains the same (red) while the total energy stored in the ankle and knee spring (black) can be drastically increased (Figure 7.6(d)).

7.5 Summary

Single-legged hopping is used to investigate the hardware and actuation performance and to evaluate control algorithms for balancing dynamic gaits. On a step-to-step basis, the angle of attack is adjusted to achieve a desired horizontal acceleration in the upcoming stance phase. As soon as the leg makes contact, the COG velocity has to be redirected through the application of supporting forces. Inspired by the SLIP model which holds as an accurate template of dynamic gaits found in nature, we apply virtual model and inverse dynamics control techniques to achieve a very similar oscillation behavior. Thereby, we could manifest that the highly compliant actuation principles used in our robot largely support the motion. By temporarily storing and releasing energy in the mechanical springs, more than 60% of the required hopping energy can be provided passively and the motor needs only to compensate for damping and impact losses. We showed that this exploitation of the natural system dynamics can be improved on one hand by numerical optimization and learning algorithms which change the actuation profile, and on the other hand, by adding an extremely lightweight foot segment with optimized ankle springs. However, to keep Star $LETH$ fully controllable, the passive ankle joints are not realized on the quadruped robot.

Chapter 8

Quadruped Experiments

The research presented in this thesis in the areas of hardware, actuation, and control development finally culminates in a series of experiments with the quadrupedal robot Star*LETH*. By combining the individual building blocks presented beforehand, the quadrupedal robot can perform different gaits from static walking to dynamic running on varying terrain.

Starting with a series of performance tests, we demonstrate that the hardware and actuation is robust and powerful enough for static and dynamic locomotion tasks. These tests include payload capability measurements and drop-down experiments. To achieve a compliant but actively damped behavior, a generalized virtual model controller (Section 5.1) is applied to emulate spring-damper force elements acting on the main body of the system.

The second series of experiments is dedicated to low-speed static walking. As the quadruped has always three or more legs in ground contact, balancing the robot is not an issue. In contrary, the multi-contact configuration allows to exploit different load distributions. Using the sequential inverse dynamic control approach presented in Section 5.4, we compare the effects of joint torque and contact force minimization with regard to energetic efficiency and robustness against slippage. We showcase the simplicity of integrating joint torque and position saturations and we outline an interpolation method for a smooth change in the contact situation. As a step towards extending the range of operation to unstructured terrain, we exemplify a method to align the contact force with the local surface, which improves robustness against slippage. We further confirm the benefits of hybrid OSC which allows to combine fast joint position control of the swing legs with inverse dynamics control in the remainder of the system (Section 5.6).

When transitioning to dynamic gaits, Star ETH becomes *truly-underactuated* and the desired motion must not only be constraint consistent, it moreover needs to be consistent with the floating base dynamics. To guarantee this, we make use of the combined inverse dynamics control approach presented in Section 5.5. Integrating this with foot location planning allows balancing a walking and running trot even under substantial external disturbances resulting from pushes or unforeseen ground elevation. Although there remain few simultaneous contact points in dynamic gaits (for trotting only the two diagonal ones), an internal force direction allows optimizing the joint torque or contact force distribution. The experimental section is concluded with an interesting point for discussions, namely measurements of the energy consumption in autonomous long-distance trotting.

All methods and findings are tested in simulations (*Sim*) and validated in hardware experiments (*Exp*) without any change in the controller implementation. This enforces to carefully tune the desired behavior and control parameters as a function of hardware and actuation limitations. To this end, some guidelines are summarized in Appendix A.9. All our experiments use pure task-space inverse dynamics control without any (low-gain) joint position regulation. Furthermore, Star ETH is operating without visual feedback or beforehand knowledge about terrain elevation. Hence, the robot has no information about its surrounding which only allows to adapt the footholds in a reactive way based on haptic information that is collected by the contact and joint torque sensors. As a quantitative evaluation of the performance of the developed hardware and control structures is often difficult to capture in numbers and figures, all experiments are supported by video material listed in Section 1.4.

8.1 Experimental Setup

Star ETH is secured from the ceiling by a mobile crane (A). In most experiments the machine is operated on a large-scale, custom-made treadmill (B) with the dimensions of about $2.90\text{ m} \times 1.60\text{ m}$. To establish ground truth data and to automatically adjust the treadmill speed, an *OptiTrack S250e* motion capture system with 8 cameras (C) was integrated. Although ground truth data is available, this is not used for control but only for post processing of experimental data. Instead, all controllers rely on state estimations based on onboard sensing (Section 3.5.2). The energy consumption (*Exp 17*) was tested in a fully autonomous configuration with an onboard PC and batteries, all other experiments were conducted with an external power source and host PC.

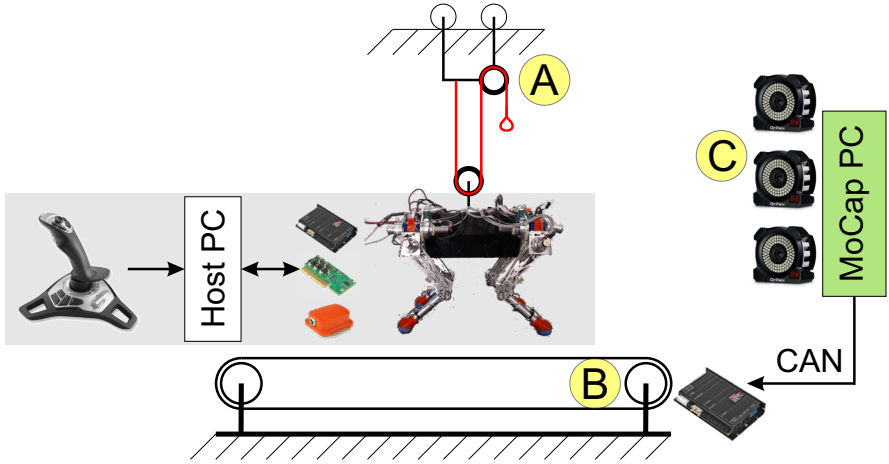


Figure 8.1: The experimental setting for StarLETH consists of a mobile crane (A) to secure the robot from the ceiling, a large-scale treadmill (B) (2.90 m × 1.60 m), and an external MoCap system (C) to establish ground truth data and to automatically adjust the treadmill speed.

8.2 Performance Evaluation

This section evaluates two important performance criteria for quadrupedal robots, namely *payload* capability and *robustness*.

8.2.1 Payload (*Exp 1*)

Walking and running machines need to provide sufficient torque that enables them not only to conduct various maneuvers but also to carry batteries and sensor equipment. This enables a long operation time and full autonomy in a completely unknown environment. A representative scenario to demonstrate the payload capability is standing up from a completely crouched position (Figure 8.2). Due to the large hip and knee bending angle this requires maximal joint torques. StarLETH is able to stand up with an additional payload of 25 kg, which is more than the total weight of the actual robot. In theory, the peak torque in all actuators of 30 Nm with a lever arm of 0.2 m results in a maximal total lift force of $F_{\max} = 4 \cdot \frac{30 \text{ Nm}}{0.2 \text{ m}} = 600 \text{ N}$ or a maximal theoretical stand-up payload of $\approx 35 \text{ kg}$. However, such peak forces should only occur for short periods in highly dynamic maneuvers and were hence not experimentally validated as payload.

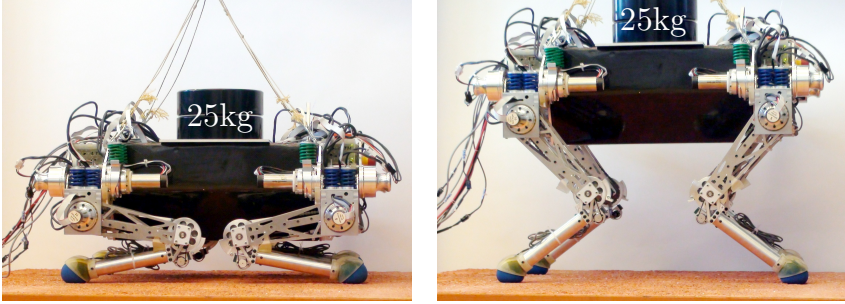


Figure 8.2: *Exp 1:* The torque capability was experimentally validated in a stand-up maneuver with 25kg payload.

8.2.2 Robustness (*Exp 2*)

To perform dynamic maneuvers, it is crucial that the robot can cope with impacts. In contrast to a stiff actuation principle, the elasticity in series to the motor and gearbox decouples them from the output link. This ensures that, even if all motors are blocked, none of the gearboxes gets damaged by high peak forces. As a result, StarLETH can robustly damp out the kinetic pre-impact energy or temporarily store it without harming the gearbox. To demonstrate this virtue, we dropped StarLETH from a height of the full leg length or ≈ 0.4 m (Figure 8.3(a)). The recorded vertical position of the main body is depicted in Figure 8.3(b). The highly compliant and low damped springs in the joints lead to large oscillations (red solid) including a number of short rebounds (grey background) after landing. While being advantageous in terms of efficient energy recovery, this behavior is undesired when it comes to perform a proper landing maneuver. In a next experiment, we suppress the disturbing oscillations by active damping using the generalized virtual model control concept introduced in Section 5.1. Thereby, we virtually impose a spring-damper force \mathbf{F}_v and torque $\boldsymbol{\tau}_v$ at the base ($\mathbf{r}_v = \mathbf{r}_b$)

$$\mathbf{F}_v = \mathbf{k}_p (\mathbf{r}_{b,\text{des}} - \mathbf{r}_b) + \mathbf{k}_d (\dot{\mathbf{r}}_{b,\text{des}} - \dot{\mathbf{r}}_b), \quad (8.1)$$

$$\boldsymbol{\tau}_v = \mathbf{k}_p (\boldsymbol{\varphi}_{b,\text{des}} - \boldsymbol{\varphi}_b) + \mathbf{k}_d (\dot{\boldsymbol{\varphi}}_{b,\text{des}} - \dot{\boldsymbol{\varphi}}_b), \quad (8.2)$$

with the main body position \mathbf{r}_b and orientation $\boldsymbol{\varphi}_b$. The matrices \mathbf{k}_p and \mathbf{k}_d represent the virtual stiffness and damping. This controller prevents the undesired body oscillation after landing (Figure 8.3(b), blue dashed) and none of the feet loses contact after landing anymore.

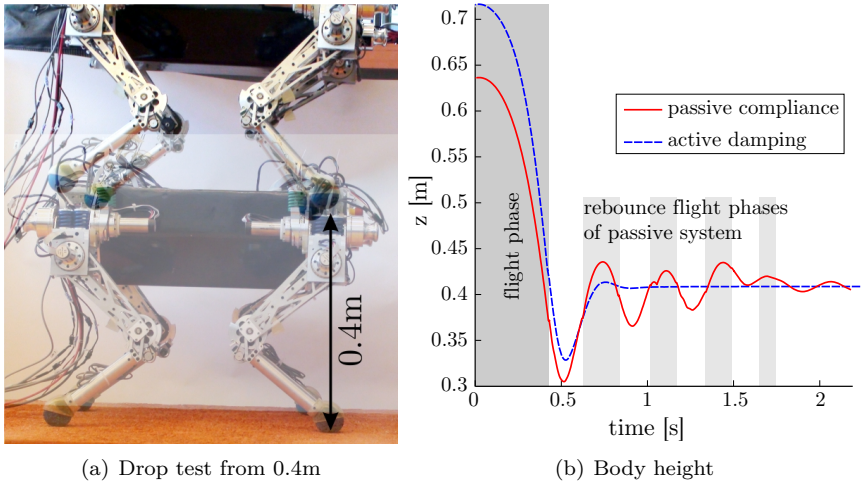


Figure 8.3: *Exp 2:* The passive compliance in the joints of StarLETH protects the actuators from large peak forces at landing. The vertical main body position was estimated using IMU values during flight and kinematic information during contact phase. The red solid curve shows the high oscillations due to the passive compliance with intermittent rebounding phases (grey area). This can be actively damped (blue dashed) using virtual model control.

8.3 Static Gaits

Static walking gaits are applied for slow locomotion speed and in particular when it comes to crossing challenging terrain. With three or more legs in ground contact, static stability can be continuously ensured. The *overconstrained* contact situation thereby offers potential to optimize the contact force respectively joint torque distribution. As the quadruped robot is never *truly-underactuated* in static walking maneuvers, we apply the sequential approach introduced in Section 5.4. The task-space motion optimization to generate $\dot{\mathbf{q}}$ is equally performed in all experiments. To this end, the support constraint (2.6) with $\mathbf{A}_1^q = \mathbf{J}_s$ and $\mathbf{b}_1^q = -\dot{\mathbf{J}}_s \dot{\mathbf{q}}$ has the highest priority P_1^q . The base position and orientation are combined in a single, six dimensional task of second priority P_2^q with $\mathbf{A}_2^q = [\mathbf{J}_b^T \quad \mathbf{J}_R^T]^T$ and $\mathbf{b}_2^q = \dot{\mathbf{r}}_{2,\text{des}} - [\mathbf{J}_b^T \quad \mathbf{J}_R^T]^T \dot{\mathbf{q}} = \ddot{\mathbf{r}}_2^{FF} + \mathbf{k}_p (\mathbf{r}_{2,\text{des}} - \mathbf{r}_2) + \mathbf{k}_d (\dot{\mathbf{r}}_{2,\text{des}} - \dot{\mathbf{r}}_2) - [\dot{\mathbf{J}}_b^T \quad \dot{\mathbf{J}}_R^T]^T \dot{\mathbf{q}}$. Thereby, $\mathbf{J}_b = \frac{\partial \mathbf{r}_b}{\partial \mathbf{q}}$ represents the translational base Jacobian, $\mathbf{J}_R = \frac{\partial \boldsymbol{\Omega}_b}{\partial \mathbf{q}}$ the rotational Jacobian, $\boldsymbol{\Omega}_b$ the main body rotation speed, and \mathbf{r}_2 the stacked vector of main body position and orientation. The desired base position and body yaw angle are replanned using the method outlined in Section 6.3 while the body pitch and roll angle are always regulated to zero.

During the shifting as well as the stepping sequence, at least $n_s \geq 3$ points are in contact with the ground. Using Definition 2, the system is $n_c = 3n_s - 6$ times *overconstrained*. Taking the constrained dynamics task (5.20) as highest priority P_1^T there remains a n_c -dimensional subspace for contact force respectively joint torque optimization with lower priority such that the motion is not impaired. For *Sim* and *Exp* 3, 4, 5, and 6, we compare energy expenditure and risk of slippage as a function of the optimization objectives and actuator saturation. As a measure for energy consumption of electrically driven robots, the most commonly used objective function is the integral of the square of actuator torques (Remy et al., 2012a)

$$E_\tau = \int \boldsymbol{\tau}^T \boldsymbol{\tau} dt. \quad (8.3)$$

To quantify the risk of slippage, we calculate the mean of the relation between tangential and normal contact force

$$\bar{\mu} = \text{mean} \left(\frac{F_{\text{tangential}}(t)}{F_{\text{normal}}(t)} \right). \quad (8.4)$$

The smaller this fraction, the lower the risk of slippage at the evaluated contact point. Since there are no precise contact force sensors incorporated, these forces are estimated in the experiments by (2.16) based on joint torque,

Table 8.1: Static walking experiments with different optimization objectives

	P_1^τ	P_2^τ	P_3^τ	E_τ [N ² m ² s]	$\bar{\mu}$ [-]	τ_{KFE}^{\max} [Nm]	$\overline{\Delta \mathbf{r}}$ [mm]
Sim 3	inv dyn*	$\tau \min^\ddagger$	-	3985	0.27	12.2	3.7
Exp 3	inv dyn*	$\tau \min^\ddagger$	-	4701	0.20	12.4	7.7
Sim 4	inv dyn*	$\mathbf{F}_s \min^\S$	-	5730	0.04	16.0	4.1
Exp 4	inv dyn*	$\mathbf{F}_s \min^\S$	-	5544	0.04	13.7	3.3
Sim 5	$\tau \lim^\dagger$	inv dyn*	$\tau \min^\ddagger$	4034	0.29	10.0	4.3
Exp 5	$\tau \lim^\dagger$	inv dyn*	$\tau \min^\ddagger$	4557	0.24	10.4	7.2
Sim 6	$\tau \lim^\dagger$	inv dyn*	$\mathbf{F}_s \min^\ddagger$	5502	0.10	10.0	4.9
Exp 6	$\tau \lim^\dagger$	inv dyn*	$\mathbf{F}_s \min^\S$	5485	0.07	10.6	3.8

*inv dyn: $\mathbf{A}_i^\tau = \mathbf{Q}_u^T \mathbf{S}^T$, $\mathbf{b}_i^\tau = \mathbf{Q}_u^T (\mathbf{M}\ddot{\mathbf{q}} + \mathbf{h})$

$^\dagger \tau \lim (\tau_{KFE_{LF}} < 10 \text{ Nm})$: $\mathbf{A}_i^\tau = [0 \ 0 \ 1 \ 0 \ \dots \ 0]$, $\mathbf{b}_i^\tau = 10$

$^\ddagger \tau \min (\mathbf{W}_\tau = \mathbf{I}, \mathbf{b}_\tau = \mathbf{0})$: $\mathbf{A}_i^\tau = \mathbf{W}_\tau$, $\mathbf{b}_i^\tau = \mathbf{0}$

$^\S \mathbf{F}_s \min (\mathbf{W}_F = \mathbf{I}, \mathbf{b}_F = \mathbf{0})$: $\mathbf{A}_i^\tau = \mathbf{R}^{-1} \mathbf{Q}_c^T \mathbf{S}^T$, $\mathbf{b}_i^\tau = \mathbf{R}^{-1} \mathbf{Q}_c^T (\mathbf{M}\ddot{\mathbf{q}} + \mathbf{h})$

encoder, and IMU signals. Due to an accurate model and precise torque measurements, this approximation yields quite exact results as validated for the single leg by Fankhauser et al. (2012).

All walking experiments and simulations show a minimal difference among each other in the actual base position and orientation. As a quantification: The average absolute distance error $\overline{\Delta \mathbf{r}}_{b_i} = \text{mean} |\mathbf{r}_{b_i}(t) - \bar{\mathbf{r}}(t)|$ of each recorded time series $\mathbf{r}_{b_i}(t)$ to the mean $\bar{\mathbf{r}}(t) = \frac{1}{n} \sum_{i=1}^n \mathbf{r}_{b_i}(t)$ of all simulations and measurements is less than 8 mm. As we are working with exactly the same controller in simulation and on the hardware, this small difference indicates that the underlying models are indeed very accurate. The results are summarized in Table 8.1 and discussed in detail subsequently.

8.3.1 Actuator Efficiency Optimization (*Sim/Exp 3*)

The energy consumption is optimized by applying a least square problem (5.22) with $\mathbf{A}_2^\tau = \mathbf{W}_\tau = \mathbf{I}$ and $\mathbf{b}_2^\tau = \mathbf{b}_\tau = \mathbf{0}$ with priority P_2^τ . With this method, a walking sequence of 3 full cycles (3 steps with each leg) corresponds to a cost of $E_\tau^{\text{sim}} = 3985 \text{ N}^2 \text{ m}^2 \text{ s}$ in simulations and $E_\tau^{\text{exp}} = 4701 \text{ N}^2 \text{ m}^2 \text{ s}$ in experiments. Analyzing the contact forces shows that the mean required friction coefficients are $\bar{\mu}^{\text{sim}} = 0.27$ and $\bar{\mu}^{\text{exp}} = 0.20$ correspondingly.

8.3.2 Contact Force Optimization (*Sim/Exp 4*)

Minimizing the total contact force is equivalent to removing all internal forces that do not contribute to the net resulting force on the ground. This is likewise to work that was done based on static virtual model control (Zhou et al., 2000) where the pseudo-inversion distributes the virtual forces onto the individual contact points such that the resulting support forces are least square minimal. In the presented framework, force minimization is achieved by selecting $\mathbf{W}_F = \mathbf{I}$ and $\mathbf{b}_F = \mathbf{0}$, respectively $\mathbf{A}_2^\tau = \mathbf{R}^{-1}\mathbf{Q}_c^T\mathbf{S}^T$ and $\mathbf{b}_2^\tau = \mathbf{R}^{-1}\mathbf{Q}_c^T(\mathbf{M}\ddot{\mathbf{q}} + \mathbf{h})$ (see (5.24)). Conducting the same walking experiment with this controller, the tangential contact forces are significantly reduced ($\bar{\mu}^{sim} = 0.04$, $\bar{\mu}^{exp} = 0.04$) and the actuation costs ((8.3), $E_\tau^{sim} = 5730 \text{ N}^2\text{m}^2\text{s}$, $E_\tau^{exp} = 5544 \text{ N}^2\text{m}^2\text{s}$) are increased.

8.3.3 Joint Torque Limitation (*Sim/Exp 5,6; Sim 7*)

A simple method to account for actuator torque limitations $|\tau_i| < \tau_{sat}$ is to tackle these inequality constraints as outlined in Section 5.3.3. Limitations are generally disabled, but as soon as torque limitations are violated, a high priority task with $\mathbf{A}_1^\tau = \mathbf{W}_\tau = [0 \ 0 \ 1 \ 0 \ \dots \ 0]$ and $\mathbf{b}_1^\tau = \mathbf{b}_\tau = \pm\tau_{sat}$ is introduced and all other tasks are shifted to lower priorities. If multiple saturate, they are stacked at the same priority. The procedure guarantees that the generated torque profiles meet all actuator limitations and that non-saturated actuators take more load to still achieve the desired acceleration. Star ETH can perform the same walking maneuvers as in the previous experiments but with (arbitrarily) limited knee joint torque to 10 Nm. As summarized in Table 8.1, the energetic consumption remains more or less equal if the maximal knee torque is limited. However, the limitation slightly increases the risk of slipping since the contact force cannot be aligned as well as without torque saturation. As depicted in Figures 8.4(a) and 8.4(c), the motion is equal for *Exp 3* and *Exp 5* independent of the joint torque distribution. At the same time, the knee torque (Figure 8.4(d)) can be limited to 10 Nm: in this region, mainly HFE of the same leg but also other joints take part of the load (Figure 8.4(b)). The violation of the 10 Nm boundary with the knee joint (gray circle, Figure 8.4(d)) happens due to (external) disturbances acting on the system.

The method of introducing high priority saturation tasks produces solutions that are consistent with the system dynamics as long as Lemma 3 is fulfilled for the inverse dynamics task at P_2^τ . Otherwise, consistency is violated and the desired motion can only be executed to certain extent. Figure 8.5 illustrates this in a simulation (*Sim 7*) of a vertical position step

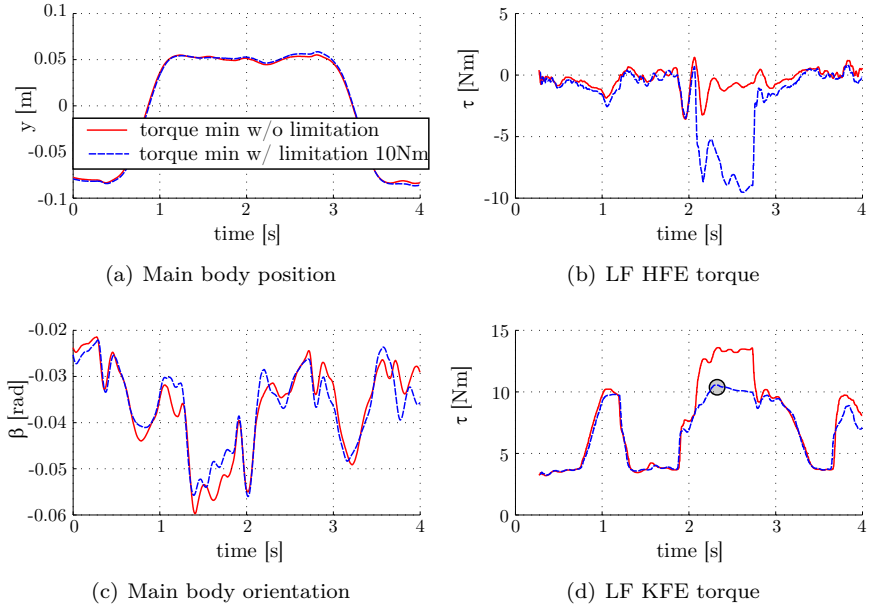
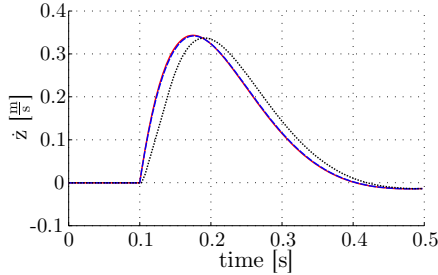


Figure 8.4: A comparison of experimental results with (blue dashed, *Exp 5*) and without (red solid, *Exp 3*) joint torque limitations show nearly perfect matching in terms of motion (a,c). During the phase where τ_{KFE} is saturated (d), HFE (and others) takes over part of the load (b).

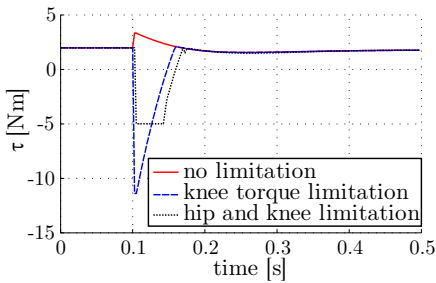
command signal applied to the body height: As long as only the knee joint torque (KFE) is saturated, the desired motion is perfectly executed since the hip (mainly HFE) is taking part of the load (blue dashed). If the torque of hip flexion (HFE) is limited as well, the desired motion cannot be followed anymore (black dotted).

8.3.4 Joint Position Limitation (*Exp 8, 9*)

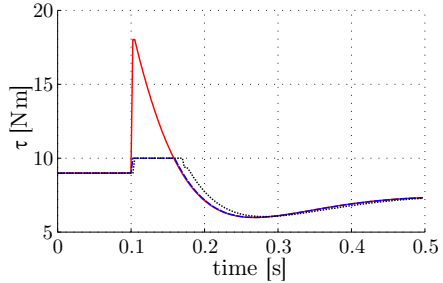
In addition to torque saturation, most robots suffer from a limited joint or tasks space range of operation. This is usually handled by soft limitations when planning the desired motion. However, joint range limitations should also be ensured if the actual motion is significantly offset from the desired motion, e.g. by external disturbances. This happens in particular when regulating the robot with very low feedback gains to emulate a compliant behav-



(a) Vertical main body velocity



(b) LF HFE torque



(c) LF KFE torque

Figure 8.5: (*Sim 7*): As long as only τ_{KFE} is saturated, the desired motion of a vertical step input on the main body position is perfectly executed since the hip (mainly HFE) is taking over part of the load (blue dashed). If the τ_{HFE} saturates as well, the desired motion cannot be followed anymore (black dotted).

ior. As a solution, we propose to include the position limitation as inequality constraints in the motion controller (Section 5.3.3). As a showcase scenario, we command a simple base shift in forward direction. At the same time, we restrict the maximal HFE angle to 0.9 rad from the main body x-axis as indicated in Figure 8.6. This limitation is arbitrarily chosen to demonstrate the working principle when separating main body position and orientation tasks into different priorities. In *Exp 8*, we choose the support constraint with highest priority P_1^q as in the previous examples. The second priority task P_2^q attributes to regulate the body position in xy-plane (stability). As P_3^q we ensure that the body orientation is aligned with the environment while P_4^q keeps the ground clearance constant. In *Exp 9*, the order of P_3^q and P_4^q is changed such that ground clearance becomes more important than the body orientation.

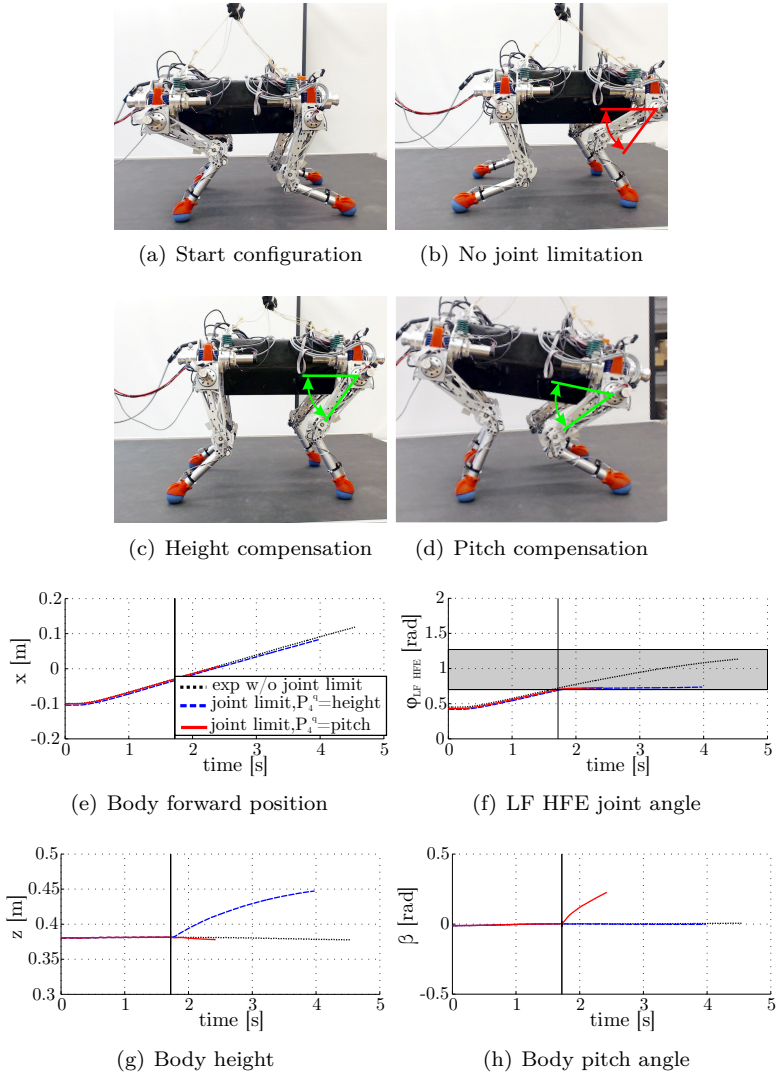
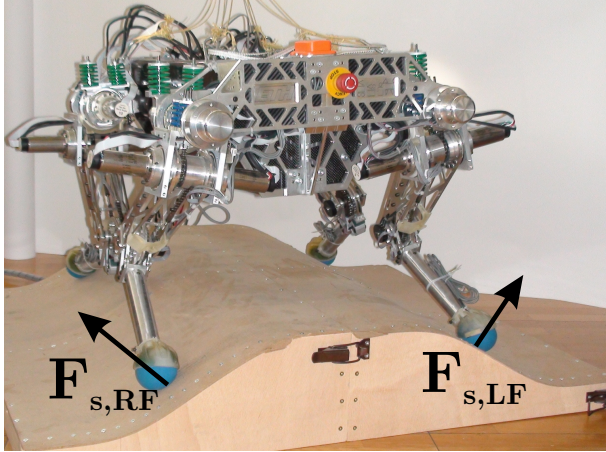


Figure 8.6: The presented framework compensates for joint angle limitations (e.g. φ_{HFE}) while shifting the main body forward. Its motion is distorted either by lifting the main body upward (*Exp 8*, low priority in z posture, (c)) or by tilting the main body forward (*Exp 9*, low priority for body pitch angle, (d)).

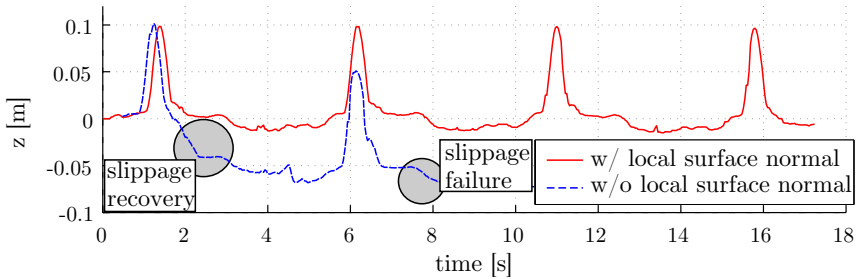
Body shifting in forward direction, while keeping body height and orientation constant, is first conducted without considering the limits (Figure 8.6(b)). Thereby, the hip joint angle limitation is violated (Figure 8.6(f), black dotted). This can be avoided by activating the limitation tasks as done in *Exp 8* (Figure 8.6(c)) and *Exp 9* (Figure 8.6(d)). As soon as the limitation in HFE is reached, a task with P_2^q is introduced that ensures that the angle is not growing anymore in this direction, respectively that the corresponding joint acceleration is pushing away from the soft joint angle limitation. All remaining tasks are shifted to lower priorities. It can be observed that HFE does not exceed the limitation (Figure 8.6(f)) but the body motion is distorted by violating the lowest priority task. In *Exp 8* (blue dashed), the robot starts to increase the body clearance (Figures 8.6(c) and 8.6(g)). In this way, it can continuously shift its base forward without impairing the joint angle limitation. In *Exp 9* (red solid), the robot starts pitching its body to avoid the joint limitation (Figures 8.6(d) and 8.6(h)).

8.3.5 Terrain Dependent Optimization (*Exp 10*)

Stability respectively no slippage at the contact points can only be guaranteed if the contact forces are within the local friction cone at all time. To keep the tangential forces as small as possible while traversing non-flat terrain, we propose to align the contact forces with the local surface normal directions. To this end, the force weighting matrix (5.24) is changed to $\mathbf{W}_F = \text{blockdiag}(\alpha_i \mathbf{t}_i^T)$ with $\mathbf{t}_i \in \mathbb{R}^{3 \times 2}$ being the local tangential plane at each contact point. This control approach was tested in static, in-place walking on a half-cylindrical shaped surface with known geometry (Figure 8.7(a)). To quantify slippage, the feet positions were measured by post-processing of the recorded movie using a color blob tracker for the ball feet. As indicated in Figure 8.7(b), robustness against slippage can be extremely improved by this contact force alignment and slippage free locomotion is achieved if the robot holds itself on the terrain by producing internal contact forces (red solid). In (Hutter et al., 2012b) we compare this analytical approach based on weighted local surface tangential planes with a quadratic program (QP) solver that minimizes the local friction coefficient. For this experiment, the results of the nonlinear optimization are not considerably better as the proposed analytical solution but in return require significantly more computational power. Still, generalizing these findings to any type of gait and terrain requires further investigation.



(a) StarlETH on curved surface



(b) LF foot position during tree stem walking experiment

Figure 8.7: (*Exp 10*): If the contact forces are aligned with the local surface normal direction by applying internal forces, StarlETH can walk on a half-cylinder surface (a) without slipping (b, red solid). Considering the surface as flat ground leads to failure after the first step (b, blue dashed).

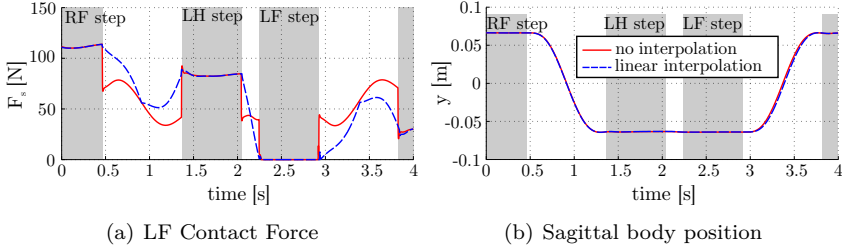


Figure 8.8: (*Sim 11*): The proposed interpolation method leads to smooth contact transitions while walking (a) without changing the body motion (b). The resulting torque trajectories can be followed by low bandwidth series elastic actuators.

8.3.6 Smooth Contact Force Distribution (*Sim 11*)

A change in the contact situation entails a discrete change in the support Jacobian \mathbf{J}_s . As a consequence, applying inverse dynamics leads to undesired discontinuities in the actuator torques $\boldsymbol{\tau}$ and contact forces \mathbf{F}_s . To make these changes smooth, we propose an interpolation method between two subsequent contact situations. In case of static walking, transitions occur always between three and four contact point situations in both directions.

In the first step, the original contact force problem is solved to generate the optimal load distribution \mathbf{F}^{opt} for four contact points. Subsequently, the desired contact force at the changing contact is (linearly) scaled to $\mathbf{F}_j = w\mathbf{F}_j^{opt}$ as a function of the interpolation parameter $w \in [0 \ 1]$ which is determined by the gait phase or time. Increasing w from 0 to 1 corresponds to loading a leg, decreasing to unloading. In the second step, the optimization problem is solved again with an additional high priority task $(\mathbf{A}_2^T, \mathbf{b}_2^T)$ with $\mathbf{W}_F = \mathbf{S}_j$ and $\mathbf{b}_F = \mathbf{F}_j$, whereby \mathbf{S}_j corresponds to the selection matrix of the interpolated contact force \mathbf{F}_j . As a result, the load distribution is smoothly transitioned between loading four ($\mathbf{F}_j = \mathbf{F}_j^{opt}$) or only three ($\mathbf{F}_j = \mathbf{0}$) legs. This method differs from approaches used by Dietrich et al. (2012) in a way that the interpolation directly shapes the contact forces and not the corresponding null-space projectors \mathbf{N}_i .

As indicated in Figure 8.8(a), undesired steps (red solid) in the contact forces and joint torques due to a discrete change in the support configuration are fully avoided by a continuous interpolation between subsequent contact situations (blue dashed). Again, the body motion is not affected at all by this change in load distribution (Figure 8.8(b)). This method was successfully tested in different walking experiments.

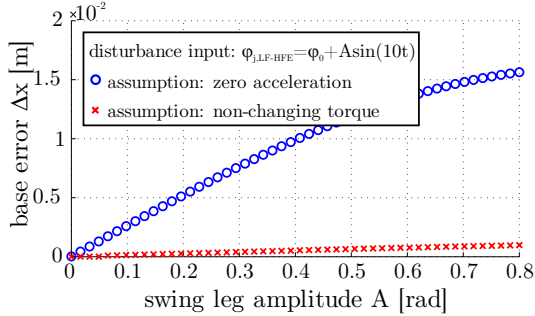


Figure 8.9: (*Sim 12*): The disturbances occurring at the main body due to swing leg oscillation with increasing amplitude can be significantly lowered by a disturbance compensation with torque measurements (red x) in comparison to assuming non-accelerated motion (blue o).

8.3.7 Hybrid OSC (*Sim 12*)

The locomotion skills of a robot largely depend on a fast and precise swing leg control performance. For a compliant robot such as Starl*ETH*, this requires to build on high performance position controllers in the swing leg joints (cf. Section 4.3) and hence to consider the control problem as hybrid.

Sim 12 illustrates the benefit of swing leg compensation which was first presented in (Hutter et al., 2012b). To represent typical foot positioning tasks, Starl*ETH* is standing on three legs while the hip swing angle is position controlled to follow an oscillation with a varying amplitude from 0 – 0.8 rad at a moderate frequency of 10 rad/s. Figure 8.9 depicts the tracking error of the base position. Without compensation ($\mathbf{A}_i^c = [\mathbf{S}_p \ \mathbf{0}]$, $\mathbf{b}_i^c = \mathbf{0}$), respectively with the assumption of a non-accelerated motion, the acceleration of the joint corresponds to an unobservable disturbance. With growing amplitude, this more and more deviates the main body from its nominal position (blue o). If compensation is activated by assuming that the torque in the position controlled joints remains constant (red x, $\mathbf{A}_i^c = [\mathbf{0} \ \mathbf{S}_p \mathbf{S}^T]$, $\mathbf{b}_i^c = \hat{\boldsymbol{\tau}}_p$), the errors can be significantly improved. These findings make hybrid OSC to be a valuable approach for combining fast position control with compliant whole body regulation.

8.4 Dynamic Gaits

The final set of experiments investigates the dynamic locomotion performance of StarLETH. In dynamic gaits, the robot experiences *truly-underactuated* contact phases and the gait can only be stabilized on a step-to-step basis. To ensure consistency of the control variables with the EOM, we apply the combined approach (Section 5.5). A summary of the individual tasks of different priorities is given in Table 8.2. They are described either in inertial frame I or in body fixed frame B . We use the rotation matrix \mathbf{C}_{BI} to transform translation Jacobians ${}_I\mathbf{J} = \frac{\partial {}_I\mathbf{r}}{\partial \mathbf{q}}$ and rotation Jacobians ${}_I\mathbf{J}_R = \frac{\partial {}_I\boldsymbol{\Omega}}{\partial \mathbf{q}}$ from inertial to the body fixed frame and vice versa such that ${}_B\mathbf{J} = \mathbf{C}_{BI} \cdot {}_I\mathbf{J}$. In all equations, \mathbf{S}_i represent selection matrices with unit entries for the corresponding directions.

For the subsequent experiments, the desired body height ${}_I z_{\text{des}}(t)$ oscillates as a function of time respectively phase of the gait. For a calm walking trot, the vertical main body position is kept almost constant. For a running trot on the other side, large vertical oscillations are excited to achieve a natural behavior. In all experiments, the main body orientation in roll and pitch is regulated to zero (${}_B\boldsymbol{\varphi}_{\text{des}} = \mathbf{0}$). To allow for an intuitive steering, the operator can adjust the desired walking speed in sagittal ${}_B\dot{x}$ (${}_B\mathbf{e}_x$ forward direction in main body frame) and coronal direction ${}_B\dot{y}$ (${}_B\mathbf{e}_y$ sideward direction in main body frame), as well as the turning rate ${}_I\dot{\psi}$ about the vertical axis ${}_I\mathbf{e}_z$ of the inertial frame. Figure 8.10 illustrates a typical dynamic trotting gait at about 0.7 m/s whereby the treadmill was kept at zero velocity.

Table 8.2: Motion task priorities for dynamic locomotion with StarLETH.

Prio	reference signal	\mathbf{A}_i^c	\mathbf{b}_i
P_1^q	support constraint	${}_I\mathbf{J}_s$	$-{}_I\dot{\mathbf{J}}_s\dot{\mathbf{q}}$
P_2^q	base height ${}_I z$	$\mathbf{S}_z {}_I\mathbf{J}$	$k_p^z ({}_I z_{\text{des}} - {}_I z) + k_d^z ({}_I \dot{z}_{\text{des}} - {}_I \dot{z})$
P_3^q	body roll, pitch ${}_B\boldsymbol{\varphi}$	$\mathbf{S}_{\varphi} {}_B\mathbf{J}_R$	$\mathbf{k}_d^{\varphi} ({}_B\boldsymbol{\varphi}_{\text{des}} - {}_B\boldsymbol{\varphi}) + \dots$ $\mathbf{k}_d^{\varphi} ({}_B\dot{\boldsymbol{\varphi}}_{\text{des}} - {}_B\dot{\boldsymbol{\varphi}}) - \mathbf{S}_{\varphi} {}_B\dot{\mathbf{J}}_R\dot{\mathbf{q}}$
P_4^q	base rot rate ${}_I\dot{\psi}$	$\mathbf{S}_{\psi} {}_I\mathbf{J}_R$	$k_d^{\psi} ({}_I\dot{\psi}_{\text{des}} - {}_I\dot{\psi}) - \mathbf{S}_{\psi} {}_I\dot{\mathbf{J}}_R\dot{\mathbf{q}}$
P_5^q	base velocity ${}_B\mathbf{v}$	$\mathbf{S}_{xy} {}_B\mathbf{J}$	$\mathbf{k}_d^{xy} ({}_B\mathbf{v}_{\text{des}} - {}_B\mathbf{v}) - \mathbf{S}_{xy} {}_B\dot{\mathbf{J}}\dot{\mathbf{q}}$

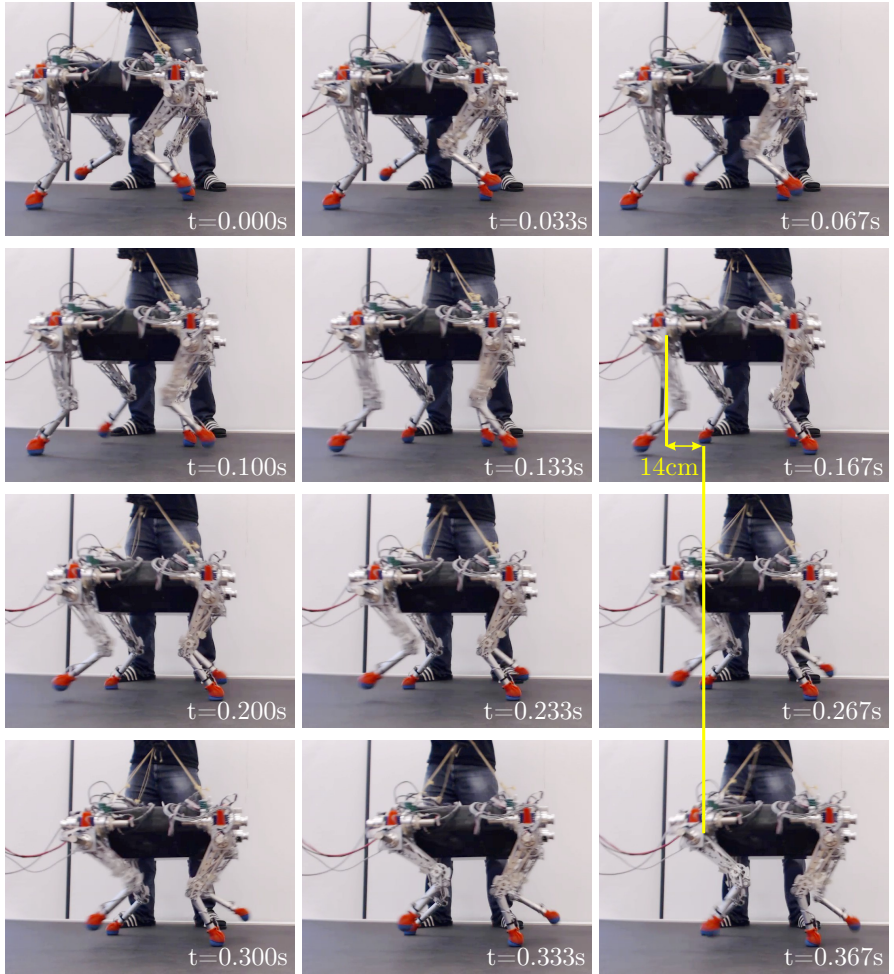


Figure 8.10: StarLETH can perform a trotting gait with a forward speed of approximately 0.7 m/s respectively 1.5 bodylength/s .

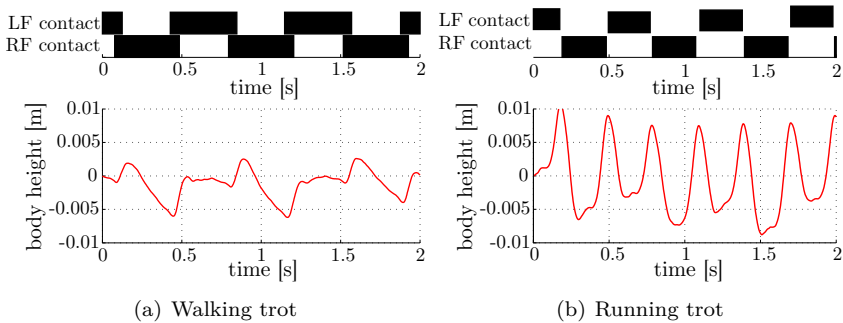


Figure 8.11: *Exp 13, 14:* Star ETH was tested in a walking (a) and running (b) trot. The latter gait shows shorter contact phases, a higher stride frequency, and larger oscillations of the body.

8.4.1 Running and Walking Trot (*Exp 13, 14*)

Trotting gaits as applied for Star ETH are characterized by a completely symmetric gait graph with alternating diagonal pairs of leg in ground contact. A duty factor (% of cycle in ground contact) of more than 50% defines a walking trot (*Exp 13*, Figure 8.11(a)). Thereby, during a short phase of contact transition, all four legs are grounded and the robot keeps the main body nearly at constant height. In contrast thereto, a running trot is defined by a duty factor smaller than 50% and hence the robot undergoes a short flight phase when alternating the diagonal pair of contact legs (*Exp 14*, Figure 8.11(b)). The stride frequency of the running trot is chosen to be higher while the main body executes larger oscillations in vertical direction. Independent of the kind of trotting gait we noticed that applying the presented control structure in simulations as well in real world experiments requires only small and intuitive gain tuning.

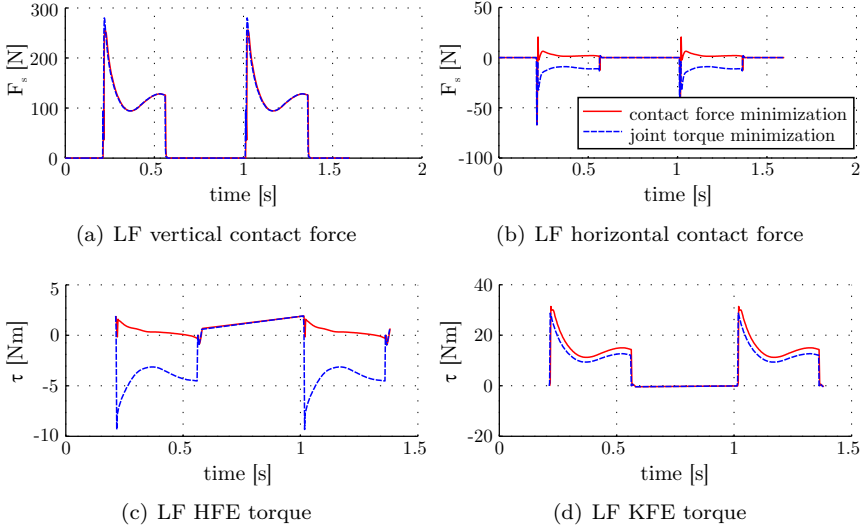


Figure 8.12: *Sim 15*: Minimizing the actuator torque ($\mathbf{W}_\tau = \mathbf{I}$, blue dashed) instead of minimizing the contact force ($\mathbf{W}_F = \mathbf{I}$, red solid) reduces the energy consumption (8.3) of a trotting gait about 20% since HFE takes part of the load. In return, the contact force increases in horizontal direction and hence also the risk of slippage.

8.4.2 Force and Torque Optimization (*Sim 15*)

Having only two feet in contact with the ground reduces the space for optimization of contact forces or joint torques to a single dimension. We tested and compared minimizing joint torques ($\mathbf{W}_\tau = \mathbf{I}$) with minimizing contact forces ($\mathbf{W}_F = \mathbf{I}$). As indicated in Figure 8.12, the different strategies slightly change the load distribution while producing exactly the same motion. The former method ($\mathbf{W}_\tau = \mathbf{I}$, blue dashed) results in a mean friction coefficient for in-place trotting of $\bar{\mu} = 0.14$, minimizing the contact force ($\mathbf{W}_F = \mathbf{I}$, red solid) lowers this to $\bar{\mu} = 0.05$ but in return increases the actuator cost (8.3) about 20%. However, none of the methods has shown a significant advantage in hardware experiments.

8.4.3 Stability and Robustness (*Exp 16*)

Stability and robustness usually determine how well a system can compensate for disturbances such as external pushes or unknown obstacles. In contrast to linear control theory that has well elaborated tools to measure this property, robustness is hard to quantify for legged systems. Maximal disturbances before tipping over can be analytically determined for static walking as the COP is not allowed to coincide with the boundary of the support triangle. This changes when analyzing dynamic gaits, in our example trotting gaits with just the diagonal pair of legs in contact. There are so many parameters of influence that a robustness analysis in most cases boils down to a qualitative evaluation in experiments to identify the stability limitations.

In general, a dynamically balancing legged robot has two means to reject disturbances. All legs in contact can produce reaction forces to counteract the perturbations as good as possible. However, to compensate for disturbances in the *truly-underactuated* subspace, the contact point locations have to be adapted accordingly. For a trotting gait, the quadruped has $n_u = 1$ *truly-underactuated* degrees of freedom which corresponds to the rotation around the line of support. Hence, for the task decomposition outlined in Table 8.2, the base velocity task P_7^T is only fulfilled as good as possible in least square sense. This implies that acceleration errors causing a rotation around the line of support can only be compensated in the subsequent contact phase or by modulating the stepping location. As an example depicted in Figure 8.13, we kicked the robot from the side. This causes a velocity error at the corresponding hip center in coronal direction and hence, due to (6.7), Star*LETH* steps sideways to compensate. Thereby, it produces a counterforce and, within two steps, finds back to the nominal trotting gait.

8.4.4 Energy Consumption (*Exp 17*)

To quantify energy consumption we performed a long term trotting experiment of about 45 min over a distance of 1150 m while advancing with constant speed. To get comparable values to the metabolic costs found in nature, Star*LETH* was operated fully autonomous with onboard PC and two 5 Ah, 22.2 V LiPo batteries. For trotting with an average speed of about 0.43 m/s the robot required an average power of $P_{el} = 296 \text{ W}$ which corresponds to a dimensionless COT of about 2.57. When the robot is fully disabled, we measured an energy loss of all electronic components of more than $P_{loss_0} = 100 \text{ W}$. Estimating the average positive mechanical power defined as joint torque times motor speed results in $P_{mech} = 32 \text{ W}$. This means on one hand that the mechanical COT including all control action required

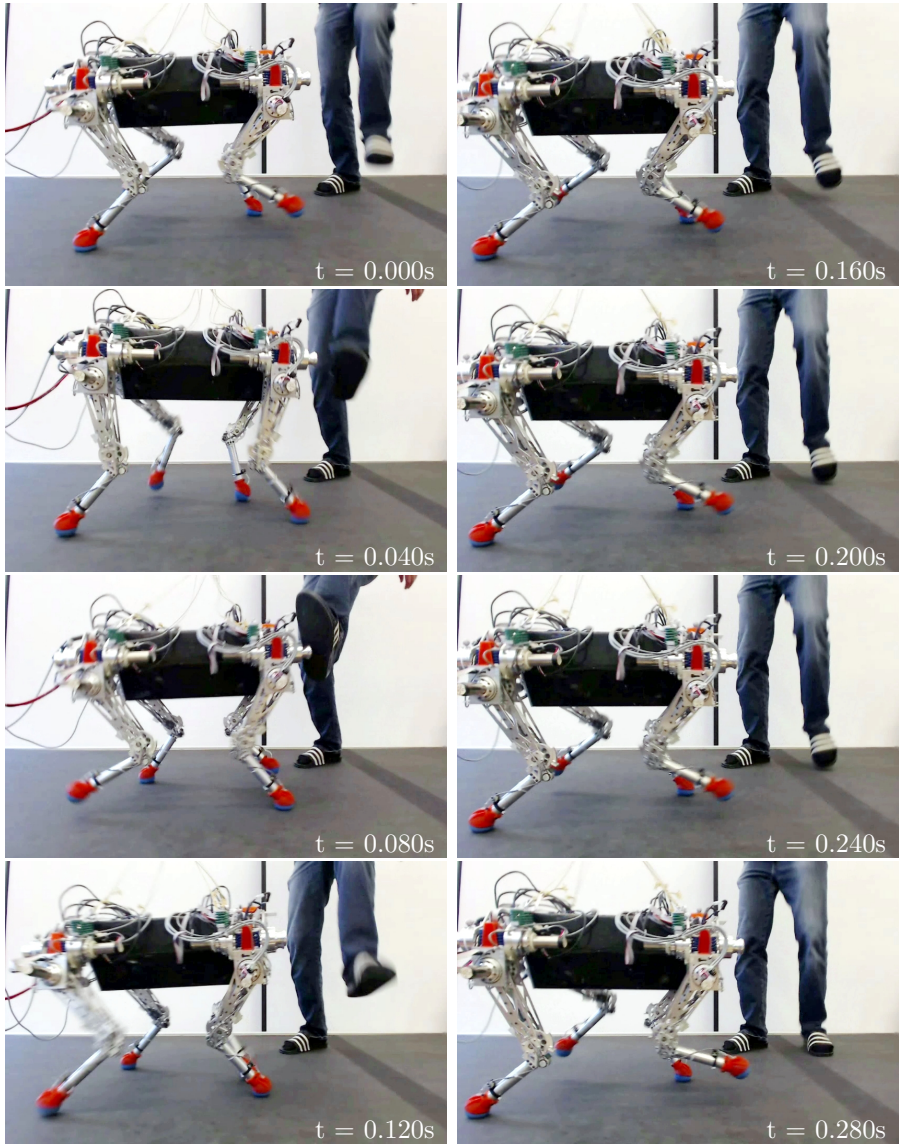


Figure 8.13: *Exp 16:* StarLETH compensates for external disturbances such as a kick while trotting by stepping sideward and generating a net counterforce.

to stabilize the robot on its nominal walking gait is $COT_{\text{mech}} = 0.28$. On the other hand, we notice that the efficiency of energy conversion from electric power in the batteries to what is actually used in the joints is as low as about 10%. This is reasonable as already the maximal possible efficiency is not more than 63%, which is determined by multiplying the values given by the manufacturer for the motor controller ($\eta_{EPOS} = 94\%$), motor ($\eta_{\text{mot}} = 90\%$), and gearbox ($\eta_{HD} = 75\%$). All components, but in particular motor and gearbox, have a significantly lower efficiency while walking due to the quickly alternating load direction in every joint.

8.5 Summary

This chapter demonstrated static and dynamic locomotion capabilities of *StarLETH* using the hierarchical task-space inverse dynamics control framework presented in Chapter 5. Starting with a series of performance evaluation tests, we highlighted power and robustness of the developed quadrupedal platform. This was followed by static walking maneuvers. Thereby, the robot benefits from multi-contact interaction which allows to optimize actuator efficiency, to reduce the risk of slipping even when walking in uneven terrain, and to achieve smooth contact transitions. We demonstrated methods to cope with torque and position saturation and evaluated the advantage of a hybrid control setup. Results on fast and robust dynamic trotting gaits under significant external disturbances finally represent the culmination of the present dissertation. For illustration we refer to the video material listed in Section 1.4.

Chapter 9

Discussion and Conclusion

This dissertation started with the vision to develop a dog-sized quadrupedal robot that achieves locomotion capabilities similar to its natural counterparts. Inspired by nature and driven by the continuous progress in system engineering, we built and controlled a legged system that is capable of performing different gaits from slow climbing to fast running. It was our clear mission not to focus on reproducing single theoretical findings but to come up with a robotic system that combines *versatility*, *speed*, *efficiency*, and *robustness* in one single device. Closing the gap between the machines we develop and the natural counterparts requires solutions that are advanced with respect to all of these properties.

9.1 Discussion of Contributions

Referring back to Figure 1.6, it is necessary to tackle a wide spectrum of problems that encompasses *system engineering*, *actuation design*, and *control development* for achieving our goal. More importantly, these topics should not be investigated independently but must be considered as tightly coupled.

9.1.1 Compliant Design

Inspired by nature where elastic elements in muscles and tendons largely contribute to an efficient running motion, our quadrupedal robot Star $LETH$ was designed based on highly compliant series elastic actuators. Mechanical springs in all joints protect the system and its environment from impact loads as they occur in dynamic maneuvers. After three years of operation of the single leg and 1.5 years of nearly daily use of Star $LETH$, the concept has

proven to be *extremely robust*. A failure occurred neither in the motor or gearbox, nor in the mechanical structure of the system. Only the predefined breaking part in the chain had to be exchanged few times after unexpected overload cases. The springs further hold as an intermittent energy storage device. After landing, kinetic energy of the system is used to load the spring and release it again before lift-off. This can be beneficial to achieve *high energetic efficiency* in legged locomotion. To highlight this aspect, we found in hopping experiments that our actuators can passively redirect about 64% of the energy required while only the remaining 36% are actively provided by the motor to compensate for damping and impact losses. Moreover, we could show that the series elasticity leads to a peak power and peak output speed amplification of more than a factor four. From a design point of view, this allows to reduce the motor size and hence to lower the weight of the system in comparison to a robot with stiff actuation. For an optimal exploitation of the internal dynamics it is crucial to design the series compliance as a function of its application. This is a paragon indicating that actuation and system design are tightly coupled and SEA development without integration in a robot is of marginal interest.

9.1.2 SEA Control

As the most important feature, the series compliance in the actuator holds as a torque sensor and hence gives the system precise joint torque controllability. We realized a cascaded control structure with an inner motor velocity and current loop that compensate for gearbox frictional effects. The closed loop actuator is stable and passive. With an identified control bandwidth up to 28 Hz, the tracking performance is comparable with state of the art research. In addition, a disturbance compensator based on joint encoder measurements improves the sensitivity of the closed loop system and significantly lowers the output impedance. As a drawback of SEAs, the compliant design introduces undesired oscillations during swing phase which reduce position control performance. We successfully tackled this problem by applying two complementary approaches. First, an augmented mechanical design with additional damper elements suppresses the oscillations in the knee joint without impairing torque control performance. Second, for both hip joints, an LQR joint position controller based on joint and motor sensor measurements replaces the outer torque control loop to actively damp out the natural oscillations. Precise torque and position controllability are the basic element for a sophisticated locomotion control strategy.

9.1.3 Model-Based Locomotion Control

Inspired by work on prioritized task-space control and kinematics-based inverse dynamics methods for floating base systems, we combined advantages of these techniques in a hierarchical least square optimization framework. Tasks defining the motion of the robot can be combined with tasks to optimize the joint torque or contact force distribution. This allows for an intuitive description of complex and *versatile* robot behaviors. At the same time, the framework avoids inversion of dynamic model properties whenever possible to improve robustness against modeling and numerical errors. All proposed control strategies were tested in simulations and, without modification, validated in real hardware experiments ranging from standing over static walking to dynamic trotting. Thanks to the full torque controllability of Starl*ETH*, pure task-space inverse dynamics control could be used without any (low-gain) joint position stabilization. In static gaits we mainly optimized the torque and force distribution that allows to increase energetic efficiency and that enables walking on terrain where the robot has to apply internal contact forces to guarantee no contact slippage. We additionally presented methods to include inequality tasks as required to deal with torque or position limitations. Towards highly dynamic locomotion, we presented results of trotting gaits whereby the controller has to balance a *truly-underactuated* robot even under significant external disturbances such as unperceived ground elevation or external pushes.

9.2 Comparison to Biology

The importance of mechanical compliance in human and animal locomotion is unquestionable (Alexander, 1990). However, biomechanical researchers are still working towards fully understanding the underlying principles and a complete transfer of this knowledge to robotic devices is still a long way to go. The results presented in this thesis contribute to the ongoing progress in closing the gap between legged machines and the natural counterparts. On a high level, it was shown that our actuators can mechanically redirect the energy of the system by compressing and releasing the series elasticity. The achieved energetic efficiency is well comparable to values documented for human and animal locomotion (e.g. Alexander, 1988; Farley et al., 1993; Ker et al., 1987; Lichtwark and Wilson, 2005). Roberts (2002) analyzed the mechanical role of tendon and muscle contractile elements during locomotion. He simulated the muscular tendon system in steady state running and found that passive compliant elements largely contribute to the power development.

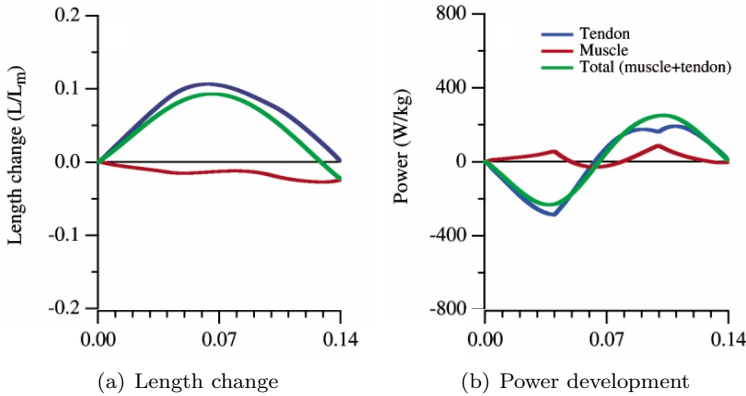


Figure 9.1: (Roberts, 2002) simulated muscle contraction during steady-speed running. The dynamics of the muscle contractile element (red), tendon (blue), and combined muscle-tendon unit (green) were monitored for a single simulated contraction. During the steady-speed simulation, energy changes of the body were stored and recovered in the tendon and little muscle power was developed.

Most of the energy change of the body was stored and recovered in the tendon, and the power profile of the tendon closely matched that of the body. The muscle produced force, but underwent little length change (Figure 9.1(a)) and therefore developed little mechanical power (Figure 9.1(b)). Comparing these results to our findings depicted in Figure 7.3 shows an astonishing level of agreement between the muscular-tendon system in nature and the highly compliant SEAs of Star $LETH$, not only in shape of position and power curves, but also in relative magnitude.

Star $LETH$ was operated in a trotting gait (average speed 0.43 m/s) at an average power of 296 W or overall COT of 2.57 (see Section 8.4.4). A similar sized dog (*canis familiaris*, 18 kg) requires for the same locomotion speed a metabolic COT of 0.73 (Taylor et al., 1970). At a first glance, this seems to be an extreme difference. However, considering that motors produce an average mechanical power of about 32 W (COT=0.32), there is large potential to optimize the electronic equipment. Ongoing progress in this field can potentially fully close this discrepancy with respect to efficiency.

Comparing individual components of the robot to humans or animal unveils more interesting aspects. For example, pure actuator performance of the robot in terms of power and torque was already superior more than 20 years ago (Hollerbach et al., 1991; Hunter and Lafontaine, 1992). The same holds

for control bandwidth that is with about 5 Hz for reflexes and less than 1 Hz for visual feedback (Fitzpatrick et al., 1992) considerably lower than what we achieve with our machines. Despite these discrete advantages, animals still largely outperform our robots and we have to continue jointly improving our *system design*, *actuation*, and *control* competence before our robots can compete with nature.

9.3 Future Work

The concept of system design, actuation, and control realized in Star $LETH$ opens a big variety of fields for future research. With a platform that can locomote virtually anywhere, the connection is made to a huge community working on navigation and planning. We recently started integrating these capabilities on our robotic device. With cameras to perceive the environment, advanced gait planning algorithms will be developed that allow conquering difficult obstacles or performing useful tasks in areas that are hardly accessible with traditional means of transportation. As Star $LETH$ is easy to handle and requires nearly no maintenance, we plan to provide it to other research laboratories that do not have access to such elaborated devices.

We are currently launching a larger research project with partners at IIT that have been working on quadrupedal systems as well (Semini et al., 2011). We jointly envision to bring these robots out of our lab environment and make them perform useful tasks that involve contact point planning and dynamic motion execution. This is a possibility to deploy Star $LETH$ and to directly apply the presented control techniques in more challenging tasks.

Observing ongoing robotics research, we identified a trend towards applying machines in dynamic environment and make them work hand in hand with human operators. This cries out for compliant mechanical designs and control to increase safety for the robot and its environment. As a contribution in this direction, we started industrial collaborations to spread out our technological findings in the field of SEAs. We are convinced that there are a large number of possible applications waiting for such solutions.

Since more than two years, our group is heavily involved in a long-term, nation-wide project, launched by the Swiss National Science Foundation, with the common objective of developing new, human-oriented robotic technology for improving our quality of life. We are contributing in a research and rescue scenario that envisions collaborative tasks with small-scale drones which deliver topological information of the surrounding to support path planning and locomotion capabilities of legged systems. We strongly believe that the rescue dog for the future will be robotic.

Appendix A

Appendix

A.1 Global Optimality for a Hierarchical Least Square Optimization

Theorem 4. *Let $f_i(\mathbf{x}) := \|\mathbf{A}_i \mathbf{x} - \mathbf{b}_i\|_2$ denote the objective function of each task indexed by i and $\mathbf{x} \in \mathbb{R}^n$ be constructed sequentially via (5.10) and (5.13).*

Then \mathbf{x} is globally optimal in the following sense:

There is no other $\tilde{\mathbf{x}}$ that fulfills a task i better than \mathbf{x} in a least square sense, while doing the higher priority ones as good as \mathbf{x} i.e.:

$$\neg \exists \tilde{\mathbf{x}} \in \mathbb{R}^n, 1 \leq i \leq n_T : \underbrace{f_i(\tilde{\mathbf{x}}) < f_i(\mathbf{x}) \wedge \forall 1 \leq k < i : f_k(\tilde{\mathbf{x}}) = f_k(\mathbf{x})}_{\Leftrightarrow: \tilde{\mathbf{x}} \prec_i \mathbf{x}}$$

Note that this implies that if a task i can be exactly fulfilled, while equally good fulfilling the higher priority tasks, (i.e. there is a $\tilde{\mathbf{x}} \preceq_i \mathbf{x}$, such that $\mathbf{A}_i \tilde{\mathbf{x}} = \mathbf{b}_i \Rightarrow f_i(\tilde{\mathbf{x}}) = 0$) the constructed \mathbf{x} will do so too because otherwise it would hold $f_i(\mathbf{x}) > 0$ and thus $\tilde{\mathbf{x}} \prec_i \mathbf{x}$.

Proof. Let $\mathcal{X}_{\text{better}} := \{(\tilde{\mathbf{x}}, i) \in \mathbb{R}^n \times \{1..n_T\} : \tilde{\mathbf{x}} \prec_i \mathbf{x}\}$ be the set of all the $\tilde{\mathbf{x}}$ better than \mathbf{x} paired with the task's index, starting at which they are better than \mathbf{x} . The statement can now be written as $\mathcal{X}_{\text{better}} = \emptyset$.

Assume the opposite: $\mathcal{X}_{\text{better}} \neq \emptyset$

Let $(\tilde{\mathbf{x}}, i) \in \mathcal{X}_{\text{better}}$ be minimal (not necessarily uniquely) in $\mathcal{X}_{\text{better}}$ with respect to i .

We now distinguish two cases for i and infer for both contradictions.

(a) $i = 1$ is contradictory:

It holds $f_1(\mathbf{x}) = f_1(\mathbf{x}_1)$ by (5.14), as it states $\mathbf{A}_1 \mathbf{x} - \mathbf{b}_1 = \mathbf{A}_1 \mathbf{N}_1 \mathbf{x}_1 - \mathbf{b}_1$ and $\mathbf{N}_1 = \mathbf{I}$.

So in this case we have $f_1(\tilde{\mathbf{x}}) < f_1(\mathbf{x}) = f_1(\mathbf{x}_1)$. But this is impossible because $\mathbf{x}_1 = \mathbf{A}_1^+ \mathbf{b}_1$ by construction (5.13) and thereby the Moore-Penrose pseudoinverse guaranties \mathbf{x}_1 to minimize just $f_1(\mathbf{x}') = \|\mathbf{A}_1 \mathbf{x}' - \mathbf{b}_1\|_2$.

(b) $i > 1$ is contradictory:

Let firstly $\hat{\mathbf{x}}_j := \sum_{k=1}^j \mathbf{N}_k \mathbf{x}_k$ denote the solution constructed for the tasks up to a given task index j and

$\mathcal{B}_i := \{\mathbf{x}' \in \mathbb{R}^n \mid \forall 1 \leq k < i : \mathbf{A}_k \mathbf{x}' = \mathbf{A}_k \hat{\mathbf{x}}_{i-1}\}$.

(i) $\tilde{\mathbf{x}} \in \mathcal{B}_i$:

It is enough to show $\forall 1 \leq k < i : \mathbf{A}_k \tilde{\mathbf{x}} = \mathbf{A}_k \mathbf{x}$ because $\mathbf{A}_k \mathbf{x} = \mathbf{A}_k \hat{\mathbf{x}}_{i-1}$ by (5.14).

Assume the opposite and let $k < i$ be minimal with $\mathbf{A}_k \tilde{\mathbf{x}} \neq \mathbf{A}_k \mathbf{x}$ and $\bar{\mathbf{x}} := \frac{1}{2}(\tilde{\mathbf{x}} + \mathbf{x})$.

The new $\bar{\mathbf{x}}$ does not change any higher priority task, because for any $j < k$ we have $\mathbf{A}_j \bar{\mathbf{x}} = \frac{1}{2}(\mathbf{A}_j \tilde{\mathbf{x}} + \mathbf{A}_j \mathbf{x}) = \mathbf{A}_j \mathbf{x}$ because $\mathbf{A}_j \tilde{\mathbf{x}} = \mathbf{A}_j \mathbf{x}$, which implies $f_j(\bar{\mathbf{x}}) = f_j(\mathbf{x})$.

But $\bar{\mathbf{x}}$ outperforms $\tilde{\mathbf{x}}$ and \mathbf{x} in task k :

$$\begin{aligned} f_k^2(\bar{\mathbf{x}}) &= \left(\frac{1}{2}(\mathbf{A}_k \tilde{\mathbf{x}} + \mathbf{A}_k \mathbf{x}) - \mathbf{b}_k\right)^2 \\ &= \frac{1}{4} \left(\underbrace{(\mathbf{A}_k \tilde{\mathbf{x}} - \mathbf{b}_k)}_{=: \tilde{\mathbf{v}}} + \underbrace{(\mathbf{A}_k \mathbf{x} - \mathbf{b}_k)}_{=: \mathbf{v}} \right)^2 \\ &= \frac{1}{4} (\tilde{\mathbf{v}}^2 + \mathbf{v}^2 + 2\tilde{\mathbf{v}}^T \mathbf{v}) < f_k^2(\mathbf{x}) \end{aligned}$$

because $\mathbf{A}_k \tilde{\mathbf{x}} \neq \mathbf{A}_k \mathbf{x} \Rightarrow \tilde{\mathbf{v}} \neq \mathbf{v}$ and $\|\tilde{\mathbf{v}}\|_2 = f_k(\tilde{\mathbf{x}}) = f_k(\mathbf{x}) = \|\mathbf{v}\|_2$, which together imply that $\tilde{\mathbf{v}}^T \mathbf{v} < \|\tilde{\mathbf{v}}\|_2 \|\mathbf{v}\|_2 = f_k^2(\mathbf{x})$ (application of the Cauchy-Schwarz inequality theorem).

Both observations together imply: $\bar{\mathbf{x}} \prec_k \mathbf{x}$ and with that $(\bar{\mathbf{x}}, k) \in \mathcal{X}_{\text{better}}$, which contradicts the minimality in the second component of $(\tilde{\mathbf{x}}, i) \in \mathcal{X}_{\text{better}}$ as $k < i$.

(ii) $f_i(\mathbf{x}) = \min_{\mathbf{x}' \in \mathcal{B}_i} f_i(\mathbf{x}')$:

By construction (5.13) and Moore-Penrose pseudoinverse properties we have:

$$\begin{aligned} \mathbf{x}_i \in \operatorname{argmin}_{\mathbf{v} \in \mathbb{R}^n} \|\mathbf{A}_i \mathbf{N}_i \mathbf{v} - \mathbf{b}_i + \mathbf{A}_i \hat{\mathbf{x}}_{i-1}\|_2 \\ &= \operatorname{argmin}_{\mathbf{v} \in \mathbb{R}^n} \|\mathbf{A}_i (\mathbf{N}_i \mathbf{v} + \hat{\mathbf{x}}_{i-1}) - \mathbf{b}_i\|_2 \\ &= \operatorname{argmin}_{\mathbf{v} \in \mathbb{R}^n} f_i(\mathbf{N}_i \mathbf{v} + \hat{\mathbf{x}}_{i-1}) \end{aligned}$$

and thus

$$\begin{aligned} f_i(\mathbf{N}_i \mathbf{x}_i + \hat{\mathbf{x}}_{i-1}) &= \min_{\mathbf{v} \in \mathbb{R}^n} f_i(\mathbf{N}_i \mathbf{v} + \hat{\mathbf{x}}_{i-1}) \\ &= \min_{\mathbf{x}' \in \{\mathbf{N}_i \mathbf{v} + \hat{\mathbf{x}}_{i-1} \mid \mathbf{v} \in \mathbb{R}^n\}} f_i(\mathbf{x}') \\ &= \min_{\mathbf{x}' \in \mathcal{B}_i} f_i(\mathbf{x}'). \end{aligned}$$

because $\{\mathbf{N}_i \mathbf{v} + \hat{\mathbf{x}}_{i-1} \mid \mathbf{v} \in \mathbb{R}^n\} = \{\mathbf{x}' \in \mathbb{R}^n \mid \forall 1 \leq k < i : \mathbf{A}_k(\mathbf{x}' - \hat{\mathbf{x}}_{i-1}) = 0\} = \mathcal{B}_i$ (per definition of \mathcal{B}_i). Together with $\mathbf{N}_i \mathbf{x}_i + \hat{\mathbf{x}}_{i-1} = \hat{\mathbf{x}}_i$ and $f_i(\hat{\mathbf{x}}_i) = f_i(\mathbf{x})$ (s. (5.14)) it follows the theses $f_i(\mathbf{x}) = \min_{\mathbf{x}' \in \mathcal{B}_i} f_i(\mathbf{x}')$.

Putting it all together we have inferred the following contradiction for case b):

$$f_i(\tilde{\mathbf{x}}) \underset{\tilde{\mathbf{x}} \prec_i \mathbf{x}}{<} f_i(\mathbf{x}) \stackrel{(ii)}{=} \min_{\mathbf{x}' \in \mathcal{B}_i} f_i(\mathbf{x}') \underset{(i)}{\leq} f_i(\tilde{\mathbf{x}})$$

Having led all possibilities for i to a contradiction we can finally conclude: the assumption of a non-empty $\mathcal{X}_{\text{better}}$ was wrong. \square

A.2 Block Matrix Pseudo-Inversion

The pseudo inverse for a block matrix $\mathbf{X}^+ = \mathbf{X}^T (\mathbf{X}\mathbf{X}^T)^{-1}$ with $\mathbf{C} = \mathbf{0}$ and \mathbf{D} invertible is

$$\begin{bmatrix} \mathbf{A} & \mathbf{B} \\ \mathbf{0} & \mathbf{D} \end{bmatrix}^+ = \begin{bmatrix} \mathbf{A}^+ & -\mathbf{A}^+\mathbf{B}\mathbf{D}^{-1} \\ \mathbf{0} & \mathbf{D}^{-1} \end{bmatrix}. \quad (\text{A.1})$$

Proof. The inverse of a block matrix with \mathbf{E}, \mathbf{H} invertible is calculated as

$$\begin{bmatrix} \mathbf{E} & \mathbf{F} \\ \mathbf{G} & \mathbf{H} \end{bmatrix}^{-1} = \begin{bmatrix} (\mathbf{E} - \mathbf{F}\mathbf{H}^{-1}\mathbf{G})^{-1} & -\mathbf{E}^{-1}\mathbf{F}(\mathbf{H} - \mathbf{G}\mathbf{E}^{-1}\mathbf{F})^{-1} \\ -\mathbf{H}^{-1}\mathbf{G}(\mathbf{E} - \mathbf{F}\mathbf{H}^{-1}\mathbf{G})^{-1} & (\mathbf{H} - \mathbf{G}\mathbf{E}^{-1}\mathbf{F})^{-1} \end{bmatrix} \quad (\text{A.2})$$

$$= \begin{bmatrix} (\mathbf{E} - \mathbf{F}\mathbf{H}^{-1}\mathbf{G})^{-1} & -(\mathbf{E} - \mathbf{F}\mathbf{H}^{-1}\mathbf{G})^{-1}\mathbf{F}\mathbf{H}^{-1} \\ -\mathbf{H}^{-1}\mathbf{G}(\mathbf{E} - \mathbf{F}\mathbf{H}^{-1}\mathbf{G})^{-1} & (\mathbf{H} - \mathbf{G}\mathbf{E}^{-1}\mathbf{F})^{-1} \end{bmatrix}. \quad (\text{A.3})$$

Applying this to the pseudo inversion of the block matrix results in:

$$\begin{aligned} \begin{bmatrix} \mathbf{A} & \mathbf{B} \\ \mathbf{0} & \mathbf{D} \end{bmatrix}^+ &= \begin{bmatrix} \mathbf{A} & \mathbf{B} \\ \mathbf{0} & \mathbf{D} \end{bmatrix}^T \left(\begin{bmatrix} \mathbf{A} & \mathbf{B} \\ \mathbf{0} & \mathbf{D} \end{bmatrix} \begin{bmatrix} \mathbf{A} & \mathbf{B} \\ \mathbf{0} & \mathbf{D} \end{bmatrix}^T \right)^{-1} \\ &= \begin{bmatrix} \mathbf{A} & \mathbf{B} \\ \mathbf{0} & \mathbf{D} \end{bmatrix}^T \begin{bmatrix} \mathbf{A}\mathbf{A}^T + \mathbf{B}\mathbf{B}^T & \mathbf{B}\mathbf{D}^T \\ \mathbf{D}\mathbf{B}^T & \mathbf{D}\mathbf{D}^T \end{bmatrix}^{-1} \\ &= \begin{bmatrix} \mathbf{A}^T & \mathbf{0} \\ \mathbf{B}^T & \mathbf{D}^T \end{bmatrix} \begin{bmatrix} \mathbf{m}_{11} & \mathbf{m}_{12} \\ \mathbf{m}_{21} & \mathbf{m}_{22} \end{bmatrix} \quad (\text{A.4}) \end{aligned}$$

$$= \begin{bmatrix} \mathbf{A}^T \mathbf{m}_{11} & \mathbf{A}^T \mathbf{m}_{12} \\ \mathbf{B}^T \mathbf{m}_{11} + \mathbf{D}^T \mathbf{m}_{21} & \mathbf{B}^T \mathbf{m}_{12} + \mathbf{D}^T \mathbf{m}_{22} \end{bmatrix} \quad (\text{A.5})$$

with \mathbf{m}_i being the elements of the inverted matrix $(\mathbf{X}\mathbf{X}^T)^{-1}$

$$\mathbf{m}_{11} = \left(\mathbf{A}\mathbf{A}^T + \mathbf{B}\mathbf{B}^T - \mathbf{B}\mathbf{D}^T (\mathbf{D}\mathbf{D}^T)^{-1} \mathbf{D}\mathbf{B}^T \right)^{-1} = (\mathbf{A}\mathbf{A}^T)^{-1} \quad (\text{A.6})$$

$$\begin{aligned} \mathbf{m}_{12} &\stackrel{(\text{A.2})}{=} - \left(\mathbf{A}\mathbf{A}^T + \mathbf{B}\mathbf{B}^T - \mathbf{B}\mathbf{D}^T (\mathbf{D}\mathbf{D}^T)^{-1} \mathbf{D}\mathbf{B}^T \right)^{-1} \mathbf{B}\mathbf{D}^T (\mathbf{D}\mathbf{D}^T)^{-1} \\ &= - (\mathbf{A}\mathbf{A}^T)^{-1} \mathbf{B}\mathbf{D}^{-1} \end{aligned} \quad (\text{A.7})$$

$$\begin{aligned} &\stackrel{(\text{A.3})}{=} - (\mathbf{A}\mathbf{A}^T + \mathbf{B}\mathbf{B}^T)^{-1} \mathbf{B}\mathbf{D}^T \left(\mathbf{D}\mathbf{D}^T - \mathbf{D}\mathbf{B}^T (\mathbf{A}\mathbf{A}^T + \mathbf{B}\mathbf{B}^T)^{-1} \mathbf{B}\mathbf{D}^{-T} \right)^{-1} \\ &= - (\mathbf{A}\mathbf{A}^T + \mathbf{B}\mathbf{B}^T)^{-1} \mathbf{B}\mathbf{D}^T \mathbf{m}_{22} \end{aligned} \quad (\text{A.8})$$

$$\begin{aligned} \mathbf{m}_{21} &= - (\mathbf{D}\mathbf{D}^T)^{-1} \mathbf{D}\mathbf{B}^T \left(\mathbf{A}\mathbf{A}^T + \mathbf{B}\mathbf{B}^T - \mathbf{B}\mathbf{D}^T (\mathbf{D}\mathbf{D}^T)^{-1} \mathbf{D}\mathbf{B}^T \right)^{-1} \\ &= - (\mathbf{D}\mathbf{D}^T)^{-1} \mathbf{D}\mathbf{B}^T (\mathbf{A}\mathbf{A}^T)^{-1} \end{aligned} \quad (\text{A.9})$$

$$\mathbf{m}_{22} = \left(\mathbf{D}\mathbf{D}^T - \mathbf{D}\mathbf{B}^T (\mathbf{A}\mathbf{A}^T + \mathbf{B}\mathbf{B}^T)^{-1} \mathbf{B}\mathbf{D}^T \right)^{-1} \quad (\text{A.10})$$

and the pre-multiplied matrix transposed

$$\mathbf{A}^T \mathbf{m}_{11} = \mathbf{A}^+ \quad (\text{A.11})$$

$$\mathbf{A}^T \mathbf{m}_{12} \stackrel{(\text{A.7})}{=} -\mathbf{A}^+ \mathbf{B}\mathbf{D}^{-1} \quad (\text{A.12})$$

$$\mathbf{B}^T \mathbf{m}_{11} + \mathbf{D}^T \mathbf{m}_{21} = \mathbf{0} \quad \text{since} \quad \mathbf{D}^T (\mathbf{D}\mathbf{D}^T)^{-1} \mathbf{D} = \mathbf{I} \quad (\text{A.13})$$

$$\begin{aligned} \mathbf{B}^T \mathbf{m}_{12} + \mathbf{D}^T \mathbf{m}_{22} &\stackrel{(\text{A.8})}{=} \left(-\mathbf{B}^T (\mathbf{A}\mathbf{A}^T + \mathbf{B}\mathbf{B}^T)^{-1} \mathbf{B}\mathbf{D}^T + \mathbf{D}^T \right) \mathbf{m}_{22} \\ &= \mathbf{D}^{-1} \mathbf{D} \left(-\mathbf{B}^T (\mathbf{A}\mathbf{A}^T + \mathbf{B}\mathbf{B}^T)^{-1} \mathbf{B}\mathbf{D}^T + \mathbf{D}^T \right) \mathbf{m}_{22} \\ &= \mathbf{D}^{-1} \mathbf{m}_{22}^{-1} \mathbf{m}_{22} = \mathbf{D}^{-1} \end{aligned} \quad (\text{A.14})$$

□

A.3 Kinetic Energy Loss

The kinetic energy loss can be written either as a function of the change in generalized velocities $\Delta\dot{\mathbf{q}}$ in combination with the generalized mass matrix \mathbf{M} or as a function of the pre-impact velocity of the contact point $\dot{\mathbf{r}}_s^-$ and the foot point inertia $\Lambda_s = (\mathbf{J}_s \mathbf{M}^{-1} \mathbf{J}_s^T)^{-1}$

$$\Delta E_{kin} = -\frac{1}{2} \Delta\dot{\mathbf{q}}^T \mathbf{M} \Delta\dot{\mathbf{q}} \quad (\text{A.15})$$

$$= -\frac{1}{2} \dot{\mathbf{r}}_s^{-T} \Lambda_s \dot{\mathbf{r}}_s^- \quad (\text{A.16})$$

Proof. To make the proof compact, we use the well-established formalism introduced by Khatib (1987) and used by Sentis (2007). This defines the *dynamically consistent generalized inverse of the support Jacobian* as

$$\bar{\mathbf{J}}_s = \mathbf{M}^{-1} \mathbf{J}_s^T \Lambda_s. \quad (\text{A.17})$$

$$\begin{aligned} \Delta E_{kin} &= \frac{1}{2} \dot{\mathbf{q}}^{+T} \mathbf{M} \dot{\mathbf{q}}^+ - \frac{1}{2} \dot{\mathbf{q}}^{-T} \mathbf{M} \dot{\mathbf{q}}^- \\ &= \frac{1}{2} (\dot{\mathbf{q}}^+ + \dot{\mathbf{q}}^-) \mathbf{M} (\dot{\mathbf{q}}^+ - \dot{\mathbf{q}}^-) \\ \dot{\mathbf{q}}^+ &\stackrel{\text{def}}{=} \dot{\mathbf{q}}^- + \Delta\dot{\mathbf{q}} && \frac{1}{2} (\Delta\dot{\mathbf{q}} + 2\dot{\mathbf{q}}^-) \mathbf{M} \Delta\dot{\mathbf{q}} \\ \Delta\dot{\mathbf{q}} &\stackrel{\text{def}}{=} -\bar{\mathbf{J}}_s \mathbf{J}_s \dot{\mathbf{q}}^- && -\dot{\mathbf{q}}^{-T} \mathbf{M} \bar{\mathbf{J}}_s \mathbf{J}_s \dot{\mathbf{q}}^- + \frac{1}{2} \Delta\dot{\mathbf{q}}^T \mathbf{M} \Delta\dot{\mathbf{q}} \\ \mathbf{J}_s \bar{\mathbf{J}}_s &\stackrel{\text{def}}{=} \mathbf{I} && -\dot{\mathbf{q}}^{-T} \mathbf{M} \bar{\mathbf{J}}_s \mathbf{J}_s \bar{\mathbf{J}}_s \mathbf{J}_s \dot{\mathbf{q}}^- + \frac{1}{2} \Delta\dot{\mathbf{q}}^T \mathbf{M} \Delta\dot{\mathbf{q}} \\ \mathbf{M} \bar{\mathbf{J}}_s \mathbf{J}_s &\stackrel{\text{def}}{=} (\bar{\mathbf{J}}_s \mathbf{J}_s)^T \mathbf{M} && -\dot{\mathbf{q}}^{-T} (\bar{\mathbf{J}}_s \mathbf{J}_s)^T \mathbf{M} \bar{\mathbf{J}}_s \mathbf{J}_s \dot{\mathbf{q}}^- + \frac{1}{2} \Delta\dot{\mathbf{q}}^T \mathbf{M} \Delta\dot{\mathbf{q}} \\ \Delta E_{kin}^q &\stackrel{\text{def}}{=} \bar{\mathbf{J}}_s \mathbf{J}_s \dot{\mathbf{q}}^- = \Delta\dot{\mathbf{q}} && -\frac{1}{2} \Delta\dot{\mathbf{q}}^T \mathbf{M} \Delta\dot{\mathbf{q}} \quad (\text{A.18}) \end{aligned}$$

$$\begin{aligned} \Delta\dot{\mathbf{q}} &\stackrel{\text{def}}{=} \mathbf{M}^{-1} \mathbf{J}_s \Lambda_s \Delta\dot{\mathbf{r}}_s && -\frac{1}{2} \Delta\dot{\mathbf{r}}_s^T \Lambda_s \underbrace{\mathbf{J}_s \mathbf{M}^{-1} \mathbf{M} \mathbf{M}^{-1} \mathbf{J}_s^T}_{\Lambda_s^{-1}} \Lambda_s \Delta\dot{\mathbf{r}}_s \end{aligned}$$

$$= -\frac{1}{2} \Delta\dot{\mathbf{r}}_s^T \Lambda_s \Delta\dot{\mathbf{r}}_s \quad (\text{A.19})$$

$$\Delta E_{kin}^x = \frac{1}{2} \dot{\mathbf{r}}_s^{-T} \Lambda_s \dot{\mathbf{r}}_s^- \quad (\text{A.20})$$

□

A.4 Null-Space Calculation using SVD

The null-space projection operator

$$\mathbf{N}_{A'} = \mathcal{N}(\mathbf{A}') \quad (\text{A.21})$$

can be calculated by the *singular value decomposition* (SVD) method (Golub and Loan, 1996). Given that the matrix \mathbf{A}' has rank r , we can write

$$\mathbf{A}' = [\mathbf{U}_1 \quad \mathbf{U}_2] \begin{bmatrix} \mathbf{\Sigma} & \mathbf{0} \\ \mathbf{0} & \mathbf{0} \end{bmatrix} \begin{bmatrix} \mathbf{V}_1^T \\ \mathbf{V}_2^T \end{bmatrix}, \quad (\text{A.22})$$

where $\mathbf{\Sigma} = \text{diag}(\sigma_1, \dots, \sigma_r)$ with $\sigma_i > 0 \quad \forall i$ and the null-space projector is given by

$$\mathbf{N}_{A'} = \mathbf{V}_2^T \quad (\text{A.23})$$

A.5 Relation to Prioritized OSC

Operational space control was introduced by Khatib (1987) and later augmented to floating base systems by Sentis (2007). This class of controllers corresponds to a general projector with

$$\mathbf{P}_{OSC} = \mathbf{S}\mathbf{N}_s\mathbf{M}^{-1}. \quad (\text{A.24})$$

Proof. Sentis and Khatib prescribe a hierarchical, support consistent framework to generate the desired joint torques

$$\boldsymbol{\tau} = \sum_{k=1}^{n_T} \mathbf{J}_{k|prec(k)}^{*T} \mathbf{F}_{k|prec(k)}, \quad (\text{A.25})$$

as a function of prioritized Jacobians

$$\mathbf{J}_{k|prec(k)}^* = \mathbf{J}_k \overline{\mathbf{S}\mathbf{N}_s} \mathbf{N}_{prec(k)}^*, \quad (\text{A.26})$$

and the operational space forces

$$\mathbf{F}_{k|prec(k)} = \boldsymbol{\Lambda}_{k|prec(k)}^* \ddot{\mathbf{r}}_k + \mathbf{h}_{k|prec(k)}^* - \boldsymbol{\Lambda}_{k|prec(k)}^* \mathbf{J}_k \mathbf{M}^{-1} (\mathbf{S}\mathbf{N}_s)^T \sum_{i=1}^{k-1} \boldsymbol{\tau}_{i|prec(i)}. \quad (\text{A.27})$$

Each of the n_T task of different priority is defined by a task Jacobian \mathbf{J}_k and a desired task-space acceleration $\ddot{\mathbf{r}}_k$. The prioritized task inertia $\boldsymbol{\Lambda}_{k|prec(k)}^*$ and differentiable force vector $\mathbf{h}_{k|prec(k)}^*$ are calculated by

$$\begin{aligned} \boldsymbol{\Lambda}_{k|prec(k)}^* &= \left(\mathbf{J}_k \mathbf{M}^{-1} (\mathbf{S}\mathbf{N}_s)^T \mathbf{J}_{k|prec(k)}^* \right)^{-1}, \quad (\text{A.28}) \\ \mathbf{h}_{k|prec(k)}^* &= \boldsymbol{\Lambda}_{k|prec(k)}^* \mathbf{J}_k \mathbf{M}^{-1} \mathbf{N}_s^T \mathbf{h} - \\ &\quad \boldsymbol{\Lambda}_{k|prec(k)}^* \dot{\mathbf{J}}_k \dot{\mathbf{q}} + \boldsymbol{\Lambda}_{k|prec(k)}^* \mathbf{J}_k \mathbf{M}^{-1} \mathbf{J}_s^T \boldsymbol{\Lambda}_s \dot{\mathbf{J}}_s \dot{\mathbf{q}}. \quad (\text{A.29}) \end{aligned}$$

For a detailed reference and explanation of the notation, the interested reader is referred to (Sentis, 2007). In inverse dynamics, we deal with a single task $n_T = 1$ to control the desired joint acceleration $\ddot{\mathbf{r}}_d = \ddot{\mathbf{q}}_d$. Hence, the task Jacobian is

$$\mathbf{J}_1 = \mathbf{I} \quad (\text{A.30})$$

$$\dot{\mathbf{J}}_1 = \mathbf{0}. \quad (\text{A.31})$$

Knowing that the first prioritized null-space projector $\mathbf{N}_{prec(1)}^* = \mathbf{I}$, the prioritized Jacobian simplifies to the dynamically weighted general inverse of $\mathbf{S}\mathbf{N}_s$ with the weight equal to \mathbf{M}^{-1} :

$$\mathbf{J}_{1|prec(1)}^* = \overline{\mathbf{S}\mathbf{N}_s} = \mathbf{M}^{-1} (\mathbf{S}\mathbf{N}_s)^T \left(\mathbf{S}\mathbf{N}_s \mathbf{M}^{-1} (\mathbf{S}\mathbf{N}_s)^T \right)^+ . \quad (\text{A.32})$$

Using the support constraint $\mathbf{J}_s \ddot{\mathbf{q}} = -\dot{\mathbf{J}}_s \dot{\mathbf{q}}$, we can further simplify

$$\Lambda_{1|prec(1)}^* = \left(\mathbf{M}^{-1} (\mathbf{S}\mathbf{N}_s)^T \overline{\mathbf{S}\mathbf{N}_s}^T \right)^{-1} = (\mathbf{M}^{-1} \mathbf{N}_s^T)^{-1} , \quad (\text{A.33})$$

$$\mathbf{h}_{1|prec(1)}^* = \Lambda_{1|prec(1)}^* \mathbf{M}^{-1} \mathbf{N}_s^T \mathbf{h} - \Lambda_{1|prec(1)}^* \mathbf{M}^{-1} \mathbf{J}_s^T \Lambda_s \mathbf{J}_s \dot{\mathbf{q}} . \quad (\text{A.34})$$

Substituting this into the into the operational space force (A.27) results in:

$$\begin{aligned} \mathbf{F}_{1|prec(1)} &= \Lambda_{1|prec(1)}^* \ddot{\mathbf{q}}_d + \mathbf{h}_{k|prec(k)}^* \\ &= \Lambda_{1|prec(1)}^* \left((\mathbf{I} - \mathbf{M}^{-1} \mathbf{J}_s^T \Lambda_s \mathbf{J}_s) \ddot{\mathbf{q}}_d + \mathbf{M}^{-1} \mathbf{N}_s^T \mathbf{h} \right) \\ &= \Lambda_{1|prec(1)}^* \left(\mathbf{M}^{-1} (\mathbf{I} - \mathbf{J}_s^T \Lambda_s \mathbf{J}_s \mathbf{M}^{-1}) \mathbf{M} \ddot{\mathbf{q}}_d + \mathbf{M}^{-1} \mathbf{N}_s^T \mathbf{h} \right) \\ &= (\mathbf{M}^{-1} \mathbf{N}_s^T)^{-1} \mathbf{M}^{-1} \mathbf{N}_s^T (\mathbf{M} \ddot{\mathbf{q}}_d + \mathbf{h}) \\ &= \mathbf{M} \ddot{\mathbf{q}}_d + \mathbf{h} . \end{aligned} \quad (\text{A.35})$$

In fact, the operational space force of an inverse dynamics controller corresponds the desired system dynamics. This can be directly used in the controller to create the joint torque

$$\begin{aligned} \boldsymbol{\tau} = \mathbf{J}_{1|prec(1)}^{*T} \mathbf{F}_{1|prec(1)} &= \left(\mathbf{S}\mathbf{N}_s \mathbf{M}^{-1} (\mathbf{S}\mathbf{N}_s)^T \right)^+ (\mathbf{S}\mathbf{N}_s) \mathbf{M}^{-1} (\mathbf{M} \ddot{\mathbf{q}}_d + \mathbf{h}) \\ &\stackrel{(2.11)}{=} (\mathbf{P}\mathbf{S}^T)^+ \mathbf{P} . \end{aligned} \quad (\text{A.36})$$

Using the property $\mathbf{N}_s \mathbf{M}^{-1} = \mathbf{M}^{-1} \mathbf{N}_s^T = \mathbf{N}_s \mathbf{M}^{-1} \mathbf{N}_s^T$ and comparing this to the generalized formulation with the projector matrix \mathbf{P} (2.11), we get the operational space projector as

$$\mathbf{P}_{OSC} = \mathbf{S}\mathbf{N}_s \mathbf{M}^{-1} . \quad (\text{A.37})$$

□

A.6 Hybrid OSC – Simplification for End-Effector Control

This appendix describes the application of a hybrid OSC framework for high-performance end-effector position control and inverse dynamics control of the remainder of the system.

A.6.1 Preamble and Notation

For simplicity we will use in the following three sets of coordinates and the corresponding selection matrices. These are position controlled coordinates $\mathbf{q}_p = \mathbf{S}_p \mathbf{q}$, torque controlled coordinates $\mathbf{q}_\tau = \mathbf{S}_\tau \mathbf{q}$, and the base coordinates $\mathbf{q}_b = \mathbf{S}_b \mathbf{q}$. The torque controlled and base coordinates are further grouped together as $\mathbf{q}_d = \begin{pmatrix} \mathbf{q}_b \\ \mathbf{q}_\tau \end{pmatrix} = \begin{bmatrix} \mathbf{S}_b \\ \mathbf{S}_\tau \end{bmatrix} \mathbf{q}$, which corresponds to all coordinates that are regulated by the inverse dynamics framework. By construction it holds that these selection matrices are in the null-space of each other

$$\mathbf{S}_p \mathbf{S}_\tau^T = \mathbf{S}_p \mathbf{S}_b^T = \mathbf{S}_\tau \mathbf{S}_b^T = \mathbf{0}. \quad (\text{A.38})$$

With this notation we can write

$$\mathbf{q} = \mathbf{S}_p^T \mathbf{q}_p + \mathbf{S}_\tau^T \mathbf{q}_\tau + \mathbf{S}_b^T \mathbf{q}_b = \mathbf{S}_p^T \mathbf{q}_p + \mathbf{S}_d^T \mathbf{q}_d, \quad (\text{A.39})$$

$$\mathbf{S}^T \boldsymbol{\tau} = \mathbf{S}_p^T \boldsymbol{\tau}_p + \mathbf{S}_\tau^T \boldsymbol{\tau}_\tau. \quad (\text{A.40})$$

A.6.2 Generic Hybrid OSC

In a generic scenario we have a set of motion tasks which describes the desired generalized accelerations of the whole system except for the position controlled joints $\mathbf{S}_d \ddot{\mathbf{q}} = \ddot{\mathbf{q}}_{d,des}$. From Section 5.6.2 we know that the disturbance introduced by the position controlled joints can be modeled by including a task based on the measured torque ($\mathbf{S}_p \boldsymbol{\tau} = \tilde{\boldsymbol{\tau}}_p$). If we neglect for a moment the torque optimization in the *overconstrained* subspace, the controller can be written as a single least square optimization problem

$$\min \left\| \begin{bmatrix} -\mathbf{P}\mathbf{M} & \mathbf{P}\mathbf{S}^T \\ \mathbf{S}_d & \mathbf{0} \\ \mathbf{0} & \mathbf{S}_p \mathbf{S}^T \end{bmatrix} \begin{pmatrix} \ddot{\mathbf{q}} \\ \boldsymbol{\tau} \end{pmatrix} - \begin{pmatrix} \mathbf{P}\mathbf{h} \\ \ddot{\mathbf{q}}_{d,des} \\ \tilde{\boldsymbol{\tau}}_p \end{pmatrix} \right\|_2. \quad (\text{A.41})$$

Using formulation (A.39), we can regroup (A.41) to

$$\min \left\| \begin{bmatrix} -\mathbf{PMS}_p^T & \mathbf{PS}_\tau^T & -\mathbf{PMS}_d^T & \mathbf{PS}_p^T \\ \mathbf{0} & \mathbf{0} & \mathbf{I} & \mathbf{0} \\ \mathbf{0} & \mathbf{0} & \mathbf{0} & \mathbf{I} \end{bmatrix} \begin{pmatrix} \ddot{\mathbf{q}}_p \\ \boldsymbol{\tau}_\tau \\ \ddot{\mathbf{q}}_d \\ \boldsymbol{\tau}_p \end{pmatrix} - \begin{pmatrix} \mathbf{Ph} \\ \ddot{\mathbf{q}}_{d,des} \\ \tilde{\boldsymbol{\tau}}_p \end{pmatrix} \right\|_2. \quad (\text{A.42})$$

Due to the properties of the pseudo inversion for block matrices as shown in Appendix A.2, it is possible to write (A.42) as

$$\min \left\| \begin{bmatrix} -\mathbf{PMS}_p^T & \mathbf{PS}_d^T \end{bmatrix} \begin{pmatrix} \ddot{\mathbf{q}}_p \\ \boldsymbol{\tau}_\tau \end{pmatrix} - (\mathbf{Ph} + \mathbf{PMS}_d^T \ddot{\mathbf{q}}_{d,des} - \mathbf{PS}_p^T \tilde{\boldsymbol{\tau}}_p) \right\|_2. \quad (\text{A.43})$$

A.6.3 End-Effector Simplification

In the case of legged robots, fast and precise position tracking is only relevant for end-effector respectively swing leg control. This allows to simplify the formulation introduced above as we can rewrite the projection matrix \mathbf{P} as

$$\mathbf{P} = \begin{bmatrix} \mathbf{S}_p \\ \mathbf{P}_u \end{bmatrix}. \quad (\text{A.44})$$

Proof. Since only joints of the swing leg are position controlled, the stacked contact position vector $\mathbf{r}_s = \mathbf{r}_s(\mathbf{q}_d)$ is independent of \mathbf{q}_p .

$$\mathbf{S}_p \mathbf{J}_s^T = \mathbf{S}_p \left(\frac{\partial \mathbf{r}_s(\mathbf{q}_d)}{\partial \mathbf{q}} \right) = \mathbf{S}_p \left(\cancel{\frac{\partial \mathbf{r}_s(\mathbf{q}_d)}{\partial \mathbf{q}_p}} \frac{\partial \mathbf{q}_p}{\partial \mathbf{q}} + \frac{\partial \mathbf{r}_s(\mathbf{q}_d)}{\partial \mathbf{q}_d} \frac{\partial \mathbf{q}_d}{\partial \mathbf{q}} \right)^T \quad (\text{A.45})$$

$$= \mathbf{S}_p \left(\frac{\partial \mathbf{r}_s(\mathbf{q}_d)}{\partial \mathbf{q}_d} \mathbf{S}_d \right)^T = \mathbf{S}_p \mathbf{S}_d^T \left(\frac{\partial \mathbf{r}_s(\mathbf{q}_d)}{\partial \mathbf{q}_d} \right)^T \stackrel{(\text{A.38})}{=} \mathbf{0} \quad (\text{A.46})$$

□

Consequently, it is possible to state (A.43) as

$$\min \left\| \begin{bmatrix} -\mathbf{S}_p \mathbf{MS}_p^T & \mathbf{S}_p \mathbf{S}_d^T \\ -\mathbf{P}_u \mathbf{MS}_p^T & \mathbf{P}_u \mathbf{S}_d^T \end{bmatrix} \begin{pmatrix} \ddot{\mathbf{q}}_p \\ \boldsymbol{\tau}_\tau \end{pmatrix} - \begin{pmatrix} \mathbf{S}_p \mathbf{h} + \mathbf{S}_p \mathbf{MS}_d^T \ddot{\mathbf{q}}_{d,des} - \mathbf{S}_p \mathbf{S}_p^T \tilde{\boldsymbol{\tau}}_p \\ \mathbf{P}_u \mathbf{h} + \mathbf{P}_u \mathbf{MS}_d^T \ddot{\mathbf{q}}_{d,des} - \mathbf{P}_u \mathbf{S}_p^T \tilde{\boldsymbol{\tau}}_p \end{pmatrix} \right\|_2 \quad (\text{A.47})$$

Using again the block diagonal inversion of Appendix A.2, we identify in this equation that the acceleration of the position controlled joints $\ddot{\mathbf{q}}_p$ is not

depending on $\boldsymbol{\tau}_\tau$ but can be calculated as

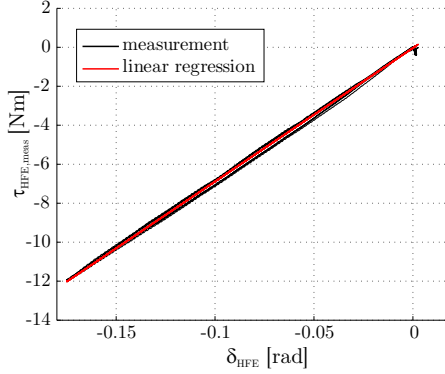
$$\ddot{\mathbf{q}}_p = (\mathbf{S}_p \mathbf{M} \mathbf{S}_p^T)^{-1} (\tilde{\boldsymbol{\tau}}_p - \mathbf{S}_p \mathbf{h} - \mathbf{S}_p \mathbf{M} \mathbf{S}_d^T \ddot{\mathbf{q}}_{d,des}). \quad (\text{A.48})$$

This direct estimation of accelerations allows applying the concept of hybrid OSC with the combined (Section 5.5) and the sequential (Section 5.4) approach. Furthermore, the torques required to perform inverse dynamics with the remainder of the system given by

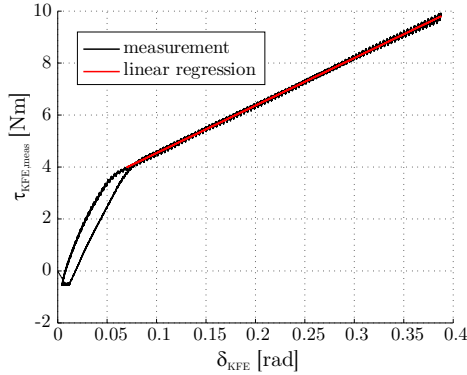
$$\min \|\mathbf{P}_u \mathbf{S}_d^T \boldsymbol{\tau}_\tau - (\mathbf{P}_u \mathbf{h} + \mathbf{P}_u \mathbf{M} \mathbf{S}_d^T \ddot{\mathbf{q}}_{d,des} - \mathbf{P}_u \mathbf{S}_p^T \tilde{\boldsymbol{\tau}}_p + \mathbf{P}_u \mathbf{M} \mathbf{S}_p^T \ddot{\mathbf{q}}_p)\|_2. \quad (\text{A.49})$$

A.7 Spring Characteristics

The joint spring characteristics were identified by a 6-axis force/torque sensor *ATI Mini45*. Figure A.1 is a plot of measured torque against the spring deflection measurement in three load cycles. HFE and KFE show high linearity and are hence well-suited as torque sensor.



(a) HFE spring characteristic



(b) KFE spring characteristic

Figure A.1: The identified hip spring characteristic has a linear regression coefficient of $R = 0.999$ and a mean absolute error of $|e|_{hip} = 0.08 \text{ Nm}$ (a). The knee spring characteristic shows high stiffness with a hysteresis and high damping in the SEA-SDA region ($\delta_s < 0.05 \text{ rad}$). During stance however, it is very linear with a regression coefficient of $R = 0.999$ and a mean absolute error of $|e|_{knee} = 0.05 \text{ Nm}$ (b).

A.8 Internal Collision in Unidirectional Spring

This appendix summarizes the effects of internal collisions and pre-compression in a uni-directional spring.

A.8.1 Impulsive Change in Speed

An internal collision leads to an instantaneous reduction in joint deflection speed $\dot{\delta}_s$, which can be expressed as a function of the shank inertia around the knee joint $\theta_{S,KFE} = \theta_S + m_S s_S^2$, the spring mass m_F , and the pulley radius r_P according to:

$$\frac{\dot{\delta}_s^+}{\dot{\delta}_s^-} = \frac{\theta_{S,KFE} - m_F r_P^2}{\theta_{S,KFE} + m_F r_P^2} = \epsilon < 1. \quad (\text{A.50})$$

Proof. The kinematic relation between the deflection angle δ_s and the linear spring compression x_F is

$$\dot{x}_F = -r_P \dot{\delta}_s \cdot \text{sign}(\delta_s). \quad (\text{A.51})$$

Crossing the neutral position of the spring (see Figure 4.8(a)) causes a reversion of the speed direction of the spring mass m_F from the pre-impact velocity \dot{x}_F^- to the post impact velocity \dot{x}_F^+ . This induces an impulse in the cable

$$\mathcal{F}_F = m_F \dot{x}_F^+ - m \dot{x}_F^- = -m r_P (\dot{\delta}_s^+ + \dot{\delta}_s^-) \cdot \text{sign}(\dot{\delta}_s). \quad (\text{A.52})$$

Due to the rotational pulley, this impulse entails a velocity change in rotational direction according to

$$\theta_{S,KFE} (\dot{\delta}_s^+ - \dot{\delta}_s^-) = r_P \mathcal{F}_F \cdot \text{sign}(\dot{\delta}_s) \stackrel{(\text{A.52})}{=} -m r_P^2 (\dot{\delta}_s^+ + \dot{\delta}_s^-). \quad (\text{A.53})$$

Hence, the ratio between post- and pre-impact angular velocity can be calculated as

$$\frac{\dot{\delta}_s^+}{\dot{\delta}_s^-} = \frac{\theta_{S,KFE} - m_F r_P^2}{\theta_{S,KFE} + m_F r_P^2}. \quad (\text{A.54})$$

□

A.8.2 Reduction in Oscillation Amplitude

This reduction in deflection speed when the leg crosses the neutral position is caused by an energy loss and consequently leads to a smaller oscillation amplitude $\hat{\delta}$. It holds that

$$\frac{\frac{1}{2}r_P\hat{\delta}_{k+1}^2 + \bar{x}_p\hat{\delta}_{k+1}}{\frac{1}{2}r_P\hat{\delta}_k^2 + \bar{x}_p\hat{\delta}_k} = \epsilon^4, \quad (\text{A.55})$$

with \bar{x}_p representing the spring pre-compression.

Proof. Neglecting all other energy losses in the spring (e.g. due to viscous damping or friction), energy is conserved from maximal deflection (potential energy) to shortly before impact (kinetic energy):

$$E_{kin,k} = E_{pot,k} \quad (\text{A.56})$$

$$\frac{1}{2}\theta_{S,KFE}\dot{\delta}_{s,k}^2 = \frac{1}{2}k_{SEA}r_P^2\hat{\delta}_k^2 + k_{SEA}\bar{x}_pr_P\hat{\delta}_k. \quad (\text{A.57})$$

In a full period, the spring undergoes two collisions in forward and backward motion. The speed over a full cycle hence scales with $\frac{\dot{\delta}_{s,k+1}}{\dot{\delta}_{s,k}} = \epsilon^2$ and consequently the energy with

$$\frac{E_{kin,k+1}}{E_{kin,k}} = \frac{\frac{1}{2}\theta_{S,KFE}\dot{\delta}_{s,k+1}^2}{\frac{1}{2}\theta_{S,KFE}\dot{\delta}_{s,k}^2} = \epsilon^4. \quad (\text{A.58})$$

Combining (A.57) and (A.58) yields

$$\frac{E_{kin,k+1}}{E_{kin,k}} = \frac{\frac{1}{2}k_{SEA}r_P^2\hat{\delta}_{k+1}^2 + k_{SEA}\bar{x}_pr_P\hat{\delta}_{k+1}}{\frac{1}{2}k_{SEA}r_P^2\hat{\delta}_k^2 + k_{SEA}\bar{x}_pr_P\hat{\delta}_k} = \frac{\frac{1}{2}r_P\hat{\delta}_{k+1}^2 + \bar{x}_p\hat{\delta}_{k+1}}{\frac{1}{2}r_P\hat{\delta}_k^2 + \bar{x}_p\hat{\delta}_k} = \epsilon^4. \quad (\text{A.59})$$

□

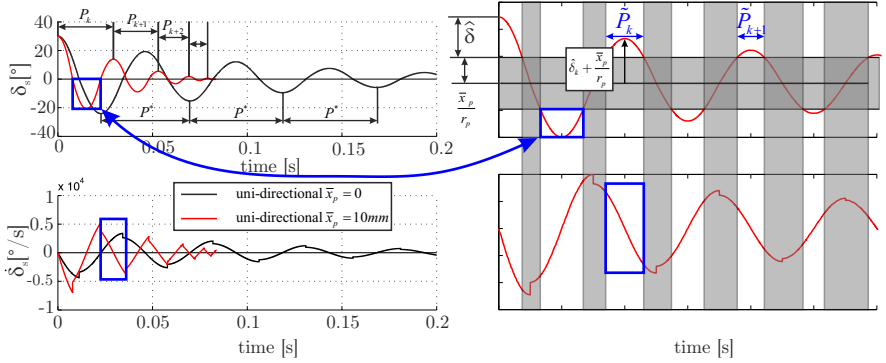


Figure A.2: Phase shortening is caused by pre-compression, which essentially removes the part of the oscillation that is smaller than $\frac{\bar{x}_p}{r_P}$.

A.8.3 Reduction in Oscillation Period

Additionally to an increase of the damping ration due to the internal collisions (A.55), the eigenfrequency of a pre-compressed spring is growing when the oscillation amplitude is getting smaller. This is illustrated in Figure A.2: If the uni-directional spring is not pre-compressed, the amplitude decreases but the periodic time P^* remains constant (black solid). Pre-compressing the spring increases the impact damping ration (A.55) and additionally reduces the period time as a function of the amplitude (red solid line). In comparison to a linear oscillation $\delta_s(t) = (\hat{\delta}_k + \frac{\bar{x}_p}{r_P}) \sin(\omega t)$, pre-compressing the spring removes all states in which $\delta_s(t) < \frac{\bar{x}_p}{r_P}$. This is indicated by the gray area. The ratio between two successive pseudo period times \tilde{P} is given by

$$\frac{\tilde{P}_{k+1}}{\tilde{P}_k} = \frac{2 \arccos\left(\frac{\bar{x}_p}{\bar{x}_p + r_P \hat{\delta}_{k+1}}\right)}{2 \arccos\left(\frac{\bar{x}_p}{\bar{x}_p + r_P \hat{\delta}_k}\right)}. \tag{A.60}$$

A.9 Choice of Task-Space Control Gains

OSC has the nice property that, by controlling the acceleration of individual points, the control parameters can be chosen independently of the actual model. The desired task-space feedback acceleration is mostly chosen as

$$\ddot{r}_i = k_p (r_{i,des} - r_i) + k_d (\dot{r}_{i,des} - \dot{r}_i), \quad (\text{A.61})$$

which describes an impedance behavior as a function of a position k_p and velocity k_d feedback gain. This corresponds to a point mass oscillator. Hence, the eigenfrequency and a dimensionless damping value of the system are given by

$$\omega = \sqrt{k_p}, \quad (\text{A.62})$$

$$D = \frac{k_d}{2\sqrt{k_p}}. \quad (\text{A.63})$$

Critical damping is achieved for $D = 1$, overcritical damping for $D > 1$ and undercritical damping for $D < 1$. The compliance of the controller can be adjusted by varying k_p . For example, assuming that the time constant respectively oscillation frequency around the nominal point should be 3 Hz, the ideal control gain k_p is 350. Furthermore, critical damping requires $k_d = 37$. This holds as good starting values for controller gain tuning.

Bibliography

- F. Aghili. Control of constrained mechanical systems with passive joints. *IEEE/RSJ International Conference on Intelligent Robots and Systems (IROS)*, 4(2):3288–3294, 2004.
- F. Aghili. A unified approach for inverse and direct dynamics of constrained multibody systems based on linear projection operator: applications to control and simulation. *IEEE Transactions on Robotics*, 21(5):834–849, 2005.
- M. Ahmadi and M. Buehler. Controlled passive dynamic running experiments with the ARL-monopod II. *IEEE Transactions on Robotics*, 22(5):974–986, Oct. 2006.
- R. M. Alexander. *Elastic mechanisms in animal movement*. Cambridge University Press, Cambridge, Mass., 1988.
- R. M. Alexander. 3 Uses for Springs in Legged Locomotion. *International Journal of Robotics Research (IJRR)*, 9(2):53–61, 1990.
- R. M. Alexander. Tendon elasticity and muscle function. *Comparative Biochemistry and Physiology Part A: Molecular & Integrative Physiology*, 133(4):1001–1011, Dec. 2002.
- R. M. Alexander. *Principles of Animal Locomotion*. Princeton University Press, Princeton, NJ, 2003.
- H. Asada. A Geometrical Representation of Manipulator Dynamics and Its Application to Arm Design. *Journal of Dynamic Systems Measurement and Control-Transactions of the Asme*, 105(3), 1983.
- S. Au and H. Herr. Powered ankle-foot prosthesis. *IEEE Robotics & Automation Magazine*, 15(3):52–59, Sept. 2008.

- S. K. Au, J. Weber, and H. Herr. Biomechanical Design of a Powered Ankle-Foot Prosthesis. In *IEEE International Conference on Rehabilitation Robotics (ICORR)*, pages 298–303, June 2007.
- R. F. Battaglia. *Design of the SCOUT II Quadruped with Preliminary Stair-Climbing*. Master thesis, Montreal, Canada, 1999.
- M. D. Berkemeier and K. V. Desai. Design of a robot leg with elastic energy storage, comparison to biology, and preliminary experimental results. In *IEEE International Conference on Robotics and Automation (ICRA)*, pages 213–218, 1996.
- P. A. Bhounsule, J. Cortell, and A. Ruina. Design and control of Ranger: An energy-efficient, dynamic walking robot. In *International Conference on Climbing and Walking Robots (CLAWAR)*, 2012.
- A. k. Björck. *Numerical Methods for Least Squares Problems*. Society for Industrial and Applied Mathematics, Jan. 1996.
- R. Blickhan. The spring-mass model for running and hopping. *Journal of Biomechanics*, 22(11):1217–1227, 1989.
- R. Blickhan and R. J. Full. Similarity in multilegged locomotion: Bouncing like a monopode. *Journal of Comparative Physiology A: Neuroethology, Sensory, Neural, and Behavioral Physiology*, 173(5):509–517, 1993.
- M. Bloesch, M. Hutter, M. Hoepflinger, and S. Leutenegger. *State Estimation and Robust Control for a Quadruped Robot*. Master thesis, ETH Zurich, 2011.
- M. Bloesch, M. Hutter, M. H. Hoepflinger, S. Leutenegger, C. Gehring, C. D. Remy, and R. Siegwart. State Estimation for Legged Robots - Consistent Fusion of Leg Kinematics and IMU. In *Robotics Science and Systems (RSS)*, Sydney, Australia, 2012a.
- M. Bloesch, M. Hutter, C. D. Remy, and R. Siegwart. Consistent Fusion of Leg Kinematics and Inertial Measurements for Legged State Estimation. In *Dynamic Walking*, Pensacola, FL, 2012b.
- M. Bloesch, C. Gehring, P. Fankhauser, M. Hutter, M. Hoepflinger, and R. Siegwart. Robust State Estimation for Legged Robots. In *IEEE/RSJ International Conference on Intelligent Robots and Systems (IROS)*, 2013a.

- M. Bloesch, M. Hutter, M. Hoepflinger, C. Gehring, and R. Siegwart. Kinematic Batch Calibration for Legged Robots. In *IEEE International Conference on Robotics and Automation (ICRA)*, Karlsruhe, Germany, 2013b.
- Boston Dynamics. <http://www.bostondynamics.com>. 2012.
- F. P. Boyle, N. K. Petek, and D. P. Smith. Method for controlling motion using an adjustable damper. The Lubrizol Corporation (29400 Lakeland Boulevard, Wickliffe, Ohio, 44092, US), 2000.
- M. Buehler, R. Playter, and M. H. Raibert. Robots Step Outside. In *International Symposium of Adaptive Motion of Animals and Machines (AMAM)*, Illmenau, Germany, 2005.
- S. Camporesi. Oscar Pistorius, enhancement and post-humans. *Journal of medical ethics*, 34(9):639, Sept. 2008.
- G. A. Cavagna, F. P. Saibene, and R. Margaria. Mechanical work in running. *J Appl Physiol*, 19(2):249–256, 1964.
- G. A. Cavagna, N. C. Heglund, and C. R. Taylor. Mechanical work in terrestrial locomotion: two basic mechanisms for minimizing energy expenditure. *AJP Regul Integr Comp Physiol*, 233(5):243–261, 1977.
- E. Colgate and N. Hogan. An analysis of contact instability in terms of passive physical equivalents. In *IEEE International Conference on Robotics and Automation (ICRA)*, pages 404–409, 1989.
- J. E. Colgate. *The control of dynamically interacting systems*. PhD thesis, 1988.
- S. Coros, A. Karpathy, B. Jones, L. Reveret, and M. van de Panne. Locomotion skills for simulated quadrupeds. In *ACM SIGGRAPH*, Vancouver, British Columbia, Canada, 2011.
- S. Curran and D. E. Orin. Evolution of a jump in an articulated leg with series-elastic actuation. In *IEEE International Conference on Robotics and Automation (ICRA)*, pages 252–258, Pasadena, CA, USA, 2008.
- M. de Lasa and A. Hertzmann. Prioritized optimization for task-space control. *IEEE/RSJ International Conference on Intelligent Robots and Systems (IROS)*, pages 5755–5762, Oct. 2009.

- H. De Man, D. Lefeber, and J. Vermeulen. Design and Control of a Robot with One Articulated Leg for Locomotion on Irregular Terrain. In A. Morecki, G. Bianchi, and M. Wojtyra, editors, *CSIM courses and lectures*, volume 405, chapter VI, pages 417–424. Springer Wien New York, 1998a.
- H. De Man, D. Lefeber, J. Vermeulen, and H. D. Man. Hopping on Irregular Terrain with One Articulated Leg. *International Symposium on Robotics (ISR)*, 1998b.
- M. H. Dickinson, C. T. Farley, R. J. Full, M. A. R. Koehl, R. Kram, and S. Lehman. How Animals Move: An Integrative View. *Science*, 288(5463): 100–106, Apr. 2000.
- A. Dietrich, T. Wimbock, A. Albu-Schaffer, and G. Hirzinger. Integration of Reactive, Torque-Based Self-Collision Avoidance Into a Task Hierarchy. *IEEE Transactions on Robotics*, 28(6):1278–1293, 2012.
- M. Donald and Q. Li. Design and performance evaluation of a rotary series elastic actuator. In *International Conference on Robotics and Applications (ICIRA)*, pages 555–564, Montreal, Canada, 2012.
- M. Ernst, H. Geyer, and R. Blickhan. Spring-Legged Locomotion on Uneven Ground: A Control Approach to Keep the Running Speed Constant. In *International Conference on Climbing and Walking Robots (CLAWAR)*, pages 639–644, Istanbul, Turkey, 2009.
- P. Fankhauser, M. Hutter, C. Gehring, and C. D. Remy. *Optimizing Robotic Single Legged Locomotion with Reinforcement Learning*. Master thesis, 2012.
- P. Fankhauser, M. Hutter, C. Gehring, M. Bloesch, M. Hoepflinger, and R. Siegwart. Reinforcement Learning of Single Legged Locomotion. In *IEEE/RSJ International Conference on Intelligent Robots and Systems (IROS)*, 2013.
- C. T. Farley, J. Glasheen, and T. A. McMahon. Running Springs - Speed and Animal Size. *Journal of Experimental Biology*, 185:71–86, 1993.
- R. Featherstone. An Empirical Study of the Joint Space Inertia Matrix. *The International Journal of Robotics Research (IJRR)*, 23(9):859–871, 2004.
- R. C. Fitzpatrick, R. B. Gorman, D. Burke, and S. C. Gandevia. Postural proprioceptive reflexes in standing human subjects: bandwidth of response

- and transmission characteristics. *The Journal of physiology*, 458:69–83, Dec. 1992.
- A. A. Frank. Automatic Control Systems for Legged Locomotion. Technical report, Los Angeles, 1968.
- R. J. Full and D. E. Koditschek. Templates and anchors: neuromechanical hypotheses of legged locomotion on land. *Journal of Experimental Biology*, 202(23):3325–3332, 1999.
- C. Gehring, M. Hutter, M. Hoepflinger, and C. D. Remy. *Operational Space Control of Single Legged Hopping*. Master thesis, 2011.
- C. Gehring, S. Coros, M. Hutter, M. Bloesch, M. H. Hoepflinger, and R. Siegwart. Control of Dynamic Gaits for a Quadrupedal Robot. In *IEEE International Conference on Robotics and Automation (ICRA)*, Karlsruhe, Germany, 2013.
- H. Geyer, R. Blickhan, and A. Seyfarth. Natural dynamics of spring-like running: emergence of selfstability. In *International Conference on Climbing and Walking Robots (CLAWAR)*, London, UK, 2002.
- H. Geyer, A. Seyfarth, and R. Blickhan. Spring-mass running: simple approximate solution and application to gait stability. *Journal of Theoretical Biology*, 232(3):315–328, 2005.
- H. Geyer, A. Seyfarth, and R. Blickhan. Compliant leg behaviour explains basic dynamics of walking and running. *Proceedings of the Royal Society B: Biological Sciences*, 273(1603):2861–2867, 2006.
- R. M. Ghigliazza, R. Altendorfer, P. Holmes, and D. Koditschek. A simply stabilized running model. *Siam Review*, 47(3):519–549, Jan. 2005.
- G. Gilardi and I. Sharf. Literature survey of contact dynamics modelling. *Mechanism and Machine Theory*, 37(10):1239–1213, 2002.
- C. Glocker. Dynamik von Starrkoerpersystemen mit Reibung und Stoessen. *VDI-Fortschrittberichte Mechanik/Bruchmechanik*, 18(182), 1995.
- C. Glocker. On frictionless impact models in rigid-body systems. *Phil. Trans. R. Soc. Lond.: Mathematical, Physical & Engineering Sciences*, 359(1789): 2304–2385, 2001.
- G. H. Golub and C. F. V. Loan. *Matrix Computations*. 1996.

- P. G. Gonzales de Santos, E. Garcia, and J. Estremera. Stability in Walking Robots. In *Quadrupedal Locomotion. An Introduction to the Control of Four-legged Robots*, volume 1, pages 33–54. Springer, Berlin, 2006.
- P. Gregorio, M. Ahmadi, and M. Buehler. Experiments with an Electrically Actuated Planar Hopping Robot. In *The 3rd International Symposium on Experimental Robotics*, pages 269–281, 1994.
- P. Gregorio, M. Ahmadi, and M. Buehler. Design, control, and energetics of an electrically actuated legged robot. *IEEE Transactions on Systems, Man, and Cybernetics. Part B: Cybernetics*, 27(4):626–634, 1997.
- J. A. Grimes and J. W. Hurst. Design of ATRIAS 1.0 A Unique Monopod, Hopping Robot. In *International Conference on Climbing and Walking Robots (CLAWAR)*, 2012.
- H. Hanafusa, T. Yoshikawa, and Y. Nakamura. Analysis and control of articulated robot with redundancy. In *IFAC Symposium on Robot Control*, volume 4, pages 1927–1932, 1981.
- H. M. Herr and A. M. Grabowski. Bionic ankle-foot prosthesis normalizes walking gait for persons with leg amputation. *Proceedings. Biological sciences / The Royal Society*, 279(1728):457–64, Feb. 2012.
- H. Hirukawa, S. Kajita, F. Kanehiro, K. Kaneko, and T. Isozumi. The Human-size Humanoid Robot That Can Walk, Lie Down and Get Up. *The International Journal of Robotics Research (IJRR)*, 24(9):755–769, 2005.
- R. Hodoshima, Y. Fukuda, T. Doi, S. Hirose, T. Okamoto, and J. Mori. Development of TITAN XI: a quadruped walking robot to work on slopes. In *IEEE/RSJ International Conference on Intelligent Robots and Systems (IROS)*, pages 792–797, Sendai, Japan, 2004.
- M. A. Hoepffinger, C. D. Remy, M. Hutter, and R. Siegwart. Extrinsic RGB-D Camera Calibration for Legged Robots. In *International Conference on Climbing and Walking Robots (CLAWAR)*, pages 94–101, Nagoya, Japan, 2011.
- M. A. Hoepffinger, D. Baschung, C. D. Remy, M. Hutter, R. Siegwart, N. Hoch, and B. Werther. Parcelbot: A Tracked Parcel Transporter with High Obstacle Negotiation Capabilities. In *International Conference on Climbing and Walking Robots (CLAWAR)*, pages 831–838, 2012.

- M. A. Hoepflinger, M. Hutter, C. Gehring, M. Bloesch, and R. Siegwart. Unsupervised Identification and Prediction of Foothold Robustness. In *International Conference on Robotics and Automation (ICRA)*, 2013.
- M. H. Hoepflinger, C. D. Remy, M. Hutter, and R. Siegwart. Haptic Terrain Classification on Natural Terrains for Legged Robots. In *International Conference on Climbing and Walking Robots (CLAWAR)*, pages 785–792, Nagoya, Japan, 2010a.
- M. H. Hoepflinger, C. D. Remy, M. Hutter, and R. Siegwart. The quadruped ALoF and a step towards real world haptic terrain classification. In *Mechatronics 2010*, Zurich, Switzerland, 2010b.
- M. H. Hoepflinger, C. D. Remy, M. Hutter, L. Spinello, and R. Siegwart. Haptic Terrain Classification for Legged Robots. In *International Conference on Robotics and Automation (ICRA)*, pages 2828–2833, Anchorage, AK, 2010c.
- N. Hogan. On the stability of manipulators performing contact tasks. *IEEE Journal on Robotics and Automation*, 4(6):677–686, 1988.
- J. M. Hollerbach, I. W. Hunter, and J. Ballantyne. A comparative analysis of actuator technologies for robotics. *Robotics Review*, 2, 1991.
- I. Hunter and S. Lafontaine. A comparison of muscle with artificial actuators. In *IEEE Solid-State Sensor and Actuator Workshop*, pages 178–185, 1992.
- J. W. Hurst. *The Role and Implementation of Compliance in Legged Locomotion*. PhD thesis, Pittsburgh, PA, 2008.
- J. W. Hurst and A. A. Rizzi. Series Elastic Actuation : Potential and Pitfalls. In *International Conference on Climbing and Walking Robots (CLAWAR)*, 2004.
- M. Hutter. Hopping with an Articulated Robotic Leg. Master Thesis, ETH Zurich, 2009.
- M. Hutter and R. Siegwart. Template Based Running with an Articulated Robotic Leg. In *Dynamic Walking Meeting*, Boston, USA, 2010.
- M. Hutter and R. Siegwart. Hybrid Operational Space Control for Compliant Quadruped Robots. In *Dynamic Walking Meeting*, Pensacola, FL, 2012.
- M. Hutter, C. D. Remy, and R. Siegwart. Design of an Articulated Robotic Leg with Nonlinear Series Elastic Actuation. In *International Conference on Climbing and Walking Robots (CLAWAR)*, Istanbul, Turkey, 2009a.

- M. Hutter, C. D. Remy, and R. Siegwart. Open-loop control strategies in passive dynamic hopping. In *Dynamic Walking Meeting*, Burnaby, Canada, 2009b.
- M. Hutter, C. D. Remy, and R. Siegwart. Adaptive Control Strategies for Open-loop Dynamic Hopping. In *International Conference on Intelligent Robots and Systems (IROS)*, St Louis, MO, 2009c.
- M. Hutter, C. D. Remy, M. H. Hoepflinger, and R. Siegwart. Full State Control of a SLIP Model by Touchdown Detection. In *International Conference on Climbing and Walking Robots (CLAWAR)*, pages 533–540, Nagoya, Japan, 2010a.
- M. Hutter, C. D. Remy, M. H. Hoepflinger, and R. Siegwart. SLIP Running with an Articulated Robotic Leg. In *International Conference on Intelligent Robots and Systems (IROS)*, pages 4934–4939, Taipei, Taiwan, 2010b.
- M. Hutter, C. Gehring, and R. Siegwart. proNEu: Derivation of Analytical Kinematics and Dynamics. Technical report, Autonomous Systems Lab, ETHZ, 2011a.
- M. Hutter, C. D. Remy, M. H. Hoepflinger, and R. Siegwart. ScarLETH: Design and Control of a Planar Running Robot. In *IEEE/RSJ International Conference on Intelligent Robots and Systems (IROS)*, pages 562–567, San Francisco, USA, 2011b.
- M. Hutter, C. D. Remy, M. H. Hoepflinger, and R. Siegwart. High Compliant Series Elastic Actuation for the Robotic Leg ScarLETH. In *International Conference on Climbing and Walking Robots (CLAWAR)*, pages 507–514, Paris, Fr, 2011c.
- M. Hutter, C. Gehring, M. Bloesch, M. H. Hoepflinger, C. D. Remy, and R. Siegwart. StarLETH: a Compliant Quadrupedal Robot for Fast, Efficient, and Versatile Locomotion. In *International Conference on Climbing and Walking Robots (CLAWAR)*, pages 483–490, 2012a.
- M. Hutter, M. H. Hoepflinger, C. D. Remy, and R. Siegwart. Hybrid Operational Space Control for Compliant Legged Systems. In *RSS Robotics Science and Systems*, Sydney, Australia, 2012b.
- M. Hutter, C. Holenstein, D. Fenner, C. D. Remy, M. H. Hoepflinger, and R. Siegwart. Improved Efficiency in Legged Running Using Lightweight

- Passive Compliant Feet. In *International Conference on Climbing and Walking Robots (CLAWAR)*, pages 491–498, 2012c.
- M. Hutter, C. Gehring, M. H. Hoepflinger, M. Bloesch, and R. Siegwart. Walking and Running with StarLETH. In *International Symposium on Adaptive Motion of Animals and Machines (AMAM)*, Darmstadt, Germany, 2013a.
- M. Hutter, C. Gehring, and R. Siegwart. Multi-task inverse dynamics based on LS-optimization. In *Dynamic Walking Meeting*, 2013b.
- M. Hutter, C. D. Remy, M. A. Hoepflinger, and R. Siegwart. Efficient and Versatile Locomotion With Highly Compliant Legs. *IEEE/ASME Transactions on Mechatronics*, 18(2):449–458, 2013c.
- S. H. Hyon and T. Mita. Development of a biologically inspired hopping robot-"Kenken". In *IEEE International Conference on Robotics and Automation (ICRA)*, pages 3984–3991, 2002.
- F. Iida, G. Gomez, and R. Pfeifer. Exploiting body dynamics for controlling a running quadruped robot. In *International Conference on Robotics and Automation (ICRA)*, pages 229–235, Barcelona, Spain, 2005.
- R. Isermann. *Mechatronic systems*. 2005.
- S. Kajita, F. Kanehiro, K. Kaneko, K. Yokoi, and H. Hirukawa. The 3D linear inverted pendulum mode: a simple modeling for a biped walking pattern generation. In *IEEE/RSJ International Conference on Intelligent Robots and Systems (IROS)*, pages 239–246, 2001.
- M. Kalakrishnan, J. Buchli, P. Pastor, M. Mistry, and S. Schaal. Fast, Robust Quadruped Locomotion over Challenging Terrain. In *IEEE International Conference on Robotics and Automation (ICRA)*, Anchorage, AK, 2010.
- O. Kanoun, F. Lamiraux, and P.-B. Wieber. Kinematic Control of Redundant Manipulators: Generalizing the Task-Priority Framework to Inequality Task. *IEEE Transactions on Robotics*, 27(4):785–792, Aug. 2011.
- R. F. Ker, M. B. Bennett, S. R. Bibby, R. C. Kester, and R. M. Alexander. The spring in the arch of the human foot. *Nature*, 325(7000):147–9, 1987.
- O. Khatib. A unified approach for motion and force control of robot manipulators: The operational space formulation. *IEEE Journal of Robotics and Automation*, 3(1):43–53, 1987.

- H. Kimura, Y. Fukuoka, and a. H. Cohen. Adaptive dynamic walking of a quadruped robot on natural ground based on biological concepts. *The International Journal of Robotics Research*, 26(5):475–490, May 2007.
- B. T. Knox and J. P. Schmiedeler. *Evaluation of a Prototype Series-Compliant Hopping Leg for Biped Robot Applications*. Undergraduate thesis, 2007.
- Z. J. Kolter, A. Y. Ng, and J. Zico Kolter. The Stanford LittleDog: A learning and rapid replanning approach to quadruped locomotion. *The International Journal of Robotics Research (IJRR)*, 30(2):150–174, Jan. 2011.
- K. Kong, J. Bae, and M. Tomizuka. Control of Rotary Series Elastic Actuator for Ideal Force-Mode Actuation in Human & Robot Interaction Applications. *IEEE/ASME Transactions on Mechatronics*, 14(1):105–118, 2009.
- K. Kong, J. Bae, and M. Tomizuka. A Compact Rotary Series Elastic Actuator for Human Assistive Systems. *IEEE/ASME Transactions on Mechatronics*, 17(2):288–297, 2012.
- A. Kuo. Choosing Your Steps Carefully: Trade-offs between economy and versatility in dynamic walking bipedal robots. *IEEE Robotics and Automation Magazine*, 14(2):18–29, June 2007.
- A. D. Kuo. A simple model of bipedal walking predicts the preferred speed-step length relationship. *Journal of Biomechanical Engineering-Transactions of the Asme*, 123(3):264–269, 2001.
- M. Latta, C. D. Remy, and M. Hutter. *Optimal Control of a Robotic Leg*. Master thesis, 2010.
- M. Latta, C. D. Remy, M. Hutter, M. A. Hoepffinger, and R. Siegwart. Towards Walking on Mars. In *Advanced Space Technologies for Robotics and Automation (ASTRA)*, Noordwijk, The Netherlands, 2011.
- G. A. Lichtwark and A. M. Wilson. In vivo mechanical properties of the human Achilles tendon during one-legged hopping. *Journal of Experimental Biology*, 208(24):4715–4725, 2005.
- T. McGeer. Passive Dynamic Walking. *The International Journal of Robotics Research (IJRR)*, 9(2):62–82, 1990a.
- T. McGeer. Passive Walking with Knees. In *International Conference on Robotics and Automation (ICRA)*, pages 1640–1645, 1990b.

- R. B. McGhee. Finite state control of quadruped locomotion. *SIMULATION*, 9(3):135–140, Sept. 1967.
- R. B. McGhee, A. A. Fkask, and A. Frank. On the stability properties of quadruped creeping gaits. *Mathematical Biosciences*, 3:331–351, Aug. 1968.
- Meka Robotics. <http://www.mekabot.com>. 2011.
- M. Mistry, J. Buchli, and S. Schaal. Inverse Dynamics Control of Floating Base Systems Using Orthogonal Decomposition. In *International Conference on Robotics and Automation (ICRA)*, pages 3406–3412, 2010.
- M. N. Mistry. *The representation, learning, and control of dexterous motor skills in humans and humanoid robots*. PhD thesis, 2009.
- F. L. Moro, N. G. Tsagarakis, and D. G. Caldwell. A human-like walking for the COmpliant huMANoid COMAN based on CoM trajectory reconstruction from kinematic Motion Primitives. In *IEEE-RAS International Conference on Humanoid Robots (Humanoids)*, pages 364–370, Oct. 2011.
- M. P. Murphy, A. Saunders, C. Moreira, A. A. Rizzi, and M. Raibert. The LittleDog Robot. *The International Journal of Robotics Research*, 2010.
- Z. Nagy, O. Ergeneman, J. J. Abbott, M. Hutter, A. M. Hirt, and B. J. Nelson. Modeling assembled-MEMS microrobots for wireless magnetic control. In *IEEE International Conference on Robotics and Automation (ICRA)*, pages 874–879, 2008.
- Y. Nakamura, H. Hanafusa, and T. Yoshikawa. Task-Priority Based Redundancy Control of Robot Manipulators. *The International Journal of Robotics Research*, 6(2):3–15, June 1987.
- J. Nakanishi, M. Mistry, and S. Schaal. Inverse Dynamics Control with Floating Base and Constraints. In *IEEE International Conference on Robotics and Automation (ICRA)*, pages 1942–1947, Apr. 2007.
- J. Nakanishi, R. Cory, M. Mistry, J. Peters, and S. Schaal. Operational Space Control: A Theoretical and Empirical Comparison. *The International Journal of Robotics Research*, 27(6):737–757, June 2008.
- P. D. Neuhaus, J. E. Pratt, and M. J. Johnson. Comprehensive summary of the Institute for Human and Machine Cognition’s experience with LittleDog. *The International Journal of Robotics Research (IJRR)*, 30(2): 216–235, Jan. 2011.

- J. Nichol. *Design for Energy Loss and Energy Control in a Galloping Artificial Quadruped*. PhD thesis, Stanford, 2005.
- J. G. Nichol and K. J. Waldron. Biomimetic Leg Design for Untethered Quadruped Gallop. In *International Conference on Climbing and Walking Robots (CLAWAR)*, Paris, France, 2002.
- J. G. Nichol, S. P. N. Singh, K. J. Waldron, L. R. Palmer III, D. E. Orin, and L. R. Palmer. System Design of a Quadrupedal Galloping Machine. *The International Journal of Robotics Research (IJRR)*, 23(10-11):1013–1027, Oct. 2004.
- T. F. Novacheck. The biomechanics of running. *Gait & Posture*, 7(1):77–95, Jan. 1998.
- C. Ott, O. Eiberger, W. Friedl, B. Bauml, U. Hillenbrand, C. Borst, A. Albuschaffer, B. Brunner, H. Hirschmuller, S. Kielhofer, R. Konietzschke, M. Suppa, T. Wimbock, F. Zacharias, and G. Hirzinger. A Humanoid Two-Arm System for Dexterous Manipulation. In *IEEE-RAS International Conference on Humanoid Robots*, pages 276–283, Dec. 2006.
- D. Owaki, M. Koyama, S. Yamaguchi, S. Kubo, and A. Ishiguro. A 2-D Passive-Dynamic-Running Biped With Elastic Elements. *IEEE Transactions on Robotics*, 27(1):156–162, Feb. 2011.
- N. Paine and L. Sentis. A New Prismatic Series Elastic Actuator with Compact Size and High Performance. In *IEEE International Conference on Robotics and Biomimetics (ROBIO)*, Guangzhou, China, 2012.
- L. R. Palmer, D. E. Orin, D. W. Marhefka, J. P. Schmiedeler, and K. J. Waldron. Intelligent control of an experimental articulated leg for a galloping machine. In *IEEE International Conference on Robotics and Automation (ICRA)*, pages 3821–3827, 2003.
- R. Pfeifer and C. Scheier. *Understanding Intelligence*. MIT Press, 2001.
- S. Pfeifer, H. Vallery, U. Keller, P. Lutz, and R. Riener. Powered Prosthesis with Serial and/or Parallel Compliance. 2012.
- F. Pfeiffer and C. Glocker. *Multibody Dynamics with Unilateral Contacts*. John Wiley & Sons, 1996.
- R. Philippsen, L. Sentis, O. Khatib, and L. Sentist. An open source extensible software package to create whole-body compliant skills in personal

- mobile manipulators. In *IEEE/RSJ International Conference on Intelligent Robots and Systems (IROS)*, pages 1036–1041, 2011.
- I. Poulakakis, J. A. Smith, and M. Buehler. Modeling and experiments of untethered quadrupedal running with a bounding gait: The Scout II robot. *International Journal of Robotics Research*, 24(4):239–256, Apr. 2005.
- G. A. Pratt and M. M. Williamson. Series elastic actuators. In *IEEE International Conference on Intelligent Robots and Systems (IROS)*, pages 399–406, Pittsburgh, PA, 1995. MIT.
- G. A. Pratt and M. M. Williamson. Elastic actuator for precise force control. 1997.
- G. A. Pratt, P. Willisson, C. Bolton, and A. Hofman. Late motor processing in low-impedance robots: impedance control of series-elastic actuators. In *American Control Conference (ACC)*, volume 4, pages 3245–3251, 2004a.
- J. Pratt. *Virtual Model Control of a Biped Walking Robot*. Master thesis, Massachusetts Institute of Technology, 1995.
- J. Pratt and B. Krupp. Design of a bipedal walking robot. In *Unmanned Systems Technology X*, 2008.
- J. Pratt, P. Dilworth, and G. Pratt. Virtual model control of a bipedal walking robot. *International Conference on Robotics and Automation (ICRA)*, pages 193–198, 1997.
- J. Pratt, C.-M. Chew, A. Torres, P. Dilworth, and G. Pratt. Virtual model control: An intuitive approach for bipedal locomotion. *International Journal of Robotics Research*, 20(2):129–143, 2001.
- J. Pratt, B. Krupp, and C. Morse. Series elastic actuators for high fidelity force control. *Industrial Robot: An International Journal*, 29(3):234–241, 2002.
- J. Pratt, B. Krupp, C. Morse, and S. Collins. The RoboKnee: an exoskeleton for enhancing strength and endurance during walking. In *IEEE International Conference on Robotics and Automation (ICRA)*, pages 2430–2435, 2004b.
- J. Pratt, J. Carff, S. Drakunov, and A. Goswami. Capture Point: A Step toward Humanoid Push Recovery. In *IEEE-RAS International Conference on Humanoid Robots (Humanoids)*, pages 200–207, 2006.

- K. Radkhah, C. Maufroy, M. Maus, Scholz D, A. Seyfarth, and O. Von Stryk. Concept and design of the biobiped1 robot for human-like walking and running. *International Journal of Humanoid Robotics*, 08(03):439–458, 2011.
- M. Raibert, M. Chepponis, and H. B. J. Brown. Running on four legs as though they were one. *IEEE Journal on Robotics and Automation*, 2(2): 70–82, 1986.
- M. Raibert, K. Blankespoor, G. Nelson, and R. Playter. BigDog, the rough-terrain quadruped robot. In *Proceedings of the 17th World Congress*, pages 10823–10825, 2008.
- M. H. Raibert. *Legged robots that balance*. MIT Press, Cambridge, Mass., 1986.
- M. H. Raibert, H. Brown Jr., M. Chepponis, E. Hastings, J. Koechling, N. M. Karl, S. S. Murthy, A. J. Stentz, H. B. Brown, and K. N. Murphy. Dynamically Stable Legged Locomotion. Technical Report 4148, 1983.
- M. H. Raibert, H. B. Brown, and M. Chepponis. Experiments in Balance with a 3D One-Legged Hopping Machine. *The International Journal of Robotics Research (IJRR)*, 3(2):75–92, June 1984.
- C. D. Remy. *Optimal Exploitation of Natural Dynamics in Legged Locomotion*. PhD thesis, 2011.
- C. D. Remy, O. Baur, M. Latta, A. Lauber, M. Hutter, M. H. Hoepflinger, C. Pradalier, and R. Siegwart. Walking and Crawling with ALoF - A Robot for Autonomous Locomotion On Four Legs. In *International Conference on Climbing and Walking Robots (CLAWAR)*, pages 501–508, Nagoya, Japan, 2010a.
- C. D. Remy, M. Hutter, and R. Siegwart. Passive Dynamic Walking with Quadrupeds - Extensions towards 3D. In *International Conference on Robotics and Automation (ICRA)*, pages 5231–5236, Anchorage, AK, 2010b.
- C. D. Remy, O. Baur, M. Latta, A. Lauber, M. Hutter, M. H. Hoepflinger, C. Pradalier, and R. Siegwart. Walking and crawling with ALoF: a robot for autonomous locomotion on four legs. *Industrial Robot: An International Journal*, 38(3):264–268, 2011a.
- C. D. Remy, M. Hutter, M. H. Hoepflinger, and R. Siegwart. ScarLETH, StarLETH, and Pegasus. In *Dynamic Walking Meeting*, Jena, D, 2011b.

- C. D. Remy, K. W. Buffinton, and R. Siegwart. Comparison of Cost Functions for Electrically Driven Running Robots. In *IEEE International Conference on Robotics and Automation (ICRA)*, pages 2343–2350, May 2012a.
- C. D. Remy, M. Hutter, M. Hoepflinger, M. Bloesch, C. Gehring, and R. Siegwart. Quadrupedal Robots with Stiff and Compliant Actuation. *at - Automatisierungstechnik*, 60(11):682–691, Nov. 2012b.
- L. Righetti, J. Buchli, M. Mistry, and S. Schaal. Inverse dynamics with optimal distribution of ground reaction forces for legged robots. In *international conference on climbing and walking robots (CLAWAR)*, 2010.
- L. Righetti, J. Buchli, M. Mistry, and S. Schaal. Inverse dynamics control of floating-base robots with external constraints: A unified view. In *International Conference on Robotics and Automation (ICRA)*, pages 1085–1090, 2011a.
- L. Righetti, J. Buchli, M. Mistry, and S. Schaal. Control of legged robots with optimal distribution of contact forces. In *IEEE-RAS International Conference on Humanoid Robots (Humanoids)*, pages 318–324, 2011b.
- L. Righetti, J. Buchli, M. Mistry, M. Kalakrishnan, and S. Schaal. Optimal distribution of contact forces with inverse dynamics control. *International Journal of Robotics Research (IJRR)*, 2013.
- T. J. Roberts. The integrated function of muscles and tendons during locomotion. *Comparative biochemistry and physiology. Part A, Molecular & integrative physiology*, 133(4):1087–99, Dec. 2002.
- D. W. Robinson, J. E. Pratt, D. J. Paluska, and G. A. Pratt. Series elastic actuator development for a biomimetic walking robot. In *International Conference on Advanced Intelligent Mechatronics (AIM)*, pages 561–568, Atlanta, USA, 1999.
- A. Ruina and J. Cortell. Homepage of Cornell Ranger, 2011, 4-legged bipedal robot. 2011.
- J. Rummel and A. Seyfarth. Stable Running with Segmented Legs. *The International Journal of Robotics Research (IJRR)*, 27(8):919–934, Aug. 2008.
- Y. Sakagami, R. Watanabe, C. Aoyama, S. Matsunaga, N. Higaki, and K. Fujimura. The intelligent ASIMO: system overview and integration. In *International Conference on Intelligent Robots and System (IROS)*, volume 3, pages 2478–2483, Lausanne, Switzerland, 2002.

- E. Saltzman and J. A. S. Kelso. Skilled Actions: A Task Dynamic Approach. *Psychological Review*, 94(1):84–106, 1987.
- S. Schaal. dynamic movement primitives - a framework for motor control in humans and humanoid robots. In *International Symposium on Adaptive Motion of Animals and Machines (AMAM)*, 2003.
- S. Schaal. The SL Simulation and Real-Time Control Software Package. Technical report, 2009.
- S. Schaal and N. Schweighofer. Computational motor control in humans and robots. *Current Opinion in Neurobiology*, 15(6):675–682, 2005.
- J. P. Schmiedeler and K. J. Waldron. Impact analysis as a design tool for the legs of mobile robots. *Advances in Robot Kinematics*, pages 129–136 442, 2000.
- J. Schmitt and P. Holmes. Mechanical models for insect locomotion: dynamics and stability in the horizontal plane I. Theory. *Biological Cybernetics*, 83(6):501–515, 2000.
- J. P. Scholz and G. Schoner. The uncontrolled manifold concept: identifying control variables for a functional task. *Experimental Brain Research*, 126(3):289–306, 1999.
- G. Schultz and K. Mombaur. Modeling and Optimal Control of Human-Like Running. *IEEE/ASME Transactions on Mechatronics*, 15(5):783–792, Oct. 2010.
- W. J. Schwind and D. E. Koditschek. Approximating the Stance Map of a 2-DOF Monoped Runner. *Journal of Nonlinear Science*, 10(5):533–568, 2000.
- J. E. Seipel and P. Holmes. Running in Three Dimensions: Analysis of a Point-mass Sprung-leg Model. *The International Journal of Robotics Research*, 24(8):657–674, Aug. 2005.
- C. Semini. *HyQ - Design and Development of a Hydraulically Actuated Quadruped Robot*. PhD thesis, Italian Institute of Technology and University of Genoa, 2010.
- C. Semini, N. G. Tsagarakis, E. Guglielmino, M. Focchi, F. Cannella, and D. G. Caldwell. Design of HyQ – a hydraulically and electrically actuated quadruped robot. *Proceedings of the Institution of Mechanical Engineers*,

- Part I: Journal of Systems and Control Engineering*, 225(6):831–849, Aug. 2011.
- J. Sensinger and R. Weir. Design and Analysis of a Non-Backdrivable Series Elastic Actuator. *International Conference on Rehabilitation Robotics (ICORR)*, pages 390–393, 2005.
- L. Sentis. *Synthesis and Control of Whole-Body Behaviors in Humanoid Systems*. PhD thesis, 2007.
- L. Sentis. Compliant Control of Whole-body Multi-contact Behaviors in Humanoid Robots. In *Motion Planning for Humanoid Robots*, pages 29–66. Springer London, 2010.
- L. Sentis and O. Khatib. Control of Free-Floating Humanoid Robots Through Task Prioritization. In *IEEE International Conference on Robotics and Automation (ICRA)*, pages 1718–1723, 2005.
- A. Seyfarth, M. Günther, and R. Blickhan. Stable operation of an elastic three-segment leg. *Biological Cybernetics*, 84(5):365–382, 2001.
- A. Seyfarth, H. Geyer, M. Gunther, and R. Blickhan. A movement criterion for running. *Journal of Biomechanics*, 35(5):649–655, 2002.
- B. Siciliano and J. J. E. Slotine. A General Framework for Managing Multiple Tasks in Highly Redundant Robotic Systems. In *International Conference on Robots in Unstructured Environments (ICAR)*, pages 1211–1216 vol.2, 1991.
- M. Slovic, N. Paine, K. Kemper, A. Metger, A. Edinger, J. Weber, and L. Sentis. Building HUME: A Bipedal Robot for Human-Centered Hyper-Agility. In *Dynamic Walking Meeting*, Pensacola, FL, 2012.
- S.-M. Song and K. J. Waldron. *Machines That Walk: The Adaptive Suspension Vehicle*. Nov. 1988.
- SpringActive. <http://www.springactive.com/>. 2013.
- H. D. Taghirad. *Analysis, Design, and Control of Hopping Robot*. Master thesis, 1993.
- R. Tajima, D. Honda, and K. Suga. Fast running experiments involving a humanoid robot. In *IEEE International Conference on Robotics and Automation (ICRA)*, pages 1571–1576, 2009.

- Y. Tassa, T. Erez, and E. Todorov. Synthesis and Stabilization of Complex Behaviors through Online Trajectory Optimization. In *IEEE/RSJ International Conference on Intelligent Robots and Systems (IROS)*, 2012.
- C. R. Taylor, K. Schmidt-Nielsen, and J. L. Raab. Scaling of energetic cost of running to body size in mammals. *The American journal of physiology*, 219(4):1104–7, Oct. 1970.
- I. The MathWorks. MATLAB Symbolic Math Toolbox. 2013.
- E. Theodorou, J. Buchli, and S. Schaal. A Generalized Path Integral Control Approach to Reinforcement Learning. *Journal of Machine Learning Research*, 11:3153–3197, Mar. 2010.
- N. Tsagarakis and Z. Li. The design of the lower body of the compliant humanoid robot "cCub". *IEEE International Conference on Robotics and Automation (ICRA)*, pages 2035–2040, 2011.
- N. Tsagarakis, M. Laffranchi, B. Vanderborght, and D. Caldwell. A compact soft actuator unit for small scale human friendly robots. *IEEE International Conference on Robotics and Automation (ICRA)*, pages 4356–4362, May 2009.
- H. Vallery, R. Ekkelenkamp, H. van der Kooij, and M. Buss. Passive and accurate torque control of series elastic actuators. In *IEEE/RSJ International Conference on Intelligent Robots and Systems (IROS)*, pages 3534–3538, Oct. 2007.
- H. Vallery, J. Veneman, E. van Asseldonk, R. Ekkelenkamp, M. Buss, and H. van Der Kooij. Compliant actuation of rehabilitation robots. *IEEE Robotics & Automation Magazine*, 15(3):60–69, Sept. 2008.
- C. L. Vaughan and M. J. O'Malley. Froude and the contribution of naval architecture to our understanding of bipedal locomotion. *Gait & Posture*, 21(3):350–362, 2005.
- R. Versluis, P. Beyl, M. Van Damme, A. Desomer, R. Van Ham, and D. Lefeber. Prosthetic feet: state-of-the-art review and the importance of mimicking human ankle-foot biomechanics. *Disability and rehabilitation. Assistive technology*, 4(2):65–75, Mar. 2009.
- P. G. Weyand and M. W. Bundle. Point: Artificial limbs do make artificially fast running speeds possible. *Journal of applied physiology*, 108(4):1011–2; discussion 1014–5, Apr. 2010.

- M. M. Williamson. *Series Elastic Actuators*. Master thesis, MIT, 1995.
- D. Winter. Human balance and posture control during standing and walking. *Gait & Posture*, 3(4):193–214, Dec. 1995.
- G. Wyeth. Control issues for velocity sourced Series Elastic Actuators. In *Proceedings of the Australasian Conference on Robotics and Automation*, June 2006.
- D. Zhou, K. H. Low, and T. Zielinska. An efficient foot-force distribution algorithm for quadruped walking robots. *Robotica*, 18(04):403–413, 2000.
- M. Zinn, B. Roth, O. Khatib, and J. K. Salisbury. A New Actuation Approach for Human Friendly Robot Design. *The International Journal of Robotics Research*, 23(4):379–398, Apr. 2004.
- M. Zucker, N. Ratliff, M. Stolle, J. Chestnutt, J. A. Bagnell, C. G. Atkeson, and J. Kuffner. Optimization and learning for rough terrain legged locomotion. *The International Journal of Robotics Research*, 30(2):175–191, Jan. 2011.

Curriculum Vitae

Marco Hutter was born in Kriessern, Switzerland on August 10th, 1985. He holds a Master of Science in Mechanical Engineering from ETH Zurich and is currently pursuing a PhD at the Autonomous System Lab at ETH Zurich under supervision of Prof. Roland Siegwart.

Marco Hutter's research interest include dynamic locomotion with legged robots, whereby he is working on the hardware design, compliant actuation principles, as well as on model-based control of walking and running gaits.

Preliminary projects included modeling of soft-magnetic MEMS devices in magnetic fields for real-time control at the Multi-Scale Robotics Lab of Prof. Brad Nelson (2007) and a year long collaborative project between ThyssenKrupp-Presta and the Institute of Control under the lead of Prof. Lino Guzzella (2007-2008). From October to December 2009 he was a visiting scholar at the group of Prof. Oussama Khatib at the Artificial Intelligence Laboratory at Stanford University where he worked on Operational Space Control techniques for quadrupedal locomotion. In July 2011 he co-organized the international summer school "Dynamic Walking and Running with Robots" at ETH Zurich.

Marco Hutter got an *Outstanding D-MAVT Bachelor Award* for the best bachelor degree in 2008 as well as the *Willi Studer Award* in 2009 for the best master degree both in Mechanical Engineering. During the master studies, he was part of the *Excellence Scholarship and Opportunity Programme* of ETH Zurich. He was further awarded with the *Hans-Eggenberger-Prize* in 2012 for his master thesis and got major funding for the hardware development of *StarETH*.



List of Publications

Journals

- M. Hutter, C. D. Remy, M. A. Hoepflinger, and R. Siegwart. Efficient and Versatile Locomotion With Highly Compliant Legs. *IEEE/ASME Transactions on Mechatronics*, 18(2):449–458, 2013c
- C. D. Remy, M. Hutter, M. Hoepflinger, M. Bloesch, C. Gehring, and R. Siegwart. Quadrupedal Robots with Stiff and Compliant Actuation. *at - Automatisierungstechnik*, 60(11):682–691, Nov. 2012b
- C. D. Remy, O. Baur, M. Latta, A. Lauber, M. Hutter, M. H. Hoepflinger, C. Pradalier, and R. Siegwart. Walking and crawling with ALoF: a robot for autonomous locomotion on four legs. *Industrial Robot: An International Journal*, 38(3):264–268, 2011a

Conferences

- M. Bloesch, C. Gehring, P. Fankhauser, M. Hutter, M. Hoepflinger, and R. Siegwart. Robust State Estimation for Legged Robots. In *IEEE/RSJ International Conference on Intelligent Robots and Systems (IROS)*, 2013a
- P. Fankhauser, M. Hutter, C. Gehring, M. Bloesch, M. Hoepflinger, and R. Siegwart. Reinforcement Learning of Single Legged Locomotion. In *IEEE/RSJ International Conference on Intelligent Robots and Systems (IROS)*, 2013
- M. Hutter, C. Gehring, M. H. Hoepflinger, M. Bloesch, and R. Siegwart. Walking and Running with StarLETH. In *International Symposium on Adaptive Motion of Animals and Machines (AMAM)*, Darmstadt, Germany, 2013a **best hardware presentation award**
- M. A. Hoepflinger, M. Hutter, C. Gehring, M. Bloesch, and R. Siegwart. Unsupervised Identification and Prediction of Foothold Robustness. In *International Conference on Robotics and Automation (ICRA)*, 2013
- C. Gehring, S. Coros, M. Hutter, M. Bloesch, M. H. Hoepflinger, and R. Siegwart. Control of Dynamic Gaits for a Quadrupedal Robot. In *IEEE International Conference on Robotics and Automation (ICRA)*, Karlsruhe, Germany, 2013

- M. Bloesch, M. Hutter, M. Hoepflinger, C. Gehring, and R. Siegwart. Kinematic Batch Calibration for Legged Robots. In *IEEE International Conference on Robotics and Automation (ICRA)*, Karlsruhe, Germany, 2013b
- M. A. Hoepflinger, D. Baschung, C. D. Remy, M. Hutter, R. Siegwart, N. Hoch, and B. Werther. Parcelbot: A Tracked Parcel Transporter with High Obstacle Negotiation Capabilities. In *International Conference on Climbing and Walking Robots (CLAWAR)*, pages 831–838, 2012
- M. Hutter, C. Hostenstein, D. Fenner, C. D. Remy, M. H. Hoepflinger, and R. Siegwart. Improved Efficiency in Legged Running Using Lightweight Passive Compliant Feet. In *International Conference on Climbing and Walking Robots (CLAWAR)*, pages 491–498, 2012c **highly commended paper award**
- M. Hutter, C. Gehring, M. Bloesch, M. H. Hoepflinger, C. D. Remy, and R. Siegwart. StarlETH: a Compliant Quadrupedal Robot for Fast, Efficient, and Versatile Locomotion. In *International Conference on Climbing and Walking Robots (CLAWAR)*, pages 483–490, 2012a **best student paper award**
- M. Hutter, M. H. Hoepflinger, C. D. Remy, and R. Siegwart. Hybrid Operational Space Control for Compliant Legged Systems. In *RSS Robotics Science and Systems*, Sydney, Australia, 2012b **NCCR robotics honorable mention award**
- M. Bloesch, M. Hutter, M. H. Hoepflinger, S. Leutenegger, C. Gehring, C. D. Remy, and R. Siegwart. State Estimation for Legged Robots - Consistent Fusion of Leg Kinematics and IMU. In *Robotics Science and Systems (RSS)*, Sydney, Australia, 2012a
- M. Latta, C. D. Remy, M. Hutter, M. A. Hoepflinger, and R. Siegwart. Towards Walking on Mars. In *Advanced Space Technologies for Robotics and Automation (ASTRA)*, Noordwijk, The Netherlands, 2011
- M. A. Hoepflinger, C. D. Remy, M. Hutter, and R. Siegwart. Extrinsic RGB-D Camera Calibration for Legged Robots. In *International Conference on Climbing and Walking Robots (CLAWAR)*, pages 94–101, Nagoya, Japan, 2011
- M. Hutter, C. D. Remy, M. H. Hoepflinger, and R. Siegwart. High Compliant Series Elastic Actuation for the Robotic Leg ScarlETH. In *International Conference on Climbing and Walking Robots (CLAWAR)*, pages 507–514, Paris, Fr, 2011c **highly commended paper award**

- M. Hutter, C. D. Remy, M. H. Hoepflinger, and R. Siegwart. ScarLETH: Design and Control of a Planar Running Robot. In *IEEE/RSJ International Conference on Intelligent Robots and Systems (IROS)*, pages 562–567, San Francisco, USA, 2011b **best paper finalist**
- C. D. Remy, M. Hutter, and R. Siegwart. Passive Dynamic Walking with Quadrupeds - Extensions towards 3D. In *International Conference on Robotics and Automation (ICRA)*, pages 5231–5236, Anchorage, AK, 2010b
- C. D. Remy, O. Baur, M. Latta, A. Lauber, M. Hutter, M. H. Hoepflinger, C. Pradalier, and R. Siegwart. Walking and Crawling with ALoF - A Robot for Autonomous Locomotion On Four Legs. In *International Conference on Climbing and Walking Robots (CLAWAR)*, pages 501–508, Nagoya, Japan, 2010a **industrial robot innovation award**
- M. Hutter, C. D. Remy, M. H. Hoepflinger, and R. Siegwart. SLIP Running with an Articulated Robotic Leg. In *International Conference on Intelligent Robots and Systems (IROS)*, pages 4934–4939, Taipei, Taiwan, 2010b
- M. Hutter, C. D. Remy, M. H. Hoepflinger, and R. Siegwart. Full State Control of a SLIP Model by Touchdown Detection. In *International Conference on Climbing and Walking Robots (CLAWAR)*, pages 533–540, Nagoya, Japan, 2010a
- M. H. Hoepflinger, C. D. Remy, M. Hutter, L. Spinello, and R. Siegwart. Haptic Terrain Classification for Legged Robots. In *International Conference on Robotics and Automation (ICRA)*, pages 2828–2833, Anchorage, AK, 2010c
- M. H. Hoepflinger, C. D. Remy, M. Hutter, and R. Siegwart. The quadruped ALoF and a step towards real world haptic terrain classification. In *Mechatronics 2010*, Zurich, Switzerland, 2010b
- M. H. Hoepflinger, C. D. Remy, M. Hutter, and R. Siegwart. Haptic Terrain Classification on Natural Terrains for Legged Robots. In *International Conference on Climbing and Walking Robots (CLAWAR)*, pages 785–792, Nagoya, Japan, 2010a
- M. Hutter, C. D. Remy, and R. Siegwart. Design of an Articulated Robotic Leg with Nonlinear Series Elastic Actuation. In *International Conference on Climbing and Walking Robots (CLAWAR)*, Istanbul, Turkey, 2009a
- M. Hutter, C. D. Remy, and R. Siegwart. Adaptive Control Strategies for Open-loop Dynamic Hopping. In *International Conference on Intelligent Robots and Systems (IROS)*, St Louis, MO, 2009c

- Z. Nagy, O. Ergeneman, J. J. Abbott, M. Hutter, A. M. Hirt, and B. J. Nelson. Modeling assembled-MEMS microrobots for wireless magnetic control. In *IEEE International Conference on Robotics and Automation (ICRA)*, pages 874–879, 2008

Workshops

- M. Hutter, C. Gehring, and R. Siegwart. Multi-task inverse dynamics based on LS-optimization. In *Dynamic Walking Meeting*, 2013b
- M. Bloesch, M. Hutter, C. D. Remy, and R. Siegwart. Consistent Fusion of Leg Kinematics and Inertial Measurements for Legged State Estimation. In *Dynamic Walking*, Pensacola, FL, 2012b
- M. Hutter and R. Siegwart. Hybrid Operational Space Control for Compliant Quadruped Robots. In *Dynamic Walking Meeting*, Pensacola, FL, 2012
- C. D. Remy, M. Hutter, M. H. Hoepflinger, and R. Siegwart. ScarLETH, StarLETH, and Pegasus. In *Dynamic Walking Meeting*, Jena, D, 2011b
- M. Hutter and R. Siegwart. Template Based Running with an Articulated Robotic Leg. In *Dynamic Walking Meeting*, Boston, USA, 2010
- M. Hutter, C. D. Remy, and R. Siegwart. Open-loop control strategies in passive dynamic hopping. In *Dynamic Walking Meeting*, Burnaby, Canada, 2009b

Reports

- M. Hutter, C. Gehring, and R. Siegwart. proNEu: Derivation of Analytical Kinematics and Dynamics. Technical report, Autonomous Systems Lab, ETHZ, 2011a
- M. Hutter. Hopping with an Articulated Robotic Leg. Master Thesis, ETH Zurich, 2009